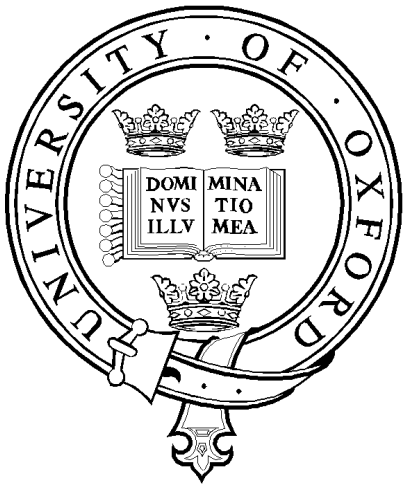
VARIABLE DENSITY SHALLOW FLOW MODEL FOR FLOOD SIMULATION



ILEKTRA – GEORGIA APOSTOLIDOU
WOLFSON COLLEGE
TRINITY TERM, 2011

Thesis submitted for the degree of Doctor of Philosophy at the University of Oxford

Department of Engineering Science
University of Oxford

VARIABLE DENSITY SHALLOW FLOW MODEL FOR FLOOD SIMULATION

Thesis submitted for the degree of Doctor of Philosophy at the University of Oxford
by Ilektra – Georgia Apostolidou, Wolfson College, Trinity Term 2011

ABSTRACT

Flood inundation is a major natural hazard that can have very severe socio-economic consequences. This thesis presents an enhanced numerical model for flood simulation. After setting the context by examining recent large-scale flood events, a literature review is provided on shallow flow numerical models. A new version of the hyperbolic horizontal variable density shallow water equations with source terms in balanced form is used, designed for flows over complicated terrains, suitable for wetting and drying fronts and erodible bed problems. Bed morphodynamics are included in the model by solving a conservation of bed mass equation in conjunction with the variable density shallow water equations. The resulting numerical scheme is based on a Godunov-type finite volume HLLC approximate Riemann solver combined with MUSCL-Hancock time integration and a non-linear slope limiter and is shock-capturing. The model can simulate trans-critical, steep-fronted flows, connecting bodies of water at different elevations.

The model is validated for constant density shallow flows using idealised benchmark tests, such as unidirectional and circular dam breaks, damped sloshing in a parabolic tank, dam break flow over a triangular obstacle, and dam break flow over three islands. The simulation results are in excellent agreement with available analytical solutions, alternative numerical predictions, and experimental data. The model is also validated for variable density shallow flows, and a parameter study is undertaken to examine the effects of different density ratios of two adjacent liquids and different hydraulic thrust ratios of species and liquid in mixed flows. The results confirm the ability of the model to simulate shallow water-sediment flows that are of horizontally variable density, while being intensely mixed in the vertical direction. Further validation is undertaken for certain erodible bed cases, including deposition and entrainment of dilute suspended sediment in a flat-bottomed tank with intense mixing, and the results compared against semi-analytical solutions derived by the author.

To demonstrate the effectiveness of the model in simulating a complicated variable density shallow flow, the validated numerical model is used to simulate a partial dam-breach flow in an erodible channel. The calibrated model predictions are very similar to experimental data from tests carried out at Tsinghua University. It is believed that the present numerical solver could be useful at describing local horizontal density gradients in sediment laden and debris flows that characterise certain extreme flood events, where sediment deposition is important.

AKNOWLEDGEMENTS

The work described in this thesis would have not been complete without the invaluable contribution of many people. I would like to thank above all Prof Alistair Borthwick for his constant supervision, helpful comments, and support. It was without doubt one of the most fruitful collaborations I have ever experienced and I am grateful for the luck I had to be under his guidance, and for his patience, motivation, enthusiasm, and immense knowledge.

Also, special acknowledgement is given to Prof Paul Taylor, whose suggestions as co-supervisor, provided solutions to many initially seeming unsolvable problems. His great perception of the nature of the problems and his positive criticism resulted to a more coherent result.

I would like to thank especially Prof Richard Soulsby, who played a crucial role for the development of the final outcome with his positive contribution to the erodible bed problems and the final formulation of the governing equations. Prof. Soulsby invariably offered helpful advice based on his considerable experience of sediment transport in environmental flows.

Besides, I would like to thank everyone in the OCEAN group for the stimulating discussions, for the endless support and for all the fun we have had in the last three years. Special thanks to Jana Orszaghova, my "Oxford sister", and to Tom Adcock for being there from the beginning till the end, and to Kuo Yan, Myron Van Damme and Mohammed Haniffah for their patience and for making our office a more enjoyable place to work. I would also like to thank Prof Rodney Eatock Taylor for contributing so much to the pleasant research environment of the Ocean Engineering Group.

My sincere thanks also go to "The Academy of Athens" (Greece) for giving me the opportunity to come to Oxford by providing a generous scholarship for the first two years of my DPhil.

Furthermore, I could never make it without the wonderful friends that made my oxford experience unforgettable. From Wolfson College, to the Mansion, Bath Street and OUWLRC, you all deserve my eternal gratitude

Last but not the least; I would like to thank my family for their endless love, support, encouragement and for being proud of me. I would finally like to dedicate this work to my grandmother.

CONTENTS

CHAPTER 1 INTRODUCTION AND LITERATURE REVIEW 1

1.1. Introduction 1

1.2. Literature review on Shallow Flow Variable Density Numerical Models 13

1.3. Aims and Objectives 20

1.4. Synopsis 22

CHAPTER 2 HORIZONTAL VARIABLE DENSITY SHALLOW WATER EQUATIONS 23

2.1. Introduction 23

2.2. Mathematical Description 24

2.2.1. Derivation of Horizontal Variable Density Shallow Water Equations 24

2.2.1.1. One-Dimensional Horizontal Variable Density Shallow Water Equations 25

2.2.1.2. Two-Dimensional Horizontal Variable Density Shallow Water Equations 33

2.2.2. Boundary Conditions 40

2.2.3. Concluding Remarks 41

CHAPTER 3 NUMERICAL SOLVER OF HORIZONTAL VARIABLE DENSITY SHALLOW WATER EQUATIONS 43

3.1. Godunov-type Solver of the Horizontal Variable Density Shallow Water Equations 43

3.1.1. Finite Volume Method 43

3.1.2. The HLLC Approximate Riemann Solver 45

3.1.3. Discretisation of Source Terms 48

3.1.4. The MUSCL–Hancock Method 48

3.1.5. Slope Limiter 50

3.1.6. Stability and Convergence 52

3.2. Wetting and Drying 53

3.3. Entrainment and Deposition 56

3.4. Hyperbolic Stage-Discharge form of Horizontal Variable Density Shallow Water Equations 57

3.5. Boundary Conditions 62

CHAPTER 4 ONE-DIMENSIONAL MODEL VALIDATION TESTS 67

4.1. Introduction 67

4.2. Constant Density Cases 67

4.2.1. Case 1: Dam-break 68

4.2.2. Case 2: Two rarefaction waves over a nearly dry bed 69

4.2.3. Case 3: Right dry bed and left dry bed Riemann problem 69

4.2.4. Case 4: Generation of a dry bed by opposing rarefaction waves 70

4.2.5. Case 5: Damped free surface oscillations in a tank with parabolic bed 70

4.2.6. Case 6: Dam break problem and flow over a triangular obstacle 72

4.3. Variable Density Cases 73

4.3.1. Case 7: Quiescent equilibrium in a tank with a sinusoidal bed 74

4.3.2. Case 8: 1-D density dam break with a single initial discontinuity 75

4.3.3. Case 9: Symmetric 1-D density dam break with two initial discontinuities 77

4.4. Erodible Bed Cases 83

4.4.1. Case 10: Deposition of dilute suspended sediment in a flat-bottomed tank with intense mixing but no net flow and no entrainment of sediment 84

4.4.2. Case 11: Entrainment of dilute suspended sediment in a flat-bottomed tank with intense mixing but no net flow and no deposition of sediment 91

4.4.3. Case 12: Simultaneous deposition and constant entrainment of dilute

suspended sediment in a flat-bottomed tank with intense mixing but no net flow 95

4.4.4. Case 13: Dam break problem and flow over a triangular obstacle with erodible bed 103

4.5. Concluding Remarks 107

CHAPTER 5 TWO-DIMENSIONAL MODEL VALIDATION TESTS 136

5.1. Introduction 136

5.2. Constant Density Cases 136

5.2.1. Case 14: Right, left, north and south dry bed Riemann problem 136

5.2.2. Case 15: Circular dam break problem 137

5.2.3. Case 16: 2-D dam break problem and flow over three islands with wetting and drying fronts 138

5.3. Variable Density Cases 139

5.3.1. Case 17: Variable density circular dam break 140

5.4. Erodible Bed Cases 146

5.4.1. Case 18: Deposition of dilute suspended sediment in a flat-bottomed 2-D tank with intense mixing but no net flow and no entrainment of sediment 147

5.4.2. Case 19: Entrainment of dilute suspended sediment in a flat-bottomed 2-D tank with intense mixing but no net flow and no deposition of sediment 147

5.4.3. Case 20: Simultaneous deposition and constant entrainment of dilute suspended sediment in a flat-bottomed 2-D tank with intense mixing but no net flow 148

5.4.4. Case 21: 2-D dam break problem and flow over a triangular obstacle with wetting and drying fronts and erodible bed 148

5.4.5. Case 22: 2-D dam break problem and flow over three islands with wetting

and drying fronts and erodible bed 150

5.5. Concluding Remarks 152

CHAPTER 6 DEMONSTRATION CASE STUDY 179

6.1. Simulation of Partial Dam-Breach Flow in an Erodible Channel 179

CHAPTER 7 CONCLUSIONS AND RECOMMENDATIONS 194

7.1. Conclusions 194

7.2. Recommendations 199

REFERENCES 204

LIST OF NOTATION

c	volumetric concentration of the species or celerity of the small amplitude surface waves
C	Chézy coefficient
C_{cfl}	Courant-Friedrichs-Lewy number
c_{eq}	the concentration of the species at the quiescent equilibrium state
c_{f}	bed friction coefficient
D	sediment deposition flux
d	median diameter
D_*	dimensionless grain size
E	sediment entrainment flux
$\mathbf{e_1}$, $\mathbf{e_2}$, $\mathbf{e_3}$	Eigenvectors of Jacobian matrix
$\mathbf{f}$	vector of the flux through the cell interfaces in the x-direction
$\mathbf{f}_*$	middle region fluxes of the shear wave for the HLLC approximate Riemann solver
Fr	Froude number
g	acceleration due to gravity
$\mathbf{g}$	vector of the flux through the cell interfaces in the y-direction
h	liquid-species mixture level above the level of the bed
h_{s}	still water depth
h_*	liquid-species mixture level above the level of the bed in the middle region of the Riemann state of the HLLC solver
i	index of the cell in the x-direction
j	index of the cell in the y-direction
$\mathrm{J_n}$	Jacobian matrix
L	length
M	entrainment constant
n	Manning coefficient
$\mathbf{n}$	vector normal to the boundary
p	porosity of the bed
q	discharge per unit width of the mixture
r	ratio of successive gradients on the solution mesh
$\mathbf{r}$	vector of the distance between (x,y) and the centre of the cell for the slope limiter
R	radius or Reynolds number
$\mathbf{s}$	vector of the source terms
s	ratio of densities of grain (sediment) to water
S_L	estimates of the speeds of the left wave of the HLLC approximate Riemann solver
S_M	estimates of the speeds of the middle (contact) wave of the HLLC approximate Riemann solver
S_R	estimates of the speeds of the right wave of the HLLC approximate Riemann solver
t	time

T	time constant
u	velocity along the horizontal Cartesian axes
$\mathbf{u}$	vector of the dependent conserved variables
u_*	friction velocity or velocity of the middle region of the Riemann state of the HLLC solver
u_b	velocity of the wet front
v	velocity along the vertical Cartesian axes
w	width
w_s	settling velocity of the sediment relative to the fluid
x	coordinate distance along the horizontal Cartesian axes
$x_\mathrm{b}(t)$	position of the moving shoreline at time t
$x_{\mathrm{b}0}$	initial shoreline position
y	coordinate distance along the vertical Cartesian axes
z_b	level of the bed above a given datum
α	empirical coefficient for the calculation of the entrainment of the sediment
β	slope limiter parameter
Δt	time step
Δx	side length of the Cartesian grid cell in the x-directions
Δy	side length of the Cartesian grid cell in the y-directions
ζ	free surface elevation above the still liquid level
η	surface liquid-species mixture level above a given datum
η_s	the surface water level above a given datum at the quiescent equilibrium state
θ	Shields parameter
θ_c	threshold Shields parameter
λ	the wave propagation speed
$\lambda_1, \lambda_2, \lambda_3$	eigenvalues of Jacobian matrix
ν	kinematic viscosity of water
ρ	density of liquid-species mixture
ρ_0	density of the saturated bed
ρ_eq	the density of the liquid-species mixture at the quiescent equilibrium state
ρ_s	density of the species
ρ_w	density of the liquid
τ_b	bed stress
τ_c	threshold shear stress of the bed
τ_w	surface stress
$\Phi(r)$	function of the ratio of gradients for the slope limiter

CHAPTER 1 INTRODUCTION AND LITERATURE REVIEW

This chapter presents a general background to numerical flood modelling, a literature review on shallow flow variable density numerical solvers, as well as the aim, the objectives and the synopsis of the thesis.

1.1. Introduction

Flooding has four main sources and is often a natural event. River (fluvial) flooding occurs as a result of water overflowing the banks of river channels. Surface water (pluvial) flooding happens when natural and man-made drainage systems have insufficient capacity to deal with the volume of rainfall. Groundwater flooding occurs when the level of water underground rises above the phreatic surface. Coastal flooding is experienced when the sea level, surge or waves overtop coastal defences and inundate the land beyond. In flood events, excess water is not restrained by the usual boundaries (such as river embankments) and follows the path of least resistance. Areas that are low lying and close to the source of a flood are therefore the most vulnerable. Flash floods may occur when the rainfall rate exceeds the capacity of storm sewers and instead rainwater collects on the ground. A typical example is surface water run-off at the bottom of a hill. Localised flooding mainly happens when the ground cannot absorb any more water in a particular area, or if sewers and underground drains become blocked or cannot cope with the excess water trying to drain into them.

In a study of flood and other natural hazards over the decade from 1988 to 1997, Berz (2000) observed the following:

"(1) Floods account for about a third of all natural catastrophes. (2) They cause more than half of the fatalities. (3) They are responsible for a third of the overall economic loss. (4) Their share in insured losses is relatively small, with an average of less than 10%."

The extreme figures in terms of total economic loss and fatalities are a result of the accumulation of values in the widespread flooded areas or/and where long-lasting events occurred. The percentage of insured losses is proportionally small mainly because the more severe events occur in developing countries where the insurance density is relatively low. Similarly, in the industrial countries, where the insurance density is higher, the insured losses are slightly increased but still not proportional to the amount of losses encountered. Another reason for the above is the difficulty for individual insurance against flood, which is expected to change with the adoption of all-risk covers.

The occurrence of major flooding events is influenced by the climate variability. Extreme values of rainfall depend on the natural variability of weather systems, which may be exacerbated by the influence of climate change on long-term trends. Areas identified by the Intergovernmental Panel on Climate Change (Bates, 2008) as most vulnerable to such hydrological impacts are the least developed countries and small island developing states, low lying densely populated coastal areas, areas affected by glacier melt, and arid areas with fragile populations, economies and environments. Changes in weather systems (El Niño/La Niña-Southern Oscillation), earthquakes, and tsunamis are responsible for a great number of water related disasters.

Human and property losses caused by floods throughout history have been enormous, even during the 20th century. The 1931 floods in Central China are considered the deadliest natural disaster ever recorded (Pietz, 2002), with an estimated death toll between

3.7 million to 4 million people. China has been struck by severe floods many times the last two centuries (in 1887, 1911, 1935, 1938, 1939, 1954, 1975), with recorded fatalities ranging from 20 thousand to 2 million people for a given event (Winchester, 1996). Between the 11th and the 18th century Netherlands experienced numerous floods causing the loss of 1,500 to 100,000 lives due to a single event (Lambert, 1971). Other countries that faced some of the deadliest floods during the 20th century include Bangladesh (1974, 28,700 deaths), Venezuela (1999, 20,006 deaths), Iran (1954, 10,000 deaths), Peru (1941, 5,000 deaths), India (1943 and 1968, 5,000 deaths each, 1998 and 2004, 3,000 deaths each) and Afghanistan (1992, 3,000 deaths). The recent 9.0-magnitude earthquake that hit the Pacific coastal areas of north-eastern and eastern Japan on the 11th of March 2011 caused an enormous tsunami, which left 14,435 people dead and 11,601 others unaccounted for.

There are many other examples of flood events occurring during the last two decades in Europe. In France 42 people died in 1992 during flash flooding in Vaison–la–Romaine. Extensive floods caused widespread disruption and losses in the Rhine and Meuse basins in 1992, 1993 and 1995. Exceptional flooding struck the river Po in Italy in 1994. In 1997, severe flooding occurred in several parts of Europe, both as localised flash floods and as basin–wide floods on major river systems, causing loss of life, disruption to utility networks and damage to properties. The year started with flash flooding in Athens in mid–January, and then in July exceptional rainfall in the Czech Republic and Poland caused catastrophic flooding of the river Oder, killing over 100 people and laying waste vast areas of the countryside. Again, in early November 1997, flash floods occurred in Spain and Portugal with over 20 people losing their lives. Outside Europe, in the 1990s, severe flooding devastated the Mississippi basin, and thousands of lives were lost directly or indirectly from flooding in many countries including Bangladesh, China, Guatemala, Honduras, Somalia and South Africa (White, 2001). Worldwide, floods pose one of the most widely distributed

natural risks to life, whereas other natural hazards such as avalanche, landslide, earthquake and volcanic activity are more regional in their distribution.

Flooding affects countries in different ways depending on climate, governmental structures and socio-economic conditions. The causes and types of flooding may differ for each country – for example, Canada and the United States face flooding from ice thaws, while countries such as Burma or Bangladesh face seasonal monsoon winds which bring massive rainfall. Furthermore, the El Niño of 1997-1998 was particularly strong (Mason et al., 1999) and brought the phenomenon to worldwide attention. The period from 1990-1994 was unusual in that El Niño events occurred in quite rapid succession (but were generally weak) (Trenberth and Hoar, 1996). There is some debate as to whether global warming increases the intensity and/or frequency of El Niño episodes. The effects of El Niño in South America are direct and stronger than in North America. An El Niño event is associated with warm and very wet summers (December-February) along the coasts of northern Peru and Ecuador, causing major flooding whenever the event is strong or extreme. The effects during the months of February, March and April may become critical. Southern Brazil and northern Argentina also experience wetter than normal conditions but mainly during the spring and early summer. Central Chile receives a mild winter with large rainfall, and the Peruvian-Bolivian Altiplano is sometimes exposed to unusual winter snowfall events. Drier and hotter weather occurs in parts of the Amazon River Basin, Colombia and Central America.

In 2007 the world experienced very severe floods. The human cost of all the floods that year was more than 8,000 deaths and over $23 billion worth of damage. The floods that struck much of the United Kingdom during June and July 2007 were extreme, affecting hundreds of thousands of people in England and Wales, and ranked as the most costly worldwide that

year. It was the most serious inland flood in the UK since 1947. In the exceptional events that took place, 13 people lost their lives, approximately 48,000 households and nearly 7,300 businesses were flooded, and billions of pounds of damage were caused. In Yorkshire and Humberside, the Fire and Rescue Service launched the "biggest rescue effort in peacetime Britain" (Hines, 2007). Across Gloucestershire, 350,000 people were left without mains water supply – this was the most significant loss of essential services since the Second World War. Other critical infrastructure was damaged and essential services including power supplies, transport links and telecommunications were disrupted. The exceptionally heavy rain resulted in two severe and disruptive flooding events; the first during the week of 20 June, and the second during the week of 18 July.

In June 2008 Michael Pitt published an Independent Review into the U.K. floods of 2007, one of the widest ranging policy reviews in the U.K. in recent times. According to Pitt (2008):

"Science and engineering is crucial to understanding flood risk and will become even more significant as we adapt to the increased risk that climate change will bring. Last summer's floods demonstrated that the UK has come a long way in terms of weather forecasting and flood prediction, but there is further to go. Predicting where flooding will occur and the potential consequences are vital if managers, emergency planners and responders are to reduce risk and the effects of flooding."

In May 2008, the Sichuan earthquake and its aftershocks caused severe damage in 18 counties in China. The Plateau Meteorological Research Institute in Chengdu warned that the pending summer flood, in tandem with heavy rains, would cause more massive and devastating geological disasters in the earthquake affected region. In Mianzhu and Deyang

cities, evacuation rehearsals have been staged, while the Ministry of Water Resources monitored changes in the rivers and lakes. Furthermore, the earthquake occurred in an area with significantly irregular topography and thus, caused many ruptures and surface displacement, followed by rock falls, landslides and debris flows (Cui et al., 2008). The landslide dams formed by the earthquakes can cause two types of flooding: upstream flooding upon creation, which is slow and is usually responsible for property damage and downstream flooding upon failure which can lead to major damage and loss of life. Also, this kind of dam is unstable, being composed of "large volumes of loosely consolidated material" (Cui et al., 2009).

In July 2010, heavy monsoon rains caused severe flooding in the Khyber Pakhtunkhwa, Sindh, Punjab and Balochistan regions of Pakistan. Almost one-fifth of Pakistan's total land area was submerged under water. According to Pakistan Government data the floods directly affected about 20 million people, mostly by destruction of property, livelihood and infrastructure, and approximately 2,000 deaths occurred. Although the death toll was much lower, the number of individuals affected by the 2010 Pakistan flood exceeds the combined total of individuals affected by the 2004 Indian Ocean tsunami, the 2005 Kashmir earthquake and the 2010 Haiti earthquake (Gulfnews, 2010). Furthermore, the floods caused major failures to the power infrastructure, shortage of clean drinking water, which induced the expansion of diseases (such as malaria and cholera) and generally poor sanitation.

Many countries face challenges with regard to flooding, such as the need to raise risk awareness, adaptation to the variability of weather systems and the implementation of engineering countermeasures (e.g. improved flood defenses and crisis response strategies).

Flood risk is the product of the probability of a flood occurring and the impact or consequences that result. The likelihood of a particular flood happening is usually expressed as a chance or probability over a period of one year. For example, “There is a 1 in 100 chance of flooding in any given year in this location”. It is necessary to know both how high the probability is of a flood occurring and the severity of any impact (which may change depending on how extreme the flood is). The risk to a particular area can be assessed only by determining both for a range of flood events of different size.

Floods are a major problem, which might be affected by changes to the environment. Since only 20% of the natural floodplains in Europe are still functional, and can consequently store water, the only sustainable solution, in order to reduce the risk of destructive floods, is to cooperate with nature and find ways to turn natural disasters into opportunities that can benefit humanity.

Of course floods are natural phenomena that cannot be avoided (McMichael, 1996; Whetton, 1993), but their risk can be minimised. It seems, however, that the already existing engineering solutions are insufficient. The two main values that interest researchers and engineers are the depth of the water and the flow velocity. Numerical models used to simulate inundation can predict flood extent, depth and local velocities over the bed topography of the area of interest. Typically, simulations are run for many different combinations of flood magnitude and types of flow in order to build up statistics of flood depth, etc. The results obtained can be assessed and used for the design of flood risk maps and evacuation plans. Knowledge of which communities are most vulnerable to flooding, leads to the evaluation of flood defences or other measures that can eliminate or reduce flood risk. So the improvement of flood simulation is an essential part of this process.

Land and water play a natural role in the management of flood risk, by holding water in flooding basins and terrains, which can function as sponges (absorbing and storing the additional water and releasing it gradually afterwards). But those areas can no longer play this role, when they are either dried out or overexploited. When rivers are narrowed and transformed into channels, the consequences of the extreme flows increase, because the water cannot escape, and floods the banks or breaks the dams, causing major disasters. Every project should be accompanied by a flood risk assessment, which should be used for determining for the continuation or rejection of the work.

The European Union has already ratified laws that could mitigate the consequences of the floods in a more natural way. The application of these laws demands the common management of land and water in a flood basin, in order to improve their ecological state. Predictive models that can simulate the prospective flood effectively can help in planning and decision making.

There is no overall lack of water on Earth but there is poor management of existing water reserves, which are unequally distributed (Wild, 2010). Possible ways of improving the above situation are the following: (i) channel the excessive rainfall water, store it in natural or artificial reservoirs and then provide it for agricultural or other rural or urban uses, for the production of hydroelectric power or/and for recreational activities, (ii) ensure that the ground and underground runaway paths are not blocked and that the manmade infrastructure is not preventing the natural circulation of runoff water, (iii) plan the urban and rural land uses and development according to the flood risk vulnerability. Thus, models that can help solve this imbalance and inform the proper redistribution of the water are of considerable value.

Amongst the many recommendations of the Pitt Review, the following three points highlight the need for development in the field of flood modelling:

1. *"The Environment Agency should further develop its tools and techniques for predicting and modelling river flooding, taking account of extreme and multiple events and depths and velocity of water."*
2. *"The Government should commit to a strategic long-term approach to its investment in flood risk management, planning up to 25 years ahead."*
3. *"There is a continuing programme of work to improve the indicative flood maps. As flood models are improved and more detailed information on defences (and the areas that benefit from them) is assimilated, results will be fed into this improvement work."*

The previous Foresight Future Flooding Study (2004) provided visions of flood risk in the UK over a 30 to 100 year timescale to help inform long-term policy. There are two main changes to the risks faced from climate change since the assessment in 2004, which are: (1) the potential increases in rainfall volume and intensity, and temperature, are greater than previously assumed; and (2) there is a greater risk of extreme sea-level rise. The Foresight Report highlights the following key policy issues: intra-urban flood risk will increase; land use is an important tool in managing flood risk, uncertainty in a changing climate; investment will be required to sustain and improve flood risk management; strong governance will be required to implement a range of flood risk management solutions.

Typical flood defences include embankments, walls, weirs, sluices and pumping stations. Of these, some may only be brought into operation when a high tide or flood is forecast or in progress. Again knowledge of flood evolution is necessary for programming all the above measures. Through flood risk management, the probability of flooding from rivers and the sea can be reduced by improved management of land, river systems, and flood and coastal

defences. The damage caused by floods can be reduced through effective land use planning, flood warning and emergency responses.

According to the High-Level Expert Panel on Water and Disaster action plan (2009):

"Natural hazards are inevitable: high death and destruction tolls are not. Ill-advised human activity can both create and accelerate the impact of water-related disasters. These water threats have been increasing with climate change and human activities, in the North and South of our planet, from East to West. But, with preparedness and planning, fatalities and destruction can be decreased. The global community has committed itself to the principles of coherent disaster prevention and response. The need is now for concrete and significant changes to make this happen."

Hydraulic engineers are in charge of estimating the potential flood inundation of a given area (usually a river basin). For the majority of projects, there are insufficient observations available of past flood inundation extent, and consequently the challenge for researchers is to construct a predictive 'model' (Bates, 2000). The type, complexity and content of this model can vary significantly. For example, results can be obtained by simply intersecting a plane representing the water surface with a Digital Elevation Model (DEM) of sufficient resolution to give the flooded area (see for example Priestnall et al., 2000), or by solving the full three-dimensional Navier–Stokes equations with sophisticated turbulence closure (see for example Thomas and Williams, 1995; Younis, 1996).

Severe challenges have to be overcome in order to create an accurate and realistic model. These include the representation of complex topography, presence of species or sediment, variations in density, multi dimensionality, and non-linear hydrodynamic behaviour.

According to Bates (2000), especially, in shallow water flows, “small errors in modelled water surface elevations may lead to large errors in the predicted inundation front position”. This means, that a successful shallow water flow model should include a robust algorithm for the simulation of the wet-dry front of the flow.

Moreover, the choice of the one-, two-, or three-dimensionality of the model is important for the outcome and should be examined separately for each case, depending on the nature of the problem, the data and the resources available. One-dimensional models involve less computational cost but cannot simulate flows that are dominated from more than a single direction.

In general, a flood model comprises a hydrological model and a hydraulic model. The hydrological model determines the runoff following a particular rainfall event, a dam break or an incident that involves release of water (Abbott, 1992; Anderson and Bates, 2001). The primary output from the hydrologic model consists of hydrographs at various locations along the waterways to describe the quantity, rate and timing of stream flow due to rainfall events (Beven, 2001). So, the hydrological approach involves flood routing (Chow et al., 1988). These hydrographs then become a key input into the hydraulic model. The hydraulic model simulates the movement of flood waters through waterway reaches, storage elements, and hydraulic structures (Singh, 1996). The hydraulic model calculates flood levels and flow patterns and also simulates the complex effects of backwater, overtopping of embankments, waterway confluences, bridge constrictions and other hydraulic structure behaviour (Néelz and Pender, 2007). The calculations are based on mass and momentum conservation. Hydraulic models are more accurate but also more expensive than the hydrological models. The complicated nature of the floodplain flow patterns and importance of obtaining

community confidence in the process require that state-of-the-art modelling techniques be adopted (Bates et al., 2005; Horritt and Bates, 2002).

Hydrologists are often faced with the challenge of predicting the timing and magnitude of rainfall-generated run-off from watersheds for flood control, pollution prevention and ecological purposes (Fiedler and Ramirez, 2000). An important component of the rainfall run-off process is Hortonian overland flow, which is the shallow flow of water over the land surface prior to the major channelization that results when the rainfall rate exceeds the soil infiltration capacity in at least some areas of the watershed. In reality, the resulting overland flow depths and velocities are highly variable and discontinuous in space and time as a result of small-scale ground surface unevenness (microtopography) and natural spatial variation of soil hydraulic properties. In part, because of numerical difficulties associated with simulating this process, hydrologic modellers have traditionally been forced to simulate complex hill slopes as plane surfaces with constant hydraulic properties using simplified equations (Emmett, 1970). Most often, the kinematic wave approximation to the full hydrodynamic equations is used (Singh, 2001). This approach, however, does not explicitly account for microtopography and spatially variable soil properties, thus the small-scale dynamic interactions between surface and subsurface flow are ignored. The kinematic wave and infiltration model parameters are then simply fitting parameters, requiring calibration data, and physically based run-off predictions are accordingly difficult (Fiedler and Ramirez, 2000).

Various efforts have been made to simulate shallow flow processes. The numerical models that have been developed vary in structure and basic principles. The next section presents a review of shallow flow models and their common characteristics.

1.2. Literature Review on Shallow Flow Variable Density Numerical Models

The general characteristic of shallow flows is that the vertical dimension is much smaller than any typical horizontal scale. Such flows are nearly horizontal, which allows a considerable simplification in the mathematical formulation and numerical solution by assuming the pressure distribution to be hydrostatic. However, such flows are not exactly two–dimensional. For example, the flow must have a three–dimensional structure due to the bed boundary layer and associated bottom friction (Vreugdenhil, 1994). Moreover, density stratification due to differences in temperature or salinity causes variations in the third (vertical) direction. Yet, in many shallow water flows these three-dimensional effects can be neglected and it is sufficient to consider the depth–averaged form, which is two–dimensional in the horizontal plane.

Laplace (1775) derived tidal equations, which are a reduced form of the shallow water equations, by considering mass and momentum conservation of water. In the French scientific community, the shallow water equations are commonly referred to as the Saint–Venant (1871) equations, although it appears that Saint–Venant derived only the one–dimensional version (Dronkers, 1964). Boussinesq (1887) and Lamb (1932) derived early versions of the shallow water equations. Modern derivations of the full nonlinear shallow water equations by depth-averaging the Reynolds averaged mass and momentum conservative equations are given by McDowell and O'Connor (1977), Falconer (1993), Ligget (1994), and Dean and Dalrymple (1984) amongst others.

The numerical solution of the shallow water equations was one of the early applications of digital computers from the late 1940s onwards, with simulations were undertaken by Charney et al. (1950) for atmospheric flows and Hansen (1956) for oceanographic flows.

Considerable development has taken place since the 1950s, and nowadays many advanced models are available based on the two–dimensional SWEs (Shallow Water Equations), e.g. ADCIRC, Mike21**,** Telemac 2D**,** Delft2D**.** Examples of the applications of numerical solvers of the SWEs include simulations of tidal flows (Hendershott, 1981), tidal mixing (Ridderrinkhof et al., 1990), residual currents (Nihoul and Ronday, 1975), storm surges (Dube et al., 1985), river flows (Ogink, 1986), flows around structures (Stelling, 1983), dam break waves (Alcrudo and García-Navarro, 1993), coastal flows (Wind and Vreugdenhil, 1986; Brocchini, 2008), tsunamis (Shokin et al., 1989), lake flows (Platzman, 1972), wave propagation (LeVeque, 1997), flows over variable topography (George, 2008) and internal flows (Garvine, 1987).

Abbott (1979) gives a systematic account of the principles of computational hydraulics and their application to free surface flows, as well as an advanced introduction to numerical modelling for hydraulic, coastal and offshore engineering systems.

According to Toro (2001) the hyperbolic inviscid shallow water equations admit solutions that include discontinuities such as shocks (or bores), contact discontinuities (present when modelling pollutant transport, for instance), shear waves and vortices (present in the two–dimensional case) and wet / dry fronts. It is these discontinuous features that pose the greatest challenge to numerical methods. Shock waves are discontinuous solutions of hyperbolic conservation laws obeying certain precise mathematical conditions. The numerical misrepresentation of a feature such as a shock wave can significantly affect, in an adverse manner, a wider region of the flow. For problems involving strong wave interaction, the resulting numerical contamination may spread over the entire flow field. Toro (2001) notes that: “Much effort has been made over a considerable period of time to compute shock waves correctly.” Nowadays, it is recognised that in order to propagate a shock at the correct

speed, one must use conservative numerical methods. In fact, 50 years ago Lax and Wendroff (1960) proved mathematically that conservative numerical methods, if convergent, do converge to correct solutions of the equations; as these are non–unique, an entropy criterion built into the numerical method will ensure that the physically correct solution is computed automatically (see e.g. Burger et al. (2000)).

Toro (1999) classifies shock-capturing schemes under the headings of classical symmetrical methods and high-resolution upwind (modern) methods. Upwind-type differencing schemes attempt to discretize hyperbolic partial differential equations by using differencing biased in the direction determined by the sign of the characteristic speeds. On the other hand, symmetric or central schemes do not consider any information about the wave propagation in the discretization. No matter what type of shock-capturing scheme is used, a stable calculation in the presence of shock waves requires a certain amount of numerical dissipation to avoid the formation of unphysical numerical oscillations. In the case of classical shock-capturing methods, numerical dissipation terms are usually linear and the same amount of artificial viscosity is uniformly applied at all grid points. Classical shock-capturing methods only provide accurate results in the case of smooth and weak-shock solutions, but when strong shock waves are present in the solutions, non-linear instabilities and oscillations can arise across discontinuities. Modern shock-capturing methods have non-linear numerical dissipation, with an automatic feedback mechanism that adjusts the amount of dissipation in any cell of the mesh, in accordance with the gradients in the solution. These schemes have proven to be stable and accurate even for problems containing strong shock waves (Cockburn and Shu, 1994).

Well known classical shock-capturing methods include the MacCormack (1969) method, Lax–Wendroff method (1960), and Beam-Warming method. Examples of modern shock-capturing schemes include higher order Total Variation Diminishing (TVD) schemes

first proposed by Harten (1983), Flux-Corrected Transport scheme introduced by Boris and Book (1976), Monotonic Upstream-centered Schemes for Conservation Laws (MUSCL) based on the Godunov approach and introduced by van Leer (1979), various Essentially Non-Oscillatory schemes (ENO) proposed by Harten et al. (1987), and the Piecewise Parabolic Method (PPM) proposed by Colella and Woodward (1984). Another important class of high resolution schemes belongs to the approximate Riemann solvers proposed by Roe (1981) and by Osher and Sethian (1988). The schemes proposed by Jameson and Baker (1983), where linear numerical dissipation terms depend on non-linear switch functions, fall between the classical and modern shock-capturing methods.

An important factor that may affect flood modelling is the transportation of debris and suspended sediment by the flood. According to Brufau et al. (2000):

"In mountain torrents, intense and localised storms may cause flash floods with important sediment transport. In steep torrents, the sediment discharge may increase so that the solid concentration often exceeds figures of 40-50%. This is the case of the debris flows that transport downstream huge volumes of sediments that are then deposited on the alluvial fans, often highly populated. These wide areas are periodically exposed to catastrophic events. To reduce the debris flow hazard, it is common to couple structural and non structural protections such as zoning of the risk prone areas and emergency plans. Protection plans require the description of scenarios that can be defined only by means of simulations with mathematical models".

Many environmental free surface shallow water flows carry suspended sediment, debris, or other materials that can affect the Newtonian properties of the fluid. In order to model hyper-concentrated sediment laden and debris flows that characterise certain extreme flood

events, it is necessary to modify further the shallow water equations so that they include the effect of density changes and non-Newtonian fluid properties.

During the past two decades considerable efforts have been made in order to model debris flow, based on the conservation of mass and momentum. As stated by Brufau et al. (2000):

"Only some of them take into account the erosion/deposition process, and the behaviour of different classes of sediment in the flow. The fluid is alternatively considered as a one-phase constant-density fluid or a two-phase variable-density mixture composed by granular material immersed in an interstitial fluid. This assumption strongly influences the choice of the rheological model: the typical situation of a debris flow stopping where the channel slope decreases may be simulated either with a constant density fluid or with a variable density mixture; but in the former case, the debris flow stops only if the rheological model allows for a yield stress. On the other hand, in a variable density mixture, the sediments settle even though the interstitial fluid continues to flow downstream."

For constant-density fluids, different rheological models have been adopted, such as the Bingham-type model (Fraccarollo 1995, Jan 1997, Jin and Fread 1997), the Herschel-Bulkley model (Laigle and Coussot 1997), and the quadratic shear stress model (O'Brien et al. 1993). Using a Bagnold rheological model in which the yield stress is not present, Takahashi and Tsujimoto (1985) simulated the entire debris flow phenomenon considering separate mechanisms for the deceleration, stopping and deposition stages. Rickenmann and Koch (1997) tested different rheological models varying from Bingham to Newtonian fluid (both under laminar and turbulent flow conditions) and from dilatant to Voellmy fluid.

Brufau et al. (2000) also stated that:

"A constant density fluid model cannot simulate the effects of sediments separation, needed to reproduce those real world events in which the coarser sediments settle in the upper part of the alluvial fan or near obstacles in the river bed. Modelling the fluid as a two-phase mixture overcomes most of the limitations mentioned above, allowing for a wider choice of rheological models."

Again, many alternatives can be found in the literature; for example: Bagnold's dilatant fluid hypothesis (Takahashi 1991, Takahashi and Nakagawa 1994, and Shieh et al. 1996); a Chézy-type equation with constant value of the friction coefficient (Hirano et al. 1997, Armanini and Fraccarollo 1997); and cohesive yield stress (Egashira et al. 1997). Other rheological models have been proposed for debris flow (see Chen 1988), and many of them are straightforward to implement in a numerical model. For a comprehensive review see Hutter et al. 1996. The change in the debris flow density can be modelled through the mass balance of both phases (solid and liquid), and the definition of the erosion/deposition rate as a function of sediment concentration. Shieh et al. (1996) introduced an empirical non-equilibrium condition for concentration when deposition occurs; assuming that concentration varies from the equilibrium in the steeper reach to the equilibrium concentration in the flatter reach according to an exponential law. Armanini and Fraccarollo (1997) assumed the concentration equal to the equilibrium value. Egashira and Ashida (1987), Hirano et al. (1997), Honda and Egashira (1997), Mizuyama and Yazawa (1987) and Takahashi et al. (1987) developed 1D and 2D models which consider non-equilibrium conditions. The first three references take only into account the coarse fraction, i.e. the interstitial fluid is nearly homogenous (water). The last two references consider also variations of the concentration of the fine fraction in the interstitial fluid.

Any variable (e.g. salinity, temperature, substance) which is transported by the liquid is referred to as species. When the concentration of certain material species in an otherwise Newtonian liquid exceeds a certain level, the liquid ceases to be Newtonian. In other words, the stress versus strain rate curve is no longer linear and does not pass through the origin – the dynamic viscosity is no longer constant throughout the fluid. Thus, in shallow flows, a species-liquid mixture has a flow pattern related to the concentration of species in the liquid by the governing variable density shallow water equations. The analysis of variable density flows, while taking into account the entrainment and the deposition of the sediment, is very useful for the approach of many environmental problems, such as the intrusion of sea water in rivers close to the coast, the pollution of underground water by agricultural nutrients, the disposal of industrial and nuclear waste, etc.

The variable density shallow water equations are also applicable to river bank erosion and bed morphological change. Shallow water-sediment flows drive the formation of the hydrological network, and so are very important for the whole water cycle within a river catchment.

Simulation of the above processes has been investigated by many researchers (see for example Cao et al., 2006; Xia et al., 2010; Yan, 2010; Leighton et al., 2010; Brufau et al., 2002; Brufau et al., 2000; Cao et al., 2004; Egashira et al., 1997; Honda and Egashira, 1997; Takahashi et al., 1987). For small concentrations, where the density and the viscosity of the fluid remain relatively stable, the characteristics of the flow are not affected by the presence of species. On the other hand, when the species concentration is large, the changes of density modify the flow, which in turn determines the transport and hydrodynamic dispersion processes of the species. The challenge is then to represent these processes, due

to the non linearity of the variable density shallow water equations which also include entrainment and deposition of the sediment and the interaction among them.

Numerical models that can simulate flood flows accurately and efficiently are required by river engineers and managers. In spite of various researches and developed methods in this area, there is much work to be done in order to achieve effective flood management.

1.3. Aims and Objectives

This research aims to improve flood modelling through numerical simulation. Advanced numerical solvers of the one-dimensional and two–dimensional constant density and variable density shallow water equations are developed and validated in the thesis. The improved numerical scheme is flexible and accounts for flooding over irregular bed topography and the erosion and the deposition of the sediment. Bed morphodynamics is included in the model.

Certain shallow water numerical models solely calculate the flow hydrodynamics, whereas others also include sediments transport and bed deformation, but without including the local variable density changes. The numerical model developed in the present research predicts the flow hydrodynamics, sediment transport, bed deformation, by using a balanced shock-capturing scheme. The model contains several novel featured: solves wetting and drying processes occurring the same time at different elevations, the horizontal variable density shallow water equations are solved in terms of free surface elevation as measured from a fixed horizontal datum, instead of the water depth or free surface elevation above still water level (used by most researchers), uses a Godunov-type finite volume HLLC approximate

Riemann solver of the horizontal hyperbolic variable density shallow water equations along with MUSCL-Hancock time integration.

The limitations of the present numerical model are essentially these of the standard shallow water equations and result from the underlying assumptions behind the equations, i.e. the depth of the liquid-species mixture is less than the wave length, the liquid-species mixture is fully mixed vertically, etc.

The detailed objectives of the D.Phil. project are:

1. To develop a validated shock capturing finite volume model of constant and variable density water flows and hence simulate flood overtopping and inundation.

2. To derive the horizontal variable density shallow flow equations from first principles and simulate hyper-concentrated sediment laden and debris flows that characterise certain extreme flood events using models based on the horizontal variable density shallow flow equations in one and two dimensions. To validate the model against idealised problems (including still water tests and variable density tests). To carry out a parameter study to investigate the effect of various components on the flow. To include bed morphodynamics in the model by solving a conservation of bed mass equation in conjunction with the variable density shallow water equations.

3. To simulate shallow flows over an erodible bed by extending the horizontal variable density shallow flow equations to include the entrainment and the deposition of the sediment. Also, to derive analytical solutions for simple test cases. Then, undertake

extensive validation tests in one and two dimensions, including comparison against the available analytical solutions.

4. To simulate a complicated demonstration case in order to test the model.

1.4. Synopsis

Chapter 1 has introduced the background to constant and variable density shallow flow numerical models, including a brief literature review. Chapter 2 describes the mathematical equations that govern the horizontal variable density shallow water flows. Chapter 3 outlines the components of the numerical model, and describes the Godunov-type finite volume method used to discretise the governing equations, the HLLC approximate Riemann solver, the MUSCL–Hancock method, the slope limiter, the stability criteria, the boundary conditions, the wetting and drying algorithm, and the special treatment required in order to include the entrainment and the deposition of the sediment. Chapters 4 and 5 discuss the results of tests undertaken to validate and verify the one and two–dimensional models respectively. These case studies include simple and more advanced constant and variable density problems, both with non-erodible and erodible bed, such as dam break, flow over a triangular obstacle, circular dam breaks, flow over three humps, and suspended sediment in a tank with no net flow. Chapter 6 describes the demonstration test case used to validate the numerical model and interprets the most important results. Chapter 7 lists the important conclusions of the project and presents recommendations for further work in the area of flood simulation.

CHAPTER 2 HORIZONTAL VARIABLE DENSITY SHALLOW WATER EQUATIONS

This chapter presents the derivation of horizontal variable density shallow water equations, starting from first principles. The equations are based on mass and momentum conservation of the mixture as well as mass conservation of the species. Erosion and deposition of the sediment are taken into account. The one-dimensional equations are then extended to two dimensions. The chapter ends with the description of the boundary conditions used for the mathematical model.

2.1. Introduction

In flood waves the vertical particle kinematics, as well as the horizontal shear stress components are relatively small and it can be assumed that the pressure distribution is hydrostatic. The shallow water equations are a time–dependent two–dimensional system of non–linear partial differential equations (Toro, 2001) that describe the flow below a pressure surface (usually the free surface) in a fluid.

The initial objective of this study is the derivation of the horizontal variable density shallow flow equations from first principles. Simulation of hyper-concentrated sediment laden and debris flows that characterise certain extreme flood events can then be undertaken using a model based on the horizontal variable density shallow flow equations taking into account the erodibility of the bed through the entrainment and deposition of sediment. The model will be validated against idealised problems (including still water and variable density tests). A parameter study will be carried out to investigate the effect of various components on the

flow. Bed morphodynamics will be included in the model by solving a conservation of bed mass equation in conjunction with the variable density shallow water equations.

2.2. Mathematical Description

2.2.1. Derivation of Horizontal Variable Density Shallow Water Equations

The shallow water equations may be derived by considering a fluid element (see Figure 2.1), on which the laws of mass and momentum conservation are applied. The shallow water equations hold in cases where the horizontal length scale is much greater than the vertical length scale. Under this condition, conservation of mass implies that the vertical velocity of the fluid is negligible. It can be shown from the momentum equation that vertical pressure gradients are nearly hydrostatic, and that horizontal pressure gradients are due to the displacement of the pressure surface, implying that the velocity field is nearly constant throughout the depth of the fluid. The shallow water equations are suitable for steep-fronted (even discontinuous) flows and smoothly varied flow break downs, for example, across a hydraulic jump.

The boundary conditions are that there is no slip at the bed (i.e. all water particle velocities are zero there), and any water particle at the free surface remains there (the kinematic free surface boundary condition). It is also assumed that on the free surface the atmospheric pressure is zero.

The resulting set of equations is a subset of more general equations for water sediment transport (see for example Cao et al., 2006). The present equations do not include the bed load component but on the other hand they have not undergone any special manipulation.

They result from the basic principles of fluid dynamics (i.e. the mass and momentum conservation equations) and the physics of the problem are obvious in the relevant components. Also the use of the surface water level above a given datum (η) instead of the water level above the level of the bed (h) benefits the stability of the model especially for problems that include wet and dry fronts. Figure 2.2 illustrates the different depths and elevations used in the equations.

2.2.1.1. One-Dimensional Horizontal Variable Density Shallow Water Equations

The one-dimensional horizontal variable density shallow water equations are based on the mass and momentum conservation equations for the mixture of species and liquid and the species mass conservation equation.

The one-dimensional mass conservation equation for the mixture can be written as (see e.g. Abbott (1979) and Leighton et al. (2010)):

$$\frac{\partial(\rho h)}{\partial t} + \frac{\partial(\rho uh)}{\partial x} = 0 \tag{2.1}$$

in which t is time, h is the free surface elevation of the mixture above a given horizontal datum, such as the mean liquid (or mixture) free surface level, x and u are coordinate distance and velocity along the horizontal Cartesian axes, and ρ is the density of liquid-species mixture defined as:

$$\rho = \rho_w + c(\rho_s - \rho_w) \tag{2.2}$$

in which ρ_w is the density of the liquid and ρ_s is the density of the species and c is the volumetric concentration of the species.

The momentum conservation equation for the mixture is expressed by Leighton et al. (2010) as:

$$\frac{\partial(\rho uh)}{\partial t} + \frac{\partial(\rho u^2 h)}{\partial x} = -\rho g h \frac{\partial \zeta}{\partial x} - \tau_b \tag{2.3}$$

where g is the acceleration due to gravity, ζ is the water elevation above the still liquid level, and the bed stresses are given by $\tau_b = \rho c_f u|u|$ in which the bed friction coefficient, $c_f = \frac{g}{C^2} = \frac{gn^2}{h^{1/3}}$ where C is the Chézy coefficient and n is the Manning coefficient. The tangential surface stress component is neglected.

Finally, the species mass conservation equation is as follows:

$$\frac{\partial(\rho_s ch)}{\partial t} + \frac{\partial(\rho_s uch)}{\partial x} = 0 \tag{2.4}$$

Noting that the discharge per unit width of the mixture, $q = uh$, the variable density shallow water equations may be written:

$$\frac{\partial(\rho h)}{\partial t} + \frac{\partial(\rho q)}{\partial x} = 0 \ , \tag{2.5}$$

$$\frac{\partial(\rho\, q)}{\partial t}+\frac{\partial(\rho\, q^2/h)}{\partial x}=-\rho\, g\, h\frac{\partial \zeta}{\partial x}-\tau_b \quad , \tag{2.6}$$

and

$$\frac{\partial(\rho_s ch)}{\partial t}+\frac{\partial(\rho_s cq)}{\partial x}=0. \tag{2.7}$$

The one-dimensional horizontal variable density shallow water equations can be also written in conventional hyperbolic form. The hyperbolic variable density shallow water equations are commonly derived by splitting the $gh\frac{\partial \zeta}{\partial x}$ term as follows: $gh\frac{\partial \zeta}{\partial x}=\frac{\partial}{\partial x}(\frac{1}{2}gh^2)+gh\frac{\partial z_b}{\partial x}$, where z_b is the bed elevation from the datum (z_b=0).

The resulting conventional hyperbolic horizontal variable density shallow water equations are:

$$\frac{\partial(\rho\, h)}{\partial t}+\frac{\partial(\rho\, uh)}{\partial x}=0 \quad , \tag{2.8}$$

$$\frac{\partial(\rho\, uh)}{\partial t}+\frac{\partial(\rho\, u^2h+\frac{1}{2}\rho\, gh^2)}{\partial x}=-\rho\, gh\frac{\partial z_b}{\partial x}-\tau_b \quad , \tag{2.9}$$

and

$$\frac{\partial(\rho_s ch)}{\partial t}+\frac{\partial(\rho_s uch)}{\partial x}=0 \quad , \tag{2.10}$$

or, alternatively,

$$\frac{\partial(\rho h)}{\partial t}+\frac{\partial(\rho q)}{\partial x}=0\ , \tag{2.11}$$

$$\frac{\partial(\rho q)}{\partial t}+\frac{\partial(\rho q^2/h+\frac{1}{2}\rho g h^2)}{\partial x}=-\rho g h\frac{\partial z_b}{\partial x}-\tau_b\ , \tag{2.12}$$

and

$$\frac{\partial(\rho_s c h)}{\partial t}+\frac{\partial(\rho_s c q)}{\partial x}=0. \tag{2.13}$$

However, when the above set of equations is applied to non-uniform bed topography, the mathematical formulation of Roe's approximate Riemann solver (used in the numerical model) can lead to numerical instabilities. The cause of these instabilities is the splitting of the source term in the momentum conservation equation and is independent of the geometry of the problem.

Following the Rogers *et al*. (2003) approach for balancing the flux gradient and source terms in Godunov schemes, which overcomes the above problem, the source term in the momentum equation can be split as $gh\frac{\partial\zeta}{\partial x}=\frac{\partial}{\partial x}(\frac{1}{2}g(\zeta^2+2\zeta h_s))+g\zeta\frac{\partial z_b}{\partial x}$, where h_s is the still water depth and ζ the free water surface elevation above the still water depth (i.e. $h=\zeta+h_s$). In this way the mass and momentum are conserved and the model produces meaningful results as the still water depth can be calculated separately from the free surface elevation, accounting for the irregular bed topography. In order to balance the flux and the

source terms, the equilibrium state of the flux gradients should be subtracted from the left hand side of the equations (Rogers et al, 2001).

Based on the above approach, Leighton *et al*. (2010) obtained the following deviatoric version of the variable density shallow water equations:

$$\frac{\partial\left(\rho h-\rho_{\mathrm{eq}} h_{\mathrm{eq}}\right)}{\partial t}+\frac{\partial(\rho u h)}{\partial x}=0 \ , \tag{2.14}$$

$$\frac{\partial(\rho u h)}{\partial t}+\frac{\partial\left(\rho u^{2} h+\frac{1}{2} \rho g h^{2}-\frac{1}{2} \rho_{\mathrm{eq}} g {h_{\mathrm{eq}}}^{2}\right)}{\partial x}=-\rho g h \frac{\partial z_{b}}{\partial x}+\rho_{\mathrm{eq}} g h_{\mathrm{eq}} \frac{\partial z_{b}}{\partial x}-\tau_{b}, \tag{2.15}$$

and

$$\frac{\partial\left(\rho_{s} c h-\rho_{s} c_{e q} h_{e q}\right)}{\partial t}+\frac{\partial\left(\rho_{s} u c h\right)}{\partial x}=0 \ , \tag{2.16}$$

or, alternatively

$$\frac{\partial\left(\rho h-\rho_{\mathrm{eq}} h_{\mathrm{eq}}\right)}{\partial t}+\frac{\partial(\rho q)}{\partial x}=0 \ , \tag{2.17}$$

$$\frac{\partial(\rho q)}{\partial t}+\frac{\partial\left(\rho q^{2} / h+\frac{1}{2} \rho g h^{2}-\frac{1}{2} \rho_{\mathrm{eq}} g {h_{\mathrm{eq}}}^{2}\right)}{\partial x}=-\rho g h \frac{\partial z_{b}}{\partial x}+\rho_{\mathrm{eq}} g h_{\mathrm{eq}} \frac{\partial z_{b}}{\partial x}-\tau_{b}, \tag{2.18}$$

and

$$\frac{\partial(\rho_s ch - \rho_s c_{eq} h_{eq})}{\partial t} + \frac{\partial(\rho_s cq)}{\partial x} = 0 \tag{2.19}$$

where h_{eq} is the liquid depth, ρ_{eq} is the density of the liquid-species mixture and c_{eq} is the concentration of the species at the quiescent equilibrium state. By choosing $\rho_{\text{eq}} = \rho_{\text{w}}$, where ρ_{w} is the density of the liquid, $h_{\text{eq}} = h_{\text{s}}$, where h_{s} is the still liquid depth, and $c_{\text{eq}} = 0$, then:

$$\frac{\partial(\rho h - \rho_{\text{w}} h_{\text{s}})}{\partial t} + \frac{\partial(\rho uh)}{\partial x} = 0 \ , \tag{2.20}$$

$$\frac{\partial(\rho uh)}{\partial t} + \frac{\partial(\rho u^2 h + \frac{1}{2}\rho gh^2 - \frac{1}{2}\rho_{\text{w}} g h_{\text{s}}^{\ 2})}{\partial x} = -\rho gh\frac{\partial z_b}{\partial x} + \rho_{\text{w}} gh_{\text{s}}\frac{\partial z_b}{\partial x} - \tau_b \, , \tag{2.21}$$

and

$$\frac{\partial(\rho_s ch)}{\partial t} + \frac{\partial(\rho_s uch)}{\partial x} = 0 \ . \tag{2.22}$$

By using η which is the surface water level above a given datum instead of h which is the water level above the level of the bed ($h = \eta - z_b$); and η_s which is the surface water level above a given datum at the quiescent equilibrium state ($h_s = \eta_s - z_b$), where z_b is the level of the bed, the above equations become:

$$\frac{\partial(\rho \eta - \rho_{\text{eq}} \eta_{\text{eq}})}{\partial t} + \frac{\partial(\rho uh)}{\partial x} = 0 \ , \tag{2.23}$$

$$\frac{\partial(\rho uh)}{\partial t}+\frac{\partial(\rho u^2h+\frac{1}{2}\rho g(\eta^2-2\eta z_b)-\frac{1}{2}\rho_{\mathrm{eq}}g(\eta_{\mathrm{eq}}^2-2\eta_{\mathrm{eq}}z_b))}{\partial x}=-\rho g\eta\frac{\partial z_b}{\partial x}+\rho_{\mathrm{eq}}g\eta_{\mathrm{eq}}\frac{\partial z_b}{\partial x}-\tau_b, \quad (2.24)$$

and

$$\frac{\partial\left(\rho_s ch-\rho_s c_{\mathrm{eq}}h_{\mathrm{eq}}\right)}{\partial t}+\frac{\partial(\rho_s uch)}{\partial x}=0\,. \quad (2.25)$$

This formulation is particularly well suited to flooding and drying (for further details see Liang and Borthwick, 2008). By choosing again $\rho_{\mathrm{eq}}=\rho_{\mathrm{w}}$, $\eta_{\mathrm{eq}}=\eta_{\mathrm{s}}=h_s+z_b$, and $c_{\mathrm{eq}}=0$, then:

$$\frac{\partial\left(\rho\eta-\rho_{\mathrm{w}}\eta_{\mathrm{s}}\right)}{\partial t}+\frac{\partial(\rho uh)}{\partial x}=0\ , \quad (2.26)$$

$$\frac{\partial(\rho uh)}{\partial t}+\frac{\partial(\rho u^2h+\frac{1}{2}\rho g(\eta^2-2\eta z_b)-\frac{1}{2}\rho_{\mathrm{w}}g(\eta_s^2-2\eta_s z_b))}{\partial x}=-\rho g\eta\frac{\partial z_b}{\partial x}+\rho_{eq}g\eta_{eq}\frac{\partial z_b}{\partial x}-\tau_{bx}, \quad (2.27)$$

and

$$\frac{\partial(\rho_s ch)}{\partial t}+\frac{\partial(\rho_s uch)}{\partial x}=0\ . \quad (2.28)$$

Taking into account the entrainment and the deposition of the sediment that takes place on the bed; the mixture mass conservation and suspended sediment mass conservation equations should be modified and an additional equation should be added in order to

represent the change in bed elevation (see e.g. Soulsby, 1997). So, the modified set of equations is:

$$\frac{\partial(\rho\eta-\rho_{\mathrm{w}}\eta_{\mathrm{s}})}{\partial t}+\frac{\partial(\rho uh)}{\partial x}=-\rho_0\frac{D-E}{1-p}+\frac{\partial\rho z_b}{\partial t}\ , \tag{2.29}$$

$$\frac{\partial(\rho uh)}{\partial t}+\frac{\partial(\rho u^2h+\frac{1}{2}\rho g(\eta^2-2\eta z_b)-\frac{1}{2}\rho_{\mathrm{w}}g(\eta_s^2-2\eta_s z_b))}{\partial x}=-\rho g\eta\frac{\partial z_b}{\partial x}+\rho_w g\eta_s\frac{\partial z_b}{\partial x}-\tau_b\,, \tag{2.30}$$

$$\frac{\partial(\rho_s ch)}{\partial t}+\frac{\partial(\rho_s uch)}{\partial x}=\rho_s(E-D)\ , \tag{2.31}$$

and

$$\frac{\partial(z_b)}{\partial t}=\frac{D-E}{1-p}\ . \tag{2.32}$$

where $\rho_0=\rho_w p+\rho_s(1-p)$ is the density of the saturated bed, p is the porosity of the bed and E and D are the sediment entrainment and deposition fluxes respectively, at the surface of the bed. In practice, E and D are evaluated using empirical equations related to the problem under consideration and available data (Soulsby 1997, Cao et al. 2006, Van Rijn 1993). The entrainment and the deposition are expressed in units of volume of sediment entrained or deposited respectively, per unit area of bed, per unit time, excluding any existing pore water.

In order to validate the model an analytical solution for each of the erodible bed problems has been derived. For simplicity, the equations used for the analytical solution are in terms

of *h*, which is the liquid-mixture free surface elevation above the bed. Analytical solutions for certain test cases are developed in chapter 4. The solutions are useful later in helping to validate the numerical model.

2.2.1.2. Two-Dimensional Horizontal Variable Density Shallow Water Equations

In two dimensions, the mass conservation equation can be written as:

$$\frac{\partial(\rho h)}{\partial t}+\frac{\partial(\rho uh)}{\partial x}+\frac{\partial(\rho vh)}{\partial y}=0 \tag{2.33}$$

in which t is time, h is the free surface elevation of the mixture, u and v are the horizontal depth-averaged velocity components in the x and y directions, and ρ is the density of liquid-species mixture defined as in equation (2.2), $\rho=\rho_w+c(\rho_s-\rho_w)$, in which ρ_w is the density of the liquid and ρ_s is the density of the species and c is the volumetric concentration of the species.

The two-dimensional momentum conservation equation for the mixture (neglecting the surface stress τ_w) is expressed as:

$$\frac{\partial(\rho uh)}{\partial t}+\frac{\partial(\rho u^2h)}{\partial x}+\frac{\partial(\rho uvh)}{\partial y}=-\rho gh\frac{\partial\zeta}{\partial x}-\tau_{bx} \quad , \tag{2.34}$$

and

$$\frac{\partial(\rho vh)}{\partial t}+\frac{\partial(\rho uvh)}{\partial x}+\frac{\partial(\rho v^2h)}{\partial y}=-\rho gh\frac{\partial\zeta}{\partial y}-\tau_{by} \quad , \tag{2.35}$$

where g is the acceleration due to gravity, ζ is the water elevation above the still water level, τ_{bx} and τ_{by} are the bed shear stress components, and ρ_s is the species density. The bed shear stresses are estimated from:

$$\tau_{bx} = \rho c_f u\sqrt{u^2+v^2} \quad \text{and} \quad \tau_{by} = \rho c_f v\sqrt{u^2+v^2} \ , \tag{2.36}$$

in which c_f is the bed friction coefficient $c_f = \frac{g}{C^2} = \frac{gn^2}{h^{1/3}}$, where C is the Chézy coefficient and n is the Manning coefficient.

Finally the two-dimensional species mass conservation equation is as following:

$$\frac{\partial(\rho_s ch)}{\partial t} + \frac{\partial(\rho_s uch)}{\partial x} + \frac{\partial(\rho_s vch)}{\partial y} = 0 \tag{2.37}$$

Noting that $q_x = uh$ and $q_y = vh$, the variable density shallow water equations become:

$$\frac{\partial(\rho h)}{\partial t} + \frac{\partial(\rho q_x)}{\partial x} + \frac{\partial(\rho q_y)}{\partial y} = 0 \ , \tag{2.38}$$

$$\frac{\partial(\rho q_x)}{\partial t} + \frac{\partial(\rho q_x^2/h)}{\partial x} + \frac{\partial(\rho q_x q_y/h)}{\partial y} = -\rho gh\frac{\partial \zeta}{\partial x} - \tau_{bx} \ , \tag{2.39}$$

$$\frac{\partial(\rho q_y)}{\partial t} + \frac{\partial(\rho q_x q_y/h)}{\partial x} + \frac{\partial(\rho q_y^2/h)}{\partial y} = -\rho gh\frac{\partial \zeta}{\partial y} - \tau_{by} \ , \tag{2.40}$$

and

$$\frac{\partial(\rho_s ch)}{\partial t}+\frac{\partial(\rho_s cq_x)}{\partial x}+\frac{\partial(\rho_s cq_y)}{\partial y}=0\,. \tag{2.41}$$

The hyperbolic two-dimensional horizontal variable density shallow water equations are derived by splitting the terms $gh\frac{\partial\zeta}{\partial x}$ and $gh\frac{\partial\zeta}{\partial y}$ as follows:

$$gh\frac{\partial\zeta}{\partial x}=\frac{\partial}{\partial x}(\tfrac{1}{2}gh^2)+gh\frac{\partial z_b}{\partial x} \qquad \text{and} \qquad gh\frac{\partial\zeta}{\partial y}=\frac{\partial}{\partial y}(\tfrac{1}{2}gh^2)+gh\frac{\partial z_b}{\partial y}\,. \tag{2.42}$$

The resulting hyperbolic two-dimensional horizontal variable density shallow water equations are:

$$\frac{\partial(\rho h)}{\partial t}+\frac{\partial(\rho uh)}{\partial x}+\frac{\partial(\rho vh)}{\partial y}=0\ , \tag{2.43}$$

$$\frac{\partial(\rho uh)}{\partial t}+\frac{\partial\left(\rho u^2h+\frac{1}{2}\rho gh^2\right)}{\partial x}+\frac{\partial(\rho uvh)}{\partial y}=-\rho gh\frac{\partial z_b}{\partial x}-\tau_{bx}\ , \tag{2.44}$$

$$\frac{\partial(\rho vh)}{\partial t}+\frac{\partial(\rho uvh)}{\partial x}+\frac{\partial\left(\rho v^2h+\frac{1}{2}\rho gh^2\right)}{\partial y}=-\rho gh\frac{\partial z_b}{\partial y}-\tau_{by}\ , \tag{2.45}$$

and

$$\frac{\partial(\rho_s ch)}{\partial t}+\frac{\partial(\rho_s uch)}{\partial x}+\frac{\partial(\rho_s vch)}{\partial y}=0\ , \tag{2.46}$$

or, alternatively

$$\frac{\partial(\rho h)}{\partial t}+\frac{\partial(\rho q_x)}{\partial x}+\frac{\partial(\rho q_y)}{\partial y}=0 \quad , \tag{2.47}$$

$$\frac{\partial(\rho q_x)}{\partial t}+\frac{\partial(\rho q_x^2/h+\frac{1}{2}\rho g h^2)}{\partial x}+\frac{\partial(\rho q_x q_y/h)}{\partial y}=-\rho g h\frac{\partial z_b}{\partial x}-\tau_{bx} \quad , \tag{2.48}$$

$$\frac{\partial(\rho q_y)}{\partial t}+\frac{\partial(\rho q_x q_y/h)}{\partial x}+\frac{\partial(\rho q_y^2/h+\frac{1}{2}\rho g h^2)}{\partial y}=-\rho g h\frac{\partial z_b}{\partial y}-\tau_{by} \quad , \tag{2.49}$$

and

$$\frac{\partial(\rho_s ch)}{\partial t}+\frac{\partial(\rho_s cq_x)}{\partial x}+\frac{\partial(\rho_s cq_y)}{\partial y}=0\,. \tag{2.50}$$

Following the Rogers *et al*. (2003) approach for balancing the flux gradient and source terms in Godunov schemes, Leighton et al. (2010) obtained the following deviatoric version of the Variable Density Shallow Water Equations:

$$\frac{\partial(\rho h-\rho_{\mathrm{eq}}h_{\mathrm{eq}})}{\partial t}+\frac{\partial(\rho uh)}{\partial x}+\frac{\partial(\rho vh)}{\partial y}=0 \quad , \tag{2.51}$$

$$\frac{\partial(\rho uh)}{\partial t}+\frac{\partial(\rho u^2h+\frac{1}{2}\rho gh^2-\frac{1}{2}\rho_{\mathrm{eq}}gh_{\mathrm{eq}}{}^2)}{\partial x}+\frac{\partial(\rho uvh)}{\partial y}=-\rho gh\frac{\partial z_b}{\partial x}+\rho_{eq}gh_{eq}\frac{\partial z_b}{\partial x}-\tau_{bx}, \tag{2.52}$$

$$\frac{\partial(\rho vh)}{\partial t}+\frac{\partial(\rho uvh)}{\partial x}+\frac{\partial\left(\rho v^2 h+\frac{1}{2}\rho gh^2-\frac{1}{2}\rho_{\mathrm{eq}}gh_{\mathrm{eq}}^2\right)}{\partial y}=-\rho gh\frac{\partial z_b}{\partial y}+\rho_{eq}gh_{eq}\frac{\partial z_b}{\partial y}-\tau_{by}, \qquad (2.53)$$

and

$$\frac{\partial\left(\rho_s ch-\rho_s c_{\mathrm{eq}}h_{\mathrm{eq}}\right)}{\partial t}+\frac{\partial(\rho_s uch)}{\partial x}+\frac{\partial(\rho_s vch)}{\partial y}=0. \qquad (2.54)$$

By choosing again $\rho_{\mathrm{eq}}=\rho_{\mathrm{w}}$, $h_{\mathrm{eq}}=h_{\mathrm{s}}$, and $c_{\mathrm{eq}}=0$, then:

$$\frac{\partial\left(\rho h-\rho_{\mathrm{w}}h_{\mathrm{s}}\right)}{\partial t}+\frac{\partial(\rho uh)}{\partial x}+\frac{\partial(\rho vh)}{\partial y}=0 \quad , \qquad (2.55)$$

$$\frac{\partial(\rho uh)}{\partial t}+\frac{\partial(\rho u^2 h+\frac{1}{2}\rho gh^2-\frac{1}{2}\rho_{\mathrm{w}}gh_{\mathrm{s}}{}^2)}{\partial x}+\frac{\partial(\rho uvh)}{\partial y}=-\rho gh\frac{\partial z_b}{\partial x}+\rho_{\mathrm{w}}gh_{\mathrm{s}}\frac{\partial z_b}{\partial x}-\tau_{bx}, \qquad (2.56)$$

$$\frac{\partial(\rho vh)}{\partial t}+\frac{\partial(\rho uvh)}{\partial x}+\frac{\partial\left(\rho v^2 h+\frac{1}{2}\rho gh^2-\frac{1}{2}\rho_{\mathrm{w}}gh_{\mathrm{s}}^2\right)}{\partial y}=-\rho gh\frac{\partial z_b}{\partial y}+\rho_{\mathrm{w}}gh_{\mathrm{s}}\frac{\partial z_b}{\partial y}-\tau_{by}, \qquad (2.57)$$

and

$$\frac{\partial(\rho_s ch)}{\partial t}+\frac{\partial(\rho_s uch)}{\partial x}+\frac{\partial(\rho_s vch)}{\partial y}=0. \qquad (2.58)$$

The two-dimensional hyperbolic horizontal variable density shallow water equations, reformulated in terms of stage-discharge (i.e. by using η which is the surface water level

above a given datum instead of h which is the water level above the level of the bed ($h=\eta-z_b$); where z_b is the level of the bed above a prescribed horizontal datum), are as follows:

$$\frac{\partial\left(\rho\eta-\rho_{\mathrm{eq}}\eta_{\mathrm{eq}}\right)}{\partial t}+\frac{\partial\left(\rho uh\right)}{\partial x}+\frac{\partial(\rho vh)}{\partial y}=0, \tag{2.59}$$

$$\frac{\partial(\rho uh)}{\partial t}+\frac{\partial(\rho u^2h+\frac{1}{2}\rho g(\eta^2-2\eta z_b)-\frac{1}{2}\rho_{\mathrm{eq}}g(\eta_{\mathrm{eq}}^2-2\eta_{\mathrm{eq}}z_b))}{\partial x}+\frac{\partial(\rho uvh)}{\partial y}=-\rho g\eta\frac{\partial z_b}{\partial x}+\rho_{eq}g\eta_{eq}\frac{\partial z_b}{\partial x}-\tau_{bx}, \tag{2.60}$$

$$\frac{\partial(\rho vh)}{\partial t}+\frac{\partial(\rho uvh)}{\partial x}+\frac{\partial(\rho v^2h+\frac{1}{2}\rho g(\eta^2-2\eta z_b)-\frac{1}{2}\rho_{\mathrm{eq}}g(\eta_{\mathrm{eq}}^2-2\eta_{\mathrm{eq}}z_b))}{\partial y}=-\rho g\eta\frac{\partial z_b}{\partial y}+\rho_{\mathrm{eq}}g\eta_{\mathrm{eq}}\frac{\partial z_b}{\partial y}-\tau_{by}, \tag{2.61}$$

and

$$\frac{\partial\left(\rho_s ch-\rho_s c_{\mathrm{eq}}h_{\mathrm{eq}}\right)}{\partial t}+\frac{\partial\left(\rho_s uch\right)}{\partial x}+\frac{\partial\left(\rho_s vch\right)}{\partial y}=0. \tag{2.62}$$

By choosing $\rho_{\mathrm{eq}}=\rho_{\mathrm{w}}$, $\eta_{\mathrm{eq}}=\eta_{\mathrm{s}}=h_s+z_b$, and $c_{\mathrm{eq}}=0$, then:

$$\frac{\partial\left(\rho\eta-\rho_{\mathrm{w}}\eta_{\mathrm{s}}\right)}{\partial t}+\frac{\partial\left(\rho uh\right)}{\partial x}+\frac{\partial(\rho vh)}{\partial y}=0 \quad , \tag{2.63}$$

$$\frac{\partial(\rho uh)}{\partial t}+\frac{\partial(\rho u^2h+\frac{1}{2}\rho g(\eta^2-2\eta z_b)-\frac{1}{2}\rho_{\mathrm{w}}g(\eta_{\mathrm{s}}^2-2\eta_{\mathrm{s}}z_b))}{\partial x}+\frac{\partial(\rho uvh)}{\partial y}=-\rho g\eta\frac{\partial z_b}{\partial x}+\rho_{w}g\eta_{s}\frac{\partial z_b}{\partial x}-\tau_{bx}, \tag{2.64}$$

$$\frac{\partial(\rho vh)}{\partial t}+\frac{\partial(\rho uvh)}{\partial x}+\frac{\partial(\rho v^2h+\frac{1}{2}\rho g(\eta^2-2\eta z_b)-\frac{1}{2}\rho_{\mathrm{w}}g(\eta_{\mathrm{s}}^2-2\eta_{\mathrm{s}}z_b))}{\partial y}=-\rho g\eta\frac{\partial z_b}{\partial y}+\rho_{w}g\eta_{\mathrm{s}}\frac{\partial z_b}{\partial y}-\tau_{by}, \tag{2.65}$$

and

$$\frac{\partial(\rho_s ch)}{\partial t}+\frac{\partial(\rho_s uch)}{\partial x}+\frac{\partial(\rho_s vch)}{\partial y}=0. \tag{2.66}$$

As for the one-dimensional model, when taking into account the entrainment and the deposition of sediment that takes place on the bed, the modified equation set is as follows:

$$\frac{\partial(\rho\eta-\rho_w\eta_s)}{\partial t}+\frac{\partial(\rho uh)}{\partial x}+\frac{\partial(\rho vh)}{\partial y}=-\rho_0\frac{D-E}{1-p}+\frac{\partial\rho z_b}{\partial t}\ , \tag{2.67}$$

$$\frac{\partial(\rho uh)}{\partial t}+\frac{\partial(\rho u^2h+\frac{1}{2}\rho g(\eta^2-2\eta z_b)-\frac{1}{2}\rho_w g(\eta_s^2-2\eta_s z_b))}{\partial x}+\frac{\partial(\rho uvh)}{\partial y}=-\rho g\eta\frac{\partial z_b}{\partial x}+\rho_w g\eta_s\frac{\partial z_b}{\partial x}-\tau_{bx}, \tag{2.68}$$

$$\frac{\partial(\rho vh)}{\partial t}+\frac{\partial(\rho uvh)}{\partial x}+\frac{\partial(\rho v^2h+\frac{1}{2}\rho g(\eta^2-2\eta z_b)-\frac{1}{2}\rho_w g(\eta_s^2-2\eta_s z_b))}{\partial y}=-\rho g\eta\frac{\partial z_b}{\partial y}+\rho_w g\eta_s\frac{\partial z_b}{\partial y}-\tau_{by}, \tag{2.69}$$

$$\frac{\partial(\rho_s ch)}{\partial t}+\frac{\partial(\rho_s uch)}{\partial x}+\frac{\partial(\rho_s vch)}{\partial y}=\rho_s(E-D)\ , \tag{2.70}$$

and

$$\frac{\partial(z_b)}{\partial t}=\frac{D-E}{1-p}. \tag{2.71}$$

2.2.2. Boundary Conditions

When the spatial domain of the problem at hand is unbounded, a numerical treatment usually requires the introduction of an artificial boundary, in order to make the computational domain finite (Givoli, 1991). The time evolution of the system is governed not only by the state in the interior of the region, but also by waves which enter the region from outside its boundaries. Therefore, boundary conditions which describe the incoming waves are required to specify completely the behaviour of the system. The outgoing waves are usually described by characteristic equations, whereas the incoming waves are often specified by non-reflecting boundary conditions (Thompson, 1987).

In order to decide the appropriate open boundary condition for each domain, both the value of the normal velocity through the boundary ($\mathbf{u}\cdot\mathbf{n}=un_x + vn_y$) and the local Froude number ($Fr = (\mathbf{u}\cdot\mathbf{n})/c$, where c is the celerity of the wave) are taken into account (Brufau et al., 2002). According to Hirsch (1990) there are four different combinations of types of flow and boundary conditions: (i) supercritical inflow ($\mathbf{u}\cdot\mathbf{n} \leq -c$), where all the variables must be imposed; (ii) subcritical inflow ($-c < \mathbf{u}\cdot\mathbf{n} \leq 0$), where two variables must be imposed; (iii) supercritical outflow ($\mathbf{u}\cdot\mathbf{n} > c$), where none of the variables must be imposed; and (iv) subcritical outflow ($0 < \mathbf{u}\cdot\mathbf{n} \leq c$), where one variable must be imposed.

In the case of closed boundaries slip or no-slip conditions may be applied (Rogers et al., 2001), where the velocity normal to the solid wall is set to zero, in order to prevent the flux through the boundary. In the case of no-slip boundary, the tangential velocity component at the boundary end of the cell is also set to zero.

2.2.3. Concluding Remarks

Equations 2.29 to 2.32 are solved in the one-dimensional model and equations 2.67 to 2.71 are solved in the two-dimensional model. The next chapter describes the details of the numerical model.

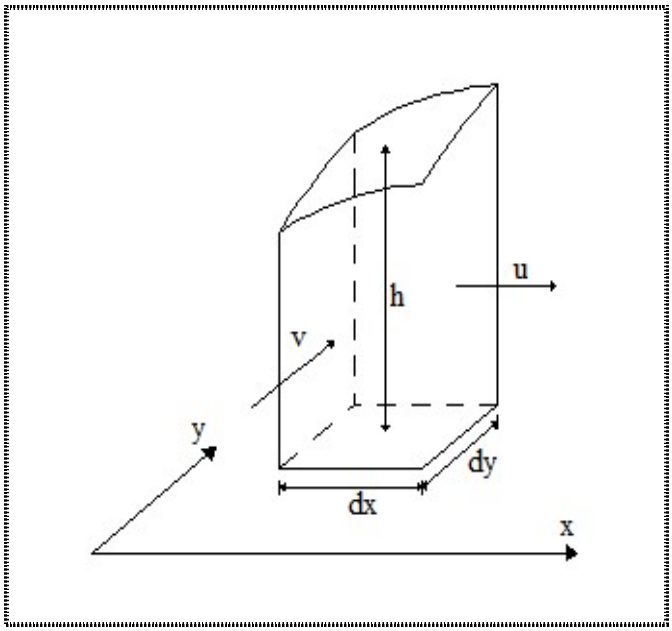


Fig. 2.1 Sketch illustrating the fluid element used for the definition of mass and momentum conservation while deriving the horizontal variable density shallow water equations.

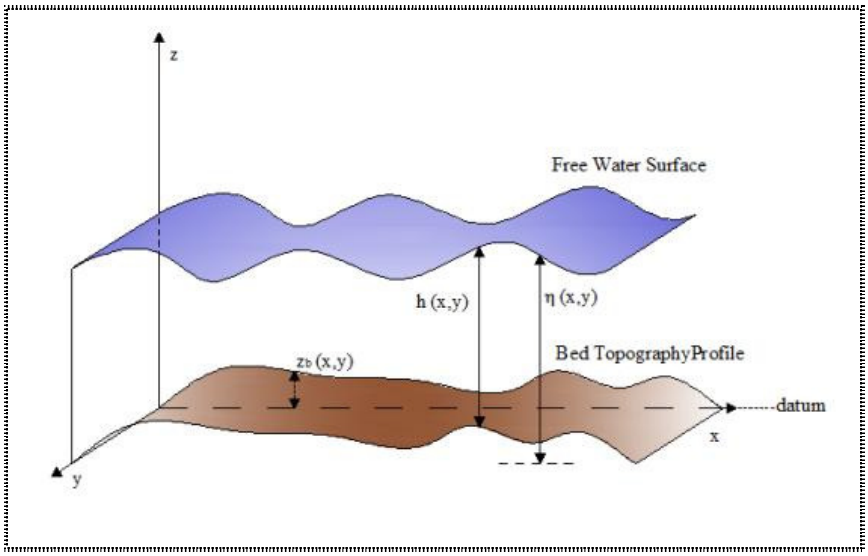


Fig. 2.2 Sketch illustrating the definition of the datum, the water depth (h(x,y)), the free water surface elevation (η(x,y)), and the bed elevation (z_b(x,y)).

CHAPTER 3 NUMERICAL SOLVER OF HORIZONTAL VARIABLE DENSITY SHALLOW WATER EQUATIONS

The flood simulation model developed in this research consists of a finite volume Godunov-type HLLC approximate Riemann solver of the hyperbolic shallow water equations. MUSCL-Hancock time integration is used so that the solver is second-order accurate. A non-linear slope limiter is implemented, in order to estimate the values of the fluxes across volume interfaces. A wet-dry algorithm is developed, in order to calculate the flow from one elevation to another. The source terms are modified accordingly, to encounter for entrainment and deposition of sediment (when present). The hyperbolic stage-discharge form of the horizontal variable density shallow water equations for one and two dimensions is solved within the numerical model. The boundary conditions can vary according to the test case considered.

3.1. Godunov-type Solver of the Horizontal Variable Density Shallow Water Equations

3.1.1. Finite Volume Method

In the finite volume method, volume integrals in a partial differential equation that contain a divergence term are converted to surface integrals, using the divergence theorem. These terms are then evaluated as fluxes at the surfaces of each finite volume. Because the flux entering a given volume is identical to that leaving the adjacent volume, the finite volume method is conservative. Another advantage of the finite volume method is that it is easily formulated to allow for unstructured meshes.

The first step in the finite volume method is to divide the domain into discrete control volumes. The boundaries (or faces) of control volumes are positioned midway between adjacent nodes. Thus each node is surrounded by a control volume or cell. A Cartesian grid is used, in which the indices (*i*,*j*) represent a particular cell. The scheme is cell-centred, so $\eta_{i,j}$, is considered as the average stage (water level) within the cell and is stored at its centre. The east, west, north and south face are referred by *E*, *W*, *N* and *S* respectively. The key step of the finite-volume method is the integration of the governing equations over a control volume to yield a discretised equation at its nodal point (Figure 3.1).

The corresponding integral form of the horizontal variable density shallow water equations is:

$$\frac{\partial}{\partial t}\int_{\Omega}\mathbf{u}d\Omega+\int_{\Omega}(\frac{\partial\mathbf{f}}{\partial x}+\frac{\partial\mathbf{g}}{\partial y})d\Omega=\int_{\Omega}\mathbf{s}d\Omega \quad , \tag{3.1}$$

where **u**, **f**, **g** and **s** are vectors of dependent conserved variables, Cartesian components of the flux, and source terms, respectively and *Ω* is the control volume. After conversion to surface integrals (3.1) becomes:

$$\oint_{S}\mathbf{F}dS=(\mathbf{F}_{E}-\mathbf{F}_{W})\Delta y+(\mathbf{F}_{N}-\mathbf{F}_{S})\Delta x \qquad , \tag{3.2}$$

where *Δx* and *Δy* are the side lengths of the Cartesian grid cell in the *x*- and *y*-directions respectively; and $\mathbf{F}_{\mathrm{E}}$, $\mathbf{F}_{\mathrm{W}}$, $\mathbf{F}_{\mathrm{N}}$ and $\mathbf{F}_{\mathrm{S}}$ are the flux vectors across the cell interfaces. The integrated form of equation (3.2) is discretised using an explicit scheme, which applies Euler discretization to the time derivative, and, on the Cartesian grid with spacing (*Δx* , *Δy*), leads to the inherently conservative method:

$$\mathbf{u}_{i,j}^{n+1} = \mathbf{u}_{i,j}^{n} - \frac{\Delta t}{\Delta x}(\mathbf{f}_E - \mathbf{f}_W) - \frac{\Delta t}{\Delta y}(\mathbf{g}_N - \mathbf{g}_S) + \Delta t \mathbf{s}_{i,j} \quad , \tag{3.3}$$

where superscript n represents the present time level; subscripts i,j are the cell indexes; Δt is the time step; $\mathbf{f}_W$ and $\mathbf{f}_E$ are the fluxes through the west and east cell interfaces; and $\mathbf{g}_N$ and $\mathbf{g}_S$ are the fluxes through the north and south cell interfaces. The fluxes and source terms are evaluated at time level n but the index has been dropped for brevity.

3.1.2. The HLLC Approximate Riemann Solver

The HLLC approximate Riemann solver (Toro, 2001) is a modification of the HLL solver that takes into account the effect of intermediate waves. The HLLC solver captures strong shocks without producing spurious oscillations, propagates rarefactions in the presence of low-density flow while preserving the entropy condition (Remaki et al., 2002) and preserves initially positive densities and pressures. Centred methods can be considered as Godunov-type methods (upwind), where the solution of the Riemann problem is approximated and not explicitly computed (Toro, 2001). The approximate Riemann solver of Roe (1981) is used to represent physically the decomposition of the fluxes. Within each cell the approximate solution is continuous whereas discontinuities can occur at the cell edges (Hirsch, 1990). The locally linearised Riemann problem at each cell edge divides the flux into three components that represent a shock, a rarefaction and a shear (contact) wave (Figure 3.2).

According to the HLLC approximate Riemann solver, the flux at the east interface, $\mathbf{f}_E$, is estimated as:

$$\mathbf{f}_E = \begin{cases} \mathbf{f}_L & \text{if } 0 \le S_L \\ \mathbf{f}_{*\mathrm{L}} & \text{if } S_L \le 0 \le S_M \\ \mathbf{f}_{*\mathrm{R}} & \text{if } S_M \le 0 \le S_R \\ \mathbf{f}_{\mathrm{R}} & \text{if } 0 \ge S_R \end{cases} , \tag{3.4}$$

where $\mathbf{f}_{\mathrm{L}}=\mathbf{f}(\mathbf{u}_{\mathrm{L}})$ and $\mathbf{f}_{\mathrm{R}}=\mathbf{f}(\mathbf{u}_{\mathrm{R}})$ are calculated from the left and right Riemann states $\mathbf{u}_{\mathrm{L}}$ and $\mathbf{u}_{\mathrm{R}}$ for a local Riemann problem. The fluxes $\mathbf{f}_{*\mathbf{L}}$ and $\mathbf{f}_{*\mathbf{R}}$ correspond to the left and right sides of the shear (contact) wave; and S_L, S_M and S_R are estimates of the speeds of the left, middle (contact) and right waves. The middle region fluxes $\mathbf{f}_{*\mathbf{L}}$ and $\mathbf{f}_{*\mathbf{R}}$ are different at each side of the shear wave, and are calculated as

$$\mathbf{f}_{*L} = \begin{bmatrix} f_{*1} \\ f_{*2} \\ v_L f_{*1} \end{bmatrix} \quad \text{and} \quad \mathbf{f}_{*R} = \begin{bmatrix} f_{*1} \\ f_{*2} \\ v_R f_{*1} \end{bmatrix} , \tag{3.5}$$

where v_L and v_R are the left and right tangential velocity components of the Riemann states. By applying the integral form of the conservation laws at each cell, the flux at the middle region is evaluated as (Harten et al., 1983)

$$\mathbf{f}_* = \frac{S_R\mathbf{f}_L - S_L\mathbf{f}_R + S_L S_R(\mathbf{u}_R - \mathbf{u}_L)}{S_R - S_L} , \tag{3.6}$$

The wave speed estimates S_L and S_R are evaluated as suggested by Fraccarollo and Toro (1995) from

$$S_L = \begin{cases} u_R - 2\sqrt{gh_R} & \text{if } h_L = 0 \\ \min(u_L - \sqrt{gh_L}, u_* - \sqrt{gh_*}) & \text{if } h_L > 0 \end{cases}$$

and (3.7)

$$S_R = \begin{cases} u_L - 2\sqrt{gh_L} & \text{if } h_R = 0 \\ \max(u_R - \sqrt{gh_R}, u_* - \sqrt{gh_*}) & \text{if } h_R > 0 \end{cases}$$

where u_L, u_R, h_L and h_R are the left and right components of the Riemann states; and u_* and h_* are values in the middle region given by

$$u_* = \frac{1}{2}(u_L + u_R) + \sqrt{gh_L} - \sqrt{gh_R} \quad , \tag{3.8}$$

and

$$h_* = \frac{1}{g}[\frac{1}{2}(\sqrt{gh_L} - \sqrt{gh_R}) + \frac{1}{4}(u_L + u_R)] \quad . \tag{3.9}$$

To estimate the middle wave speed S_M, Toro (2001) suggests the following formula

$$S_M = \frac{S_L h_R (u_R - S_R) - S_R h_L (u_L - S_L)}{h_R (u_R - S_R) - h_L (u_L - S_L)} \tag{3.10}$$

The remaining interface fluxes $\mathbf{f}_W$, $\mathbf{g}_N$ and $\mathbf{g}_S$ are calculated by following a similar procedure to that outlined above.

3.1.3. Discretisation of Source Terms

Discretisation of source terms is essential not only because the source terms are part of the mathematical model but also because the flux can vary spatially even when the conservative variables do not. After discretisation, the flux gradients and the source terms must remain balanced (Hubbard and García-Navarro, 2000). In combination with Roe's scheme, the discretisation leads to the approximation of the conservation laws and the construction of appropriate discrete forms for the additional terms, not only in the first-order case but also in the presence of flux- and slope-limited corrections. The source terms are cell-centred and the bed slope terms $\partial z_b / \partial x$ and $\partial z_b / \partial y$ are approximated by second order accurate central differences as follows

$$-\frac{\tau_{bx}}{\rho} - g\eta\frac{\partial z_b}{\partial x} = -(\frac{\tau_{bx}}{\rho})_{i,j}^{n,m} - g\eta_{i,j}^{n,m}(\frac{z_{bE} - z_{bW}}{\Delta x}) \quad , \tag{3.11}$$

and

$$-\frac{\tau_{by}}{\rho} - g\eta\frac{\partial z_b}{\partial y} = -(\frac{\tau_{by}}{\rho})_{i,j}^{n,m} - g\eta_{i,j}^{n,m}(\frac{z_{bN} - z_{bS}}{\Delta y}) \quad ,$$

where z_{bE}, z_{bW}, z_{bN} and z_{bS} are the bed elevations at the mid-point of the eastern, western, northern and southern interface of each cell respectively.

3.1.4. The MUSCL–Hancock Method

As a hyperbolic system of partial differential equations, the horizontal variable density shallow water equations may permit discontinuities in the gradients of the dependent

variables. In the vicinity of these discontinuities the numerical model may create spurious oscillations. The MUSCL–Hancock finite volume scheme (van Leer, 1985) is able to deal with discontinuous behaviour (Mingham and Causon, 1998; Hu et al. 2000). It is a high-resolution, second-order accurate Godunov-type scheme which provides solutions to the local Riemann problem at cell interfaces (Shiach et al., 2004). MUSCL (Monotonic Upwind Schemes for Conservation Laws) schemes use the values of the conserved variables at the surrounding cells of cell *i,j* to calculate a slope-limited gradient which ensures that there are no spurious oscillations at the interfaces. The MUSCL–Hancock scheme is a predictor–corrector method (van Leer, 1985). The three main steps are: i) reconstruction of the data, ii) evaluation of extrapolated values, and iii) solution of the Riemann problem (Toro, 2001). The predictor stage is given as

$$\bar{\mathbf{u}}_{i,j}^{n+1/2} = \mathbf{u}_{i,j}^{n} - \frac{\Delta t}{2\Delta x}(\mathbf{f}_E - \mathbf{f}_W) - \frac{\Delta t}{2\Delta y}(\mathbf{g}_N - \mathbf{g}_S) + \frac{\Delta t}{2}\mathbf{s}_{i,j}, \tag{3.12}$$

where n is the time step counter; i,j are the cell indices; Δt is the time step; $\mathbf{f}_W$, $\mathbf{f}_E$, $\mathbf{g}_N$ and $\mathbf{g}_S$ are the fluxes at the cell interfaces and are calculated using slope limited gradients based upon neighbouring cell data. MINBEE (or MINMOD) or the SUPERBEE slope limiter functions are used and the values of the conserved variables can be found at the cell interfaces by using linear interpolation. Therefore, the predictor step is non-conservative. However, the overall numerical scheme remains conservative as the corrector stage provides a fully conservative solution over one time step, using the HLLC approximate Riemann solver.

3.1.5. Slope Limiter

Flux limiters are used in the MUSCL-Hancock scheme to avoid the spurious oscillations (wiggles) that would otherwise occur with the high order spatial discretisation scheme due to shocks, discontinuities or sharp changes in the solution domain (Harten and Osher, 1987). The use of flux limiters within a high resolution scheme makes the solution total variation diminishing (TVD). For smoothly changing waves, the flux limiters do not operate and the spatial derivatives can be represented by higher order approximations without introducing non-real oscillations. For the calculation of the interface fluxes, both at the predictor and corrector steps the formula is as follows

$$\mathbf{u}(x, y) = \mathbf{u}_{i,j} + \Phi(r)\mathbf{r}\forall\mathbf{u}_{i,j} \ , \tag{3.13}$$

where *(x,y)* represent the point where the interpolation is required; **r** is the vector of the distance between *(x,y)* and the centre of the cell (in this case east and north are positive in *x*- and *y*-directions respectively); and *Φ(r)* is the function of the ratio of gradients. In the predictor step, if the edge fluxes can be represented by low and high resolution schemes, then a flux limiter can switch between these schemes depending on the gradients of the neighboring cells, as follows

$$\mathbf{u}_W^n = \mathbf{u}_{i,j}^n - \frac{1}{2}\Phi(r)(\mathbf{u}_{i,j}^n - \mathbf{u}_W^n) \quad \text{and} \quad \mathbf{u}_E^n = \mathbf{u}_{i,j}^n + \frac{1}{2}\Phi(r)(\mathbf{u}_{i,j}^n - \mathbf{u}_W^n) \ , \tag{3.14}$$

where *Φ(r)* is the limiter function. *Φ(r)* is constrained to be greater than or equal to zero. Therefore, when the limiter is equal to zero (sharp gradient, opposite slopes or zero gradient), the flux is represented by a low resolution scheme. Similarly, when the limiter is

equal to 1 (smooth solution), it is represented by a high resolution scheme as follows (Hirsch, 1990)

$$\Phi(r) = \max[0, \min(\beta r, 1), \min(r, \beta)], \tag{3.15}$$

where r represents the ratio of successive gradients on the solution mesh, i.e.,

$$r = \frac{\eta_e - \eta_{i,j}}{\eta_{i,j} - \eta_w}, \quad r = \frac{(uh)_e - (uh)_{i,j}}{(uh)_{i,j} - (uh)_w} \quad \text{and} \quad r = \frac{(vh)_e - (vh)_{i,j}}{(vh)_{i,j} - (vh)_w}, \tag{3.16}$$

for the three conserved variables in the *x*-direction. The subscripts 'e' and 'w' represent the eastern and western adjacent cells and β ($1 \le \beta \le 2$) is the limiter parameter. The value of β equals 1 for the minimod limiter and 2 for the Roe's superbee limiter. Similar formulae are used in the y-direction.

In the corrector stage, the slope limiter is used for the calculation of the interface fluxes within the HLLC approximate Riemann solver. For example, at the eastern interface the formula is

$$\mathbf{u}_E^L = \bar{\mathbf{u}}_{i,j}^{n+1/2} + \frac{1}{2}\Phi(r)(\mathbf{u}_{i,j}^n - \mathbf{u}_W^n) \quad \text{and} \quad \mathbf{u}_E^R = \bar{\mathbf{u}}_e^{n+1/2} - \frac{1}{2}\Phi(r)(\mathbf{u}_e^n - \mathbf{u}_{i,j}^n), \tag{3.17}$$

where $\bar{\mathbf{u}}_{i,j}^{n+1/2}$ and $\bar{\mathbf{u}}_e^{n+1/2}$ are the predicted values at the centre of the cell (*i,j*) and at its eastern adjacent cell. Similar approaches are used for the three other faces.

3.1.6. Stability and Convergence

When Godunov-type schemes are used, the time-step is restricted to ensure that the fastest waves will not traverse more than one cell each time. The linearised stability condition is as follows (Toro, 2001)

$$\left|C_{cfl}\right| \leq 1, \tag{3.18}$$

where C_{cfl} is the Courant-Friedrichs-Lewy number corresponding to the maximum wave speed at each time level given by

$$C_{cfl} = \frac{\lambda dt}{dx} = \frac{\lambda}{dx/dt}, \tag{3.19}$$

where λ is the wave propagation speed. C_{cfl} is taken equal to 0.9 for most of the computations. Equation (3.19) leads to the following constraint for the two-dimensional model

$$dt = C_{cfl} \min(dt_x, dt_y), \tag{3.20}$$

where

$$dt_x = \min_{i,j} \frac{dx_{i,j}}{|u| + \sqrt{gh_{i,j}}} \qquad \text{and} \qquad dt_y = \min_{i,j} \frac{dy_{i,j}}{|v| + \sqrt{gh_{i,j}}} \tag{3.21}$$

When dealing with problems that involve wetting and drying fronts the above procedure may not be sufficient, as the waves travel very fast (Toro, 2001) and therefore they should be treated separately.

3.2. Wetting and Drying

When dealing with wetting and dry fronts, the method used, should not produce excessive wiggles by irregular wetting and drying and should conserve global and local mass (Balzano, 1998). Key aspects of these methods are the criterion for the declaration of the wet or dry status of the cells in the computational mesh, the effective evaluation of the retention volume in each cell and the computation of water depth between two adjacent cells.

The boundary condition at a moving boundary can be written as:

$$\eta - z_b = 0 \quad \text{at} \quad x_b(t) = x_{b_0} + \int u_b dt, \tag{3.22}$$

where $x_b(t)$ is the position of the moving shoreline at time t; u_b is the velocity of the wet front; and x_{b0} the initial shoreline position. There are three major categories of methods for the solution of the above equation based either on natural coordinates (fixed grid or adaptive grid) or on transformed coordinates. Fixed grid methods are the most popular. A drawback of these models arises from the discrete and fixed steps by which the wet area must advance or recede during the process. The under- and overestimation of retention volumes can be alleviated by reducing the grid size.

Considering the speed of the moving boundary in the one-dimensional case, u_b, in the time step, *dt,* a distance is covered equal to:

$$u_b dt = \frac{u_b}{\sqrt{gh}} \frac{dt}{dx} \sqrt{gh} dx = Fr C_{cfl} dx, \tag{3.23}$$

where Fr is the Froude number and C_{cfl} is the Courant-Friedrichs-Lewy number.

In the wetting and drying scheme used in this research, the calculations take place only inside the wet domain. When a wet cell is adjacent to a dry cell, there are two cases (Liang and Borthwick, 2008):

1. A wet (left) cell next to a dry (right) cell on the right, where $h_L \neq 0$, $h_R = 0$ and $\eta_R = z_{bR} > \eta_L$. This means that the model should ensure that there is no flux through the interface (Figure 3.3(a)). For that reason the velocities at the interface are set to zero and the following local bed modification is considered

$$\begin{aligned} \Delta\eta &= \eta_R - \eta_L \ , \\ \eta_R' &= \eta_R - \Delta\eta \ , \\ z_{bR}' &= \eta_R' . \end{aligned} \tag{3.24}$$

2. The bed surface elevation of the right hand dry cell is smaller than (or equal to) that of the left hand wet cell and consequently the flow continues to flood the dry cell by integrating the right cell in the computational domain (Figure 3.3(b)).

When a cell is dried or the water depth in it is below the critical level, h_{crit}, it is excluded from the computational domain and the velocities are set to zero (Figure 3.3(c)). If the bed slope is too steep, the huge velocities in any over-dried cell may create negative depths

without physical meaning. In order to overcome this problem, the velocities are set to zero and an amount of 'negative' water is added to the direct neighbouring cell that contains maximum amount of water or, if there are more than one wet domains, to the next neighbouring wet cell in the direction of the flow. The velocities in the cell from which the water is subtracted are modified accordingly, so that the fluxes remain the same (Brufau et al., 2004). If none of the neighbouring cells contains sufficient water (above the h_{crit}) the 'negative' water is stored and transferred to the next time step, until there is sufficient water at the adjacent cells or until the cell itself is wetted again. In the case of a dry cell next to another dry cell with a different bed level the local bed modification of Case 1 is adopted in order to avoid the creation of unrealistic fluxes.

For the cases involving wetting and drying, flags are used to identify each cell, according to whether it is wet or dry or at a particular wet-dry interface. In this way, cells of each type are treated separately, making the computational scheme more efficient. Certain other modifications were implemented in the numerical model. For example, any dry cell whose bed level is below the water level of either of its neighbours is included in the computational domain. Furthermore, when the bed of a dry cell is below the bed of its neighbouring wet cell at the wet/dry front and when the water mass is disjoint, (i.e. two wet neighbouring cells with the water level of the one below the bed level of the other), the following modification is invoked

$$\eta_R' = z_{bL} \quad \text{and} \quad z_{bR}' = \eta_R' - h_R, \quad \text{when} \quad z_{bL} > \eta_R \tag{3.25}$$

The flags of the cells and therefore the computational domain are updated at every time step. Particular care is taken for the boundary cells.

The same approach is followed for the y-direction in the two-dimensional model. The wetting and drying scheme can be applied to a variety of constant and variable density problems with different levels of accuracy and complexity.

3.3. Entrainment and Deposition

When using the one-dimension full balanced variable density shallow water equations, which take into account also the entrainment and the deposition of the sediment, the mass conservation equation used in the numerical model should be modified as follows:

$$\frac{\partial(\rho\eta-\rho_{\mathrm{w}}\eta_{\mathrm{s}})}{\partial t}+\frac{\partial(\rho uh)}{\partial x}=-\rho_0\frac{D-E}{1-p}+\frac{\partial\rho z_b}{\partial t} \tag{3.26}$$

Owing to the dependence of the density of the mixture, ρ, and the bed elevation, z_b, the $\frac{\partial\rho z_b}{\partial t}$ term cannot be calculated explicitly, so an iteration scheme is adopted.

The same applies for the two-dimensional full balanced variable density shallow water equations, which take into account the entrainment and the deposition of the sediment. Consequently, the mass conservation equation used in the numerical model should be modified as follows:

$$\frac{\partial(\rho\eta-\rho_{\mathrm{w}}\eta_{\mathrm{s}})}{\partial t}+\frac{\partial(\rho uh)}{\partial x}+\frac{\partial(\rho vh)}{\partial y}=-\rho_0\frac{D-E}{1-p}+\frac{\partial\rho z_b}{\partial t} \tag{3.27}$$

Again, for the same reasons as in the one-dimensional model, the $\frac{\partial \rho z_b}{\partial t}$ term is calculated by an iteration scheme.

3.4. Hyberbolic Stage-Discharge form of Horizontal Variable Density Shallow Water Equations

By taking into account the continuity equation, introducing the depth-averaged velocity components, using Leibniz's formula for differentiation of an integral (Falconer 1993), and ignoring Coriolis effects and surface vectors, the conservative (in terms of momenta) two-dimensional shallow water equations can be written in stage-discharge hyperbolic form as follows:

$$\frac{\partial \mathbf{u}}{\partial t} + \frac{\partial \mathbf{f}}{\partial x} + \frac{\partial \mathbf{g}}{\partial y} = \mathbf{s} \tag{3.28}$$

where **u**, **f**, **g** and **s** are vectors of dependent conserved variables, Cartesian components of the flux, and source terms, respectively, in which:

$$\mathbf{u} = \begin{bmatrix} \rho\eta - \rho_{\mathrm{w}}\eta_{\mathrm{s}} \\ \rho uh \\ \rho vh \\ \rho_s ch \\ z_b \end{bmatrix},$$

$$\mathbf{f} = \begin{bmatrix} \rho uh \\ \rho u^2 h + \frac{1}{2} g\rho(\eta^2 - 2\eta z_b) - \frac{1}{2}\rho_w g(\eta_s^2 - 2\eta_s z_b) \\ \rho uvh \\ \rho_s uch \\ 0 \end{bmatrix},$$

$$\mathbf{g} = \begin{bmatrix} \rho vh \\ \rho uvh \\ \rho v^2 h + \frac{1}{2} g\rho(\eta^2 - 2\eta z_b) - \frac{1}{2}\rho_w g(\eta_s^2 - 2\eta_s z_b) \\ \rho_s vch \\ 0 \end{bmatrix},$$

and

$$\mathbf{s} = \begin{bmatrix} -\rho_0 \frac{D-E}{1-p} + \frac{\partial \rho z_b}{\partial t} \\ -\rho g\eta \frac{\partial z_b}{\partial x} + \rho_w g\eta_s \frac{\partial z_b}{\partial x} - \tau_{bx} \\ -\rho g\eta \frac{\partial z_b}{\partial y} + \rho_w g\eta_s \frac{\partial z_b}{\partial y} - \tau_{by} \\ \rho_s (E-D) \\ \frac{D-E}{1-p} \end{bmatrix} \qquad (3.29)$$

where η is the surface water level above a given datum; η_s is the surface water level above a given datum at the quiescent equilibrium state ($h_s = \eta_s - z_b$); z_b is the level of the bed above the same datum; h is the water level above the level of the bed ($h=\eta-z_b$); u and v are

depth-averaged velocity components in the two Cartesian directions; g is the acceleration due to gravity; τ_{bx} and τ_{by} are the bed stress components; E is the entrainment of the sediment; D is the deposition of the sediment; ρ_w is the density of the liquid and ρ is the density of the liquid-species mixture.

For the one-dimensional model the equation (3.28) is reduced to:

$$\frac{\partial \mathbf{u}}{\partial t} + \frac{\partial \mathbf{f}}{\partial x} = \mathbf{s} \tag{3.30}$$

where **u**, **f** and **s** are vectors of dependent conserved variables, flux, and source terms, respectively, in which:

$$\mathbf{u} = \begin{bmatrix} \rho\eta - \rho_{\mathrm{w}}\eta_{\mathrm{s}} \\ \rho uh \\ \rho_s ch \\ z_b \end{bmatrix},$$

$$\mathbf{f} = \begin{bmatrix} \rho uh \\ \rho u^2 h + \frac{1}{2} g\rho(\eta^2 - 2\eta z_b) - \frac{1}{2}\rho_{\mathrm{w}} g(\eta_{\mathrm{s}}^2 - 2\eta_{\mathrm{s}} z_b) \\ \rho_s uch \\ 0 \end{bmatrix},$$

and

$$\mathbf{s} = \begin{bmatrix} -\rho_0 \dfrac{D-E}{1-p} + \dfrac{\partial \rho z_b}{\partial t} \\ -\rho g \eta \dfrac{\partial z_b}{\partial x} + \rho_w g \eta_s \dfrac{\partial z_b}{\partial x} - \tau_{bx} \\ \rho_s (E-D) \\ \dfrac{D-E}{1-p} \end{bmatrix} \tag{3.31}$$

The bed shear stresses represent the retarding effect of bed roughness on the flow and can be estimated from the following empirical formula:

$$\tau_{bx} = \rho C_f U \sqrt{U^2 + V^2} \quad \text{and} \quad \tau_{by} = \rho C_f V \sqrt{U^2 + V^2} \tag{3.32}$$

where C_f is an empirical friction coefficient which varies with the bed roughness and can be evaluated from Chezy friction law or from Manning's formula

$$C_f = \frac{g}{C^2} \quad \text{or} \quad C_f = g \frac{{n_m}^2}{h^{1/3}} \tag{3.33}$$

where C is the Chézy coefficient and n_m is the Manning coefficient.

The entrainment, E, is given by the following formula (Soulsby, 1997):

$$E = \begin{cases} M\left(\dfrac{\tau_b - \tau_c}{\tau_c}\right), & \text{when} \quad \tau_b > \tau_c \\ 0, & \text{when} \quad \tau_b \le \tau_c \end{cases} \tag{3.34}$$

where M is the entrainment constant, τ_b is the shear stress of the bed in the relevant direction, and τ_c is the threshold shear stress of the bed. By choosing M, τ_b, and τ_c to have constant values, the entrainment, E, is also constant.

For the calculation of the deposition of the sediment the following empirical formula is used $D=w_s\ c$, where w_s is the settling velocity of the sediment relative to the fluid and c the concentration of the sediment.

The Jacobian matrix, J_n, of the flux ($\mathbf{F}\cdot\mathbf{n}=\mathbf{f}n_x+\mathbf{g}n_y$) is:

$$J_n = \frac{\partial(\mathbf{F}\cdot\mathbf{n})}{\partial\mathbf{u}} = \frac{\partial\mathbf{f}}{\partial\mathbf{u}}n_x + \frac{\partial\mathbf{g}}{\partial\mathbf{u}}n_y \tag{3.35}$$

and is evaluated as:

$$J_n = \begin{bmatrix} 0 & n_x & n_y \\ (c^2-U^2)n_x - UVn_y & 2Un_x + Vn_y & Un_y \\ -UVn_x + (c^2-V^2)n_y & Vn_x & Un_x + 2Vn_y \end{bmatrix} \tag{3.36}$$

where n_x and n_y are the Cartesian components of the unit vector in x- and y-directions; and $c=\sqrt{gh}$ is the celerity of the small amplitude surface waves.

The respective eigenvalues are:

$$\lambda_1 = un_x + vn_y + c$$

$$\lambda_2 = un_x + vn_y \tag{3.37}$$

$$\lambda_3 = un_x + vn_y - c$$

and the eigenvectors are:

$$\mathbf{e_1} = \begin{bmatrix} 1 \\ U + cn_x \\ V + cn_y \end{bmatrix} \quad , \qquad \mathbf{e_2} = \begin{bmatrix} 0 \\ -cn_y \\ cn_x \end{bmatrix} \quad , \qquad \mathbf{e_3} = \begin{bmatrix} 1 \\ U - cn_x \\ V - cn_y \end{bmatrix} \tag{3.38}$$

The eigenvalues correspond to the characteristic speeds and the eigenvectors correspond to the characteristic directions. In that way, they form a picture of the propagation of the flux and can be used for approximations that ensure the transmission of waves in the correct directions (Alcrudo and García-Navarro, 1993).

3.5. Boundary Conditions

When dealing numerically with the Riemann problem, fictitious cells are created at the beginning and the end of the domain in order to generate the boundary conditions at each edge. There are different ways of calculating the boundary values (see for example Toro, 2001; Rogers et al., 2001). The boundary conditions depend on the nature of the flow of each test case and are either transmissive (in the case of outflow or inflow), or reflective (when the boundary is considered as solid wall) or moving in the case of wetting and drying fronts, as described in Section 3.2.

In the absence of waves that vary the flow significantly the following approach is considered. For transmissive boundaries at either end of the computational domain

$$\eta_{0,j}^{n}=\eta_{1,j}^{n} \qquad h_{0,j}^{n}=h_{1,j}^{n} \qquad \rho_{0,j}^{n}=\rho_{1,j}^{n}$$
$$\eta_{i\max+1,j}^{n}=\eta_{i\max,j}^{n}, \qquad h_{i\max+1,j}^{n}=h_{i\max,j}^{n}, \qquad \rho_{i\max+1,j}^{n}=\rho_{i\max,j}^{n},$$

$$u_{0,j}^{n}=u_{1,j}^{n} \qquad v_{0,j}^{n}=v_{1,j}^{n}$$
$$u_{i\max+1,j}^{n}=u_{i\max,j}^{n} \quad \text{and} \quad v_{i\max+1,j}^{n}=v_{i\max,j}^{n} \tag{3.39}$$

and for reflective boundaries at both ends

$$\eta_{0,j}^{n}=\eta_{1,j}^{n} \qquad h_{0,j}^{n}=h_{1,j}^{n} \qquad \rho_{0,j}^{n}=\rho_{1,j}^{n}$$
$$\eta_{i\max+1,j}^{n}=\eta_{i\max,j}^{n}, \qquad h_{i\max+1,j}^{n}=h_{i\max,j}^{n}, \qquad \rho_{i\max+1,j}^{n}=\rho_{i\max,j}^{n},$$

$$u_{0,j}^{n}=-u_{1,j}^{n} \qquad v_{0,j}^{n}=-v_{1,j}^{n}$$
$$u_{i\max+1,j}^{n}=-u_{i\max,j}^{n} \quad \text{and} \quad v_{i\max+1,j}^{n}=-v_{i\max,j}^{n} \tag{3.40}$$

The superscript n denotes the current time step, i and j are the indices of the cell number at x- and y-direction respectively and 0 and i_{max+1} are the indices of the ghost cells at the beginning and the end of the domain respectively. In the above equations, η is the elevation of the water surface above the datum, h is the water depth, ρ is the density of the mixture, u_i^n corresponds to the depth averaged velocity component to the x-direction and v_i^n corresponds to the depth averaged velocity component to the y-direction.

At reflective boundaries slip or no-slip conditions may be applied. For slip boundaries at both ends

$$\eta^n_{0,j} = \eta^n_{1,j} \qquad h^n_{0,j} = h^n_{1,j} \qquad \rho^n_{0,j} = \rho^n_{1,j}$$
$$\eta^n_{i\max+1,j} = \eta^n_{i\max,j}, \qquad h^n_{i\max+1,j} = h^n_{i\max,j}, \qquad \rho^n_{i\max+1,j} = \rho^n_{i\max,j},$$

$$u^n_{0,j} = -u^n_{1,j} \qquad v^n_{0,j} = v^n_{1,j}$$
$$u^n_{i\max+1,j} = -u^n_{i\max,j} \quad \text{and} \quad v^n_{i\max+1,j} = v^n_{i\max,j} \tag{3.41}$$

For no-slip boundaries at either end of the computational mesh the boundary conditions are the same as in Equation (3.40).

It should be noted that in the case of an open boundary, the Froude number is taken into account (as described in Section 2.2.2), by using Riemann invariants. For subcritical flow ($Fr < 1$)

$$h^n_{b,j} = (\sqrt{h^n_{i,j}} \pm \frac{1}{2\sqrt{g}}(u^n_{i,j} - u^n_{b,j}))^2 \tag{3.42}$$

where the velocity $u^n_{b,j}$ is prescribed and

$$u^n_{b,j} = u^n_{i,j} \pm 2\sqrt{g}(\sqrt{h^n_{i,j}} - \sqrt{h^n_{b,j}}) \tag{3.43}$$

where the water depth $h^n_{b,j}$ is prescribed. The subscript *b* refers to the boundary value and the subscript *i* refers to the value of the inner cell at time step *n*. The positive sign corresponds to outflow, and the negative to inflow. For supercritical ($Fr > 1$) inflow all the variables should be prescribed, whereas for supercritical outflow the transmissive boundary condition is used, i.e. $h^n_{0,j} = h^n_{1,j}$, $u^n_{0,j} = u^n_{1,j}$ and $v^n_{0,j} = v^n_{1,j}$. A similar procedure is followed in the *y*-direction.

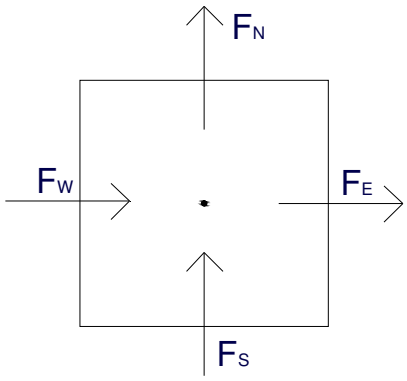


Fig. 3.1 Fluxes through the boundaries of one cell (control volume).

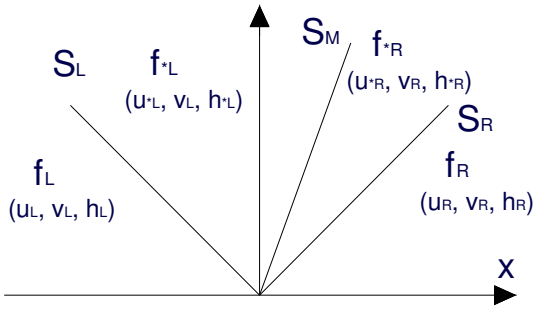
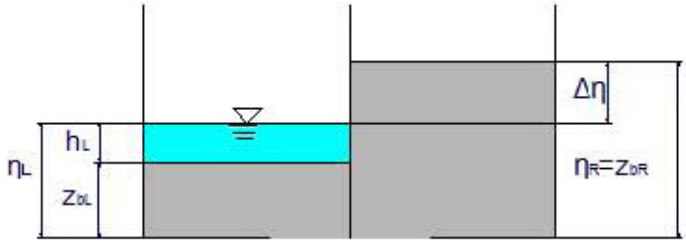
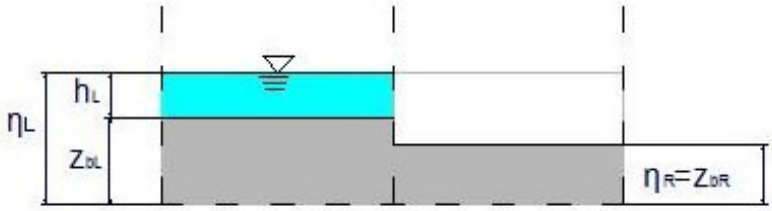


Fig. 3.2 The HLLC Riemann solver for 2D shallow water equations in the x-direction. The locally linearised Riemann problem at each cell edge divides the flux into three components that represent a shock, a rarefaction and a shear (contact) wave. The middle (star) region has two sub-regions (left and right of the contact wave).

(a)



(b)



(c)

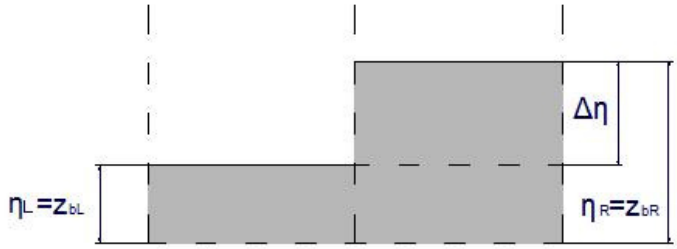


Fig. 3.3 Local bed modifications for: (a) $h_L \neq 0$, $h_R = 0$ and $\eta_R = z_{bR} > \eta_L$; (b) $h_L \neq 0$, $h_R = 0$ and $\eta_R = z_{bR} \leq \eta_L$; and (c) $h_L = 0$, $h_R = 0$.

CHAPTER 4 ONE-DIMENSIONAL MODEL VALIDATION TESTS

4.1. Introduction

Both the one- and two-dimensional numerical models were tested using a comprehensive range of benchmark cases, and the results compared against available analytical solutions. The one-dimensional model was validated for constant and variable density flows, wet/dry fronts, and erodible bed problems. The idealised test cases are useful for checking conservation of mass and momentum, in that potential errors are easy to identify given that the terms tend to be treated in isolation. The more complex test cases demonstrate the potential of the model in practice. In such cases, experimental data are useful for verification.

4.2. Constant Density Cases

When applying the one-dimensional variable density shallow flow equations solver to constant density flows, the equations effectively reduce to the constant density shallow water equations. Nevertheless, these tests are important in order to check that the numerical model can perform such computations without significant errors, even when some of the variables tend to zero. Effects on the stability of the model are also examined.

For the one-dimensional model, the constant density cases that were considered were the one-dimensional dam break, two rarefaction waves over a nearly dry bed, the right and left dry bed Riemann problems, generation of a dry bed by opposing rarefaction waves, damped free surface oscillations in a tank with parabolic bed, and dam break flow followed by interaction with a triangular obstacle.

4.2.1. Case 1: Dam-break

Considerable efforts have been made in past years to obtain satisfactory solutions for the dam-break problem (Abbott 1979; Tan 1992; and Chaudhry 1993). One feature of the hyperbolic shallow water equations is that they permit solutions involving rapidly varied discontinuous flow, such as at bore fronts. An important basis for validating the numerical method is whether or not the scheme can capture dam-break bore waves accurately. The quantities that most interest engineers in practice are water depths, their maximum values and wave propagation times. The problem of the instantaneous removal of a dam in a frictionless horizontal rectangular channel with infinite length was analytically solved by Ritter in 1892.

The first case concerns the instantaneous removal of a dam placed across a uniform rectangular frictionless channel of length 50 m. The channel initially contains water of depth 1 m and velocity 2.5 m/s for $x < 10$ m, and still water of depth 0.1 m for $x > 10$ m. The end boundaries are open, and the conditions are approximated using extrapolation of the dependent variables. The emergent wave pattern is that of a centred wave system with a left rarefaction wave and a right shock wave (Toro, 2001). The initial conditions ($t = 0$) for the water depth, h, are represented in Figure 4.1(a). Figures 4.1(b) and (c) illustrate the water surface profile and the velocity distribution respectively at the instant $t = 7$ s. The results are in perfect accordance with the analytical solution (Ritter, 1982) and an alternative numerical prediction (Toro, 2001).

4.2.2. Case 2: Two rarefaction waves over a nearly dry bed

The initial conditions considered are two rarefaction waves travelling at 5 m/s in opposite directions in water that is everywhere 1 m deep in a 50 m long channel (as shown in Figure 4.2(a)). The flow discontinuity occurs at the middle of the channel at x=25 m, and so the problem is symmetrical. The simulation time is 2.5 s (Figures 4.2(b) and (c)), and the time step is 0.001 s. The challenge for the model is not to compute negative depths in the vicinity of very shallow water produced by the strong opposing rarefaction waves (Toro 2001). The results shown in Figure 4.2 are in very good agreement with those presented by Toro using his weighted-average flux WAF scheme.

4.2.3. Case 3: Right dry bed and left dry bed Riemann problem

The solution of the right dry bed Riemann problem devised by Toro (2001) is a single left rarefaction wave, which represents the left eigenvalue of the Riemann problem $\lambda_1 = u - a$, with the wet/dry front attached to the tail of the rarefaction wave (Toro, 2001). The channel is again 50 m long. The initial conditions considered are 1 m water depth for $x < 20$ m and dry bed for $x > 20$ m, as shown in Figure 4.3(a). Extrapolation boundary conditions are applied at the ends of the domain. The time step is 0.001 s. Figures 4.3 (b) and (c) show the flow state at time $t = 4$ s. As shown in Figure 4.4, the left dry bed Riemann problem is the exact mirror picture of the right dry bed Riemann problem. According to Toro (2001) the difficulty is to propagate the wet/dry front at the correct speed and to avoid spurious oscillations around it. The present results obtained are very similar to those obtained by Toro, providing further validation of the numerical model for wet/dry flows over a horizontal bed.

4.2.4. Case 4: Generation of a dry bed by opposing rarefaction waves

Figure 4.5 (a) indicates the initial conditions for this test, comprising two rarefaction waves of speed 3 m/s travelling in opposite directions from the centre of a 50 m long channel. The water depth is everywhere 0.1 m. The time step is again 0.001 s. Extrapolation boundary conditions are applied at either end of the channel. Figures 4.5 (b) and (c) depict the simulated water depth and velocity profiles along the channel at time t = 5 s. Two rarefaction waves are evident, with a small area of dry bed between them. The results obtained by the model are almost identical to those given by the exact solution (Toro, 2001).

4.2.5. Case 5: Damped free surface oscillations in a tank with parabolic bed

The test case of damped sloshing in a parabolic tank was examined by Sampson *et al.* (2006) and Liang and Borthwick (2008), amongst others. The parabolic bed profile of the tank is given by

$$z_b(x) = h_0 (x/a)^2, \tag{4.1}$$

where z_b is the elevation of the bed above the datum; and h_0 = 10 m and a = 3 km are constants. The analytical solution of the water surface depends on time according to the following formula (Sampson et al., 2006)

$$\eta(x,t) = h_0 + \frac{a^2 B^2 e^{-\tau}}{8g^2 h_0}(-s\tau \sin 2st + (\tau^2/4 - s^2)\cos 2st) - \frac{B^2 e^{-\tau}}{4g} - \frac{e^{-\tau/2}}{g}(B\cos st + \frac{\tau B}{2}\sin st)x, \tag{4.2}$$

where η is the free surface elevation, B is a constant, $s = \sqrt{p^2 - \tau^2}/2$ and $p = \sqrt{8gh_0/a^2}$ is a hump amplitude parameter, τ is a bed friction parameter (related to the Chézy bed friction coefficient by $C_f = h\tau/\sqrt{u^2+v^2}$). The bed friction and the bed slope (source terms) are taken into account, whereas the Coriolis effect is neglected. In this case, B = 5 m/s and τ = 0.001 s^{-1}. The computational domain is 10000 m in horizontal extent. The time step is 0.001 s, and the number of grid points is 128. Figure 4.6 shows the numerical and analytical water profiles along the channel at different times up to t = 6000 s. It can be seen that the wet and dry fronts are calculated correctly and the overall results of the numerical model are in very good agreement with the analytical solution. The wetting and drying algorithm simulates successfully the sloshing motion of the water surface and its gradual deceleration due to the bed friction.

As well as being useful as a guide to choosing a suitable scheme, grid spacing and time step, systematic grid convergence tests can indicate the magnitude of error. For example, when refining the grid, if the solution does not approach the correct answer (and hence the error does not approach zero), it means zeroth order accuracy, i.e. wrong (Roache, 1998).
The methodology for selecting the most suitable combination of Δt and Δx for a given test case in this research is the following:

(1) A timestep is chosen (e.g. 0.01 s) in order to check grid convergence. With this timestep the scheme is run for various values of Δx (e.g. 10, 100, 200, 1000 m etc.).

(2) For each of the combinations the maximum error, i.e. $E_{\max} = \max\left\{\frac{\left|\eta_i - \eta_{anal_i}\right|}{\eta_{anal_i}}\right\}$ and the root mean square relative error, i.e. $E = \sqrt{\frac{\sum_{i=`}^{n}\left|\eta_i - \eta_{anal_i}\right|^2}{\sum_{i=`}^{n}\eta_{anal_i}^{\ 2}}}$ are calculated.

(3) For the *dx* that gives the minimum error, different *dt* are tried in order to find out the maximum *dt* that can be used without affecting stability.

With the above procedure the accuracy tests are separated from the stability ones. Table 4.1 lists the root-mean-square relative error and the maximum error for the case of damped free surface oscillations in a tank with parabolic bed during the grid convergence analysis at time *t*=500 seconds. For this test case Liang and Borthwick (2008) are using *dx* = 78.125 m which was examined in the grid convergence test as well. Finally, spatial step of *dx* = 40 m and time step *dt* = 0.001 s is chosen. For this time step the maximum error was 1.3%, whereas for time step *dt* = 0.1 s the model becomes unstable. Figure 4.7 shows the results of the grid convergence test for *dx* = 10, 40, 200 and 500 m.

4.2.6. Case 6: Dam break problem and flow over a triangular obstacle

This test case involves a dam-break wave which interacts with a triangular obstacle. The numerical predictions are compared with alternative numerical results obtained by Brufau et al. (2002) and experimental data obtained by the Recherches Hydrauliques Lab. Châtelet together with the University of Bruxelles (Belgium) under the supervision of J.M. Hiver. The experimental model consisted of a reservoir connected to a rectangular channel of total length 22.5 m. The dam is situated at *x* = 15.5 m. The symmetric triangular obstacle is 6 m

long and 0.4 m high, and its crest is situated at x = 28.5m. The initial water depth in the reservoir is 0.75 m and in the rest of the channel the bed is dry (as shown in Figure 4.8). The fixed boundaries are considered reflective (solid walls). A free outlet is located at the right hand side of the channel. The bed roughness coefficient is $C_f = g\frac{n_m^2}{h^{1/3}}$, where n_m=0.0125 is the Manning coefficient.

Table 4.2 lists the normalised and maximum errors as calculated for the grid convergence tests. The comparison was made against results obtained on the finest grid of dx=0.02 m as there was no available analytical solution. The time step chosen is 0.001 s and the spatial step is 0.1 m. Figure 4.9 shows the results of the grid convergence test for dx=0.2, 0.1 and 0.02 m. Figures 4.10 (a-e) show the numerical results obtained for the water depth at different times t =3s; 5 s; 10 s; 20 s and 40 s. The one-dimensional character of the flow renders the one-dimensional model appropriate for this test. The agreement with other published results (Brufau, 2002) is satisfactory, as shown in Figures 4.11 (a-d). It can be observed that the prediction of the transitions from wet to dry is correct. Figure 4.12 shows the time evolution of the water depth during 40 s, as measured at the Recherches Hydrauliques Lab. Châtelet and computed by the model at gauging points: G4, G10, G11, G13 and G20 (4, 10, 11, 13, and 20 meters downstream from the initial position of the dam). The numerical results are again in very good agreement with the laboratory data.

4.3. Variable Density Cases

The test cases in this section simulate vertically homogeneous shallow flows with variable horizontal density. As mentioned previously, the term ‘species’ refers to material transported with the liquid flow. Flows over regular and irregular bed topography are examined.

Following Leighton (2010), the 1-D variable density validation cases comprise the following: quiescent equilibrium of liquid of variable density in a tank with a sinusoidal bed, a density dam break with a single initial discontinuity, and a dam break with two initial discontinuities. For the last test case, a parameter study is carried out by varying the ratio of species to liquid density.

4.3.1. Case 7: Quiescent equilibrium in a tank with a sinusoidal bed

Consider a rectangular tank of length *L* and sinusoidal bed with the following topography:

$$z_b(x) = A\left[1 - \cos\left(\frac{2\pi x}{L}\right)\right], \tag{4.3}$$

where *A* is the amplitude of the bed perturbation, and *x* is horizontal distance along the channel. For quiescent equilibrium in the tank, which means no flow at steady state, i.e. zero velocity and unchanging properties in time, the terms $\frac{\partial(\rho\eta - \rho_w \eta_s)}{\partial t}, \frac{\partial(\rho uh)}{\partial t}, \frac{\partial(\rho_s ch)}{\partial t}$ and $\frac{\partial(\rho_s uch)}{\partial x}$, as well as τ_b, *E* and *D* of the full variable density shallow water equations are zero. So, the unbalanced momentum conservation equation can be simplified as follows:

$$\frac{\partial(\frac{1}{2}\rho g(\eta^2 - 2\eta z_b))}{\partial x} = -\rho g\eta\frac{\partial z_b}{\partial x}, \tag{4.4}$$

And after substituting $\eta = h + z_b$, the above equation becomes:

$$\frac{\partial(\frac{1}{2}\rho g h^2)}{\partial x} = -\rho g h \frac{\partial z_b}{\partial x}, \tag{4.5}$$

or,

$$\frac{\partial(\rho h^2)}{\partial x} = -\rho 2 h \frac{\partial z_b}{\partial x}. \tag{4.6}$$

At steady state equilibrium, the density and the water depth are solely functions of the distance along the channel ($\rho = \rho(x)$ and $h = h(x)$, as shown by Leighton (2010)) and consequently the above gives an ordinary differential equation. If the bed is horizontal, then $\frac{\partial z_b}{\partial x} = 0$, and

$$\rho h^2 = \text{ constant}. \tag{4.7}$$

However, if the bed has a slope or irregular topography, then $\frac{\partial z_b}{\partial x} \neq 0$, and differentiation of Equation (4.6) gives:

$$\frac{h}{\rho}\frac{\partial \rho}{\partial x} + 2\frac{\partial h}{\partial x} = -2\frac{\partial z_b}{\partial x} \tag{4.8}$$

The tank is filled with a liquid-species mixture such that $\rho h^2 = \text{ constant}$. The initial condition is the analytical steady state (zero flow) solution. In this case, the system should remain in the equilibrium solution for infinite time.

The variable-density equilibrium solution for the mixture depth and density at steady-state is the following:

$$h_{eq}(x) = h_0, \qquad \rho_{eq}(x) = \rho_0 \exp\left[\frac{2A}{h_0}\cos\left(\frac{2\pi x}{L}\right)\right] \tag{4.9}$$

The values used are the following: the length of the channel is $L = 100$ m, the amplitude of the sinusoidal bed perturbation is $A = 0.1$ m, the initial/steady state water depth is $h_0 = 1$ m, the steady state density of the mixture for horizontal bed is ρ_0 = 1000 kg/m^3, the liquid density is ρ_w = 1000 kg/m^3, the species density is ρ_s = 2000 kg/m^3, and the acceleration of gravity is g = 9.81 m/s^2. The effects of viscosity, wind, turbulence and friction are ignored. The computational domain is divided into 1000 cells. The time step is $\Delta t = 0.01$ s and the total simulation time is $t = 300$ s. The boundaries at either end of the computational domain are considered as solid walls (reflective boundary conditions).

Figure 4.13 (a) shows the water elevation and the bed profile (dotted red line) at steady state equilibrium in the tank with the sinusoidal bed. Figure 4.13 (b) shows the density of the mixture at steady state equilibrium and the density of the mixture (constant) if the bed was horizontal (dotted red line). The numerical results verify that the system remains unchanged during the model run time.

4.3.2. Case 8: 1-D density dam break with a single initial discontinuity

This case involves a horizontal channel of length *L*, which is filled with two adjacent liquids of different density but with the same initial depth, each of them occupying half of the channel and separated by an infinitesimally thin wall. At time *t*=0 s the wall collapses instantly and the system is set free.

The values used for this test are: length of the channel L = 500 m, density of the liquid to the left of the wall $\rho_L = 10$ kg/m^3, density of the liquid to the right of the wall $\rho_R = 1$ kg/m^3, initial uniform water depth for both resting liquids at rest h_0 = 1 m, gravity acceleration $g = 1$ m/s^2. The effects of viscosity, wind, turbulence and friction are ignored.

Figure 4.14 shows the results of the grid convergence test for dx = 10, 2.5, 0.1 and 0.05 m. The spatial step chosen is 0.1 m and the time step is 0.001 s. Figures 4.15 (a-c) present stacked x-t plots of the evolution of the free surface elevation, the depth averaged velocity and the species concentration respectively for the first 100 seconds (at 4 s intervals). As shown in Figure 4.15 (a), after the removal of the wall (at time t=0), the higher density liquid on the left is pushing the lower density liquid further to the right, while the free surface elevation of the latter is rising in order to conserve mass. The above wave created by the density dam break is also obvious in Figure 4.15 (b), where the velocity of the lower density liquid on the right is rising in a similar manner to the depth change profile. As expected, there is no change in the values of the species concentration plot (Figure 4.15 (c)) as there is no mixing of the two liquids as diffusion is neglected. The only evolution is the movement of the interface on the right as the bore travels forward.

The results from this test case are in very good agreement with those of Leighton (2010). This test case is valuable for the validation of the horizontal variable density shallow water equations solver as a density dam break is similar to a dam break (induced by a step change in depth of a liquid of constant density) examined in Case 1. In both cases, a rarefaction, a shock, and a contact wave are formed. The liquid depth and velocity profiles obtained for the density and gravity dam breaks also exhibit remarkable similarity in terms of shape and wave propagation.

4.3.3. Case 9: Symmetric 1-D density dam break with two initial discontinuities

This test case involves a parameter study which aims to draw some conclusions about the effect of the presence of a band of liquid of different density inserted in liquid that otherwise has uniform density. The parameter is based on the ratio of the densities of the two liquids.

The computational domain consists of a horizontal channel of length L and closed boundaries at either end (reflective boundary conditions), which is filled with two liquids of different density but with the same initial depth. The liquid of density ρ_2 and width w is situated in the middle of the channel forming a column, whereas the remainder of the channel (either side of the liquid band of density ρ_2) is filled with liquid of density ρ_1, as shown in Figure 4.16. The two liquids are separated by an infinitesimally thin wall. At time t = 0 s the wall is instantly removed and the system is set free. For this problem it is assumed that the length of the channel is sufficiently long that changes to the liquid depth in the central column do not affect significantly the liquid depth of the rest of the channel; i.e. the width of the central column is significantly smaller than the length of the channel and consequently the conservation of the volumes of the liquids is valid. Moreover, the chosen length should be big enough so that the equilibrium state is achieved before the waves created are reflected from the boundaries of the computational domain and thus affect the equilibrium.

The length of the channel is L = 100 m, the initial liquid depth is $h = 1$ m for the whole domain, the width of the column of liquid of density ρ_2 is $w = 1$ m the density of the outside liquid is $\rho_1 = 1$ kg/m^3, and the gravitational acceleration is $g = 1$ m/s^2. For the parameter study, the density of the central liquid is varied such that $\rho_2 = 0.1$, 1, 10, 100 and 1000 kg/m^3. The effects of viscosity, wind, turbulence and friction are ignored. Figure 4.17 shows

the results of the grid convergence test for Case 9.1 ($\rho_2 = 100$ kg/m^3) with *dx*=2, 0.5, 0.05 and 0.01 m. The spatial step chosen is 0.05 m and the time step is 0.001 s.

Leighton (2010) obtained an analytical solution of the problem by considering the relation between the ratio of the densities and the balance of the hydrostatic thrusts of the liquids in order to reach equilibrium state after the walls are removed. When the system is set free, the central column will either rise or fall, depending on whether the density ratio ρ_2/ρ_1 is less or greater than unity respectively, until it reaches the state of equilibrium. At this state, the pressure thrusts of the two liquids at the interfaces should be equal, i.e.

$$\rho_1 g h_1^2 = \rho_2 g h_2^2 \tag{4.10}$$

where h_1 is the new equilibrium depth of the liquid of density ρ_1 , and h_2 is the new equilibrium depth of the liquid of density ρ_2. The width of the central column of density ρ_2 will accordingly settle to a new equilibrium value w_2. By considering Equation (4.10) and taking into account the assumption that the length of the channel is sufficiently long that $h_1 \approx h$, the equilibrium depth of the central column can be expressed as

$$h_2 = h\sqrt{\frac{\rho_1}{\rho_2}} \tag{4.11}$$

From conservation of volume, the equilibrium width of the central column is

$$w_2 = w\frac{h}{h_2} \tag{4.12}$$

Table 4.3 lists the different values of density ρ_2 considered for the parameter study, as well as the equilibrium depth and the equilibrium width calculated analytically, using equations (4.11) and (4.12).

Case 9.1: ρ_2 = 1 kg/m^3

In this test the density ρ_2 is the same as ρ_1 and consequently 1 kg/m^3 throughout the whole channel. The system, as expected, remains in equilibrium condition and there is no change in any of the variables (free surface elevation, depth averaged velocity and concentration). Figures 4.18 (a-c) present stacked *x-t* plots of the evolution of the free surface elevation, the depth averaged velocity and the species concentration respectively for the first 50 seconds.

Case 9.2: ρ_2 = 10 kg/m^3

In this case, the density ratio of the central liquid column to the outside liquid is 10. This density difference drives the system to a new equilibrium condition which according to the analytical solution should settle to an equilibrium height of h = 0.316 m and an equilibrium width of w = 3.162 m for the central column of higher density liquid. Figures 4.19 (a-c) show the stacked *x-t* plots of the evolution of the free surface elevation, the depth averaged velocity and the species concentration respectively for the first 50 seconds (for 2.5 s intervals). Figures 4.20 (a-f) show the numerical results for the free surface elevation and the depth averaged velocity for t=1, 5, 10, 20, 30 and 50 seconds respectively. The symmetry of the results is obvious throughout the whole computational run time.

The flow evolution is as follows. Within the first second after the system is released, the liquid in the centre of the channel reaches a height very close to the equilibrium value, being driven by gravity forces. Two shock-type bores are created that travel towards either end of the domain at a speed of approximately 0.6 m/s. Meanwhile, a pair of rarefaction waves travels inwards towards the centre of the channel. After 5 seconds, the two opposing bores continue to travel towards the ends of the channel, while the liquid in the central column readjusts to a new width as its height falls below the equilibrium value. At the same time the two rarefaction waves collide at the centre and reflect in opposite directions. After 10 seconds, the two bores are slowing down slightly, with their speed reduced to approximately 0.4 m/s. The height of the central column liquid is rising again, approaching the equilibrium value while the width of the column is increasing in order to conserve mass. At time t = 20 s, a second pair of bore waves starts travelling outwards from the central column towards the ends of the channel, but with less speed than the first one. The central column is already settling to the equilibrium height and depth, achieving a state of balance again. By t = 30 s, the initial pair of bores is approaching the boundaries of the domain as the central column begins to approach steady state equilibrium. After 50 seconds, the second pair of waves keeps travelling outwards with reduced speed and height.

Case 9.3: ρ_2 = 100 kg/m^3

In this case, the density ratio of the central column to the outside liquid is 100. In a similar way as for Case 9.2, the density difference drives the system to a new equilibrium condition which according to the analytical solution should settle to an equilibrium height of h = 0.1 m and an equilibrium width of w = 10 m for the central column of higher density liquid. Figures 4.21 (a-c) show the stacked x-t plots of the evolution of the free surface elevation, the depth averaged velocity and the species concentration respectively for the first 180

seconds (for 9 s intervals). Figures 4.22 (a-f) show the numerical results for the free surface elevation and the depth averaged velocity for t = 6, 18, 36, 72, 108 and 180 seconds respectively.

At time t = 6 s after the system is set free, the liquid in the centre of the domain almost reaches the bottom of the channel, while two shock-type bores travel outwards (towards the ends of the domain) at speeds of approximately 1 m/s. After t = 18 s, the width of the central column continues to increase as it reaches the bed of the channel. The two bores keep travelling outwards with speeds of approximately 0.8 m/s. After t = 36 s, the central column starts recovering to its equilibrium height and width; the outer interface gradually narrows and the height increases. By t = 72 s, the central part of the high density liquid is continuing to approach the equilibrium height and width. The initial shock-type bores have already reached the boundaries of the computational domain, where they have reflected. At t = 108 s, these reflected bores can be seen travelling back towards the centre at speeds of about 0.3 m/s. At t = 180 s, the central part of the system has almost reached equilibrium, with the mixture almost stationary.

In Case 9.3, the time required to reach equilibrium is approximately three times greater than for Case 9.2, due to the bigger density difference.

Case 9.4: $\rho_2 = 0.1$ kg/m^3

In this case, the density ratio of the central to the outside liquid is 1/10. This density difference drives the system to a new equilibrium condition which according to the analytical solution should settle to an equilibrium height of h = 3.16 m and an equilibrium width of w = 0.316 m for the central column of lower density liquid. Figures 4.23 (a-c) show

the stacked *x-t* plots of the evolution of the free surface elevation, the depth averaged velocity and the species concentration respectively for the first 50 seconds (for 2.5 s intervals). Figures 4.24 (a-f) show the numerical results for the free surface elevation and the depth averaged velocity for t = 1, 2.5, 5, 10, 30 and 50 seconds respectively.

Unlike the two previous tests, in Case 9.4 the central column initially rises instead of dropping after the system is set free. By t = 1 s, the liquid at the centre of the channel reaches a height very close to the equilibrium value, while two shock-type bores are travelling inwards this time, from either of the two interfaces of the two liquids, accompanied by two rarefaction waves travelling outwards to either end of the channel at speeds of approximately 0.6 m/s. At t = 2.5 s, the rarefaction waves can be observed travelling outwards with slightly reduced speeds of 0.4 m/s, while the width of the central column is gradually increasing. By t = 5 s, the rarefaction wave speeds has reduced further to 0.3 m/s. The height of the central column has reached the equilibrium value while gradually approaching the equilibrium width value as well. At t = 10 s, the central column takes its final form, which remains almost constant until the end of the simulation. At t = 30 s, the speed of the rarefaction waves is 0.1 m/s, whereas the central band of liquid has reached equilibrium. At t = 50 s, the initial rarefaction waves have just reached the boundaries of the domain with speed of 0.08 m/s. It is obvious from the velocity history that the rarefaction waves naturally spread out as they evolve.

4.4. Erodible Bed Cases

In order to validate the model for entrainment and deposition, the numerical predictions were compared against analytical solutions derived for certain erodible bed problems. For simplicity, the equations used for the analytical solution are in terms of h, which is the

liquid-mixture free surface elevation above the bed, and in the unbalanced source-flux gradient form. Analytical solutions for each particular test case are developed below, and the results compared against predictions by the numerical model.

4.4.1. Case 10: Deposition of dilute suspended sediment in a flat-bottomed tank with intense mixing but no net flow and no entrainment of sediment

The analytical solution for the deposition of dilute suspended sediment in a flat-bottomed tank with intense mixing but no net flow and no entrainment of sediment is computed below.

After suitable manipulation the unbalanced variable density shallow water equations in terms of water depth (h) for erodible bed can be expressed as:

$$\frac{\partial(h)}{\partial t}+\frac{\partial(uh)}{\partial x}=\frac{E-D}{1-p}\ , \tag{4.13}$$

$$\frac{\partial(uh)}{\partial t}+\frac{\partial(u^2h+\frac{1}{2}gh^2)}{\partial x}=-gh\frac{\partial z_b}{\partial x}-\tau_b-\frac{(\rho_s-\rho_w)}{2\rho}gh^2\frac{\partial c}{\partial x}-\frac{(\rho_0-\rho)(\mathrm{E}-D)u}{\rho(1-p)}\ , \tag{4.14}$$

$$\frac{\partial(ch)}{\partial t}+\frac{\partial(uch)}{\partial x}=E-D\,, \tag{4.15}$$

and

$$\frac{\partial(z_b)}{\partial t}=\frac{D-E}{1-p}\qquad . \tag{4.16}$$

where the symbols have their usual meaning (see notation list).

For deposition of dilute suspended sediment in a flat-bottomed tank with intense mixing but no net flow and no entrainment of sediment, the following is assumed: $u = 0$; $\eta = constant$; $E = 0$; $D = w_s\, c$ (i.e. $D \propto c$); and $\tau_b = 0$. Here, w_s is the settling velocity of the sediment relative to the fluid. So the above equations are simplified as follows:

$$\frac{\partial h}{\partial t} = -\frac{D}{1-p}\ , \tag{4.17}$$

$$0 = 0 \qquad , \tag{4.18}$$

$$\frac{\partial (ch)}{\partial t} = -D \qquad , \tag{4.19}$$

and

$$\frac{\partial (z_b)}{\partial t} = \frac{D}{1-p} \qquad . \tag{4.20}$$

For $D = w_s\, c$, the above equations can be written as:

$$\frac{\partial h}{\partial t} = -\frac{w_s c}{1-p} = -\frac{\partial (z_b)}{\partial t} \quad , \tag{4.21}$$

$$\frac{\partial (ch)}{\partial t} = -w_s c \qquad , \tag{4.22}$$

and

$$\frac{\partial(z_b)}{\partial t} = \frac{w_s c}{1-p} \quad . \tag{4.23}$$

For any time, $0 < t < t_\infty$, the concentration of the sediment in the mixture can be expressed as $c = c_0 e^{-t/T}$, where T is a time constant:

$$\frac{\partial h}{\partial t} = -\frac{w_s c_0 e^{-t/T}}{1-p} = -\frac{\partial(z_b)}{\partial t} \quad , \tag{4.24}$$

$$\frac{\partial\left(c_0 e^{-t/T} h\right)}{\partial t} = -w_s c_0 e^{-t/T} \quad , \tag{4.25}$$

and

$$\frac{\partial(z_b)}{\partial t} = \frac{w_s c_0 e^{-t/T}}{1-p} \quad . \tag{4.26}$$

After integration, the equations become:

$$h - h_0 = \frac{w_s c_0 T}{1-p}(e^{-t/T} - 1) = z_{b0} - z_b \quad , \tag{4.27}$$

$$\frac{\partial h}{\partial t} c_0 e^{-t/T} + h\frac{\partial(c_0 e^{-t/T})}{\partial t} = -w_s c_0 e^{-t/T} \quad , \tag{4.28}$$

and

$$z_b - z_{b0} = -\frac{w_s c_0 T}{1-p}(e^{-t/T} - 1) \quad . \tag{4.29}$$

where h_0 , z_{b0} , and c_0 are the water height, the bed elevation, and the sediment concentration in the mixture at time $t = 0$ and h, z_b and c are the water height, the bed elevation, and the sediment concentration in the mixture at any time $t > 0$.

In order to compute the time coefficient *T,* the species mass conservation equation is written as:

$$\frac{\partial(ch)}{\partial t} = -w_s c \tag{4.30}$$

Substituting, $c = c_0 e^{-t/T}$ where T is a time constant:

$$\frac{\partial\left(c_0 e^{-t/T} h\right)}{\partial t} = -w_s c_0 e^{-t/T} \tag{4.31}$$

$$\frac{\partial h}{\partial t} c_0 e^{-t/T} + h\frac{\partial\left(c_0 e^{-t/T}\right)}{\partial t} = -w_s c_0 e^{-t/T} \tag{4.32}$$

$$\frac{\partial h}{\partial t} c_0 e^{-t/T} + h(-\frac{1}{T}) c_0 e^{-t/T} = -w_s c_0 e^{-t/T} \tag{4.33}$$

Substituting into the above equation $\frac{\partial h}{\partial t} = -\frac{w_s c}{1-p} = -\frac{w_s c_0 e^{-t/T}}{1-p}$, gives:

$$-\frac{w_s (c_0\ e^{-t/T})^2}{1-p} - \frac{h}{T} c_0 e^{-t/T} = -w_s c_0 e^{-t/T} \tag{4.34}$$

$$-\frac{w_s c_0 e^{-t/T}}{1-p} = -w_s + \frac{h}{T} \tag{4.35}$$

For $t = 0$, the above expression can be written as:

$$-\frac{w_s c_0}{1-p} = -w_s + \frac{h_0}{T} \tag{4.36}$$

and thus:

$$T = \frac{h_0}{w_s(1-\frac{c_0}{1-p})} \tag{4.37}$$

or, if the desired level of accuracy is in terms of c and not c^2 , the time constant T can be calculated as follows:

$$(\frac{\partial h}{\partial t} - \frac{h}{T})c_0 e^{-t/T} = -w_s c_0 e^{-t/T} \tag{4.38}$$

Provided $\frac{\partial h}{\partial t} << \frac{h}{T}$, then:

$$\frac{h}{T} c_0 e^{-t/T} = w_s c_0 e^{-t/T} \tag{4.39}$$

which means that for $t = 0$:

$$T = \frac{h_o}{w_s} \tag{4.40}$$

The above approximation is equivalent to $\frac{\partial h}{\partial t} << w_s$. Now, $\frac{\partial h}{\partial t} = -\frac{w_s}{1-p}$ requires $\frac{cw_s}{1-p} << w_s$, i.e. $c << 1-p$. And since any $c \le c_0$, it is necessary that $c_0 << 1-p$ for this approximation to hold. If the above assumption is valid, then $c = c_0 e^{-\frac{w_s t}{h_0}}$.

So, the above equations are written as:

$$h - h_0 = \frac{w_s c_0}{1-p} \frac{h_0}{w_s(1-\frac{c_0}{1-p})}(e^{-\frac{w_s(1-\frac{c_0}{1-p})t}{h_0}} - 1) = z_{b0} - z_b \quad , \tag{4.41}$$

$$\frac{\partial h}{\partial t} c_0 e^{-\frac{w_s(1-\frac{c_0}{1-p})t}{h_0}} + h\frac{\partial(c_0 e^{-\frac{w_s(1-\frac{c_0}{1-p})t}{h_0}})}{\partial t} = -w_s c_0 e^{-\frac{w_s(1-\frac{c_0}{1-p})t}{h_0}} \quad , \tag{4.42}$$

and

$$z_b - z_{b0} = -\frac{w_s c_0}{1-p} \frac{h_0}{w_s(1-\frac{c_0}{1-p})}(e^{-\frac{w_s(1-\frac{c_0}{1-p})t}{h_0}} - 1) \quad . \tag{4.43}$$

And if the above equation is solved for the unknown *h* at any time *t*, the following expression is derived:

$$h(t) = h_0 + \frac{c_0\ h_0}{1-p-c_0}\left(e^{-\frac{w_s\left(1-\frac{c_0}{1-p}\right)t}{h_0}} - 1\right) \tag{4.44}$$

Having computed the water height, $h(t)$, the bed elevation $z_b(t)$ can be calculated from one of the following expressions:

$$z_b(t) = z_{b0} - h(t) + h_0 \tag{4.45}$$

or,

$$z_b(t) = z_{b0} - \frac{c_0\ h_0}{1-p-c_0}\left(e^{-\frac{w_s\left(1-\frac{c_0}{1-p}\right)t}{h_0}} - 1\right) \tag{4.46}$$

For time, $t \to \infty$, the concentration of the sediment c in the mixture will tend to 0 ($c_\infty = 0$), so the above equations are written as:

$$h_\infty - h_0 = z_{b0} - z_{b\infty} \quad , \tag{4.47}$$

$$h_\infty = h_0 - \frac{c_0\ h_0}{1-p-c_0} \quad , \tag{4.48}$$

and

$$z_{b\infty} = z_{b0} + \frac{c_0\ h_0}{1-p-c_0} \quad . \tag{4.49}$$

The initial values used for this test case are the following: the acceleration due to gravity is g = 9.81 m/s^2; the density of the liquid is ρ_w = 1000 kg/m^3; the density of the sediment is ρ_s =

2000 kg/m^3; the spatial step is dx = 4 m; the length of the computational domain is L = 2000 m; the time step is dt = 0.01 s; the sediment settling velocity is w_s = 0.008 m/s; the initial free surface elevation is η = 3 m throughout the computational domain; the initial bed elevation is z_b = 1 m throughout the computational domain; and the initial species concentration is c = 0.05 for the whole tank.

The reason for considering only the deposition of the sediment and fixing the entrainment to zero is mainly in order to isolate the effects of each phenomenon and thus check the response of the numerical model to the deposition of the sediment. The tank contains still liquid-species mixture, i.e. there is no flow of the liquid-species mixture and consequently all the components of the velocity are zero throughout the computations.

For this test the numerical results are in very satisfactory agreement with the analytical solution. Figure 4.25 shows the evolution of the depth of the liquid-species mixture and the bed elevation with time for $t \leq 250$ s. As expected after the system is set free (i.e. time t = 0 s) the deposition of the sediment is causing the settlement of the sediment. The results show the increase in bed elevation and the decrease of the liquid-species mixture depth. In the absence of entrainment, when all the sediment is deposited the system remains stationary in this new equilibrium condition, with the liquid and sediment having completely separated.

4.4.2. Case 11: Entrainment of dilute suspended sediment in a flat-bottomed tank with intense mixing but no net flow and no deposition of sediment

The analytical solution for the entrainment of dilute suspended sediment in a flat-bottomed tank with intense mixing but no net flow and no deposition of sediment is calculated below.

Again consider the unbalanced variable density shallow water equations in terms of water depth (h) for an erodible bed, expressed as Equations (4.13) to (4.16). The entrainment, E, is given by the following formula (Soulsby, 1997):

$$E = \begin{cases} M\left(\dfrac{\tau_b - \tau_c}{\tau_c}\right), \text{ when } \tau_b > \tau_c \\ 0 \qquad , \text{ when } \tau_b \le \tau_c \end{cases} \tag{4.50}$$

where M is the entrainment constant, τ_b is the shear stress of the bed, and τ_c is the threshold shear stress of the bed. By choosing M, τ_b, and τ_c to have constant values, the entrainment, E, is also constant.

For the problem of the entrainment of dilute suspended sediment in a flat-bottomed tank with intense mixing but no net flow and no deposition of sediment, the following values are assumed: $u = 0$; η = constant; E = constant; $D = 0$; and $\tau_b = 0$. Equations (4.13) to (4.16) are therefore simplified to give:

$$\frac{\partial h}{\partial t} = \frac{E}{1-p} = -\frac{\partial (z_b)}{\partial t} \quad , \tag{4.51}$$

$$0 = 0 \qquad , \tag{4.52}$$

$$\frac{\partial (ch)}{\partial t} = E \qquad , \tag{4.53}$$

and

$$\frac{\partial(z_b)}{\partial t} = -\frac{E}{1-p} \quad . \tag{4.54}$$

After integration, for any time $t_0 < t < t_\infty$, the equations become:

$$h - h_0 = z_{b0} - z_b \quad , \tag{4.55}$$

$$h - h_0 = (\frac{E}{1-p})t \quad , \tag{4.56}$$

and

$$z_b - z_{b0} = -(\frac{E}{1-p})t \quad . \tag{4.57}$$

where h_0 and z_{b0} are the water height and bed elevation at $t = 0$, and h and z_b are the water height and the bed elevation for $t > 0$.

Solving the above equation for the unknown h, the following expression is derived:

$$h(t) = h_0 + (\frac{E}{1-p})t \tag{4.58}$$

Having computed the water height, h, at any time, the bed elevation z_b at the same time can be calculated from one of the following expressions:

$$z_b(t) = z_{b0} - h(t) + h_0 \tag{4.59}$$

or

$$z_b(t) = z_{b0} - (\frac{E}{1-p})t \quad . \tag{4.60}$$

At time, $t = \infty$, the above equations are written as:

$$h_\infty - h_0 = z_{b0} - z_{b\infty} \quad , \tag{4.61}$$

$$z_{b\infty} = 0 \quad , \tag{4.62}$$

and

$$h_\infty = h_0 + z_{b0} - z_{b\infty} = \eta \quad . \tag{4.63}$$

The initial values used for this test case are the following: the acceleration due to gravity is g = 9.81 m/s^2; the density of the liquid is ρ_w = 1000 kg/m^3; the density of the sediment is ρ_s = 2000 kg/m^3; the spatial step is dx = 4 m; the length of the computational domain is L = 2000 m; the time step is dt = 0.01 s; the entrainment constant is M = 0.01 m/s; the bed shear stress is τ_b = 1 N/m^2; the threshold shear stress of the bed is τ_c = 0.2 N/m^2; the initial free surface elevation is η = 3 m; the initial bed elevation is z_b = 1 m; and the initial species concentration is c = 0.05 throughout the tank.

The purpose of this test is again to examine the response of the numerical model to the entrainment of the sediment, in the absence of deposition. The mechanism is similar to a force at the bed that is causing upward turbulence and thus erosion of the bed, given that it is impossible for the species particles to settle down again. The water-sediment mixture in the tank nevertheless remains still in the horizontal direction, i.e. there is no flow of the liquid-

species mixture and consequently all the components of the velocity are zero throughout the computations. The bed sediment is of same density as the species.

The numerical results are in perfect agreement with the analytical solution. Figure 4.26 shows the evolution of the liquid depth and the bed elevation with time for $t \leq 15$ s. As expected after the system is set free (i.e. time $t = 0$ s) entrainment of the bed material causes sediment to become suspended. Consequently, there is a monotonic decrease in bed elevation accompanied by a monotonic increase in liquid-species mixture depth until the bed material is exhausted (and a fixed bed is reached, say). In the absence of deposition, when all the sediment is suspended the system remains stationary in this new equilibrium condition, with the liquid and sediment fully mixed and the bed having disappeared. The changes in this test are quite rapid, so by $t = 15$ s the equilibrium state is achieved.

4.4.3. Case 12: Simultaneous deposition and constant entrainment of dilute suspended sediment in a flat-bottomed tank with intense mixing but no net flow

The analytical solution for the simultaneous deposition and constant entrainment of dilute suspended sediment in a flat-bottomed tank with intense mixing but no net flow is as follows.

The computation of the analytical solution for this test case starts again from the unbalanced variable density shallow water equations in terms of water depth (h) for erodible bed, expressed as Equations (4.13) to (4.16). The entrainment E is given by Equation (4.50), with M, τ, and τ_c set to constant values, so that E is also constant. The deposition is given by $D =$

$w_s c$. So at the equilibrium state, at $t = \infty$, where $D = E$, the equilibrium concentration can be calculated as:

$$D = E \quad , \tag{4.64}$$

$$w_s c_{eq} = M\left(\frac{\tau_b - \tau_c}{\tau_c}\right) \quad , \tag{4.65}$$

and

$$c_{eq} = \frac{M}{w_s}\left(\frac{\tau_b - \tau_c}{\tau_c}\right) \quad . \tag{4.66}$$

For the problem of the simultaneous deposition and constant entrainment of dilute suspended sediment in a flat-bottomed tank with intense mixing but no net flow, it is assumed that: $u = 0$; η = constant; and $\tau_b = 0$. The simplified equations are:

$$\frac{\partial h}{\partial t} = \frac{E - D}{1 - p} \quad , \tag{4.67}$$

$$0 = 0 \quad , \tag{4.68}$$

$$\frac{\partial (ch)}{\partial t} = E - D \quad , \tag{4.69}$$

and

$$\frac{\partial z_b}{\partial t} = \frac{D - E}{1 - p} \quad . \tag{4.70}$$

Letting $D = w_s\, c$, the equations become,

$$\frac{\partial h}{\partial t} = \frac{E - w_s c}{1 - p} \quad , \tag{4.71}$$

$$\frac{\partial (ch)}{\partial t} = E - w_s c \quad , \tag{4.72}$$

and

$$\frac{\partial z_b}{\partial t} = \frac{w_s c - E}{1 - p} \quad . \tag{4.73}$$

After integration, and for any time, $0 < t < t_\infty$, the equations become:

$$h - h_0 = \frac{E}{1 - p} t - \frac{w_s}{1 - p} \int c dt = z_{b0} - z_b(t) \quad , \tag{4.74}$$

$$\frac{\partial (h)}{\partial t} c + h \frac{\partial c}{\partial t} = E - w_s c \quad , \tag{4.75}$$

and

$$z_b - z_{b0} = \frac{w_s}{1 - p} \int c dt - \frac{E}{1 - p} t \tag{4.76}$$

where h_0, z_{b0}, and c_0 are the water depth, bed elevation, and sediment concentration in the mixture at time $t = 0$, and h , z_b and c are the water depth, bed elevation, and sediment concentration in the mixture at any time $t > 0$.

For any time, $0 < t < t_\infty$, the concentration of the sediment in the mixture can be expressed as $c = c_0 e^{-t/T_1} + \frac{E}{w_s}(1 - e^{-t/T_2})$. By using $T_1 = \frac{h_0}{w_s(1 - \frac{c_0}{1-p})}$ (as in the analytical solution of test case 10: the deposition of dilute suspended sediment in a flat-bottomed tank with intense mixing but no net flow and no entrainment of sediment), the time constant T_2 can be calculated as follows:

$$\frac{\partial(ch)}{\partial t} = E - w_s c \tag{4.77}$$

$$\frac{\partial h}{\partial t} c + h \frac{\partial c}{\partial t} = E - w_s c \tag{4.78}$$

But, $\frac{\partial h}{\partial t} = \frac{E - w_s c}{1 - p}$, and so the above equation can be written,

$$\frac{E - w_s c}{1 - p} c + h \frac{\partial c}{\partial t} = E - w_s c \tag{4.79}$$

And after substituting $c = c_0 e^{-t/T_1} + \frac{E}{w_s}(1 - e^{-t/T_2})$, we obtain

$$\frac{Ec - w_s c^2}{1 - p} - \frac{h}{T_1} c_0 e^{-t/T_1} + \frac{Eht}{w_s} + \frac{Eh}{w_s T_2} e^{-t/T_2} = E - w_s c \tag{4.80}$$

At time $t = 0$, $h = h_0$ and $c = c_0$. So the above equation becomes:

$$\frac{Eh_0}{w_s T_2} = E - w_s c_0 + \frac{w_s {c_0}^2 - Ec_0}{1 - p} + \frac{h_0 c_0}{T_1} \tag{4.81}$$

And solving for the unknown time coefficient T_2:

$$T_2 = \frac{E}{w_s(\frac{E}{h_0} - \frac{w_s c_0}{h_0} + \frac{w_s {c_0}^2 - E c_0}{(1-p)h_0} + \frac{c_0}{T_1})} \tag{4.82}$$

For $T_1 = \frac{h_0}{w_s(1 - \frac{c_0}{1-p})}$, the above expression reduces to

$$T_2 = \frac{h_0}{w_s(1 - \frac{c_0}{(1-p)})} \tag{4.83}$$

which is equal to T_1.

So, after the substitution of the time coefficient T, the concentration c, can be expressed as:

$$c = e^{-\frac{w_s(1-\frac{c_0}{1-p})t}{h_0}}(c_0 - \frac{E}{w_s}) + \frac{E}{w_s} \tag{4.84}$$

And the integrated equation for the mass conservation of the mixture becomes:

$$h - h_0 = \frac{E}{1-p}t - \frac{w_s}{1-p}\int (e^{-t/T}(c_0 - \frac{E}{w_s}) + \frac{E}{w_s})dt = z_{b0} - z_b(t) \tag{4.85}$$

or

$$h - h_0 = \frac{w_s T c_0 - TE}{1-p}(e^{-t/T} - 1) \tag{4.86}$$

And for $T = \dfrac{h_0}{w_s(1-\dfrac{c_0}{(1-p)})}$, the above is written,

$$h - h_0 = \frac{w_s c_0 \dfrac{h_0}{w_s(1-\dfrac{c_0}{(1-p)})} - E\dfrac{h_0}{w_s(1-\dfrac{c_0}{(1-p)})}}{1-p}(e^{-\frac{w_s(1-\frac{c_0}{1-p})t}{h_0}} - 1) \tag{4.87}$$

giving

$$h - h_0 = \frac{h_0(c_0 w_s - E)}{w_s(1-p-c_0)}(e^{-\frac{w_s(1-\frac{c_0}{1-p})t}{h_0}} - 1) \tag{4.88}$$

And if the above equation is solved for the unknown h, the following expression is derived:

$$h(t) = h_0 + \frac{h_0(c_0 w_s - E)}{w_s(1-p-c_0)}(e^{-\frac{w_s(1-\frac{c_0}{1-p})t}{h_0}} - 1) \tag{4.89}$$

The bed elevation z_b is then given by

$$z_b(t) = z_{b0} - h(t) + h_0 \tag{4.90}$$

or

$$z_b(t) = z_{b0} - \frac{h_0(c_0 w_s - E)}{w_s(1-p-c_0)}(e^{-\frac{w_s(1-\frac{c_0}{1-p})t}{h_0}} - 1) \tag{4.91}$$

For time, $t=\infty$, the above equations are written as:

$$h_\infty = h_{eq} = h_0 - \frac{h_0(c_0 w_s - E)}{w_s(1-p-c_0)} \tag{4.92}$$

and

$$z_{b\infty} = z_{b\,eq} = z_{b0} + \frac{h_0(c_0 w_s - E)}{w_s(1-p-c_0)} \tag{4.93}$$

The initial values used for this test case are the following: g = 9.81 m/s^2; ρ_w = 1000 kg/m^3; ρ_s = 2000 kg/m^3; dx = 4 m; L = 2000 m; dt = 0.01 s; M = 0.01 m/s; τ_b = 1 N/m^2; τ_c = 0.2 N/m^2; w_s = 0.008, 0.05 and 0.1 m/s for tests a, b and c (Figure 4.23) respectively; η = 3 m; z_b = 1 m; and c = 0.05.

The aim of this test is to validate the numerical model for simultaneous entrainment and deposition of sediment. Different values of settling velocity are considered for constant entrainment, corresponding to different sediment deposition rates. The liquid-species mixture in the tank is effectively still. That is, there is no horizontal flow and so the velocity remains zero throughout the computations. The bed sediment and species are of the same density. Figures 4.27 (a-c) show the evolution of the liquid depth and the bed elevation with time for t≤ 100 s. In general, discrepancies can be seen between the numerical predictions and analytical solution, which grow with time. Likewise, the numerical predictions of how long it takes for the system to reach steady state disagree with the analytical model. These discrepancies become worse, the lower the value of settling velocity. This points to a problem in the way entrainment is being handled in either the analytical model or the numerical model.

The qualitative behaviour of the numerical and analytical solutions is similar however. After the system is released at time t = 0 s, entrainment of bed material brings sediment into suspension, with deposition opposing this effect. The final equilibrium depends on the ratio between the turbulent uplift and the downward settling forces. When the initial entrainment force is much stronger than the deposition one, the bed elevation falls and the liquid-species mixture depth increases until the bed material exhausted (the same as in Case 12, but at a different rate as the deposition rate is slowing down the process). Once all the sediment is suspended the system remains stationary at this new equilibrium condition, with the liquid and sediment fully mixed and the erodible bed having entirely disappeared. At higher initial ratios of deposition rate to entrainment rate, the system tends towards a steady state equilibrium condition where entrainment and deposition rates are equal. Figure 4.27 (a) shows a case when entrainment prevails over deposition and the bed material is suspended completely by t = 15 s, for settling velocity w_s = 0.008 m/s. The prediction of the numerical model is not in good accordance with the analytical solution which predicts that the bed material is exhausted by t = 25 s. Figure 4.27 (b) shows the corresponding results for a higher settling velocity, w_s = 0.05 m/s, for which the entrainment over deposition ratio is smaller. In this case, the bed material takes much longer to suspend completely at t = 100 s. The prediction of the numerical model for w_s = 0.05 m/s is in better accordance with the analytical solution than for w_s = 0.008 m/s, although not exactly the same. Figure 4.27 (c) compares the numerical and analytical predictions for w_s = 0.1 m/s, and the entrainment over deposition ratio is even smaller so that the bed material does not become fully suspended. On the contrary, the system tends to find a new balance while eroding part of the bed material until t ~ 100 s, by which time the entrainment and the deposition rates are equal (thereafter cancelling each other out). In this case, the prediction of the numerical model is in better agreement with the analytical solution.

In general, for all three combinations of simultaneous entrainment and deposition considered herein the analytical solution predicts slower rates of convergence to the equilibrium steady state solution than the numerical model.

4.4.4. Case 13: Dam break problem and flow over a triangular obstacle with erodible bed

Case 13 is similar to Case 6, in that it involves a dam-break wave which interacts with a triangular obstacle, but this time both the bed and the triangular obstacle are erodible. Although here are no published numerical predictions or analytical solutions for this problem (to the author's knowledge), Case 13 is nevertheless useful for studying the performance of the model when dealing with more complicated shallow flow water-sediment-bed interactions.

As in Case 6, the domain consists of a reservoir connected to a rectangular channel of total length 22.5 m. The dam is situated at x = 15.5 m. The symmetric triangular obstacle is 6 m long and 0.4 m high, and its crest is situated at x = 28.5 m. The initial water depth in the reservoir is 0.75 m and in the rest of the channel the bed is dry (as shown in Figure 4.8). The bed and the symmetric triangular obstacle are erodible, so both entrainment and deposition of the bed material are simulated. The left hand side of the computational domain is considered as a fixed reflective boundary (solid wall). At the right hand side boundary of the computational domain two separate conditions are implemented. In Case 13.1, a free outlet is located at the right hand side of the channel. In Case 13.2, the free outlet is replaced with a fixed reflective boundary. The bed roughness coefficient is $C_f = g\frac{n_m^{\,2}}{h^{1/3}}$, where n_m = 0.0125 is the Manning coefficient. The acceleration due to gravity is g = 9.81 m/s^2; the density of the liquid is ρ_w = 1000 kg/m^3; the density of the sediment is ρ_s = 2000 kg/m^3; the

settling velocity of the sediment (bed material) is $w_s = 0.1$ m/s; the entrainment constant is $M = 0.005$ m/s; the threshold shear stress of the bed is $\tau_c = 0.2$ N/m^2; and the initial species concentration is $c = 0$ throughout the computational domain. The time step chosen is 0.001 s and the grid spacing is 0.1 m, according to the grid convergence tests performed for Case 6 (Figure 4.9).

Figure 4.28 shows the numerical results obtained for the free surface and the bed elevation at $t = 5$, 10, 15, 30, 40, 100, 250, 1250, 2500 and 3000 s, for Case 13.1 (where the right hand boundary is open). At $t = 0$ s, the dam break occurs instantaneously. A right propagating contact wave is released along with a left propagating rarefaction. The contact wave hits the triangular obstacle and reflects causing an upstream travelling bore to be created followed by a moving hydraulic drop (also travelling upstream). At $t = 5$ s, the flow runs up the triangular obstacle, while bed material starts to be eroded upstream of the obstacle, driven by the reflected bore. At $t = 10$ seconds the upwash has overtopped the triangular obstacle, leading to a supercritical flow on the downstream face of the obstacle followed by a hydraulic jump and finally a downstream directed bore into water behind the initial bore that has already reached the right hand side boundary. The relatively high flow speed to the left of the obstacle causes bed material to be entrained and increases the concentration (not depicted) of suspended sediment immediately before the left hand slope of the obstacle. The supercritical flow descending the right hand face of the triangular obstacle has started to erode its surface. At $t = 15$ s, some of the water-sediment mixture (as the water is now carrying some bed material) is reflected from the triangular obstacle and travels back, towards the left hand side boundary. By $t = 20$ s, bed material is transported from the upstream initially flat bed to the left hand (upstream) toe of the triangular obstacle, while its right slope continues to be eroded. Part of the water-sediment mixture exits the computational domain, reducing the overall mass of water and sediment within the

computational domain. At t = 40 s, the bed elevation reaches an almost uniform elevation of 2.4 m above datum, and the triangular obstacle has been reduced to less than half its original height, while the waves reflected at the left hand side boundary keep travelling towards the obstacle and transporting bed material out of the domain. By t = 100 s, the liquid-species mixture discharge is washing out the bed material causing the bed elevation to decrease fairly consistently in the downstream direction. At t = 250 s, both the free surface elevation and the bed elevation are smoothened out as the intensity of waves is reduced. At t = 1250 s, there is a continuous flow of the water-sediment mixture towards the right hand side boundary, and out of the computational domain, while the system tends to settle to a new equilibrium position. The bed has formed a step like shape. By t = 2500 s, the flow velocity tends to zero and consequently the sediment is deposited to the bed, while the free surface elevation is almost still. At t = 3000 s, the system has reached the new equilibrium position while all the sediment has been deposited back to the bed. At this new equilibrium position the elevation of the still water is 1.91 m and the elevation of the bed is 0.17 m above the datum. In this case, entrainment dominates deposition, resulting in erosion of the bed material and the triangular obstacle. Furthermore, the flow created by the dam break carries entrained sediment out of the domain.

Figure 4.29 shows the numerical results obtained for the free surface and the bed elevation at different times, when t = 5, 10, 15, 30, 40, 100, 250, 1250, 2500 and 7000 seconds, for Case 13.2, in which the right hand side boundary is reflective. This case is useful for testing whether the model conserves the water-sediment mass (including bed material) throughout the simulation, as the reflective boundaries either end of the domain prohibit the escape of any material. Until the flow reaches the right hand boundary, the free surface and bed elevation behave in an identical way to that observed in Case 13.1 involving the open right hand boundary, as would be expected. So, at t = 5 s after the dam break, the contact wave

front reaches the triangular obstacle and starts to move up the front face. Meanwhile, bed material begins to be eroded in front of the obstacle. At t = 10 s, the flow has overtopped the triangular obstacle, while bed material continues to be eroded upstream of the obstacle. Moreover, the supercritical flow down the back face of the obstacle starts to strip away its bed surface. After the initial bore reaches the right hand side boundary (at t ~ 10 s), the results are different to those of Case 13.1, due to the influence of reflections of the water-sediment mixture back into the domain from the right hand wall. By t = 15 s, some of the water-sediment mixture is reflected from the triangular obstacle and travels back, towards the left hand boundary. Meanwhile, the water-sediment mixture reflected at the right hand end is travelling upstream towards the back slope of the triangular obstacle, accelerating its erosion. By t = 30 s, interactions between the various reflected waves lead to a somewhat smoother free surface profile and a more continuous entrainment of the bed material (along the length of the domain). In a similar fashion to Case 13.1, the entrainment process is overwhelming deposition. At t = 40 s, the predicted bed profile remains similar to that obtained at t = 30 seconds. The main difference is that as time elapses more bed material is suspended, so the concentration of the species in the liquid-species mixture continues to increase. Consequently the bed elevation decreases gradually, and the flow depth increases. By t = 100 s, the triangular obstacle has almost disappeared, while the free surface and the bed elevation are tending towards a new equilibrium state. By t = 250 s, the disturbed free surface elevation reflects the irregularity of the bed, which at this point is intensely eroded. By t = 1250 s, both the free surface and bed elevations become less fluctuating as the wave motions subside. At t = 2500 s, while the upstream (left) side of the domain has almost reached steady state, the downstream (right) side of the domain is still evolving. The bed elevation profile appears almost horizontal, with a value of 1.659 m above the datum. By t = 7000 s, both the free surface elevation and the bed have settled. The elevation of the still

water is 2.567 m and the elevation of the bed is 1.758 m above the datum throughout the computational domain.

It should be noted that the evolution of the flow for this test case is quite different to that considered in Case 6 as the erodibility of the bed, resulting to the entrainment of the bed material and the modification of the topography. The additional friction leads to the creation of irregular waves which in turn affect the erosion and deposition processes and vice versa. These irregularities are obvious in the form of sharp bores and shock waves at the free surface elevation profile.

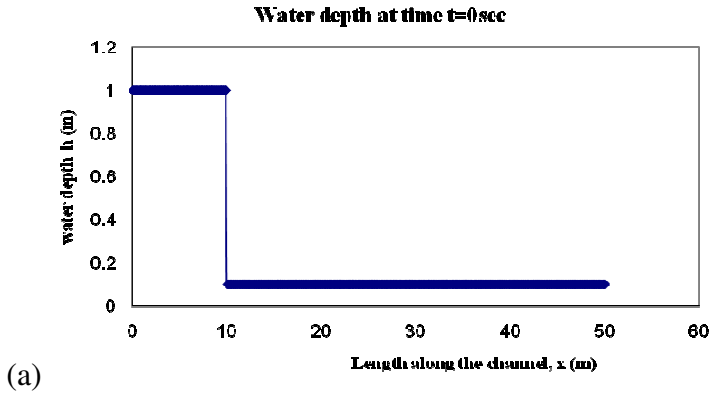
4.5. Concluding Remarks

The one-dimensional numerical solver of horizontal variable density shallow water equations has been validated for a variety of test cases and compared to analytical solutions, benchmark test results and experimental data when available. Grid convergence was checked in each case.

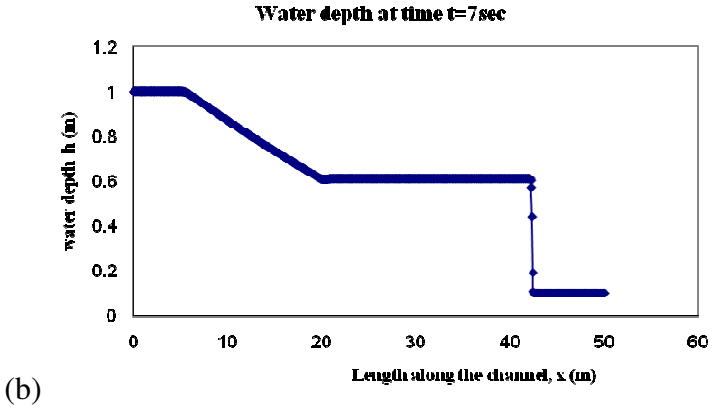
For the constant density cases considered, the predicted numerical results are in very satisfactory agreement with the alternative data used for comparison.

For the variable density cases considered, the model responded correctly to the different initial conditions encountered. For cases involving steady state solutions, the model remained at equilibrium (as expected). The model was also validated against symmetric problems, and the results were found to be acceptable.

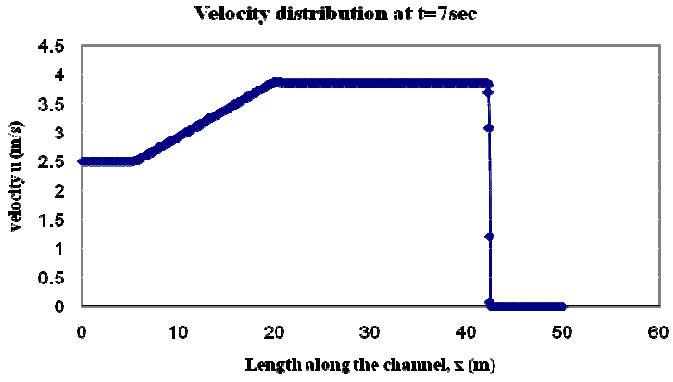
Finally, the model was tested for erodible bed problems. For Cases 10 and 11 the numerical results were in close agreement with analytical solutions demonstrating that the model can successfully simulate entrainment and deposition of the sediment, as individual processes. The results obtained for Case 12, involving simultaneous entrainment and deposition, were not in quantitative agreement with the analytical solutions, indicating that further work is needed here to resolve the discrepancies. For Case 13, no analytical solution or experimental data were available for comparison. Nevertheless, the numerical results appear reasonable, producing sensible hydrodynamic features (such as contact waves and bores), and bed morphological changes (such as the complete erosion of the triangular obstacle).



(a)

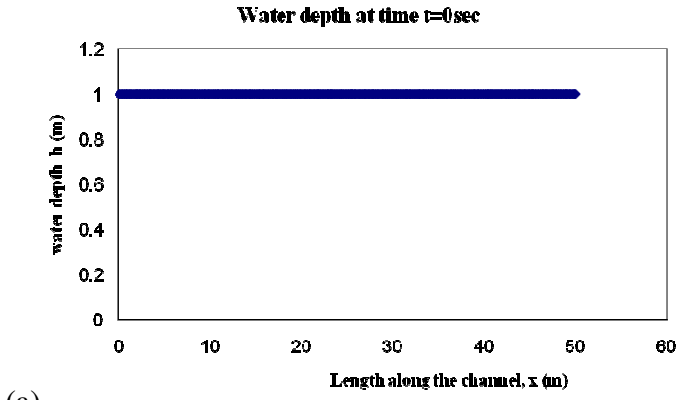


(b)

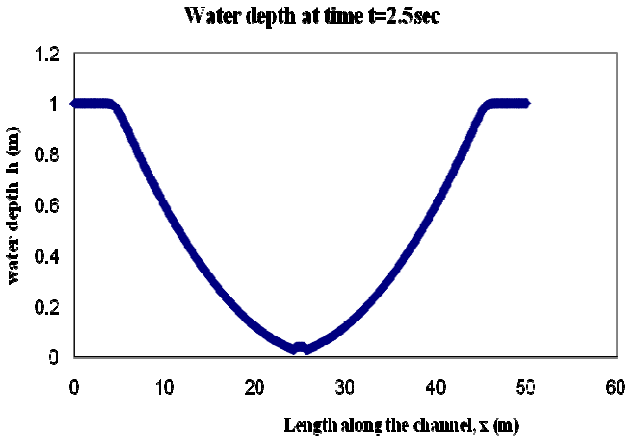


(c)

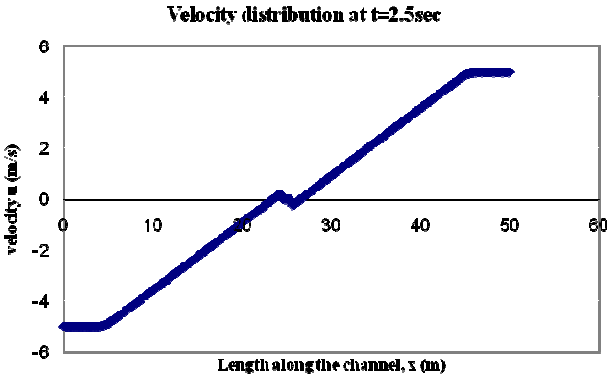
Fig. 4.1 Case 1. One-dimensional dam-break flow (a) initial depth profile, (b) depth profile at t = 7 s, (c) velocity distribution at t = 7 s.



(a)

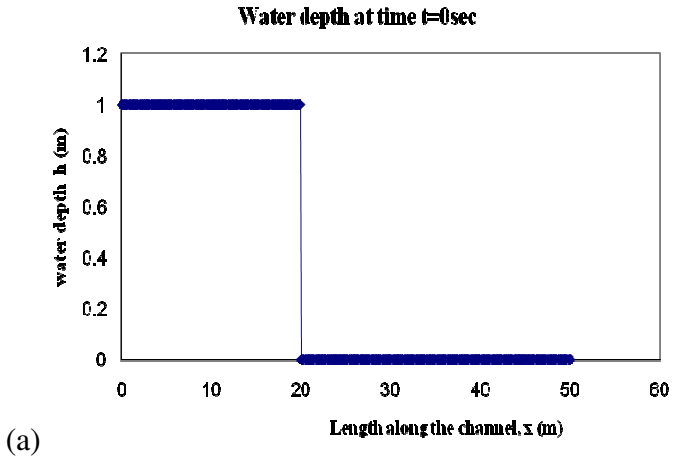


(b)

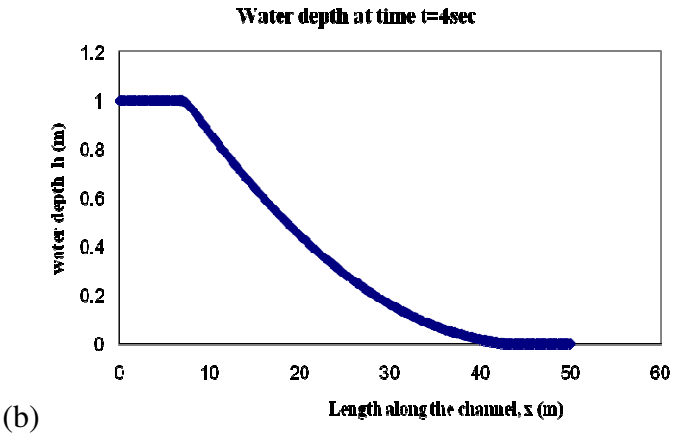


(c)

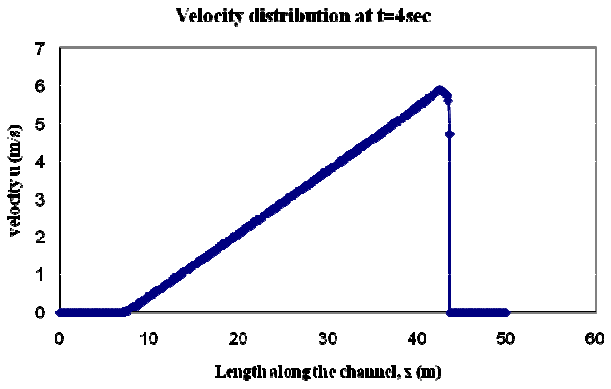
Fig. 4.2 Case 2. Two opposing rarefaction waves over a nearly dry bed (a) initial depth profile, (b) depth profile at t = 2.5 s, (c) velocity distribution at t = 2.5 s.



(a)

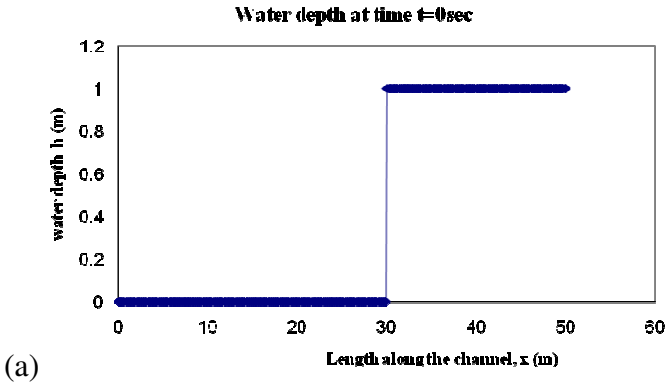


(b)

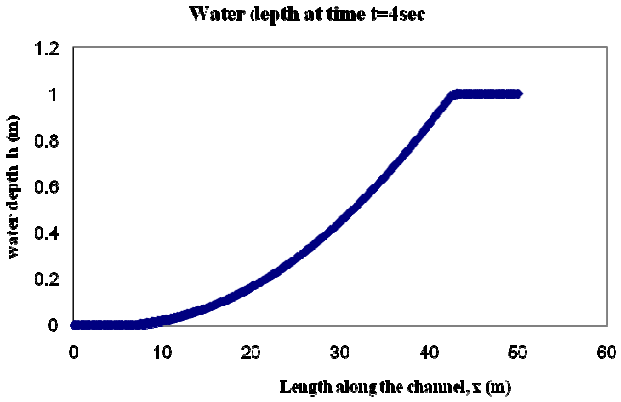


(c)

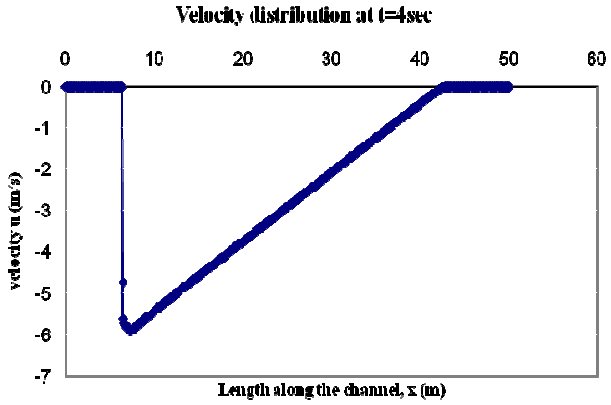
Fig. 4.3 Case 3. Right dry bed Riemann problem (a) initial depth profile, (b) depth profile at $t = 4$ s, (c) velocity distribution at $t = 4$ s.



(a)

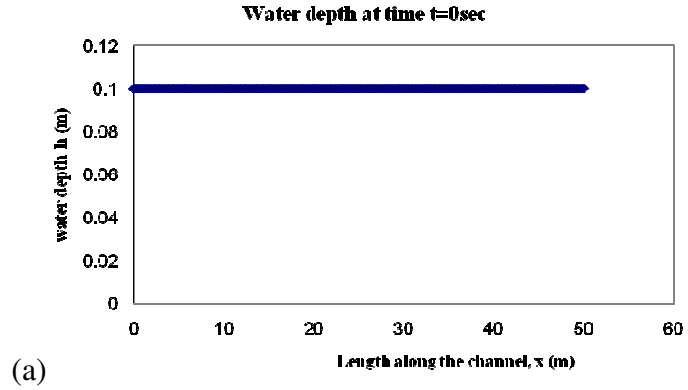


(b)

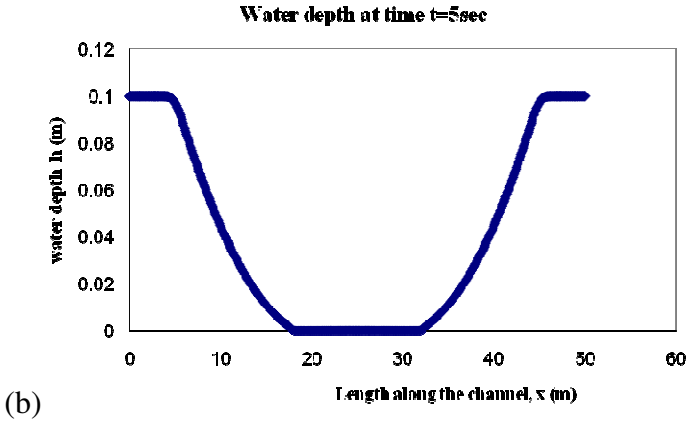


(c)

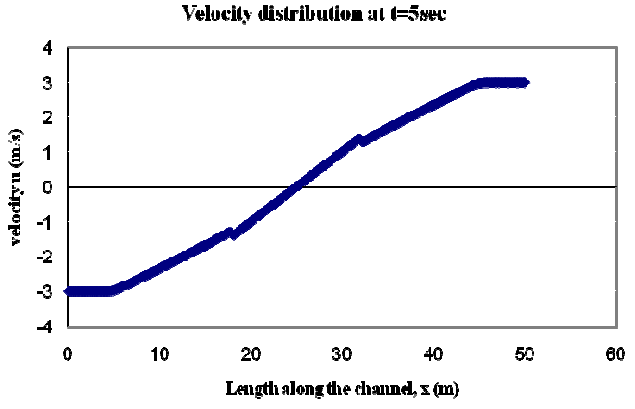
Fig. 4.4 Case 3. Left dry bed Riemann problem (a) initial depth profile, (b) depth profile at t = 4 s, (c) velocity distribution at t = 4 s.



(a)



(b)



(c)

Fig. 4.5 Case 4. Generation of dry bed by opposing rarefaction waves (a) initial depth profilr, (b) depth profile at t = 5 s, (c) velocity distribution at t = 5 s.

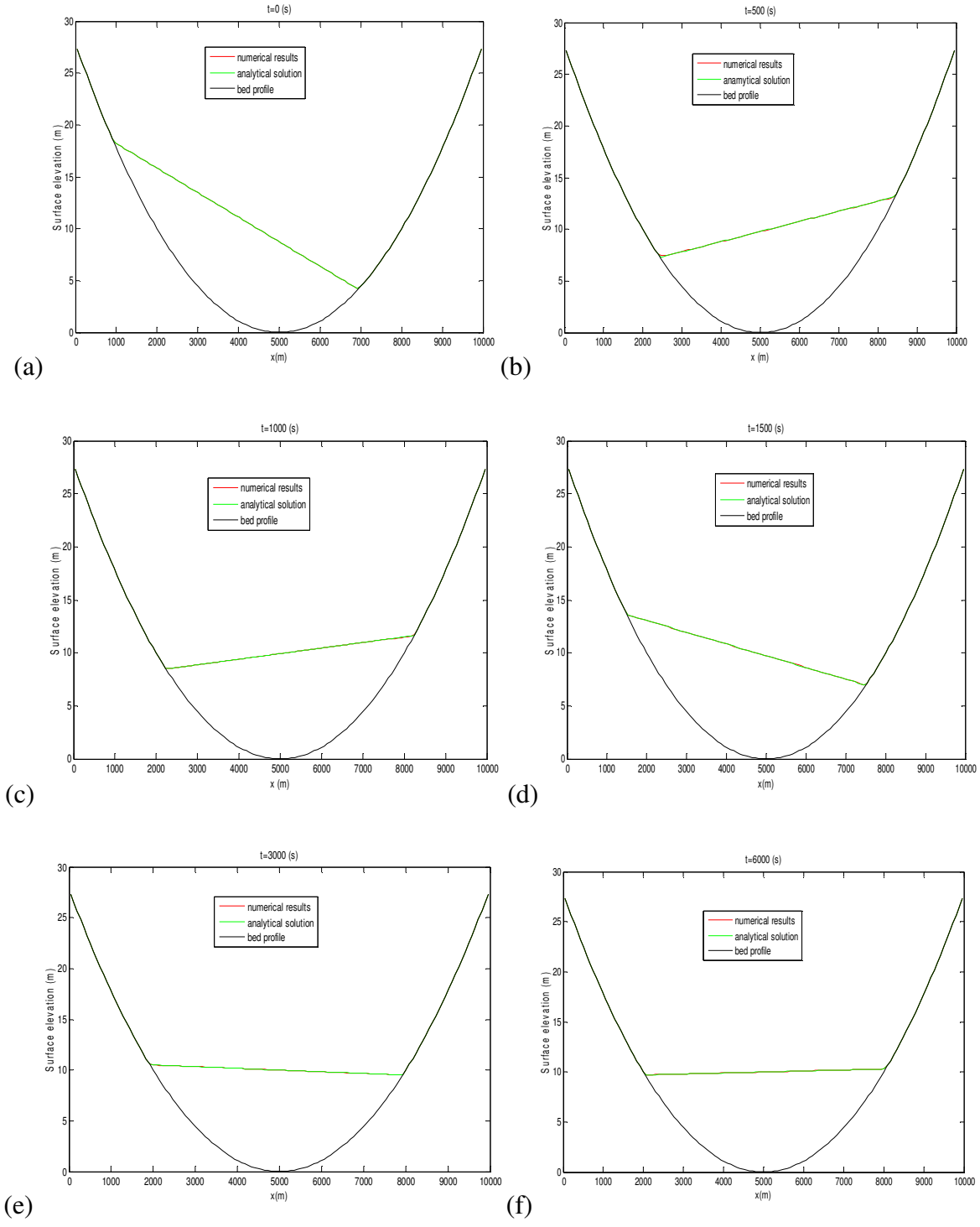


Fig. 4.6 Case 5. Damped free surface oscillations in a tank with parabolic bed (a) 0s, (b) 500s, (c) 1000s, (d) 1500s, (e) 3000s and (f) 6000s.

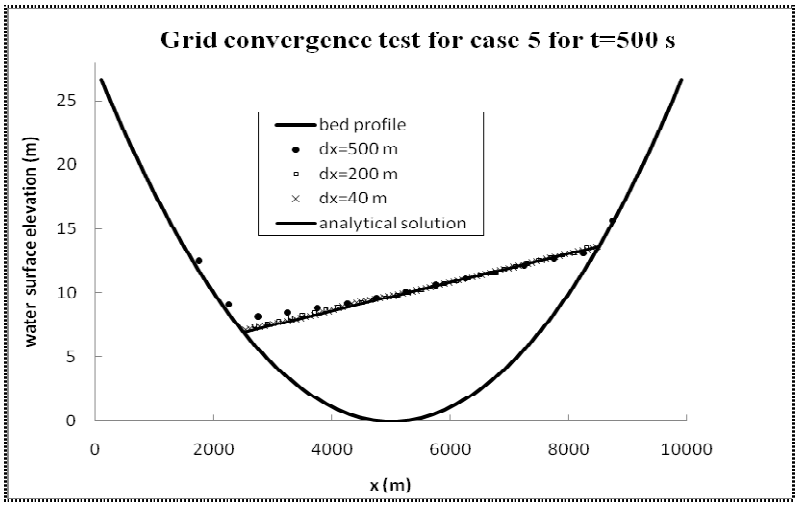


Fig. 4.7 Case 5. Damped free surface oscillations in a tank with parabolic bed – Grid convergence test results for *t*=500 s and *dx*= 10, 78.125, 100, 200, 500 and 1000 m.

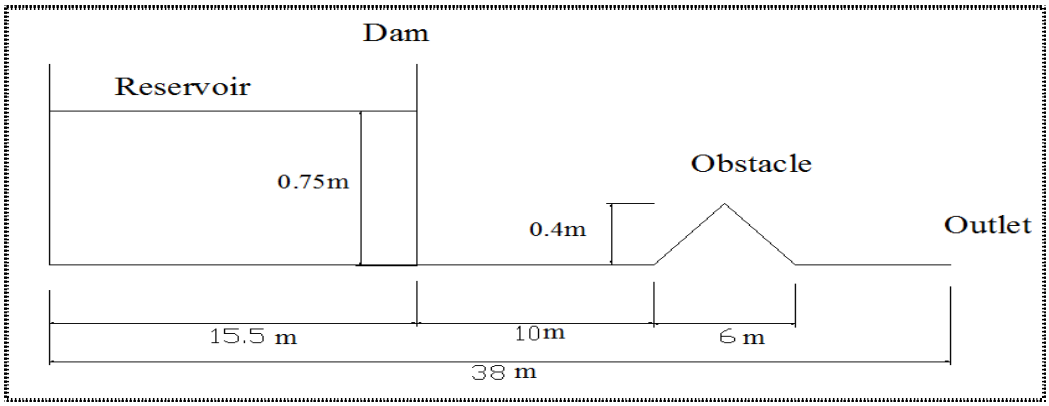


Fig. 4.8 Case 6. Geometry of the physical model of a dam-break followed by overtopping of a triangular obstacle.

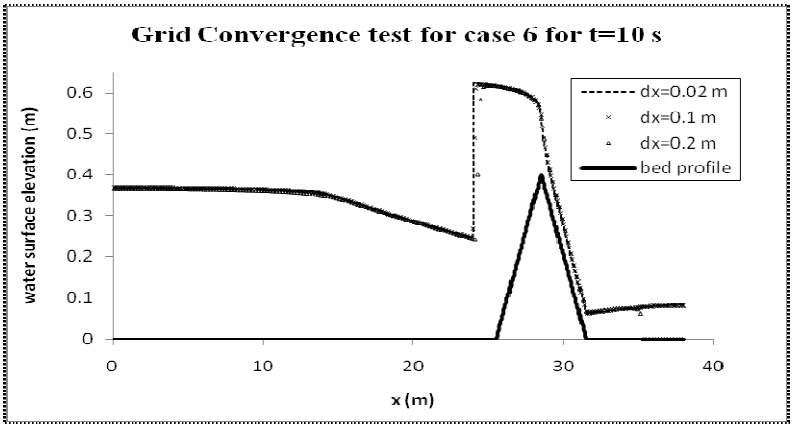


Fig. 4.9 Case 6. Dam break problem and flow over a triangular obstacle – Grid convergence test results for *t*=10 s and *dx*=0.2, 0.1and 0.02 m.

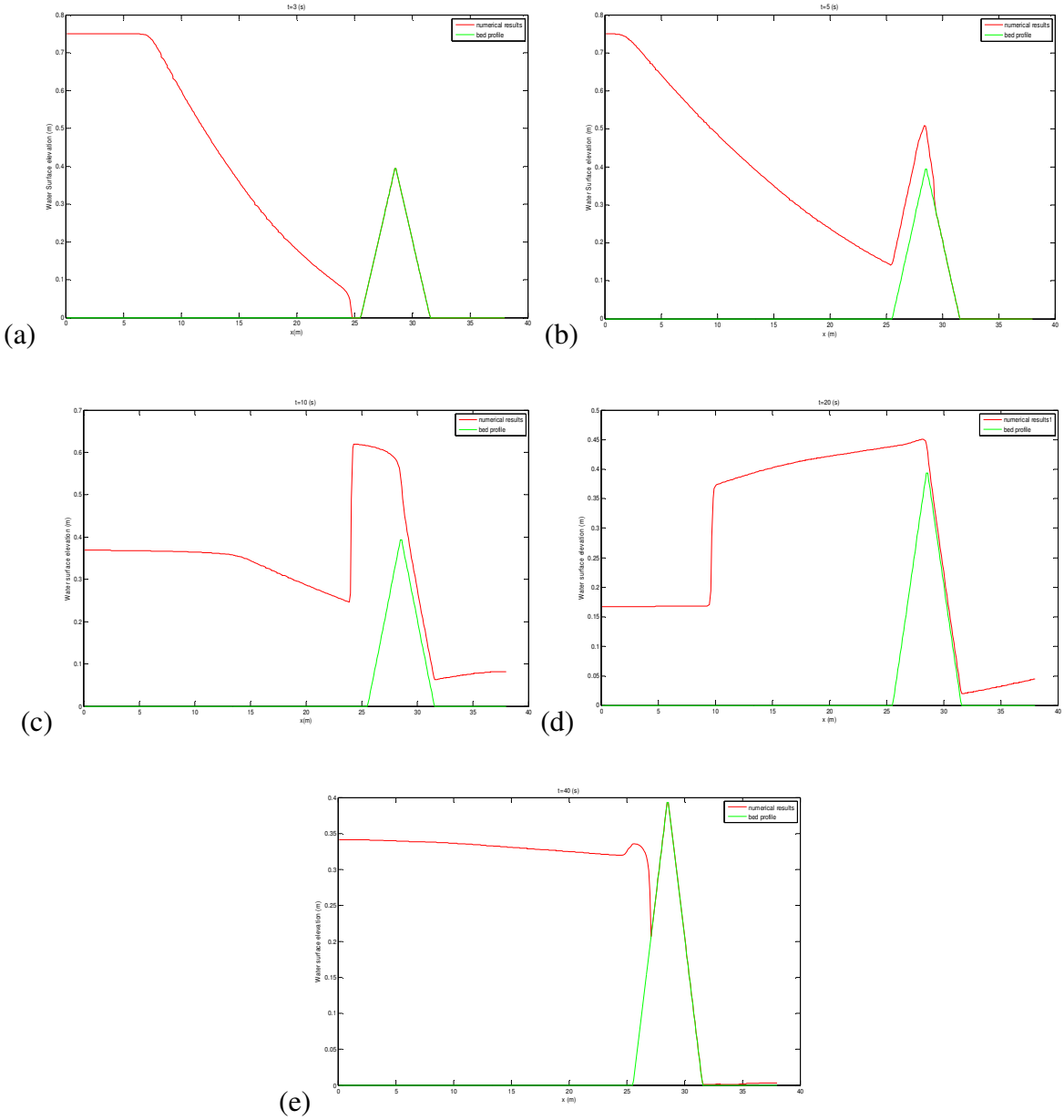


Fig. 4.10 Case 6. Interaction between a dam-break wave and a triangular obstacle (a) 3 s, (b) 5 s, (c) 10 s, (d) 20 s, and (e) 40 s.

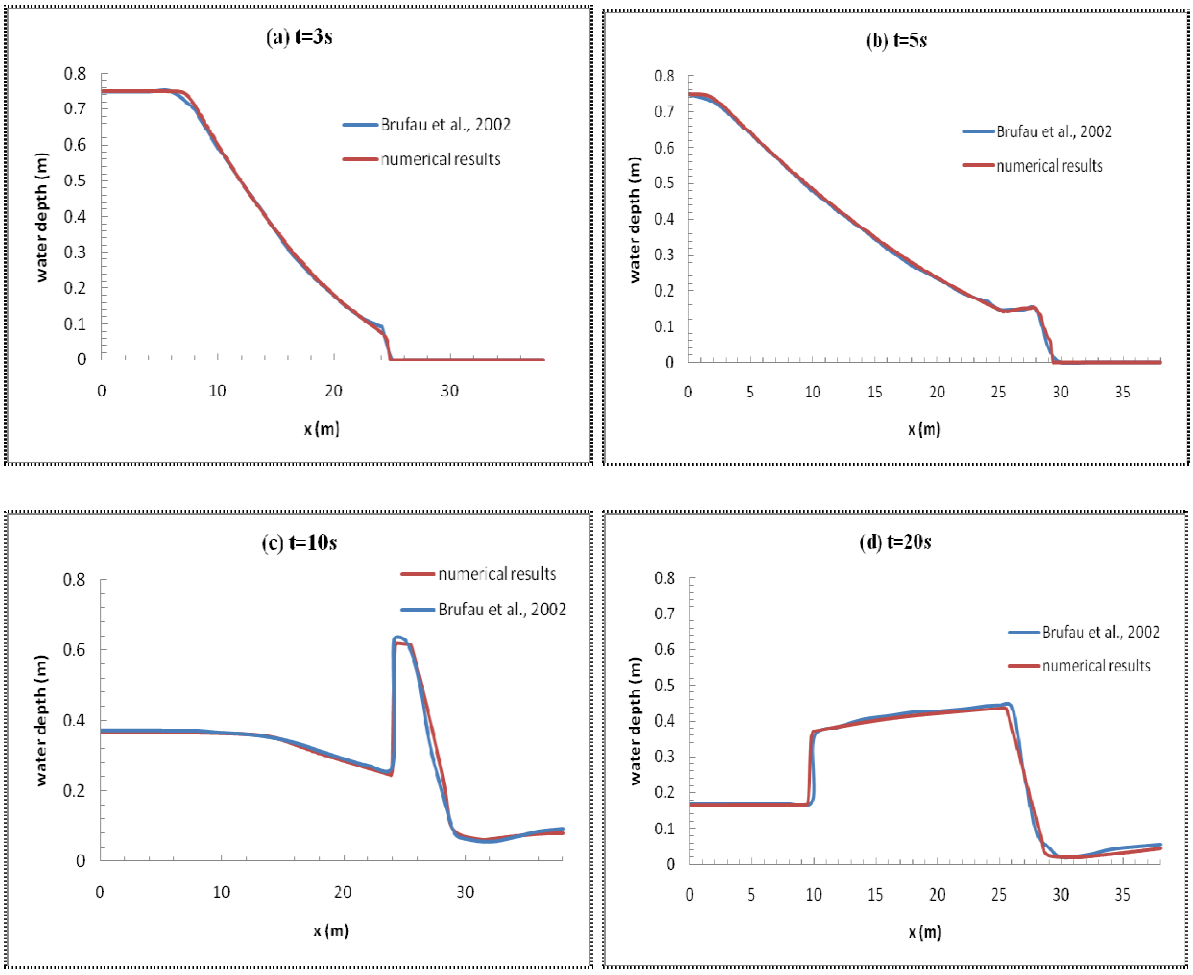


Fig. 4.11 Case 6. Interaction between a dam-break wave and a triangular obstacle – comparison of numerical results and results obtained by Brufau et al. (2002) for time (a) 3 s, (b) 5 s, (c) 10 s, and (d) 20 s.

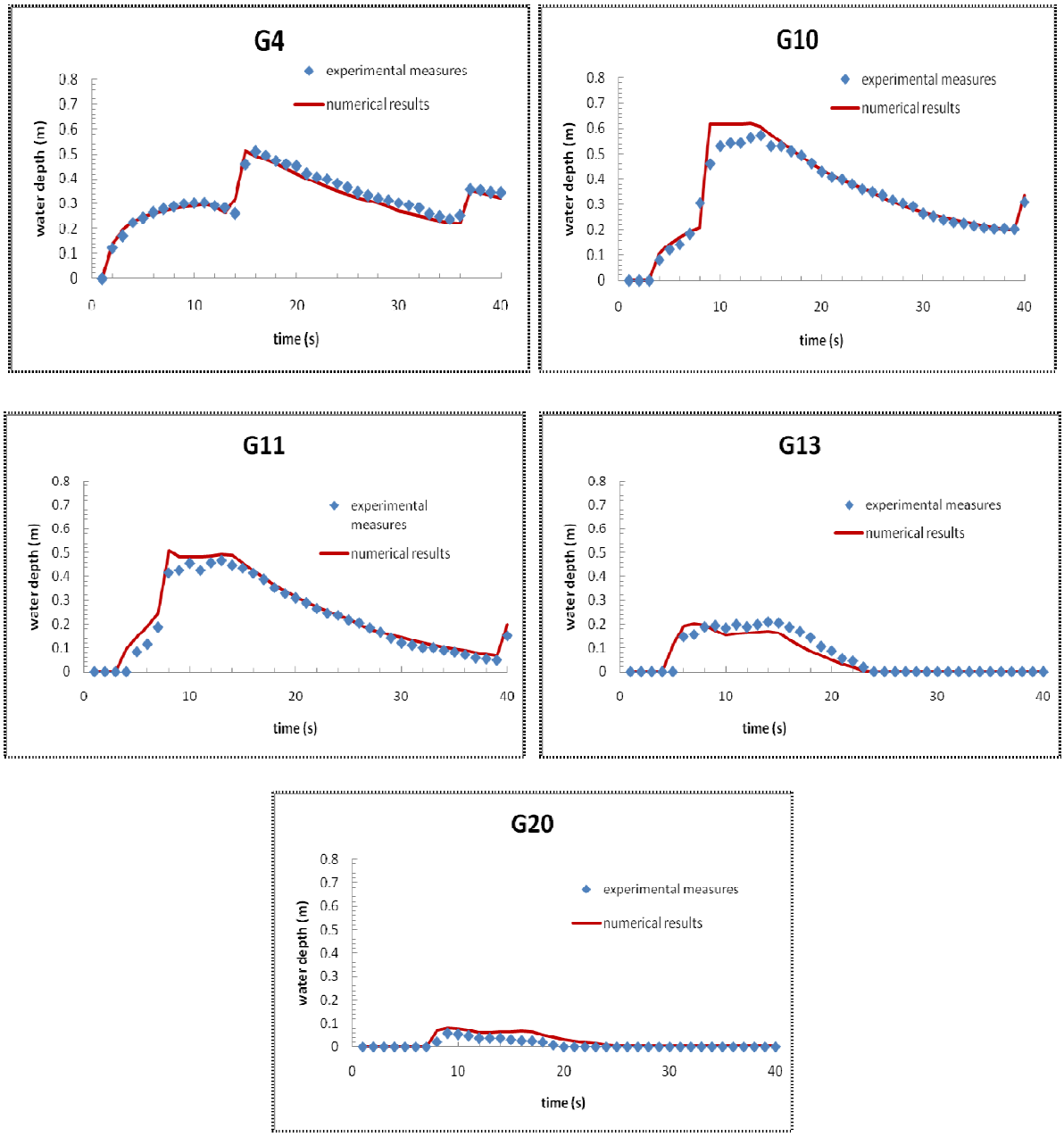
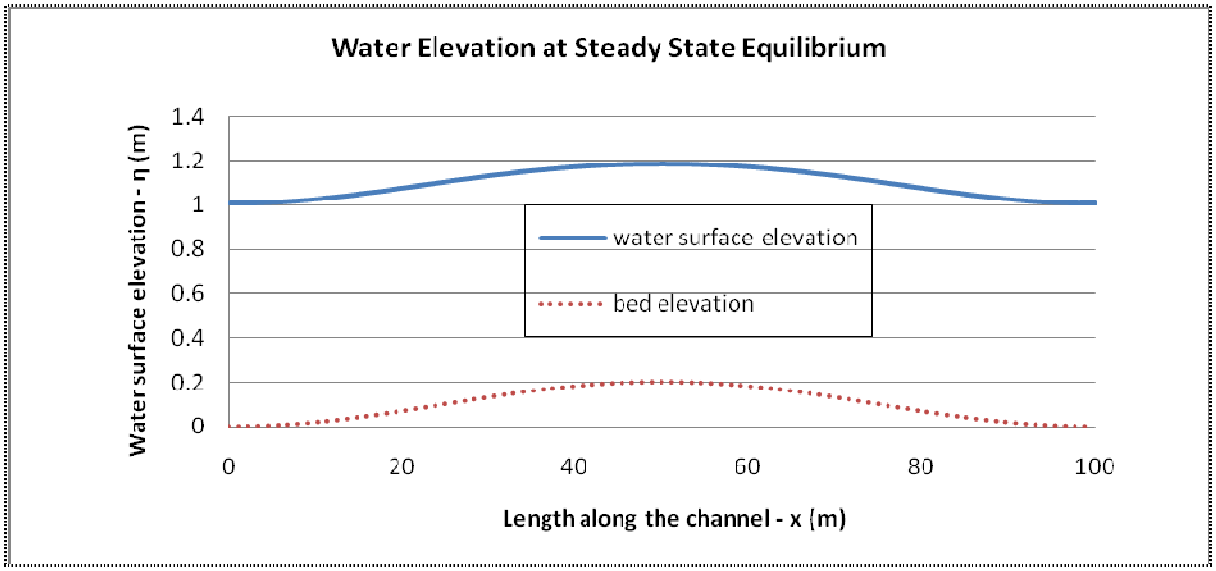


Fig. 4.12 Case 6. Interaction between a dam-break wave and a triangular obstacle – Time evolution of the water depth during 40 s as measured at the Recherches Hydrauliques Lab. Châtelet and computed by the model at gauging points: G4, G10, G11, G13 and G20 (the number corresponds to the distance in meters from the initial position of the dam).

(a)



(b)

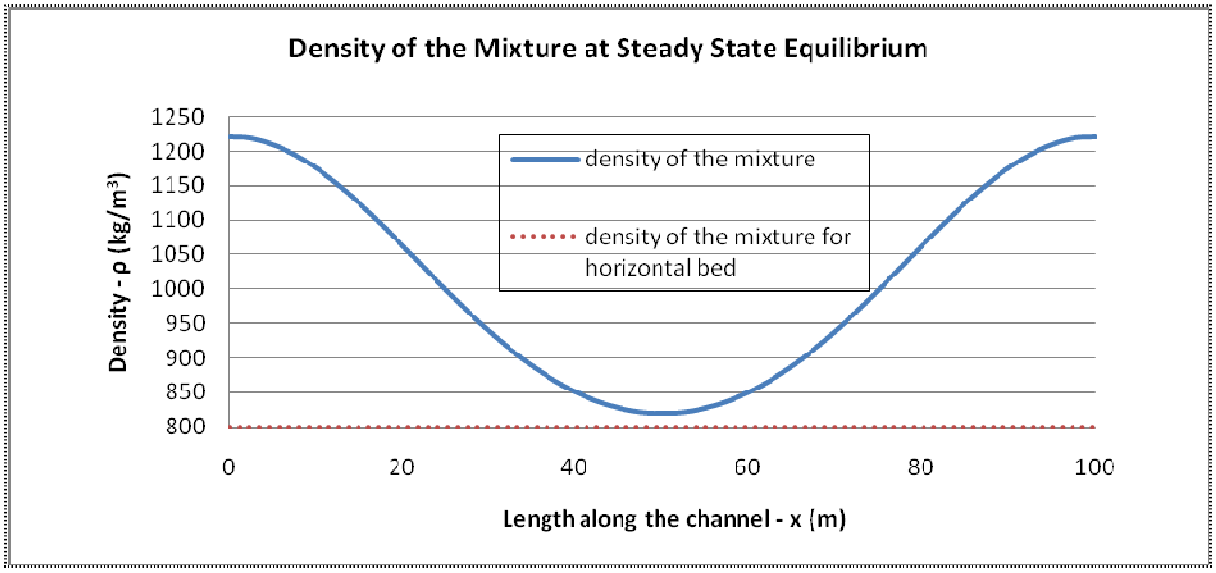


Fig. 4.13 Case 7. (a) Water elevation and (b) density of the mixture at quiescent equilibrium in a tank with a sinusoidal bed (variable density).

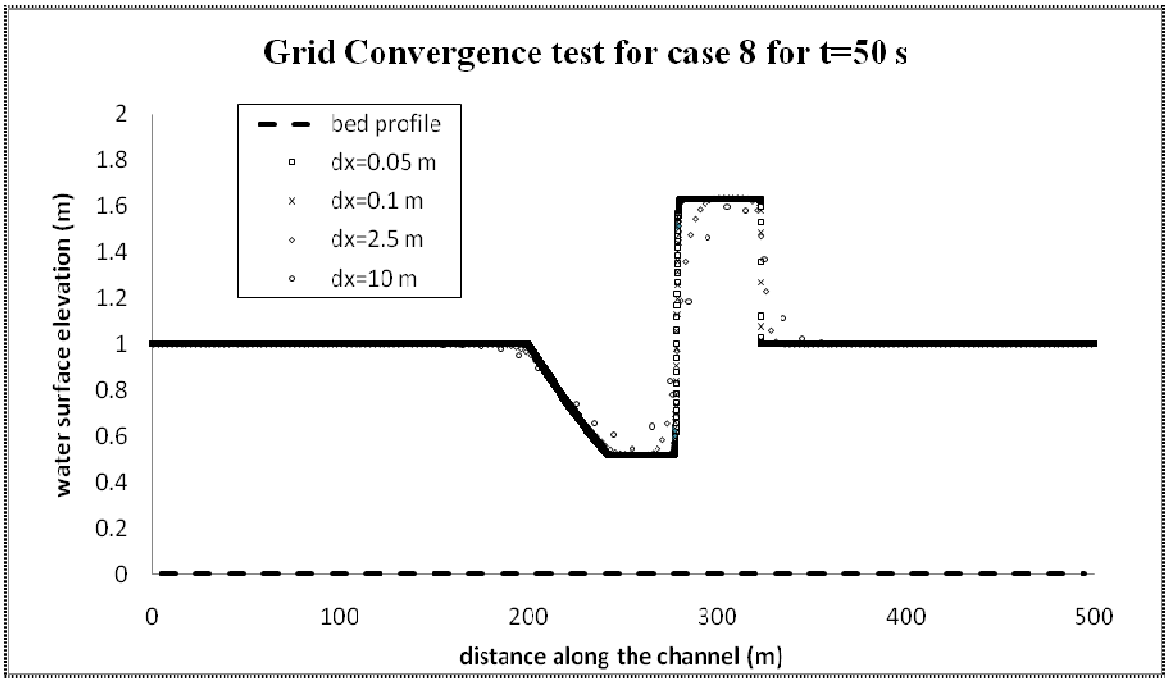


Fig. 4.14 Case 8. One-dimensional density dam break with a single initial discontinuity – Grid convergence test results for t=50 s and dx=10, 2.5, 0.1and 0.05 m.

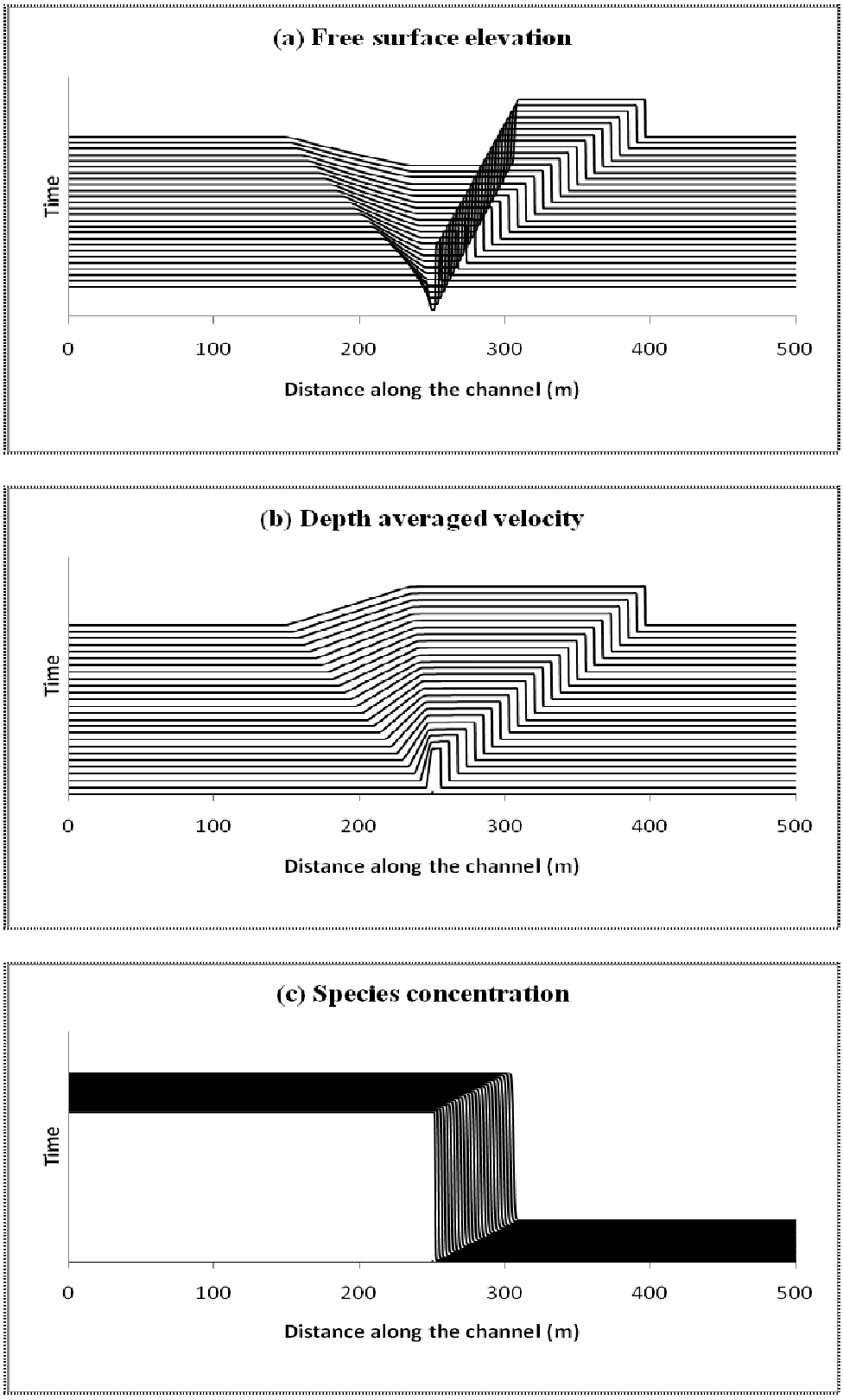


Fig. 4.15 Case 8. One-dimensional density dam break with a single initial discontinuity – Stacked *x*-*t* plots of (a) the free surface elevation, (b) the depth averaged velocity and (c) the concentration for $t \leq 100$ s.

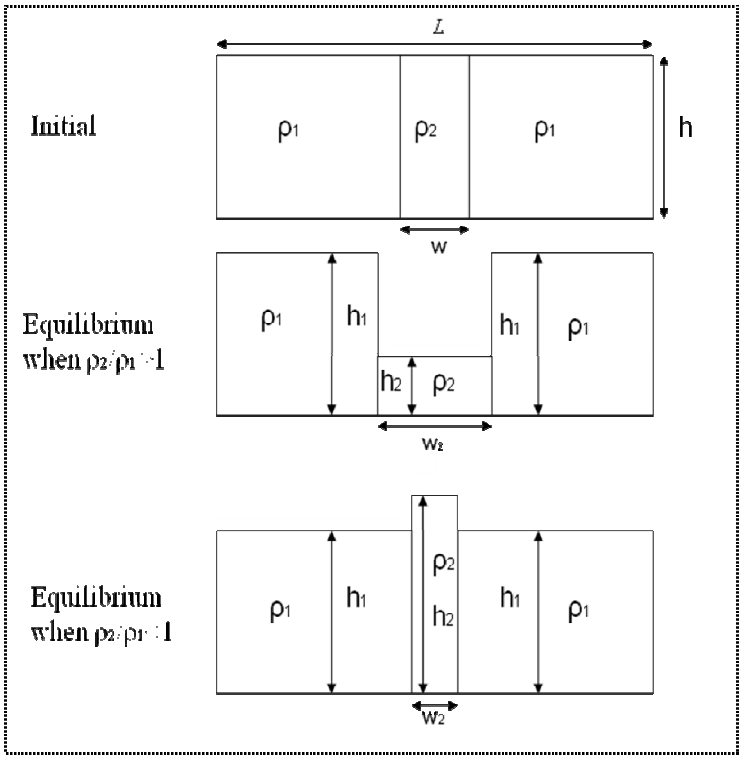


Fig. 4.16 Case 9. Symmetric 1-D density dam break with two initial discontinuities (variable density) – Initial conditions and equilibrium state of the system of the two liquids.

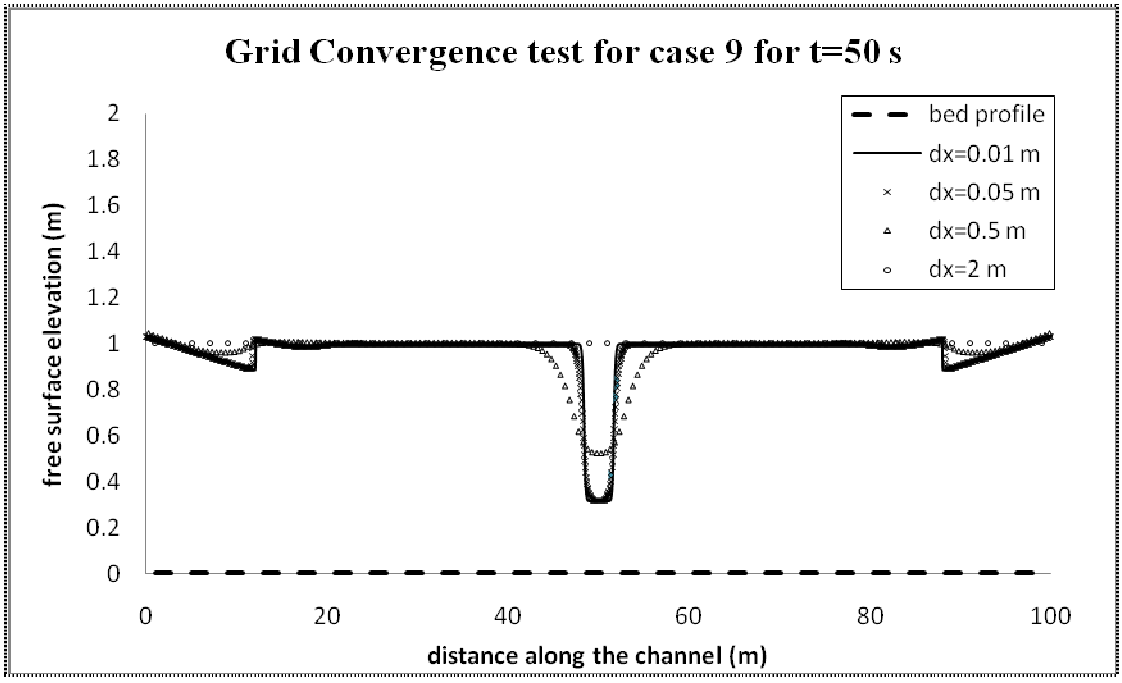


Fig. 4.17 Case 9. Symmetric 1-D density dam break with two initial discontinuities – Grid convergence test results for Case 9.1 ($\rho_2 = 100$ kg/m^3) at t=50 s and dx=2, 0.5, 0.05and 0.01 m.

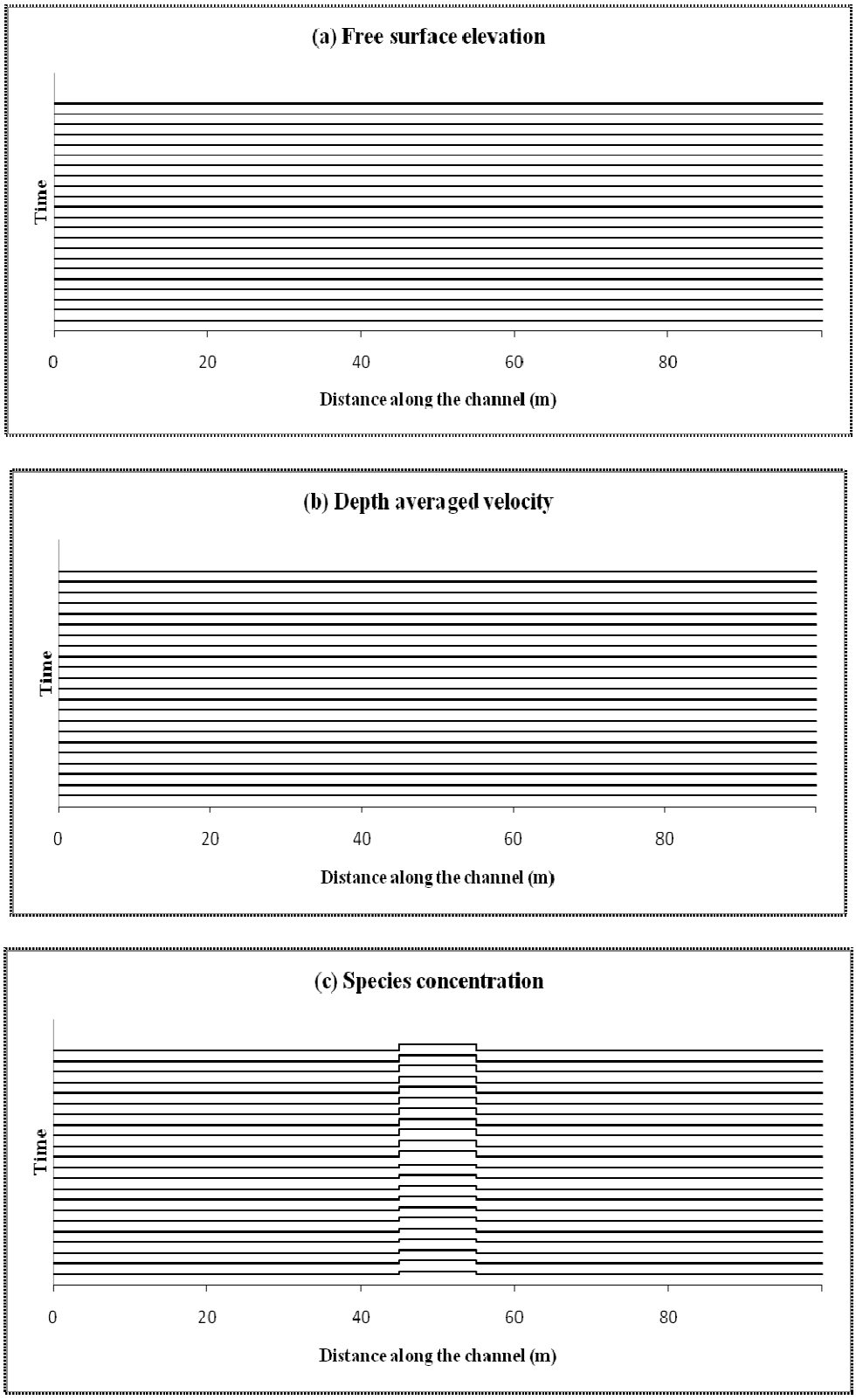


Fig. 4.18 Case 9. Symmetric 1-D density dam break with two initial discontinuities – Case 9.1 (ρ_2 = 1 kg/m^3) - Stacked *x*-*t* plots of (a) the free surface elevation, (b) the depth averaged velocity and (c) the concentration for $t \leq 50$ s.

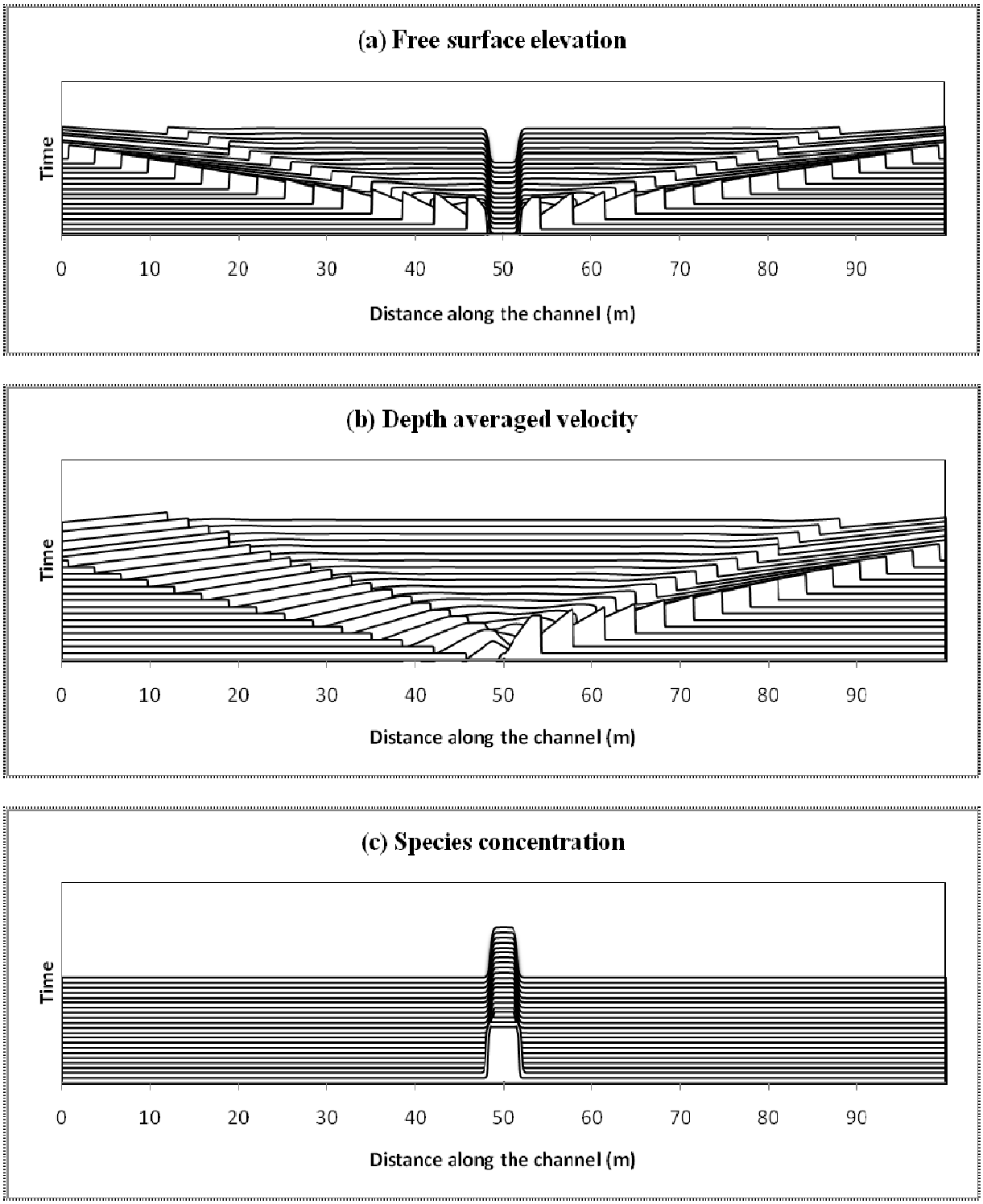


Fig. 4.19 Case 9. Symmetric 1-D density dam break with two initial discontinuities – Case 9.2 (ρ_2 = 10 kg/m^3) – Stacked *x-t* plots of (a) the free surface elevation, (b) the depth averaged velocity and (c) the concentration for $t \leq 50$ s.

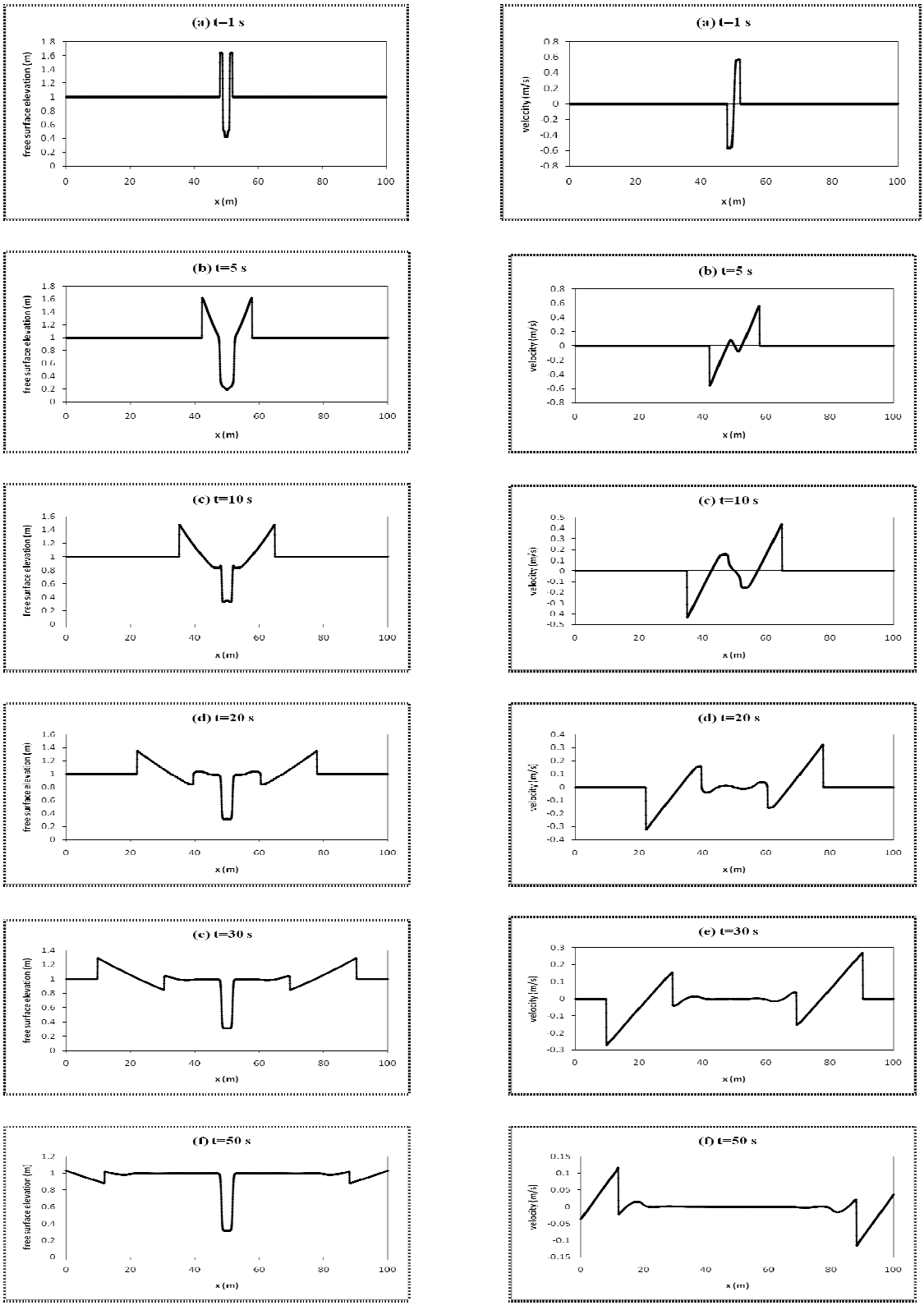


Fig. 4.20 Case 9. Symmetric 1-D density dam break with two initial discontinuities – Case 9.2 (ρ_2 = 10 kg/m^3) – Numerical results for the free surface elevation and the depth averaged velocity for t=1, 5, 10, 20, 30 and 50 s.

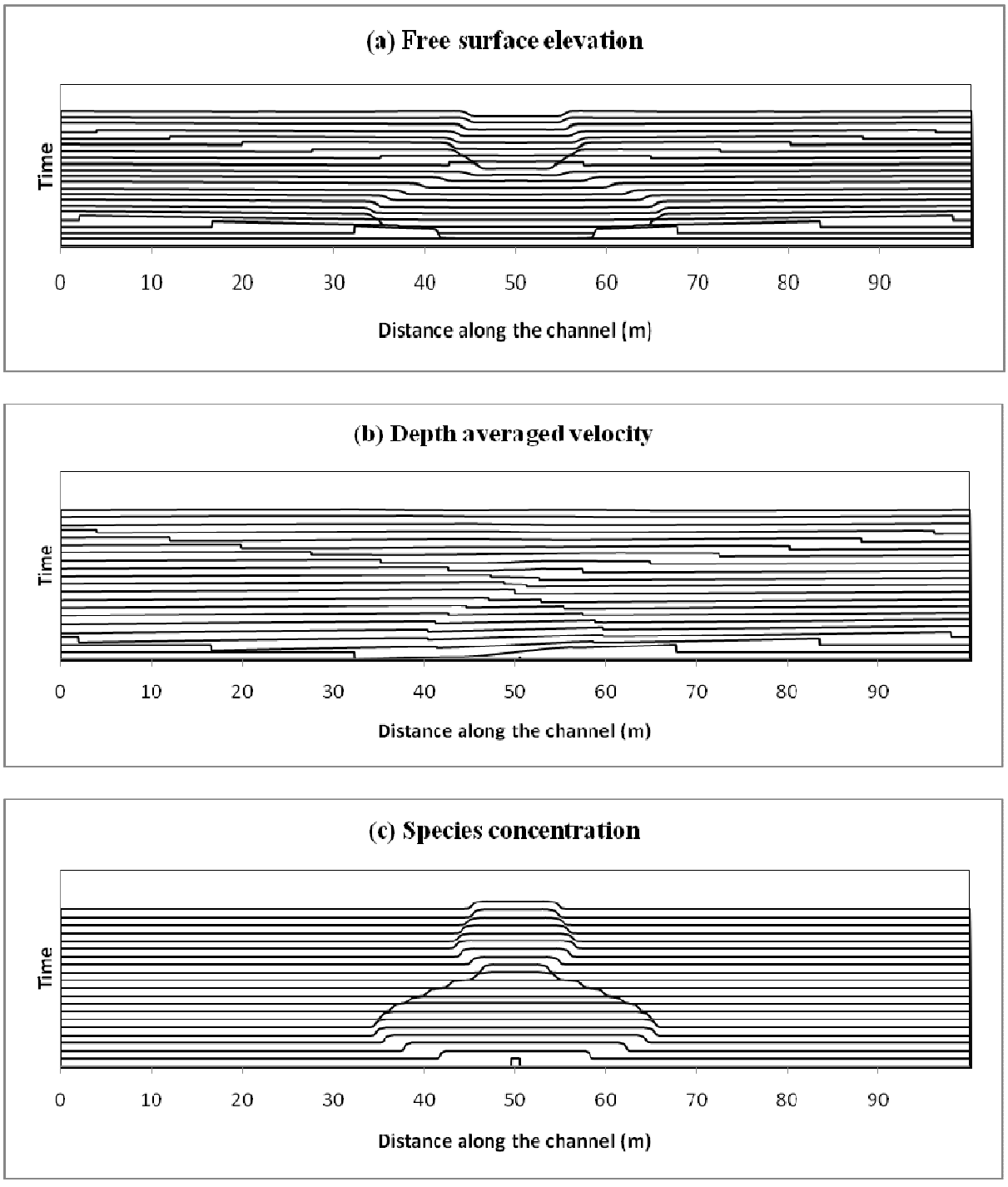


Fig. 4.21 Case 9. Symmetric 1-D density dam break with two initial discontinuities – Case 9.3 (ρ_2 = 100 kg/m^3) – Stacked *x-t* plots of (a) the free surface elevation, (b) the depth averaged velocity and (c) the concentration for $t \leq 180$ s.

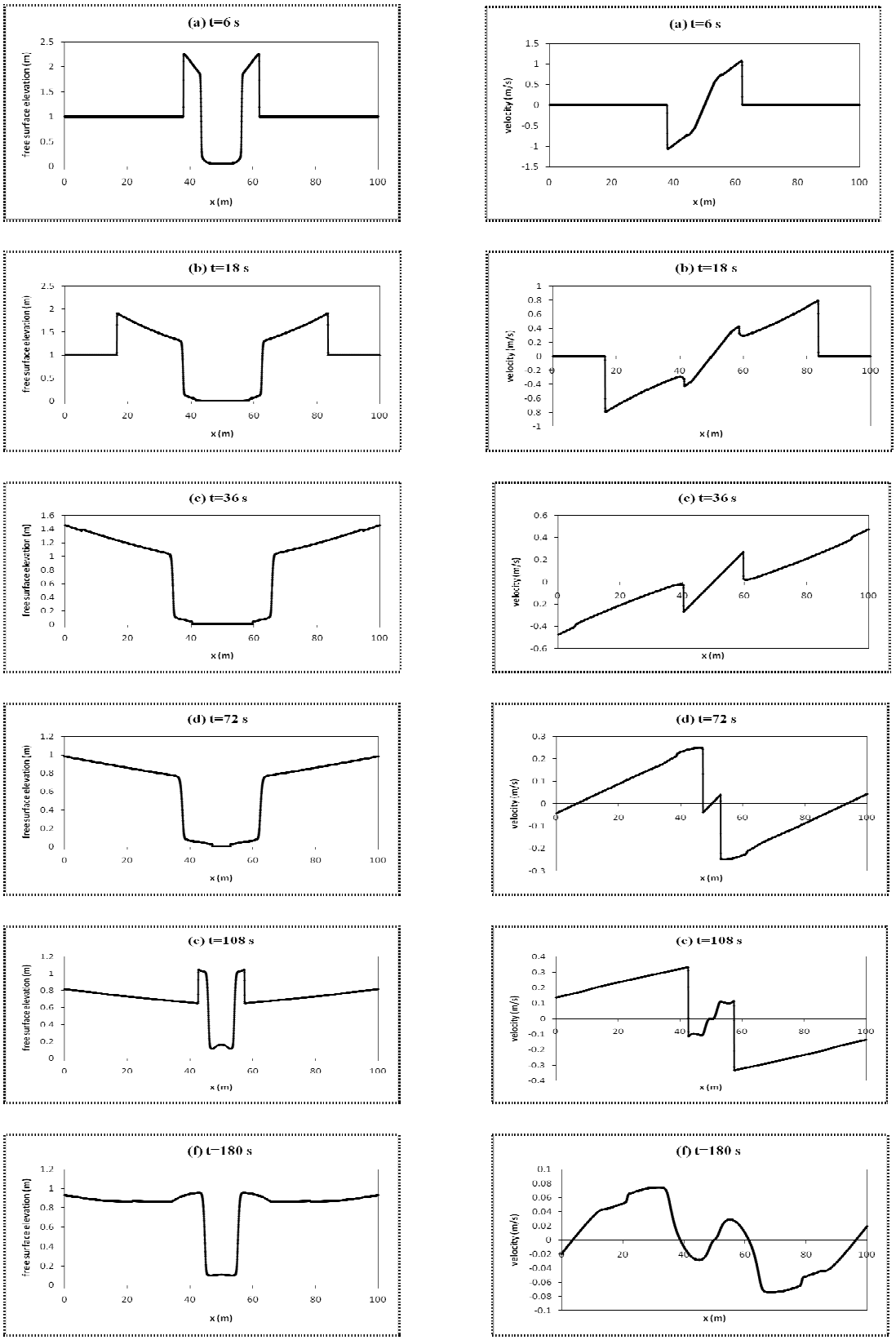


Fig. 4.22 Case 9. Symmetric 1-D density dam break with two initial discontinuities – Case 9.3 (ρ_2 = 100 kg/m^3) – Numerical results for the free surface elevation and the depth averaged velocity for t=6, 18, 36, 72, 108 and 180 s.

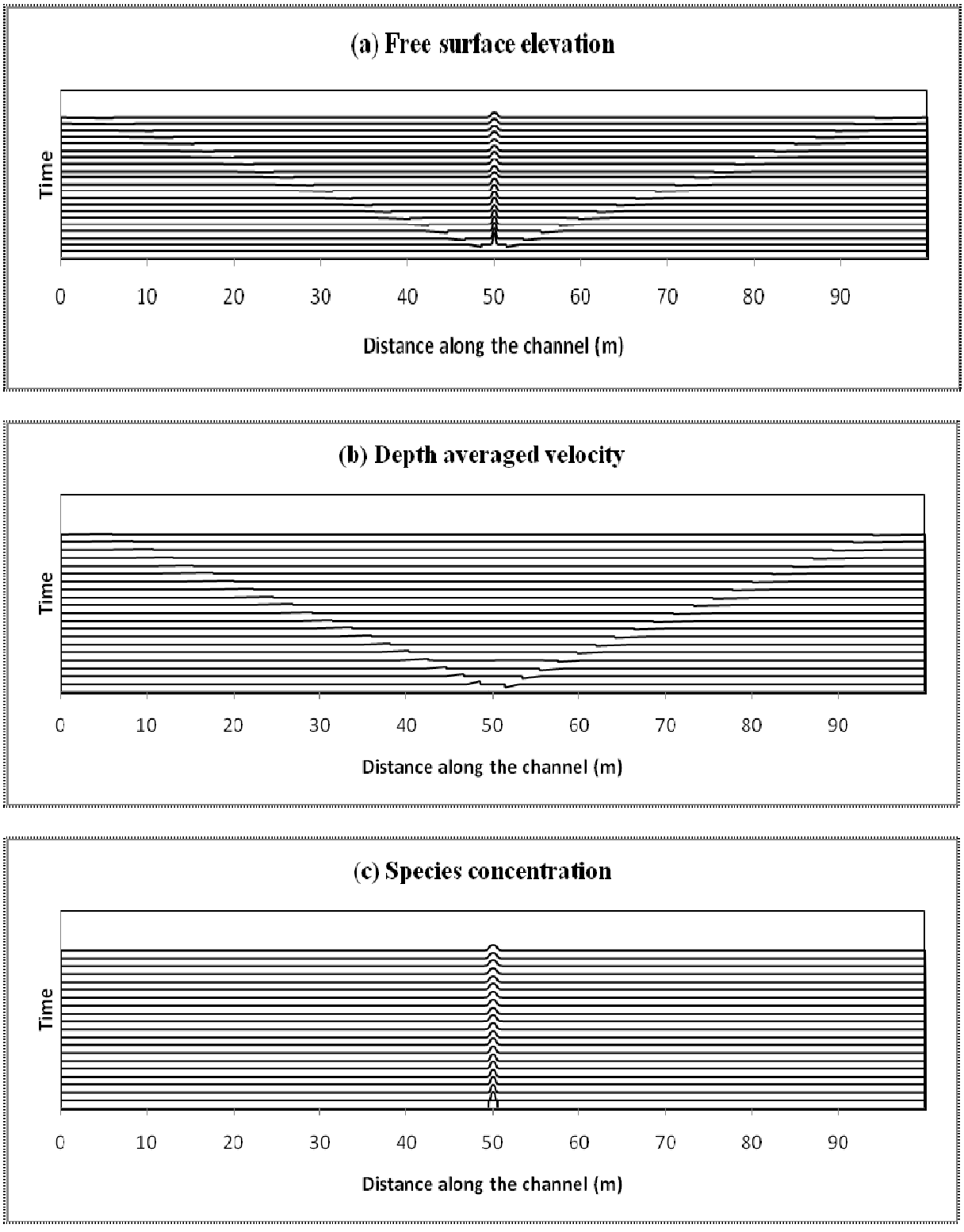


Fig. 4.23 Case 9. Symmetric 1-D density dam break with two initial discontinuities – Case 9.4 (ρ_2 = 0.1 kg/m^3) – Stacked *x-t* plots of (a) the free surface elevation, (b) the depth averaged velocity and (c) the concentration for $t \leq 50$ s.

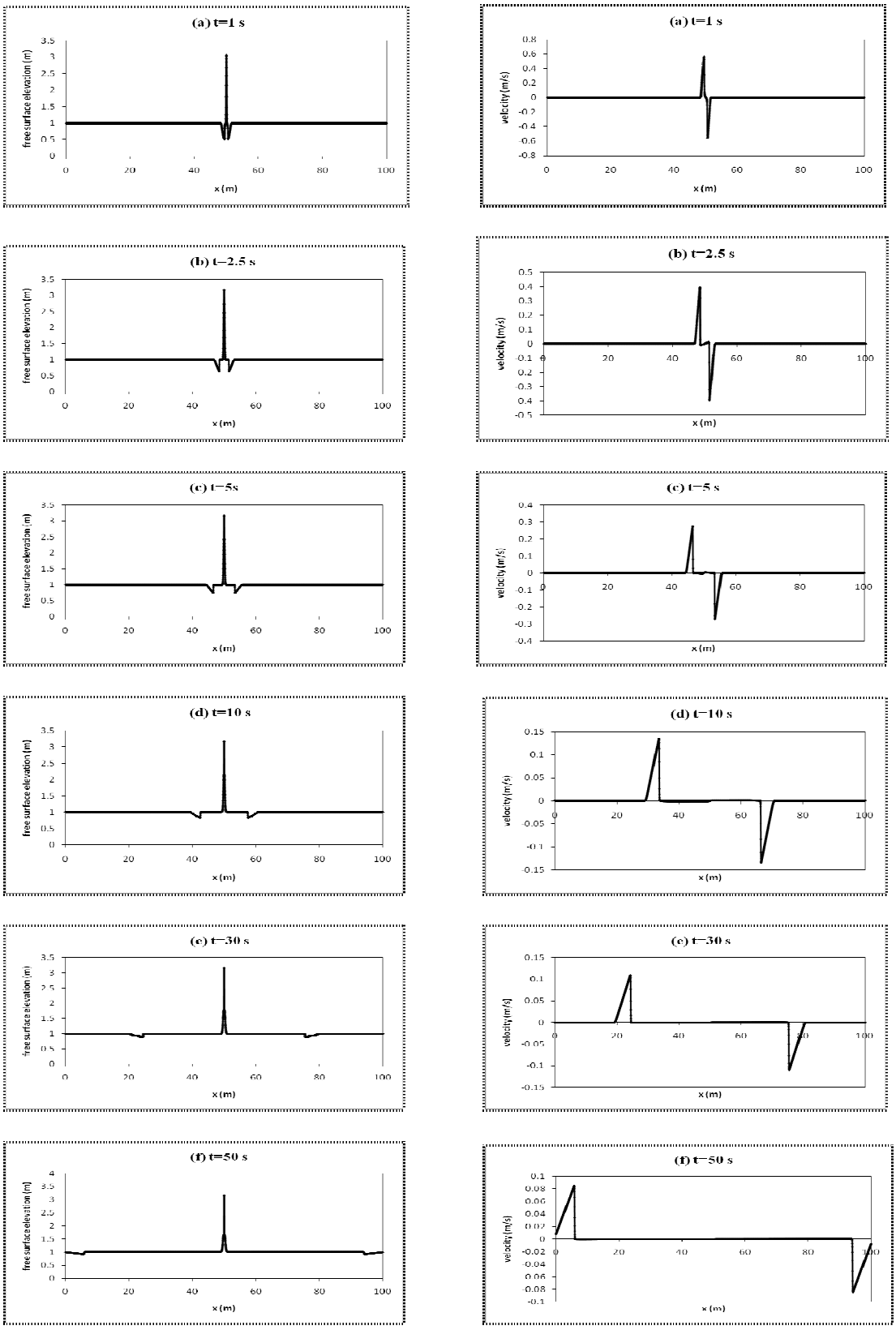


Fig. 4.24 Case 9. Symmetric 1-D density dam break with two initial discontinuities – Case 9.4 (ρ_2 = 0.1 kg/m^3) – Numerical results for the free surface elevation and the depth averaged velocity for t=1, 2.5, 5, 10, 30 and 50 s.

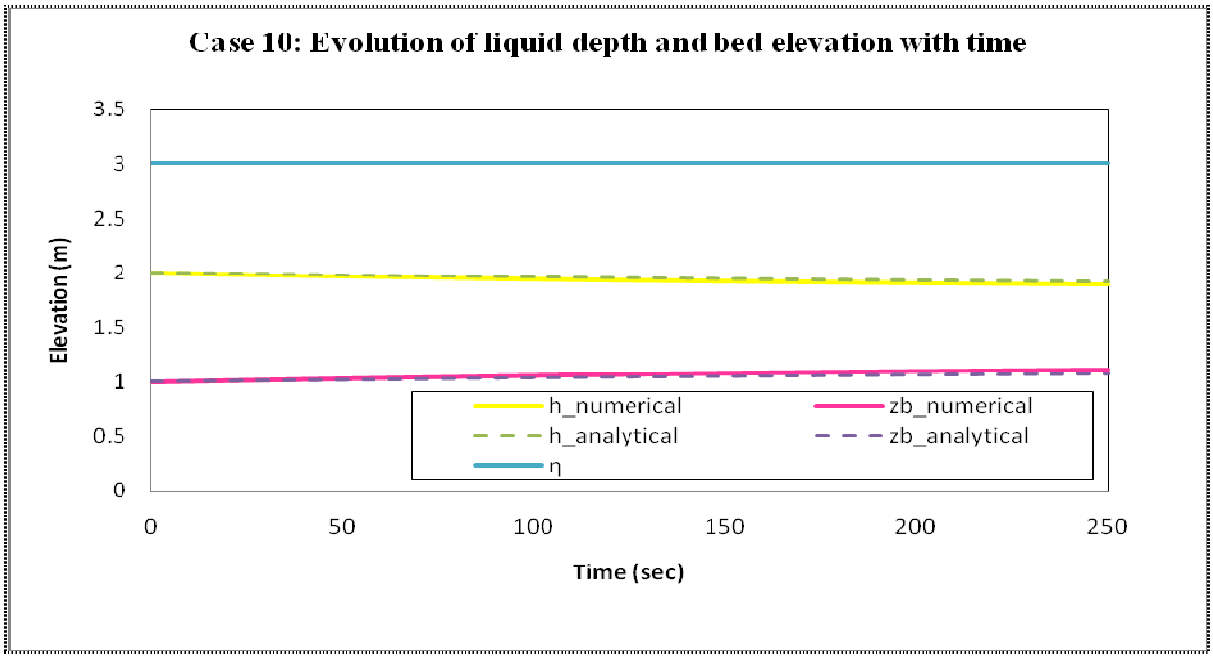


Fig. 4.25 Case 10. Deposition of dilute suspended sediment in a flat-bottomed tank with intense mixing but no net flow and no entrainment of sediment – Evolution of liquid depth and bed elevation with time for $t \leq 250$ s.

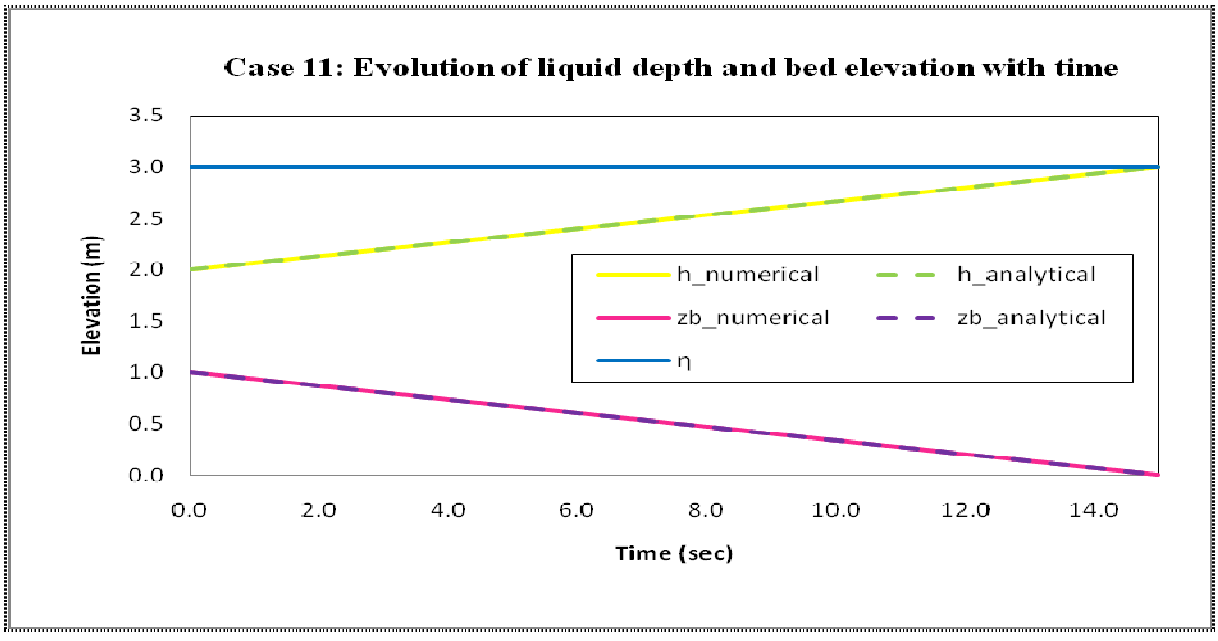


Fig. 4.26 Case 11. Entrainment of dilute suspended sediment in a flat-bottomed tank with intense mixing but no net flow and no deposition of sediment– Evolution of liquid depth and bed elevation with time for $t \leq 15$ s.

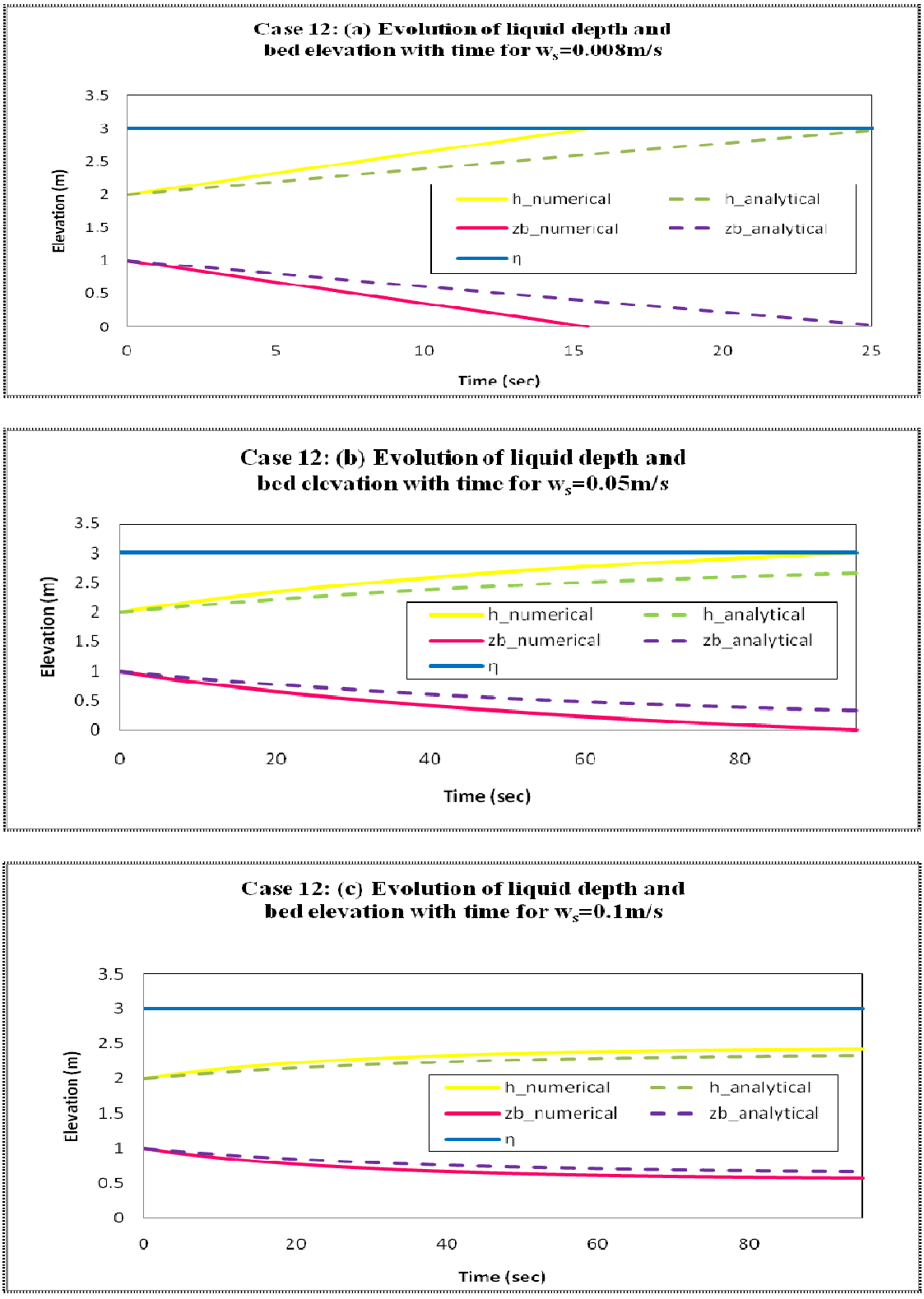


Fig. 4.27 Case 12. Simultaneous deposition and constant entrainment of dilute suspended sediment in a flat-bottomed tank with intense mixing but no net flow – Evolution of liquid depth and bed elevation with time for (a) w_s=0.008 m/s, (b) w_s=0.05 m/s, and (c) w_s=0.01 m/s and for $t \leq 100$ s.

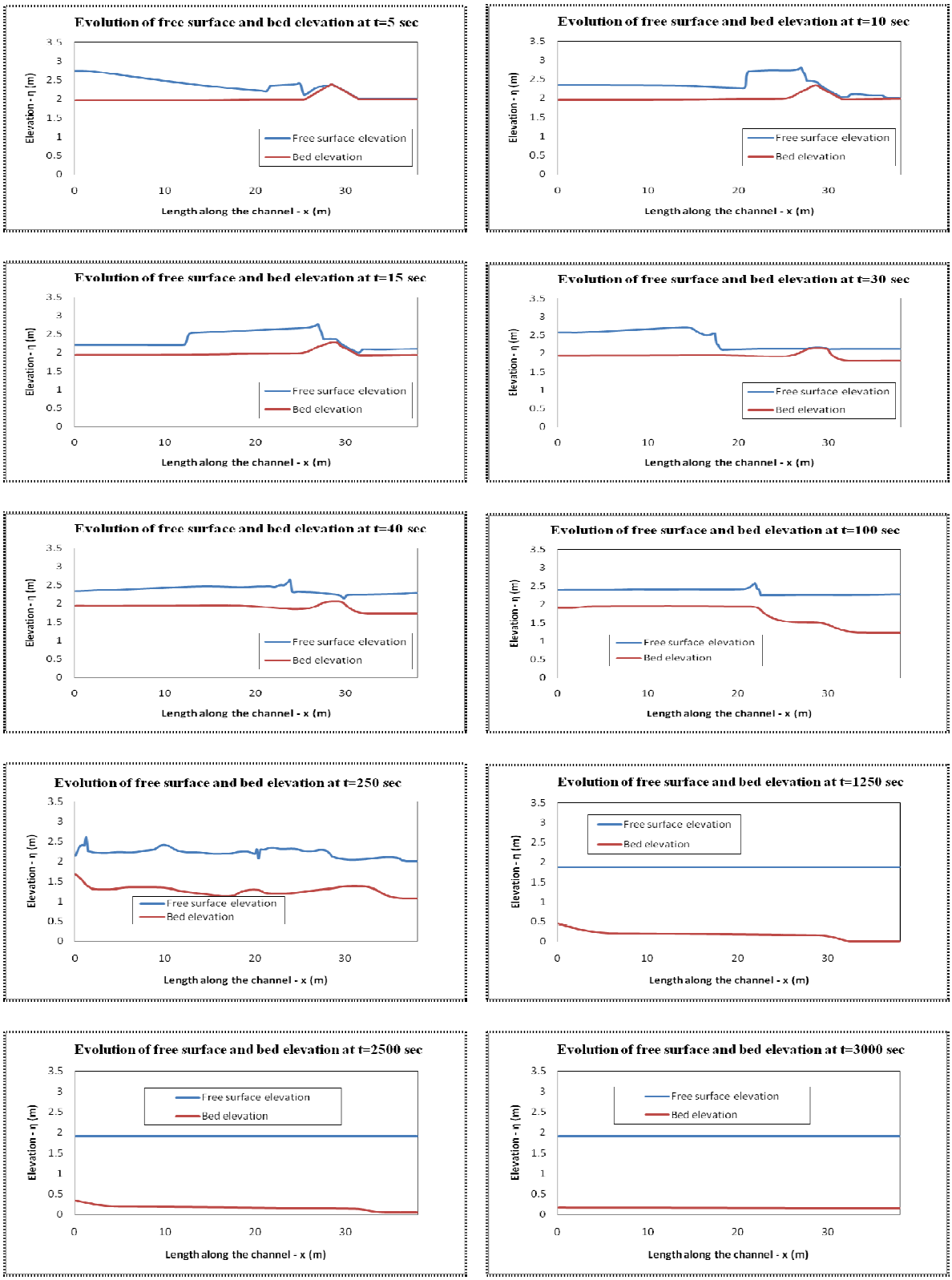


Fig. 4.28 Case 13.1. Dam break problem and flow over a triangular obstacle with erodible bed with open right hand side boundary. - Evolution of free surface and bed elevation with time for *t*=5, 10, 15, 30, 40, 100, 250, 1250, 2500 and 3000 s.

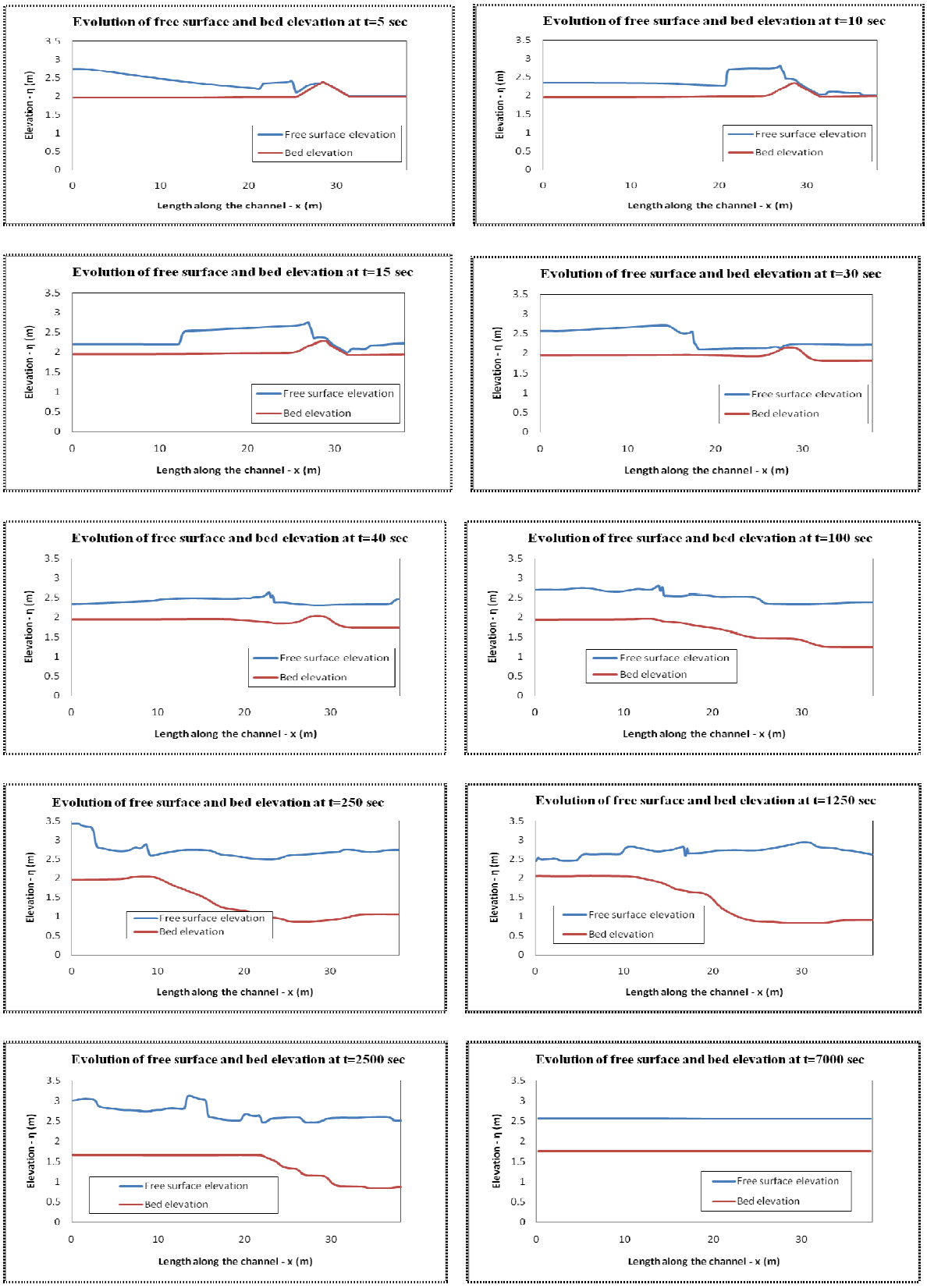


Fig. 4.29 Case 13.2. Dam break problem and flow over a triangular obstacle with erodible bed with reflective boundaries. - Evolution of free surface and bed elevation with time for *t*=5, 10, 15, 30, 40, 100, 250, 1250, 2500 and 7000 seconds.

Table 4.1		
Grid Converegence Table for Case 5: Damped Free Surface Oscillations in a Tank with Parabolic Bed (dt=0.001 s, t=500 s)		
dx (m)	E_{max}*	E**
1000	0.119641085	0.04401379
500	0.131576979	0.03704871
200	0.031374468	0.01039244
100	0.031878247	0.00524749
78.125	0.016658198	0.00519917
40	0.013281514	0.00276288
10	0.009143779	0.00084762

$$*E_{\max} = \max\left\{\frac{\left|\eta_i - \eta_{anal_i}\right|}{\eta_{anal_i}}\right\} \qquad **E = \sqrt{\frac{\sum_{i=`}^{n}\left|\eta_i - \eta_{anal_i}\right|^2}{\sum_{i=`}^{n}\eta_{anal_i}^{\ 2}}}$$

Table 4.1 Case 5. Damped free oscillations in a tank with parabolic bed – Grid convergence.

Table 4.2		
Grid Convergence Table for Case 6: Dam break and flow over a triangular obstacle for *t*=10 s and *dt*=0.001 s		
dx (m)	E_{max}*	E**
0.5	1.00000000	0.215746238
0.2	1.00000000	0.030449595
0.1	0.00376081	0.000628667
0.04	0.00061101	0.052812402

$$*E_{\max} = \max\left\{\frac{\left|\eta_i - \eta_{anal_i}\right|}{\eta_{anal_i}}\right\} \qquad **E = \sqrt{\frac{\sum_{i=`}^{n}\left|\eta_i - \eta_{anal_i}\right|^2}{\sum_{i=`}^{n}\eta_{anal_i}^{\ 2}}}$$

Table 4.2 Case 6. Dam break problem and flow over a triangular obstacle – Grid convergence.

Table 4.3			
Case 9: Symmetric 1-D density dam break with two initial discontinuities - Parameter Study			
Case	ρ_2 (kg/m^3)	Equilibrium depth (m)	Equilibrium width (m)
9.1	1	1	1
9.2	10	0.316	3.162
9.3	100	0.1	10
9.4	0.1	3.16	0.316

Table 4.3 Case 9. Symmetric 1-D density dam break with two initial discontinuities - Parameter Study – Values of density of the central column and the equilibrium depth and width.

CHAPTER 5 TWO-DIMENSIONAL MODEL VALIDATION TESTS

5.1. Introduction

The two-dimensional numerical model was also tested against a comprehensive range of case studies and the predictions compared with analytical solutions. The tests include constant and variable density shallow flow, wet/dry front, and erodible bed problems. The two-dimensional model should provide a sensible representation of flood simulation on complicated terrain, as it accounts for the directional fluxes that are very important in the flow evolution.

5.2. Constant density problems

The two-dimensional model was tested against constant density idealised problems, including the propagation of a single rarefaction wave, a circular dam-break, and a two-dimensional dam break flow over three islands (with wetting and drying fronts).

5.2.1. Case 14: Right, left, north and south dry bed Riemann problem

The flow domain comprises a channel that is 50 m long in the streamwise direction, and 2 m wide in the transverse direction. Depending on the flow direction of interest, the initial water depth is 1 m at the west, east, south or north side of the domain, and the bed is dry elsewhere. The initial velocity is everywhere zero. The initial conditions are the same as in one-dimension (see Section 4.2.3), the only difference being that the other horizontal direction is also considered. Extrapolation boundary conditions are applied at the open ends. The grid spacing is dx=0.1 m in the x-direction and dy=0.2 m in the y-direction respectively

and the time step is 0.001 s. The simulation time is 4 s. The results depicted in Figure 5.1 obtained are identical to the one-dimensional predictions and almost the same as Toro's (2001) solution. This confirms the ability of the two-dimensional model to simulate flows with step-like discontinuities.

5.2.2. Case 15: Circular dam break problem

This test case consists of an idealised circular dam in a basin with horizontal bed and has been examined by many researchers, including Alcrudo and García-Navarro (1993) and Toro (2001). At t = 0 s, the infinitesimally thin wall of the dam collapses instantaneously. The challenge for the numerical model is to predict correctly the wave propagation phenomena that follow. The initial conditions are as given by Toro (2001): namely; a square computational domain 40 m x 40 m; infinitely thin circular wall of radius r_c = 2.5 m around the dam which is centred at x_c = 20 m and y_c = 20 m (symmetrical problem); zero velocities throughout the domain ($u = v = 0$); and initial water depth

$$h(x,y) = \begin{cases} h_{dam} = 2.5m & \text{if } (x\text{-}x_c)^2 + (y - y_c)^2 \le r^2 \\ h_{domain} = 0.5m & \text{if } (x\text{-}x_c)^2 + (y - y_c)^2 > r^2 \end{cases}, \qquad (5.1)$$

Figures 5.2 and 5.3 illustrate the evolution of the circular dam break at different times. The results are in close agreement with the fine grid solutions provided by Toro (2001). This test indicates that the model is not affected by grid alignment, and again can cope with flow gradient discontinuities.

5.2.3. Case 16: 2-D dam break problem and flow over three islands with wetting and drying fronts

This case considers a dam-break wave travelling over an initially dry floodplain with three humps, as examined by e.g. Kawahara and Umetsu (1986), Brufau et al. (2002), and Liang and Borthwick (2008).

The initial values used for this test case are the following: the acceleration due to gravity is g = 9.81 m/s^2; the density of the liquid is ρ_w = 1000 kg/m^3; the spatial step is dx = 0.5 m in the x-direction and dy = 0.4 m in the y-direction; the computational domain has length x_L = 75 m and the width y_L = 30 m; the time step is dt = 0.001 s; the bed shear stress is calculated with the Manning coefficient set to n = 0.018; the dam is located at x = 16 m and retains liquid with initial free surface elevation of η = 1.875 m; the initial bed elevation is z_b is given by

$$\begin{aligned} z_b(x,y) = \max[0, \quad & 1-\frac{1}{8}\sqrt{(x-30)^2+(y-6)^2}, \\ & 1-\frac{1}{8}\sqrt{(x-30)^2+(y-24)^2}, \\ & 3-\frac{3}{10}\sqrt{(x-47.5)^2+(y-15)^2}]. \end{aligned} \tag{5.2}$$

Figure 5.4 shows the initial state at the instant the dam-break flow is released. Figures 5.5 (a-e) show the free surface elevation 3-D plots and plan views at t = 2, 6, 12, 30, and 300 s (when steady state is reached). The dam-break causes a bore to travel towards the three humps and flood the computational domain. By t = 2 s (Figure 5.5 (a)), the initial wave has already reached the first two low humps and starts overtopping them, while some water penetrates between them. There is also an obvious reflection wave travelling upstream of each hump. By t = 6 s (Figure 5.5 (b)), the water has overtopped completely the first two low humps and starts climbing over the higher third hump. Reflected wave components can

be seen travelling upstream (towards the left hand side of the computational domain). By t = 12 s after the dam break (Figure 5.5 (c)), some water continues to run up the highest hump, while the remainder propagates around the hump. The two lower humps are still completely submerged. At t = 30 s (Figure 5.5 (d)), the flood wave has already reached the right hand side end of the computational domain and been reflected by the solid wall boundary. This reflected wave travels upstream (towards the left hand side of the computational domain) and runs up the lee (right hand) side of the highest hump. Meanwhile, on the front face of the hump, the shoreline drops as the water level falls. The same occurs at the front and back of the lower humps. By t = 300 s (Figure 5.5 (e)), the water has begun to settle to its equilibrium steady state. Throughout the simulation, there were repeated wave reflections at the solid lateral walls of the computational domain, causing the free surface motions to be very complicated.

The numerical results are in very good agreement with those of Brufau et al. (2002) and Liang and Borthwick (2008). Hence, it can be concluded that the numerical model properly simulates complicated wetting and drying processes.

5.3. Variable Density Cases

The test cases in this section simulate vertically homogeneous shallow flows with variable horizontal density in two dimensions. As with the one-dimensional model, the term ‘species’ refers to material transported with the liquid flow.

Following Leighton (2005), the 2-D variable density validation case involves a variable density circular dam break, for which a parameter study is carried out by varying the ratio of species to liquid density.

5.3.1. Case 17: Variable density circular dam break

This case examines a circular dam break driven by depth and/or density differences. A cylindrical dam is initially separated by the surrounding liquid by an infinitesimally thin wall. The computational domain is a square basin of length x_L = 40 m and width y_L = 40 m, with horizontal bed. Three possible combinations are considered, according to the hydrostatic pressure thrust ratio either side of the interface, i.e. $(\rho h^2)_{\text{in}} / (\rho h^2)_{\text{out}}$, which can be greater than, less than, or equal to unity (the subscript *in* denotes the hydrostatic pressure thrust inside the wall and the subscript *out* denotes the hydrostatic pressure thrust outside the wall, i.e. in the rest of the basin).

The initial values used for this test case are the following: the acceleration due to gravity is g = 9.81 m/s^2; the density of the liquid outside the wall is ρ_{out} = 1000 kg/m^3; the depth outside the wall is h_{out} = 1 m; the density of the liquid inside the wall is ρ_{in} = 1000, 250, 200 and 100 kg/m^3 (for Cases 17.1, 17.2, 17.3 and 17.4 such that the values of the hydrostatic pressure thrust ratio either side of the interface are $(\rho h^2)_{\text{in}} / (\rho h^2)_{\text{out}}$ = 4, 1, 0.8 and 0.4 respectively, Table 5.1); the depth inside the wall is h_{in} = 2 m; the spatial steps are dx = 0.1 m and dy = 0.1 m; the time step is dt = 0.002 s; the cylindrical wall has radius $R = 2.5$ m and is located at the centre of the square basin; and the velocity components are zero everywhere in the computational domain. The effects of friction and diffusion are ignored.

After the collapse of the cylindrical wall at t = 0 s the system tends toward an equilibrium steady state condition when a hydrostatic pressure thrust balance is achieved. For this condition, the equilibrium depth of the circular liquid column, h^{eq} , must satisfy the following relation

$$h^{\text{eq}} = \sqrt{\frac{(\rho h^2)_{\text{out}}}{\rho_{\text{in}}}} \quad . \tag{5.3}$$

And if mass conservation is also satisfied, then the equilibrium radius of the circular liquid column, R^{eq}, can be calculated as

$$R^{\text{eq}} = \sqrt{\frac{R^2 h_{\text{in}}}{h^{\text{eq}}}} \quad . \tag{5.4}$$

Table 5.2 lists relevant values of the equilibrium depth of the circular liquid column and the equilibrium radius of the circular liquid column for the three cases considered.

Case 17.1: ρ_{in} = 1000 kg/m^3

This case is similar to the gravity driven circular dam break of Case 15, but also involves a density difference between the two liquids. The initial density of the liquid inside the wall is ρ_{in} = 1000 kg/m^3, so the hydrostatic pressure thrust ratio either side of the interface is $(\rho h^2)_{\text{in}} / (\rho h^2)_{\text{out}}$ = 4. Figures 5.6 and 5.7 (a-e) show free surface elevation visualisations and the free surface elevation and depth averaged velocity profiles in the *x*-direction along the centreline of the domain at $y = y_L/2$ at t = 0.35, 0.65, 1, 1.25 and 1.7 s. According to equations 5.3 and 5.4, the equilibrium depth value for this test is 1 m and the new equilibrium radius is 3.563 m (Table 5.2).

At time t = 0 s, the cylindrical thin wall is removed and the system is set free. Gravity and density differences between the liquids (inside and outside the wall) cause a circular bore to

propagate outwards (towards the boundaries of the computational domain). In a similar fashion to the gravity driven circular dam break, the circular shock-like bore wave is followed by a rarefaction wave travelling inwards. By $t = 0.35$ s, the initial bore continues to travel radially outwards with a front speed of 0.2 m/s, while a portion of the circular dam closest to the centre still remains at the initial height of 2m. The rarefaction wave is travelling inwards with speed of 0.35 m/s. Circular symmetry is apparent in all the plots at t = 0.35 s. At $t = 0.65$ s, the initial bore continues travelling outwards with the same speed, but the central part of the cylindrical dam has fallen to 1.8 m. By $t = 1$ s, the speed of the bore diminishes to 0.8 m/s, while the free surface elevation in the centre of the domain has dropped below the equilibrium value. Meanwhile, inward travelling rarefaction waves collide with each other causing reflected waves to travel radially outwards, until they reach the density interface where they are re-reflected inwards again. By $t = 1.25$ s, the free surface elevation in the centre of the domain has reached a minimum of 0.3m before it starts rising again in order to settle towards the equilibrium value. Furthermore, a secondary bore has begun to travel inwards, causing the free surface elevation in the centre of the domain to drop even more. By $t = 1.7$ s, the system has almost reached the equilibrium steady state condition, with depth and radius of the circular liquid column close to those calculated analytically above. The secondary bores have been reflected and travel again outwards, allowing the free surface elevation to readjust in the new equilibrium value.

Case 17.2: $\rho_{in} = 250$ kg/m^3

This case is unique, as the initial hydrostatic pressure thrust inside the circular column is equal to that outside the column, which means that the system should remain at the equilibrium steady state condition.

The initial value for the density of the liquid inside the wall used for this test case is ρ_{in} = 250 kg/m^3, so the value of the hydrostatic pressure thrust ratio either side of the interface is $(\rho h^2)_{\text{in}} / (\rho h^2)_{\text{out}}$ = 1. Figures 5.8 and 5.9 (a) and (b) show the free surface elevation visualisations and the free surface elevation and the depth averaged velocity profiles in the *x*-direction along the centreline of the domain at $y = y_L/2$ at t = 0.55 and 0.7 s. From equations 5.3 and 5.4, the equilibrium depth and radius are 2 m and 2.5 m respectively (Table 5.2).

It can be seen that the system remains relatively stable, apart from small deviations very close to the centre of the computational domain. By $t = 0.55$ s, the density interface remains unchanged, as well as the free surface elevation outside the cylindrical thin wall. The only discrepancy is a small peak in the centre of the cylindrical column of lower density liquid. The velocities that describe this small movement have values lower than 0.03 m/s. By $t = 0.7$ s, everything remains the same except for the small peak in the centre of the domain which has experienced a small drop. The velocities this time are slightly higher but still less than 0.08 m/s. The small perturbations are possibly caused by a round off error due to the accuracy limits set by the numerical model. The alternation from a peak to a drop is due to the reflection of the small waves when they reach either the centre of the domain or the density interface.

Case 17.3: ρ_{in} = 200 kg/m^3

In this case the initial hydrostatic pressure thrust inside the circular column is less than that outside the column, which means that the process will be reverse of that in Case 17.1, when the ratio of the hydrostatic pressure thrusts was greater than unity.

The initial density of the liquid inside the wall is ρ_{in} = 200 kg/m^3, so the hydrostatic pressure thrust ratio either side of the interface is $(\rho h^2)_{\text{in}} / (\rho h^2)_{\text{out}}$ = 0.8. Figures 5.10 and 5.11 (a-e) show the predicted free surface elevation visualisations and the free surface elevation and the depth averaged velocity profiles in the x-direction along the centreline of the domain at $y = y_L/2$ at t = 0.3, 0.6, 1.05, 1.5, and 1.7 s. According to equations 5.3 and 5.4, the equilibrium depth is 2.236 m and the equilibrium radius is 2.364 m (Table 5.2).

At time t = 0 s, the cylindrical thin wall is removed and the system is set free. The gravity and density differences of the two liquids (inside and outside the wall) again cause a circular bore, but which is travelling radially inwards, towards the centre of the computational domain. As in Case 17.1, the bore is associated with an outward-directed rarefaction wave travelling (mirroring the process in Case 17.1). At $t = 0.3$ s, the initial bore is continuing to travel inwards at a frontal speed of 0.35 m/s. The portion of circular dam closest to the density interface still has a free surface elevation of 2 m, whereas the free surface elevation around the central part of the column has dropped to 1.8 m. The rarefaction wave is travelling outwards with a frontal speed of 0.2 m/s. The plots again verify the symmetry of the computation. At $t = 0.6$ s, the initial bore continues to propagate inwards with the same speed, and is just about to be reflected and thus change direction. The profile of the free surface elevation is the reverse of the previous figure (for t = 0.3 s), as the central part of the cylindrical dam has risen to 2.4 m, while the density interface around the cylindrical column has fallen to 2.1 m. By $t = 1.05$ s, the initial bores have been reflected at the centre and they now travel outwards with a frontal speed of 0.13 m/s, while the depth at the centre of the domain has now attained a nearly uniform value of 2.25 m. At the same time, the rarefaction waves that have already reached the density interface are partly reflected and partly propagated through the interface. By $t = 1.5$ s, the free surface elevation inside the density interface has almost settled to the equilibrium value, while the bores are again reflected in

the centre of the domain and start travelling outwards following the rarefaction waves. By $t = 1.7$ s, the system has almost reached steady state, with depth and radius close to those calculated analytically above. The secondary bores keep travelling outwards causing a small perturbation around the density interface.

Case 17.4: ρ_{in} = 100 kg/m^3

This case is similar to the Case 17.3 in that the initial hydrostatic pressure thrust inside the circular column is less than that outside the column again, but this time the value of the ratio of the hydrostatic pressure thrusts is even smaller, i.e. half (0.4 compared to 0.8 before). Consequently, the process is similar to that of the previous case, but happens more rapidly and the features are much more pronounced.

The initial value for the density of the liquid inside the wall is ρ_{in} = 100 kg/m^3, so the hydrostatic pressure thrust ratio either side of the interface is $(\rho h^2)_{\text{in}} / (\rho h^2)_{\text{out}}$ = 0.4. Figures 5.12 and 5.13 (a-e) show the predicted free surface elevation visualisations and the free surface elevation and the depth averaged velocity profiles in the *x*-direction along the centreline of the domain at $y = y_L/2$ for t = 0.25, 0.5, 0.85, 1.1, and 1.4 s. According to equations 5.3 and 5.4, the equilibrium depth is 3.162 m and the equilibrium radius is 1.988 m (Table 5.2).

At time t = 0 s, the cylindrical thin wall is removed and the system is set free. The gravity and density differences of the two liquids (inside and outside the wall) again generate a circular bore which travels inwards and a rarefaction wave travelling outwards. By $t = 0.25$ s, the initial bore is travelling inwards with a frontal speed of 1.2 m/s. While the region of the circular column closest to the density interface has a nearly constant free surface

elevation, at the initial value of 2.5 m, the free surface elevation around the central part of the column has dropped to 1.8 m. The rarefaction wave travels outwards with speed of 0.7 m/s, approximately triple that of Case 17.3. By $t = 0.5$ s, the initial bore continues to propagate inwards with the same speed, and a spike is formed as the liquid of lower density is squeezed up by the higher density liquid. The free surface elevation at the peak has risen to 4 m. By $t = 0.85$ s, the initial bores have been reflected at the centre and they now travel outwards at a speed of 0.6 m/s, while the free surface elevation at the centre of the domain has now a fairly constant value of 3.2 m (which is slightly lower towards the centre of the domain where a small depression has formed). By $t = 1.1$ s, the free surface elevation inside the density interface starts to peak again, as the bores again reflect at the centre of the domain and start travelling outwards, following the rarefaction waves as in Case 17.3. By $t = 1.4$ s, the system tends toward steady state with the free surface values close to those calculated analytically. The secondary bores and the rarefaction waves keep travelling outwards, while the waves inside the density interface are reflected several times causing perturbations inside the cylindrical wall.

5.4. Erodible Bed Cases

The two-dimensional model is next validated for entrainment and deposition, and the numerical predictions are compared against approximate analytical solutions derived for certain erodible bed problems. The cases used for the one-dimensional model are extended in two dimensions. For Cases 18-21, the results are expected to be the same as in the one-dimensional cases, as the only difference is the expansion in the *y*-direction. Case 22 involves the 2-D dam-break flow over an erodible bed comprising three islands, and so does not have a one-dimensional counterpart.

5.4.1. Case 18: Deposition of dilute suspended sediment in a flat-bottomed 2-D tank with intense mixing but no net flow and no entrainment of sediment

The initial conditions are essentially one-dimensional (see Case 10): the acceleration due to gravity is g = 9.81 m/s^2; the density of the liquid is ρ_w = 1000 kg/m^3; the density of the sediment is ρ_s = 2000 kg/m^3; the spatial step is dx = 4 m in the x-direction and dy = 1 m in the y-direction; the computational domain has length x_L = 2000 m and width y_L = 10 m; the time step is dt = 0.01 s; the sediment settling velocity is w_s = 0.008 m/s; the initial free surface elevation is η = 3 m throughout the computational domain; the initial bed elevation is z_b = 1 m throughout the computational domain; and the initial species concentration is c = 0.05 for the whole tank. Figure 5.14 shows the evolution of the depth of the liquid-species mixture and the bed elevation with time for $t \leq 250$ s. For this test, the numerical results are in very satisfactory agreement with the analytical solution (see Section 4.4.1) and the results from the one-dimensional Case 10.

5.4.2. Case 19: Entrainment of dilute suspended sediment in a flat-bottomed 2-D tank with intense mixing but no net flow and no deposition of sediment

Case 19 is the two-dimensional equivalent of Case 11. The initial values are: g = 9.81 m/s^2; ρ_w = 1000 kg/m^3; ρ_s = 2000 kg/m^3; dx = 4 m; dy = 1 m; x_L = 2000 m; y_L = 10 m; dt = 0.01 s; M = 0.01 m/s; τ_b = 1 N/m^2; τ_c = 0.2 N/m^2; η = 3 m; z_b = 1 m; and c = 0.05 throughout the tank. Figure 5.15 shows the evolution of the depth of the liquid-species mixture and the bed elevation with time for $t \leq 15$ s. Again the numerical results are in very satisfactory agreement with the analytical solution (see Section 4.4.2) and the 1-D results from Case 11.

5.4.3. Case 20: Simultaneous deposition and constant entrainment of dilute suspended sediment in a flat-bottomed 2-D tank with intense mixing but no net flow

Case 20 is the two-dimensional version of Case 12, and has the following initial values: g = 9.81 m/s^2; ρ_w = 1000 kg/m^3; ρ_s = 2000 kg/m^3; the dx = 4 m; dy = 1 m; x_L = 2000 m; y_L = 500 m; dt = 0.01 s; M = 0.01 m/s; τ_b = 1 N/m^2; τ_c = 0.2 N/m^2; w_s = 0.008, 0.05 and 0.1 m/s for tests a, b and c (Figure 5.16) respectively; η = 3 m; z_b = 1 m; and c = 0.05. Figure 5.16 (a-c) show the evolution of the depth of the liquid-species mixture and the bed elevation with time for $t \leq 100$ s. The numerical predictions are in very good agreement with the corresponding results for one-dimensional Case 12. The comparison with the analytical solution (as computed for Case 12, see section 4.4.3) varies for each different value of the parameter study.

5.4.4. Case 21: 2-D dam break problem and flow over a triangular obstacle with wetting and drying fronts and erodible bed

Case 21 is similar to Case 13, in that it involves a dam-break wave which interacts with a triangular obstacle, and that both the bed and the triangular obstacle are erodible. It should be noted that there are no published numerical predictions or analytical solutions for this problem (to the author's knowledge). As in Case 13, the domain consists of a reservoir connected to a rectangular channel of total length 22.5 m. The dam is situated at x = 15.5 m. The symmetric triangular obstacle is 6 m long and 0.4 m high, and its crest is situated at x = 28.5 m. The initial water depth in the reservoir is 0.75 m and throughout the rest of the channel the bed is dry (as shown in Figure 4.8). The bed and the symmetric triangular obstacle are erodible, so both entrainment and deposition of the bed material are simulated.

The left hand side of the computational domain is considered as a fixed reflective boundary (solid wall). At the right hand side boundary of the computational domain two separate conditions are implemented. In Case 21.1, a free outlet is located at the right hand side of the channel. In Case 21.2, the free outlet is replaced with a fixed reflective boundary. The bed roughness coefficient is $C_f = g\frac{n_m^{\,2}}{h^{1/3}}$, where n_m = 0.0125 is the Manning coefficient. The acceleration due to gravity is g = 9.81 m/s^2; the density of the liquid is ρ_w = 1000 kg/m^3; the density of the sediment is ρ_s = 2000 kg/m^3; the settling velocity of the sediment (bed material) is w_s = 0.1 m/s; the entrainment constant is M = 0.005 m/s; the threshold shear stress of the bed is τ_c = 0.2 N/m^2; and the initial species concentration is c = 0 throughout the computational domain. The time step chosen is dt = 0.001 s and the grid spacing is dx = 0.1 m in the x-direction and dy = 1 m in the y-direction.

The predicted numerical results are identical to those calculated for the one-dimensional Case 13 for both the open and the reflective right hand side boundary problems. Figure 5.17 shows the predicted free surface and bed elevation visualisations for t = 5, 10, 15, 30, 100, 250, 1250 and 3000 s, for Case 21.1 (where the right hand boundary is open). At t = 0 s, the dam break occurs instantaneously. A right propagating contact wave is released accompanied by a left propagating rarefaction wave. The contact wave hits the triangular obstacle and reflects, causing an upstream travelling bore to be created followed by a moving hydraulic drop (also travelling upstream). From that time onwards, the process is as described in Case 13.1.

Figure 5.18 shows the predicted free surface and bed elevation visualisations at t = 5, 10, 15, 40, 100, 1250, 2500 and 7000 s for Case 21.2, in which the right hand side boundary is reflective. In this case the water-sediment mass conservation is tested once more, as the reflective boundaries either end of the domain prohibit the escape of any material. Until the

flow reaches the right hand boundary, the free surface and bed elevation behave in an identical way to that observed in Case 21.1. After flow reflection occurs at the right hand wall, the hydrodynamic and morphodynamic processes are as described for Case 21.2. At t = 7000 s, both the free surface elevation and the bed have settled. The elevation of the still water is 2.567 m and the elevation of the bed is 1.758 m above the datum throughout the computational domain.

5.4.5. Case 22: 2-D dam break problem and flow over three islands with wetting and drying fronts and erodible bed

Case 22 is similar to Case 16, in that it involves a dam-break wave travelling over an initially dry floodplain with three humps (see e.g. Kawahara and Umetsu (1986), Liang and Bortwick (2008) and Brufau et al. (2002)), except that the bed is erodible. Although there are no published numerical predictions or analytical solutions for this problem, Case 22 is nevertheless useful for studying the performance of the model when dealing with more complicated shallow flow water-sediment-bed interactions. The initial values used for this test case are the following: g = 9.81 m/s^2; ρ_w = 1000 kg/m^3; ρ_s = 2000 kg/m^3; w_s = 0.1 m/s; M = 0.01 m/s; τ_c = 0.2 N/m^2; and c = 0 throughout the computational domain. The spatial steps are dx = 0.5 m and dy = 0.4 m. The computational domain is of length x_L = 75 m and width y_L = 30 m. The time step is dt = 0.001 s. The bed shear stress is calculated with the Manning coefficient set to n = 0.018. The dam is located at x = 16 m and retains water with initial free surface elevation η = 1.875 m. The initial bed elevation is z_b is given by

$$z_b(x,y) = \max[0,\quad 1-\frac{1}{8}\sqrt{(x-30)^2+(y-6)^2}\,,$$
$$1-\frac{1}{8}\sqrt{(x-30)^2+(y-24)^2}\,, \tag{5.5}$$
$$3-\frac{3}{10}\sqrt{(x-47.5)^2+(y-15)^2}\,].$$

The initial state at the instant the dam-break flow is released is the same as in Case 13, as shown in Figure 5.4. Figures 5.19 (a-e) show the free surface elevation 3-D plots and plan views at t = 5, 20, 40, 100 and 300 s (when steady state is reached). Mass conservation of the bed material and the liquid is checked, and found to hold, throughout the simulation.

The infinitesimally thin wall that represents the dam is removed at t = 0 s. The dam-break causes a bore to travel towards the three humps and flood the computational domain. The flow begins to erode the bed material and the humps. The processes of entrainment and deposition dictate the final equilibrium steady state condition. By t = 5 s (Figure 5.19 (a)), the initial wave has already reached the first two low humps and starts overtopping them, while some water penetrates between them or circulates around them, reaching the third higher hump and starting to ascending it. There is also an obvious reflection wave travelling upstream of each of the three humps. By t = 20 s (Figure 5.19 (b)), the water has overtopped completely the first two low humps, partially eroding them. Meanwhile, the water-species mixture (as the liquid now contains sediment eroded either from the bed or the humps) partly runs-up and over the higher third hump, and partly flows around it, before propagating towards the right hand side boundary of the computational domain. Reflected wave components can be seen travelling upstream, with wave-wave interactions evident due to multiple reflections by the humps or/and the lateral walls of the domain. By t = 40 s after the dam break (Figure 5.19 (c)), some water continues to run up the highest hump, while the remainder propagates around the hump. The two lower humps are still being eroded as the liquid-species mixture is draining down their slopes or flowing around them. Reflected

waves are evident travelling in all directions, owing to the complicated bed topography and the presence of other waves. At t = 100 s (Figure 5.19 (d)), the flood wave has already reached the right hand side end of the computational domain and been reflected by the solid wall boundary. This reflected wave travels upstream (towards the left hand side of the computational domain) and runs up the lee (right hand) side of the highest hump. Meanwhile, on the front face of the hump, the shoreline drops as the water level falls. The same occurs at the front and back of the lower humps. Furthermore, part of the peak of the highest hump has eroded causing its crest elevation to fall. By t = 300 s (Figure 5.19 (e)), the flow and bed morphodynamics have begun to settle to an equilibrium steady state. The top of the higher hump has eroded in a very complicated way, whereas the two smaller humps have similar shapes to each other (not very different from the situation at about t = 20 s). Specifically, both humps are eroded along their central line, with eroded sediment forming other small humps upstream, as a by-product of the interactions of reflected waves and bores driven by the dam break.

Throughout the simulation, repeated wave reflections occur at the solid lateral walls of the computational domain and the resulting flow disturbances interact with the bed and hump material, causing the free surface motions to become very complicated. It can be concluded that the numerical model properly simulates complicated wetting and drying processes combined with entrainment and deposition, which characterise numerous real flood events.

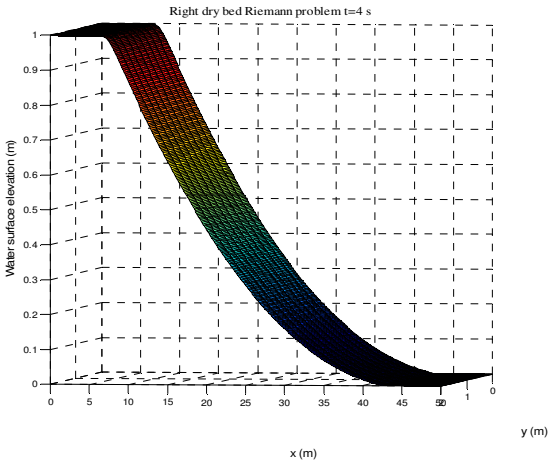
5.5. Concluding Remarks

The two-dimensional numerical solver of horizontal variable density shallow water equations has been validated for a variety of test cases and the numerical predictions compared to analytical solutions, benchmark test results and experimental data when

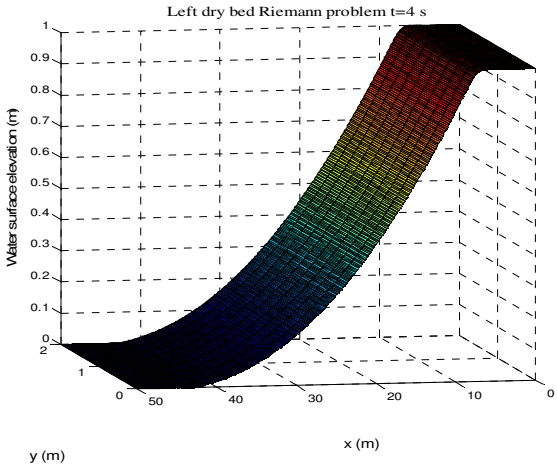
available. Grid convergence and mass conservation has been checked in each case. For the constant density cases considered, the predicted numerical results are in very satisfactory agreement with the alternative data used for comparison. For the variable density cases considered, the model responds correctly to the different initial conditions encountered. For cases involving steady state solutions, the model remains at equilibrium (as expected). The model has also been validated against symmetric problems.

Finally, the model has been tested for erodible bed problems. For pure deposition, pure erosion, and deposition and entrainment in a rectangular tank, the numerical results are in close agreement with analytical solutions. Consequently, it can be concluded that the model can successfully simulate entrainment and deposition of sediment in an erodible channel. For Case 22, no analytical solution or experimental data are available for comparison. Nevertheless, the numerical results appear reasonable, producing sensible hydrodynamic features, bed morphological changes, such as the erosion of the humps and the complicated pattern of reflected waves and bores.

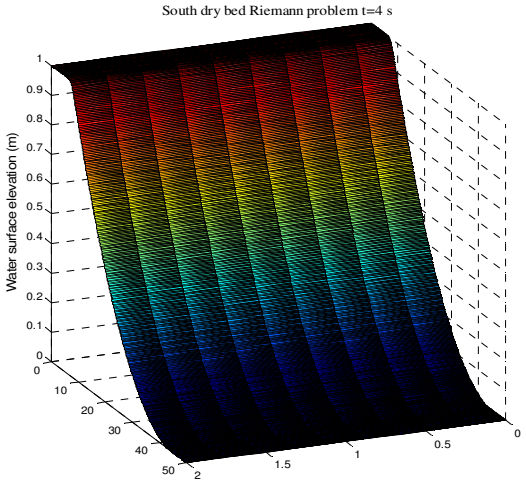
(a)



(b)



(c)



(d)

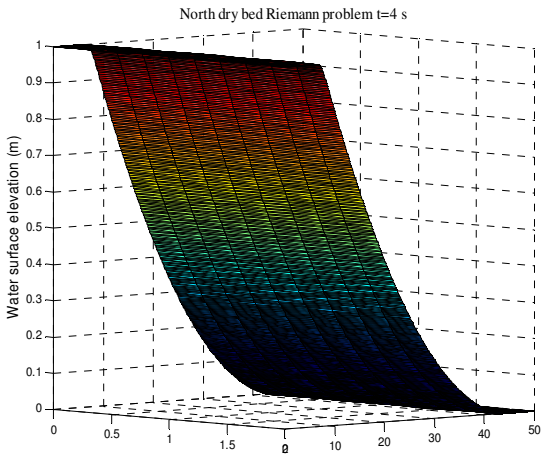
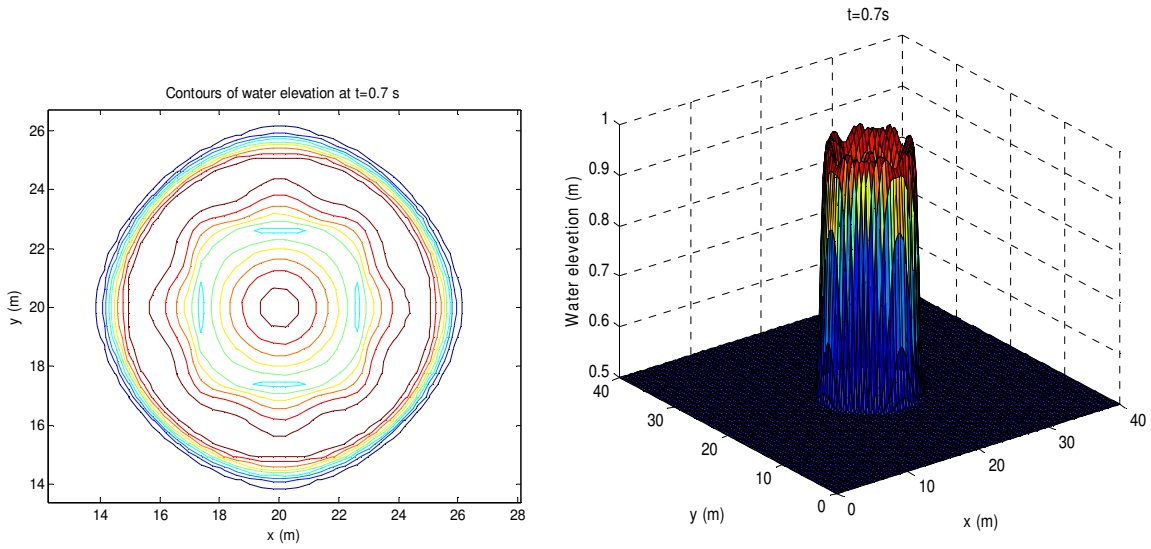


Fig. 5.1 Case 14. 2-D numerical model: predicted water surface elevations at t = 4 s, for the following dry bed Riemann problems: (a) eastward, (b) westward, (c) northward, and (d) southward propagating dam-break.

(a) (b)



(c) (d)

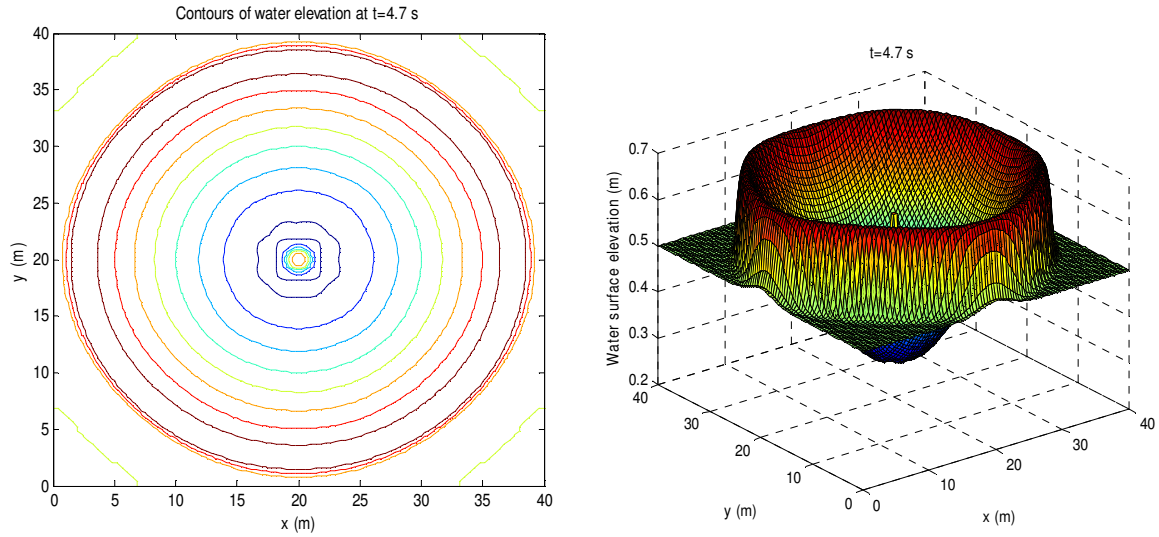
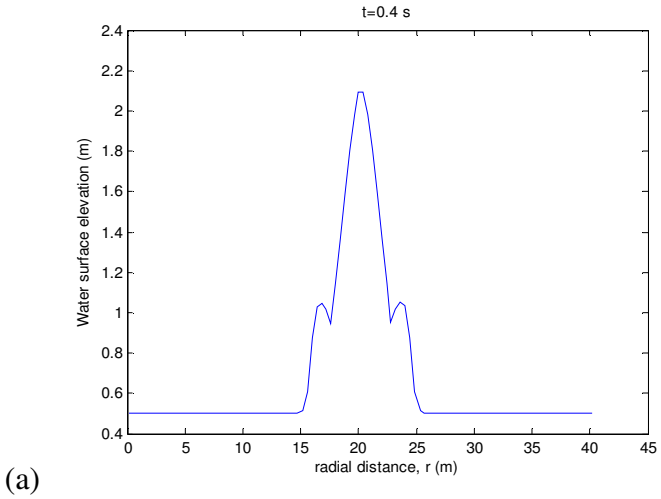
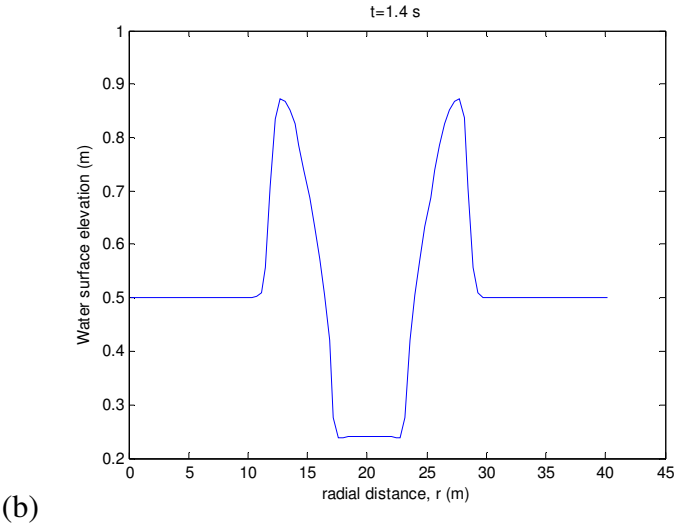


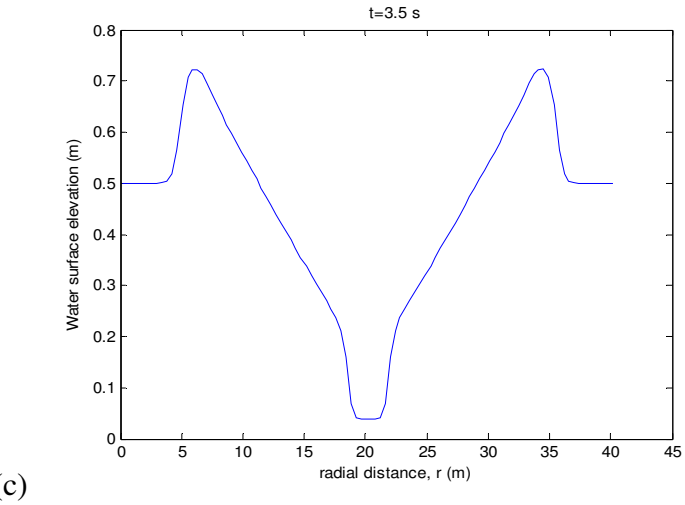
Fig. 5.2 Case 15. Circular dam-break problem. (a) Free-surface contours and (b) free surface visualisation at t = 0.7 s, (c) free-surface contours and (d) free surface visualisation at t = 4.7 s.



(a)



(b)



(c)

Fig. 5.3 Case 15. Circular dam-break problem. Free-surface elevation profiles at (a) $t = 0.4$ s (b) $t = 1.4$ s, and (c) $t = 3.5$ s.

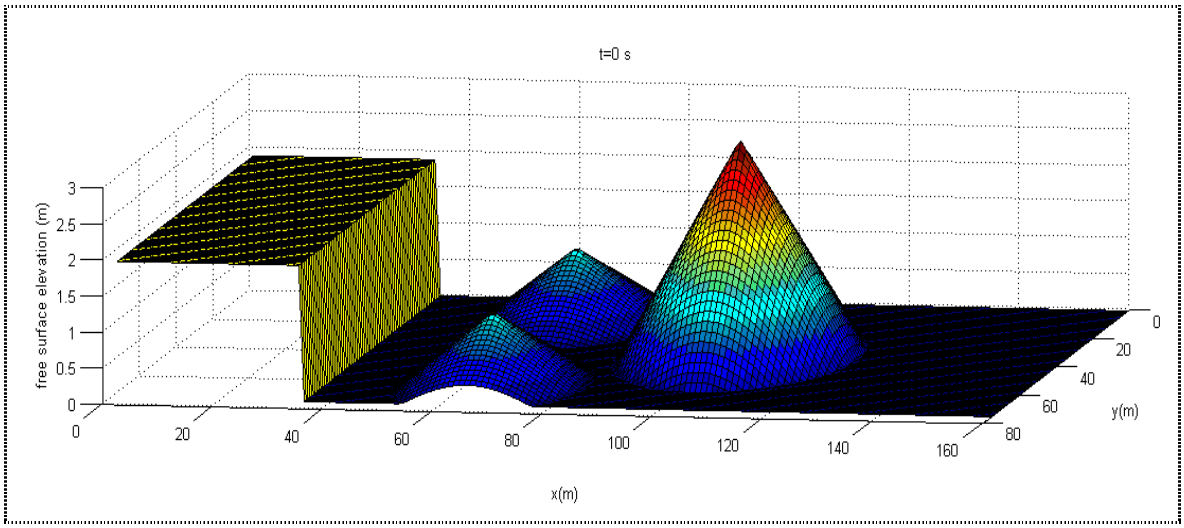
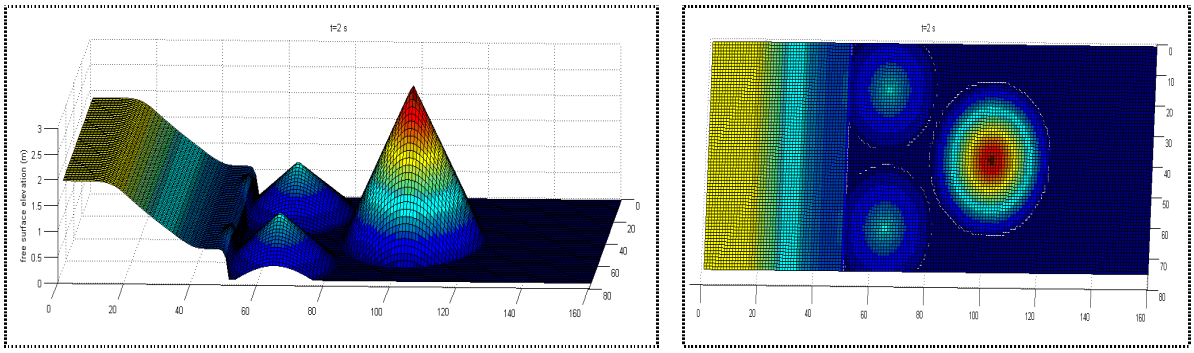
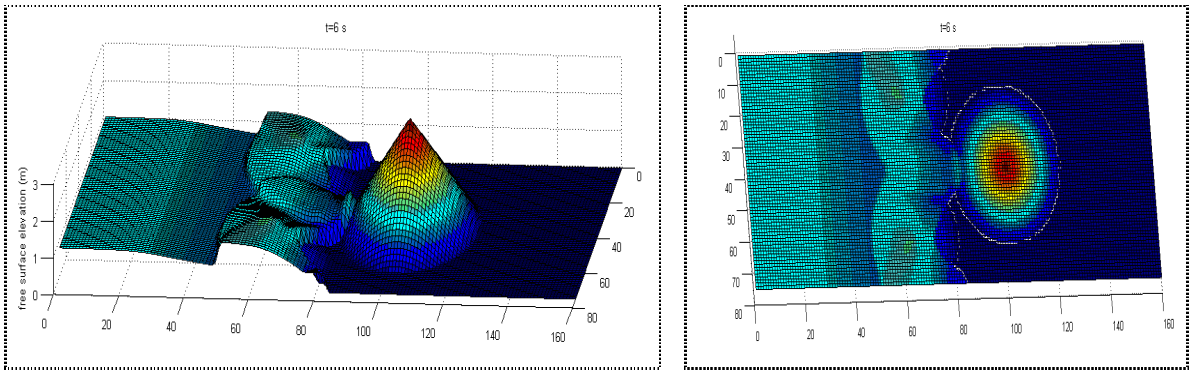


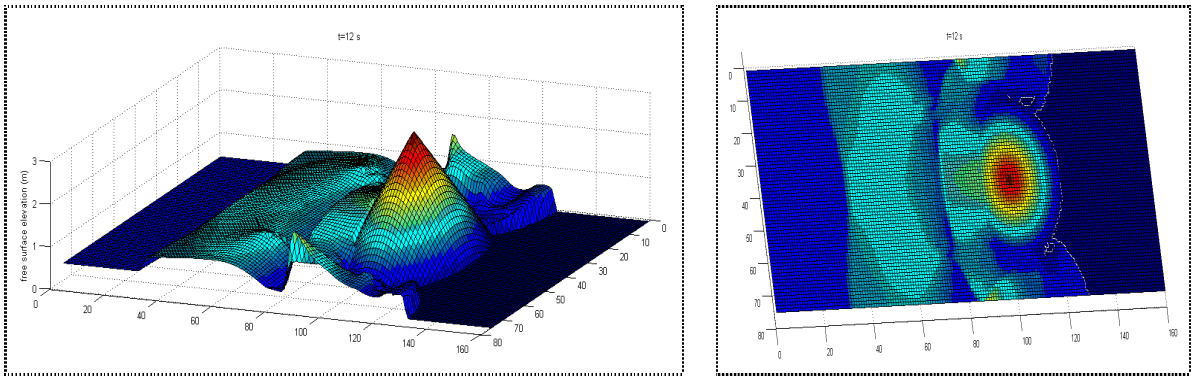
Fig. 5.4 Case 16. 2-D dam-break flow over three islands with wetting and drying fronts. – Initial state.



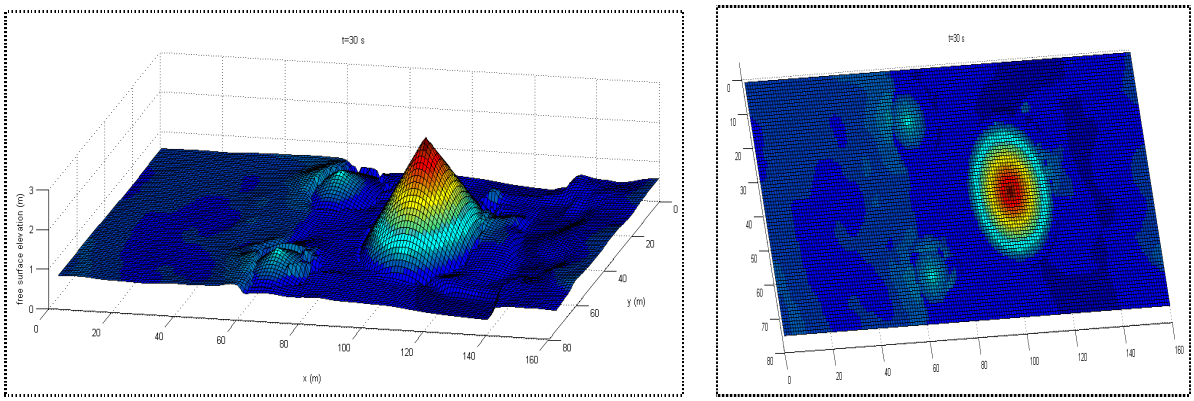
(a)



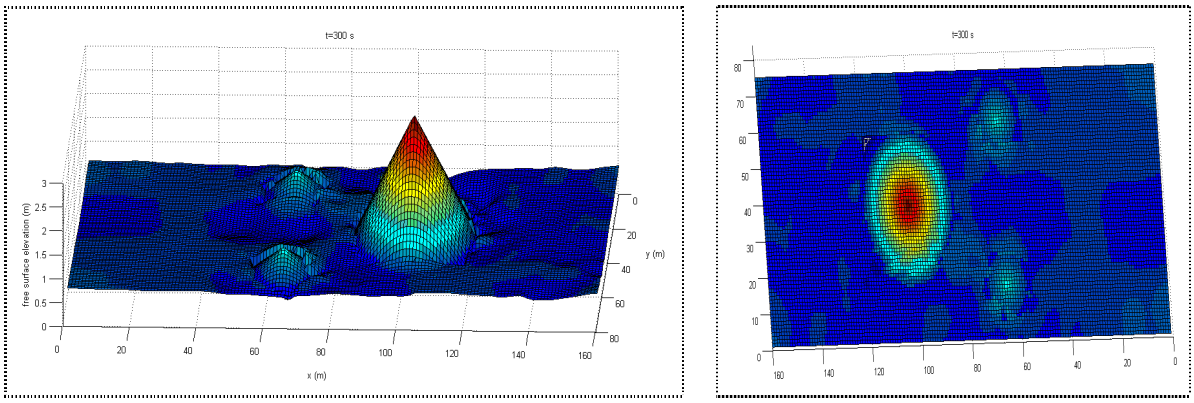
(b)



(c)

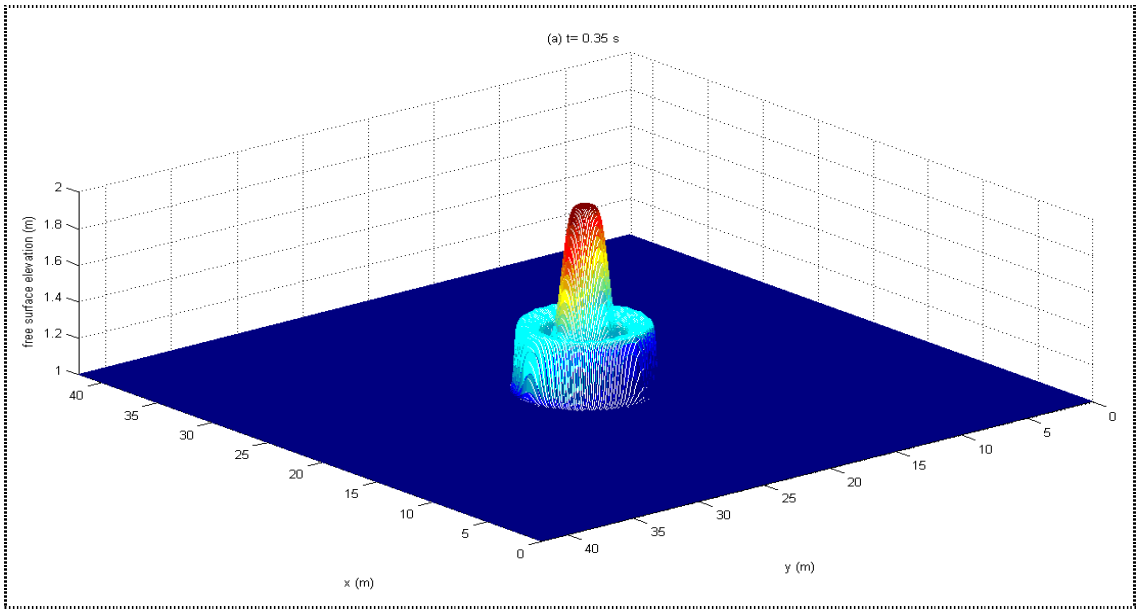


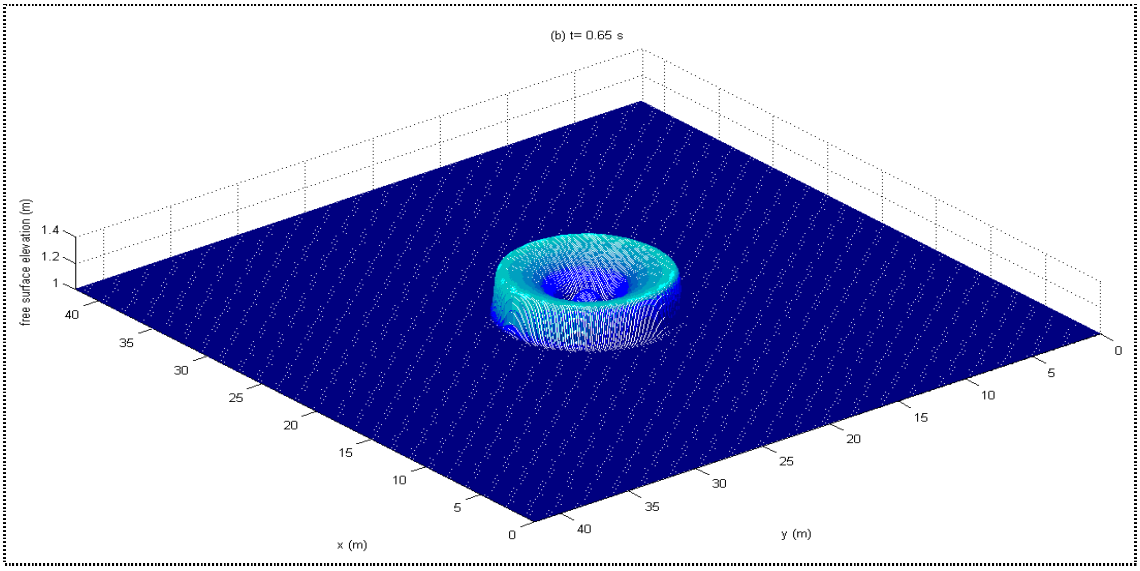
(d)

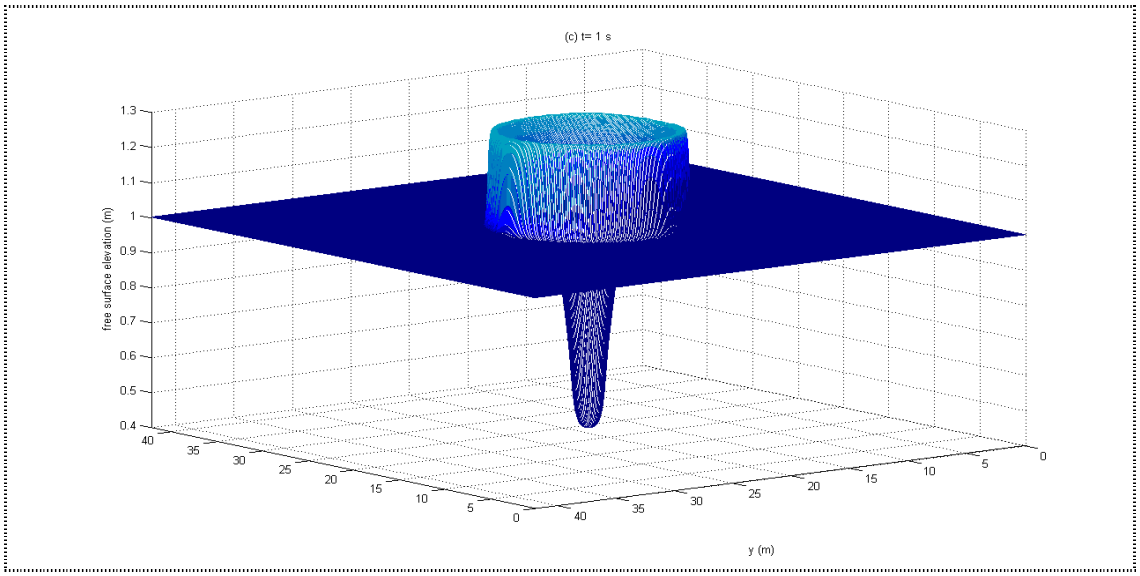


(e)

Fig. 5.5 Case 16. 2-D dam-break flow over three islands with wetting and drying – Free surface elevation visualisations and plan views for (a) t = 2 s, (b) t = 6 s, (c) t = 12 s, (d) t = 30 s and (e) t = 300 s.


(a) t= 0.35 s
free surface elevation (m)
x (m)
y (m)


(b) t= 0.65 s
free surface elevation (m)
x (m)
y (m)


(c) t= 1 s
free surface elevation (m)
y (m)

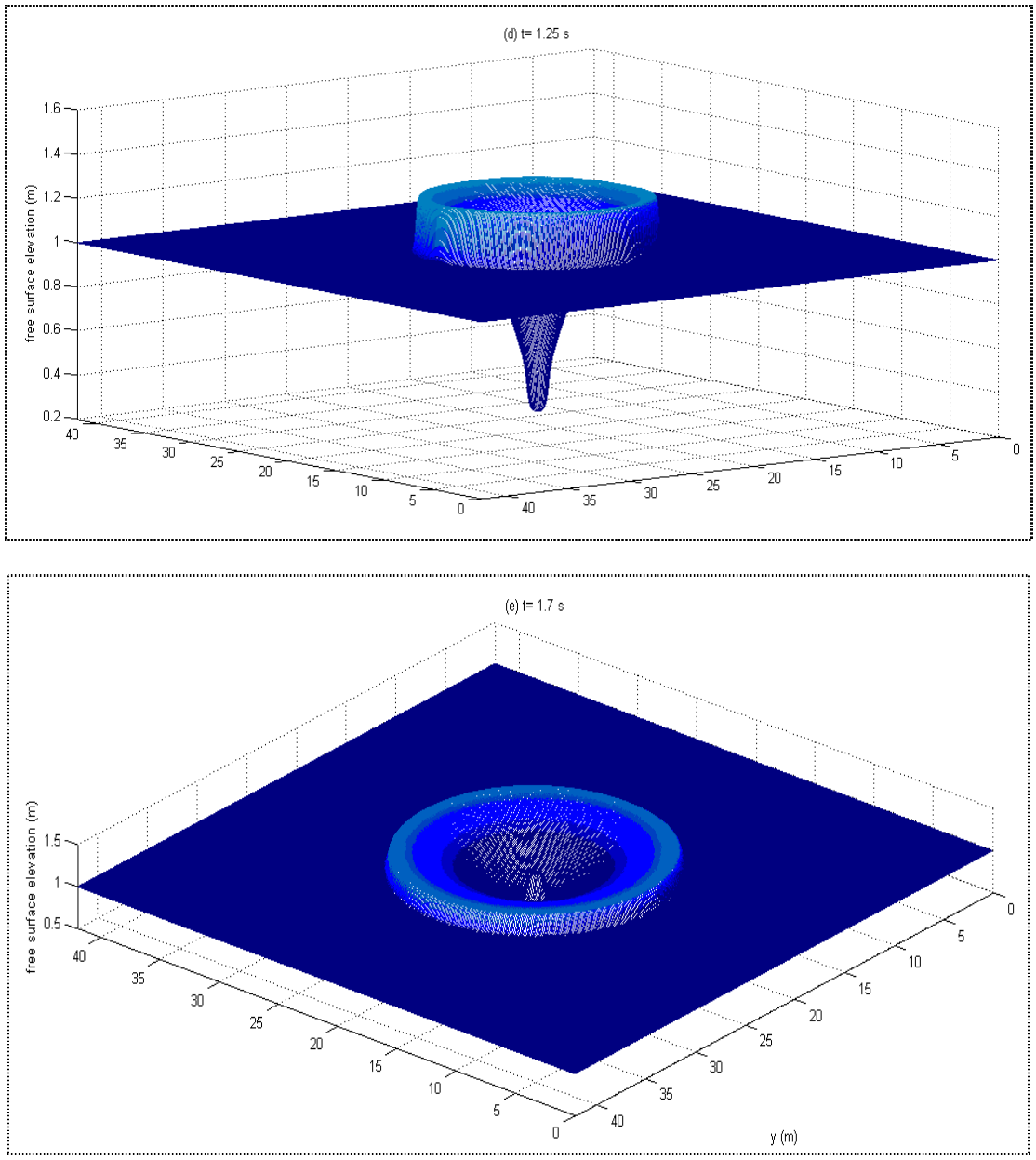


Fig. 5.6 Case 17.1. Variable density circular dam break, ρ_{in} = 1000 kg/m^3: Free surface elevation visualisations at (a) t = 0.35 s, (b) t = 0.65 s, (c) t = 1 s, (d) t = 1.25 s and (e) t = 1.7 s.

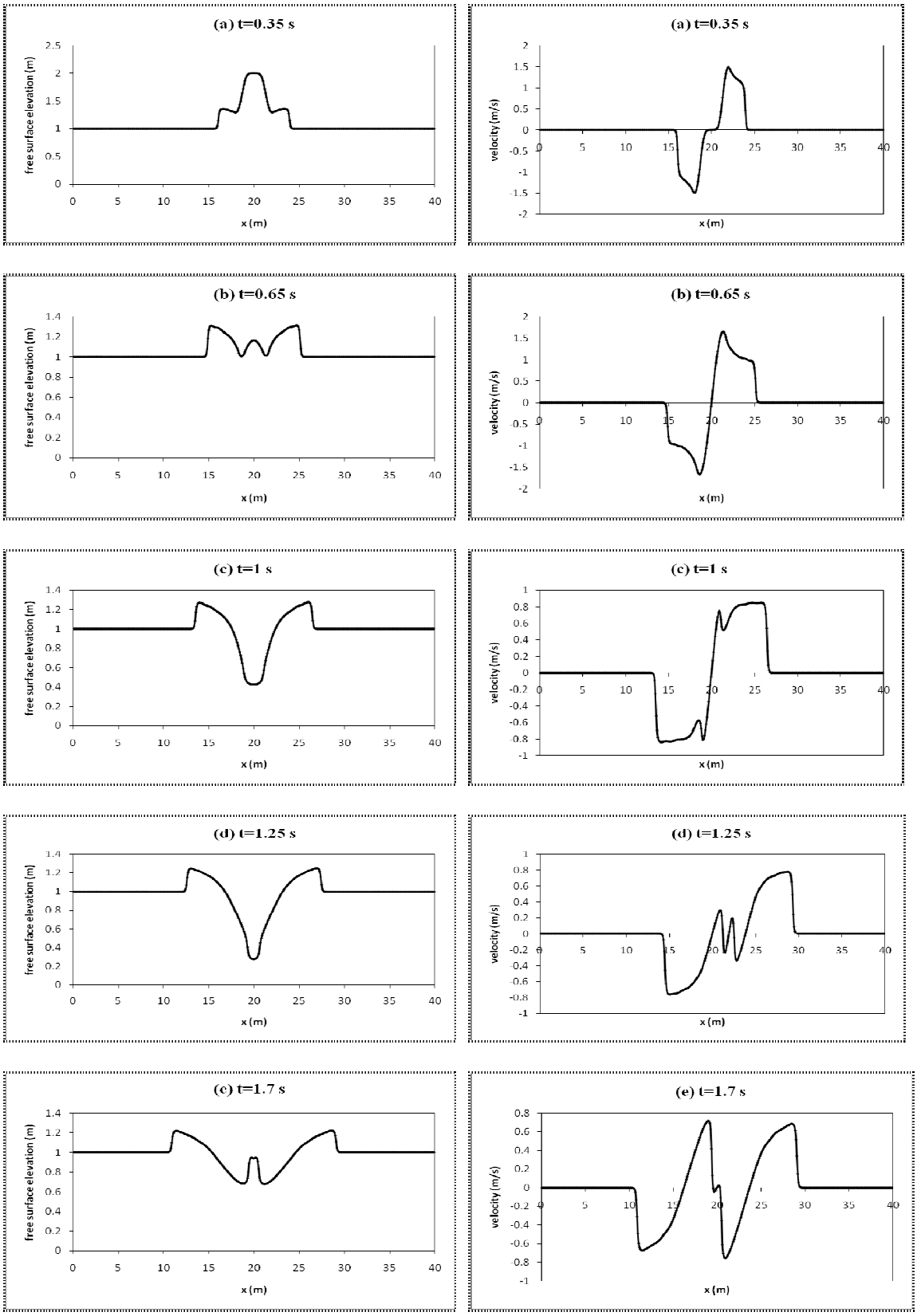


Fig. 5.7 Case 17.1. Variable density circular dam break, ρ_{in} = 1000 kg/m^3: Predicted free surface elevation and the depth averaged velocity profiles at (a) t = 0.35 s, (b) t = 0.65 s, (c) t = 1 s, (d) t = 1.25 s and (e) t = 1.7 s.

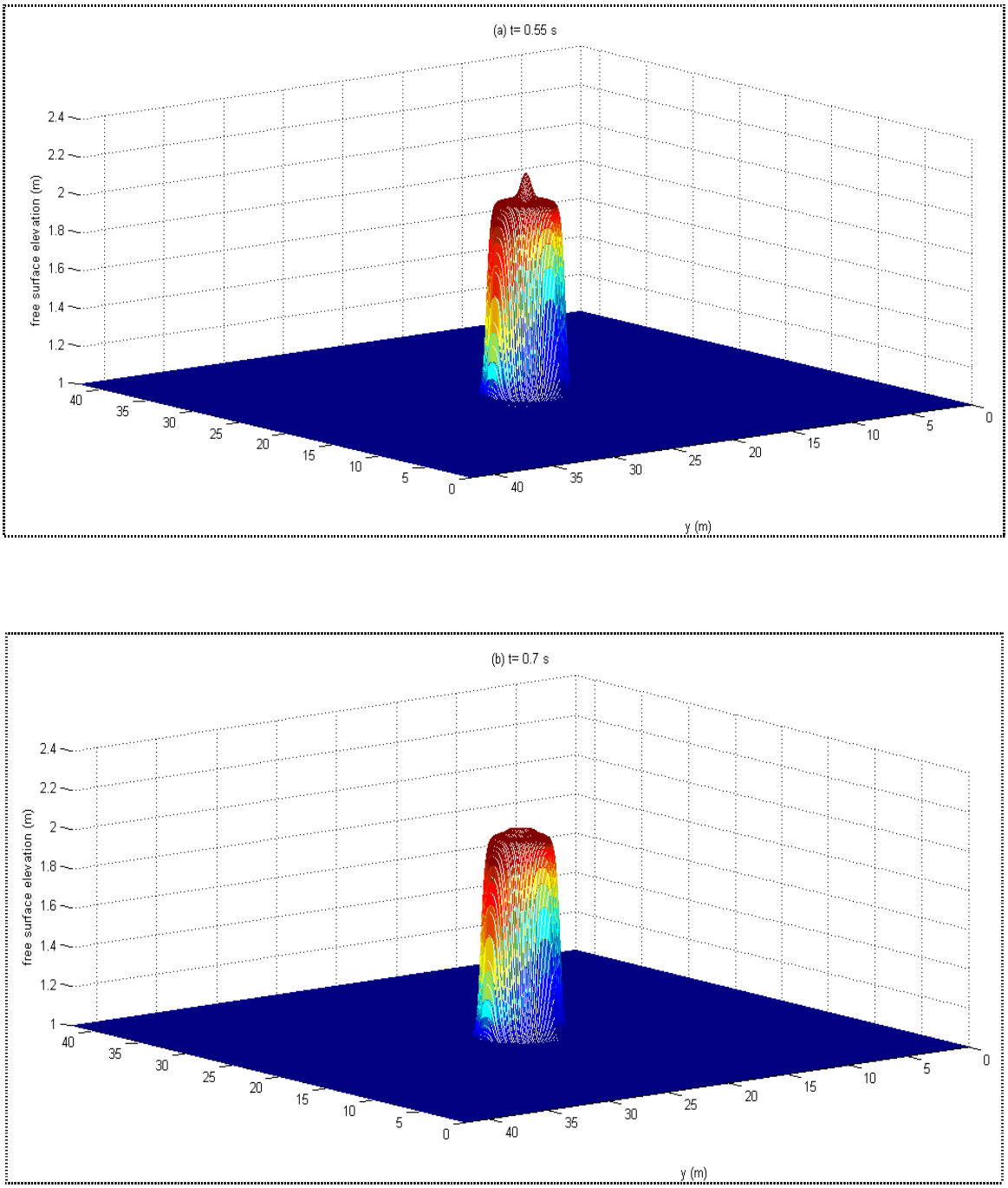


Fig. 5.8. Case 17.2. Variable density circular dam break, ρ_{in} = 250 kg/m^3: Free surface elevation visualisations at (a) t = 0.55 s and (b) t = 0.7 s.

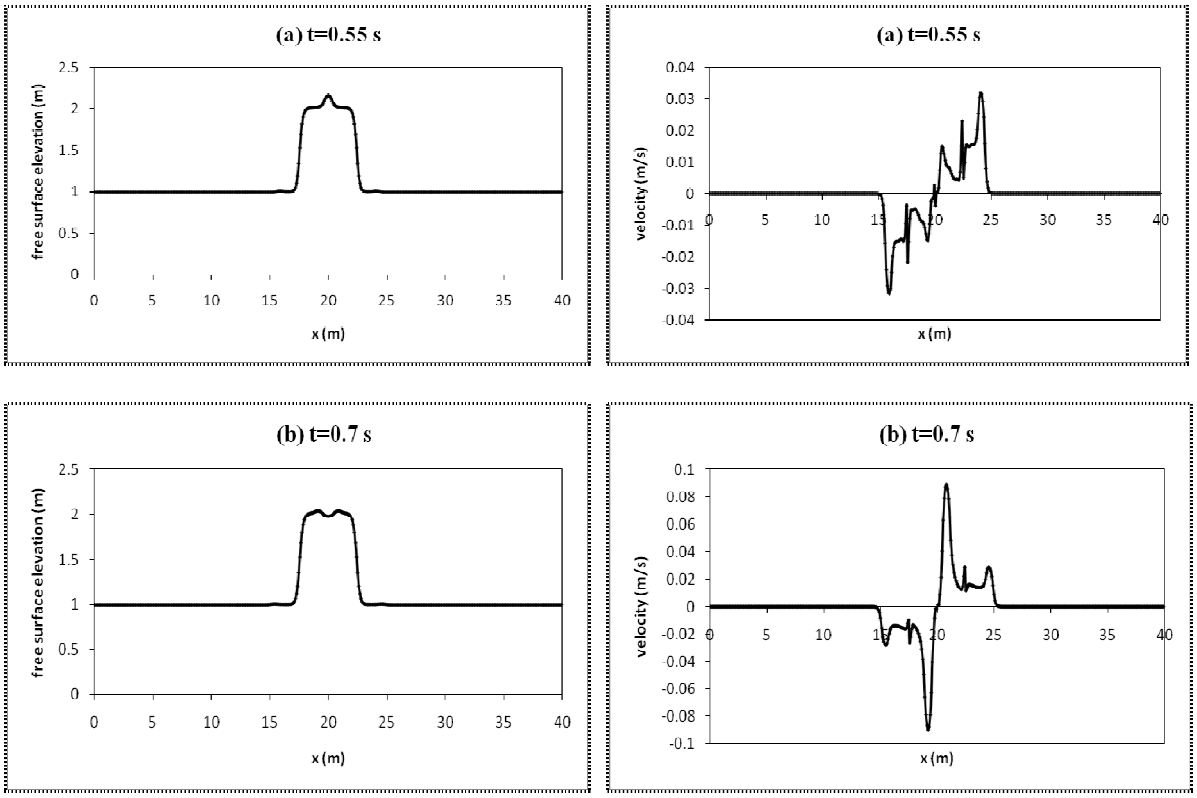
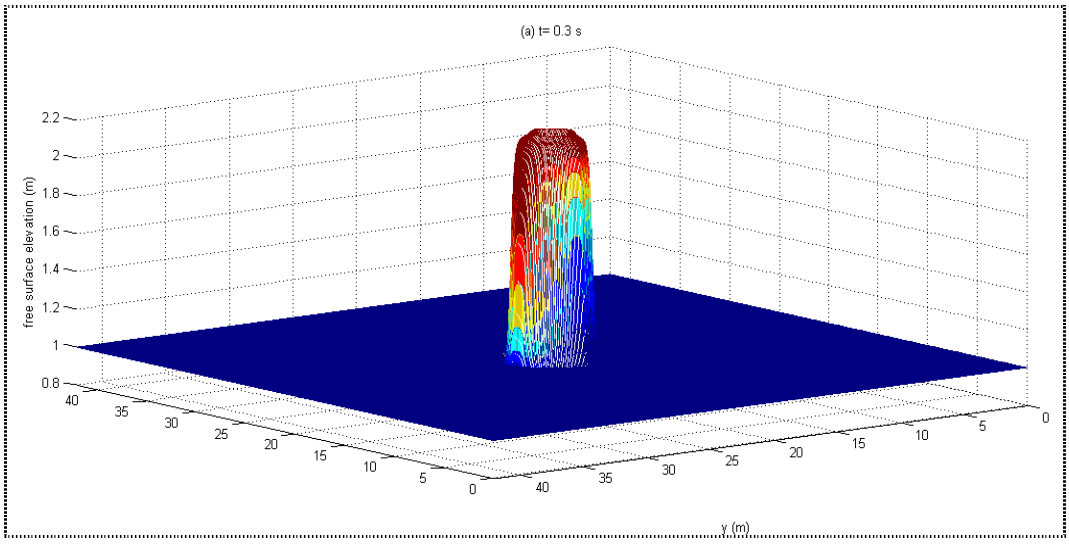
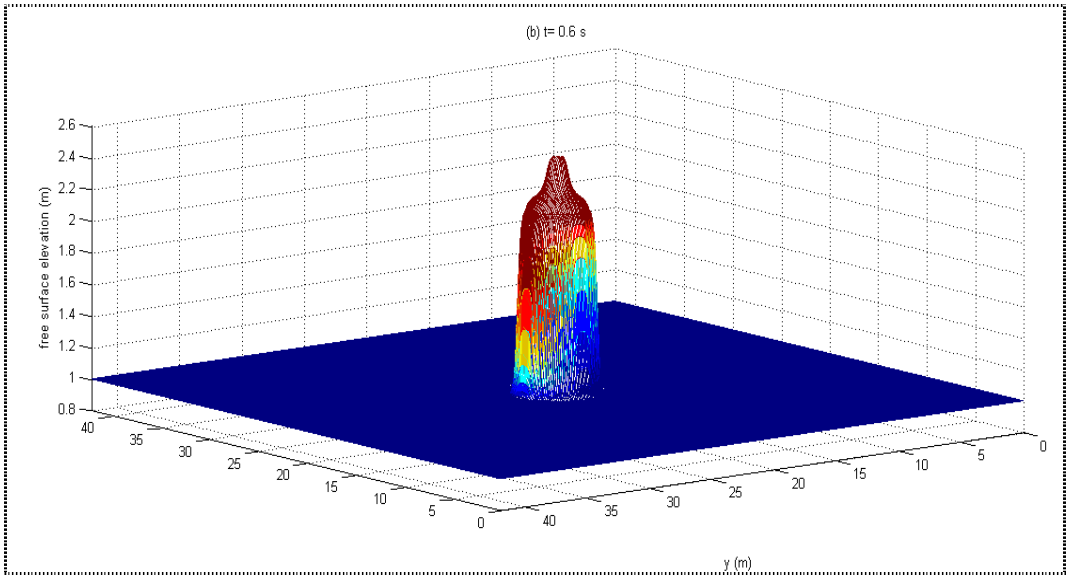
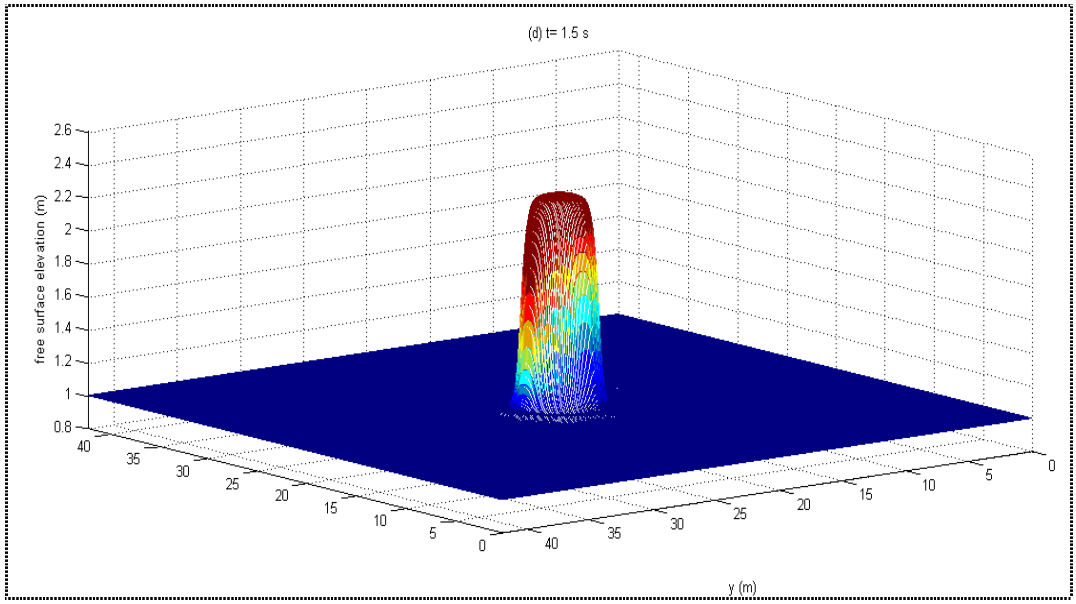


Fig. 5.9 Case 17.2. Variable density circular dam break, ρ_{in} = 250 kg/m^3: Predicted free surface elevation and depth averaged velocity profiles at (a) t = 0.55 s and (b) t = 1.7 s.


(a) t= 0.3 s
free surface elevation (m)
2.2
2
1.8
1.6
1.4
1.2
1
0.8
40 35 30 25 20 15 10 5 0
40 35 30 25 20 15 10 5 0
y (m)


(b) t= 0.6 s
free surface elevation (m)
2.6
2.4
2.2
2
1.8
1.6
1.4
1.2
1
0.8
40 35 30 25 20 15 10 5 0
40 35 30 25 20 15 10 5 0
y (m)


(d) t= 1.5 s
free surface elevation (m)
2.6
2.4
2.2
2
1.8
1.6
1.4
1.2
1
0.8
40 35 30 25 20 15 10 5 0
40 35 30 25 20 15 10 5 0
y (m)

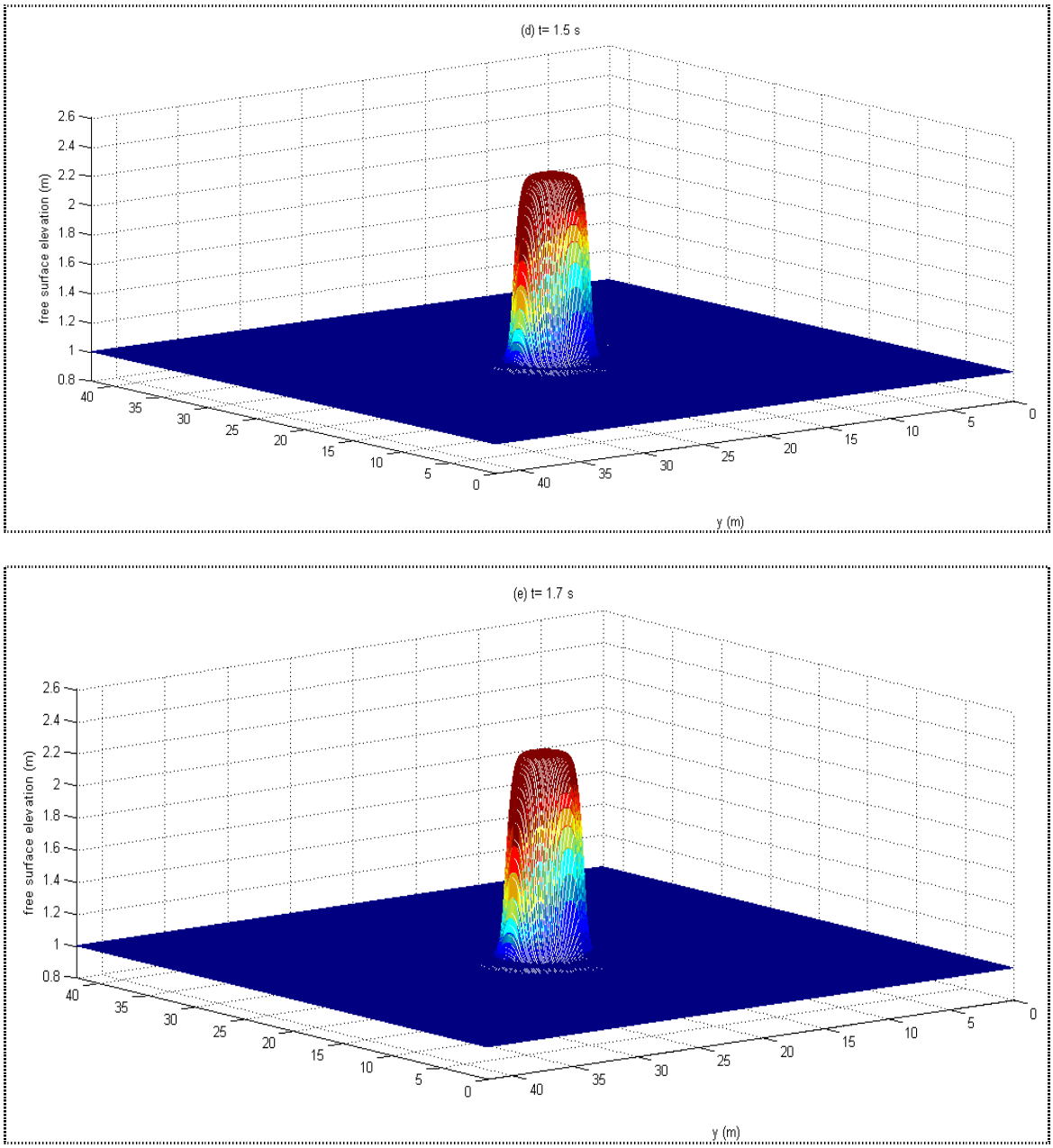


Fig. 5.10 Case 17.3. Variable density circular dam break, ρ_{in} = 200 kg/m^3: Free surface elevation visualisations at (a) t = 0.3 s, (b) t = 0.6 s, (c) t = 1.05 s, (d) t = 1.5 s and (e) t = 1.7 s.

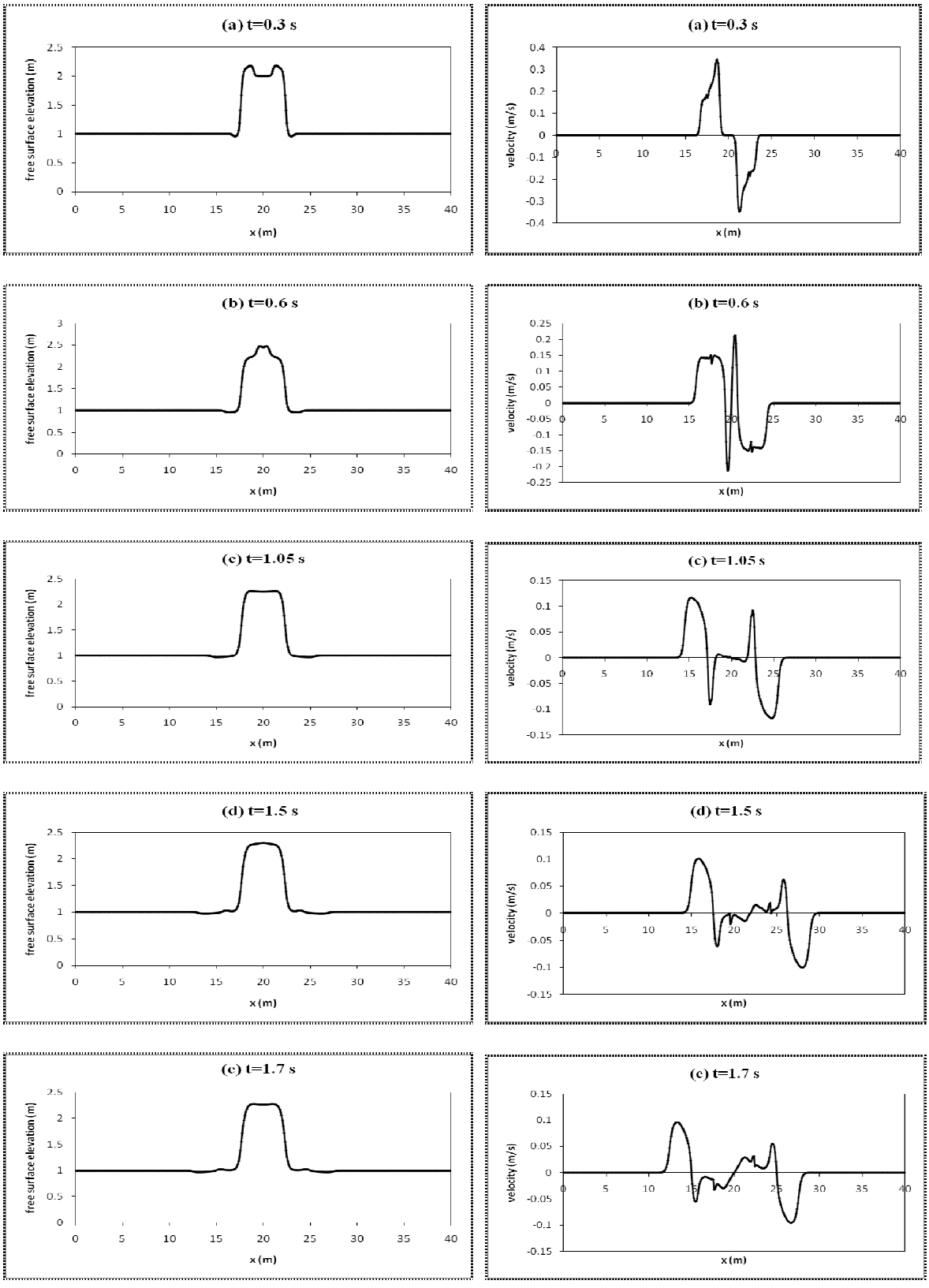
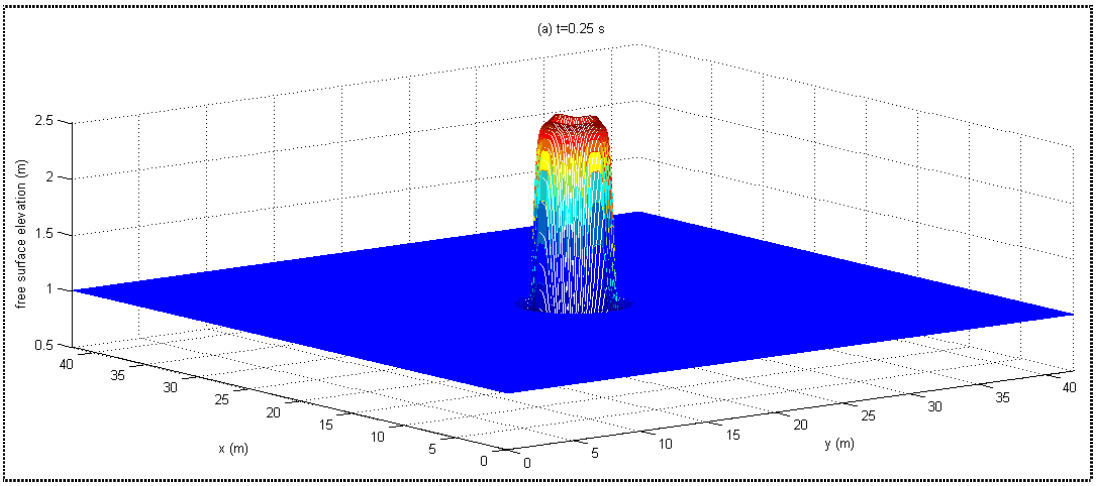
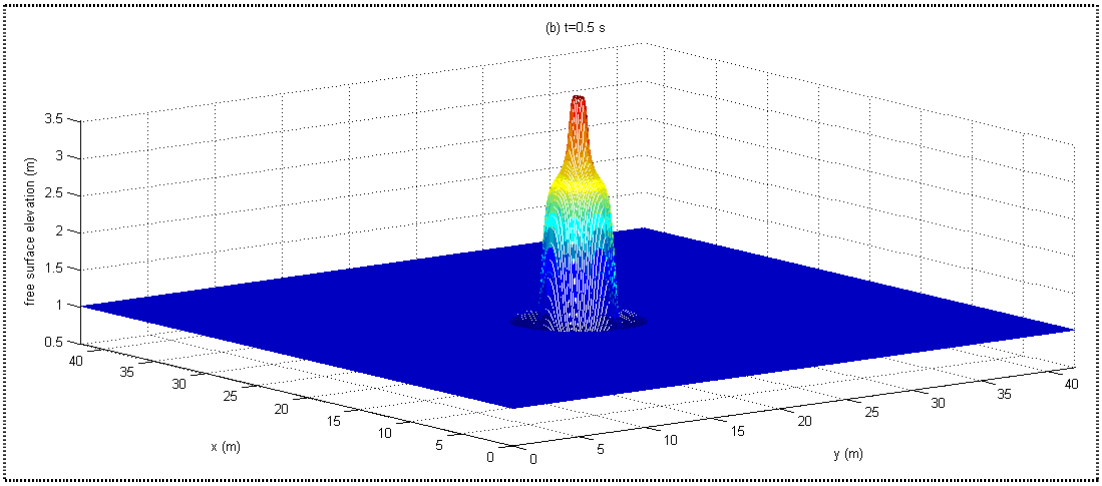
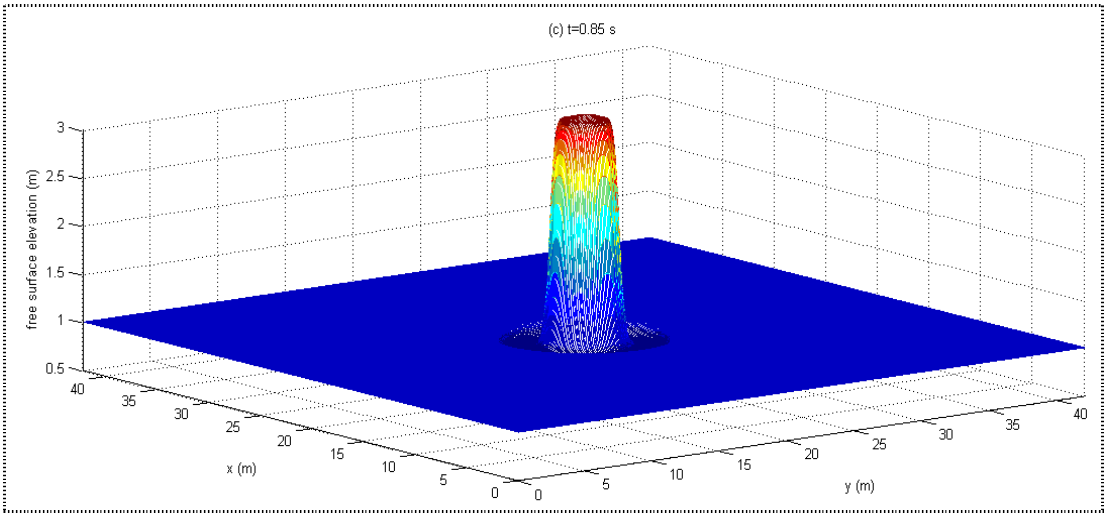


Fig. 5.11 Case 17.3. Variable density circular dam break, ρ_{in} = 200 kg/m^3: Predicted free surface elevation and depth averaged velocity profiles at (a) t = 0.3 s, (b) t = 0.6 s, (c) t = 1.05 s, (d) t = 1.5 s and (e) t = 1.7 s.


(a) t=0.25 s
free surface elevation (m)
2.5
2
1.5
1
0.5
40
35
30
25
20
15
10
5
0
x (m)
0
5
10
15
20
25
30
35
40
y (m)


(b) t=0.5 s
free surface elevation (m)
3.5
3
2.5
2
1.5
1
0.5
40
35
30
25
20
15
10
5
0
x (m)
0
5
10
15
20
25
30
35
40
y (m)


(c) t=0.85 s
free surface elevation (m)
3
2.5
2
1.5
1
0.5
40
35
30
25
20
15
10
5
0
x (m)
0
5
10
15
20
25
30
35
40
y (m)

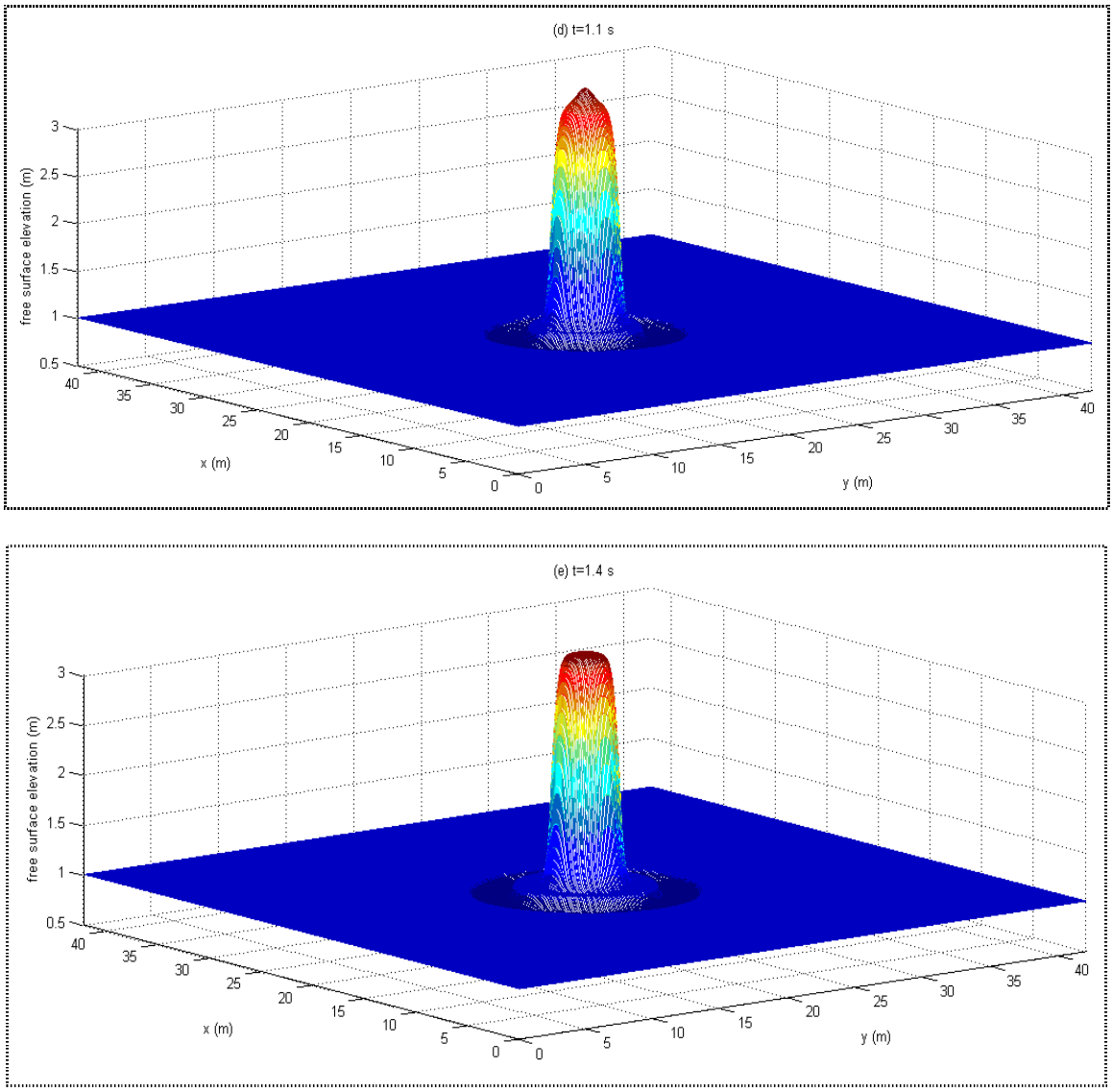


Fig. 5.12 Case 17.4. Variable density circular dam break, ρ_{in} = 100 kg/m^3: Free surface elevation visualisations at (a) t = 0.25 s, (b) t = 0.5 s, (c) t = 0.85 s, (d) t = 1.1 s and (e) t = 1.4 s.

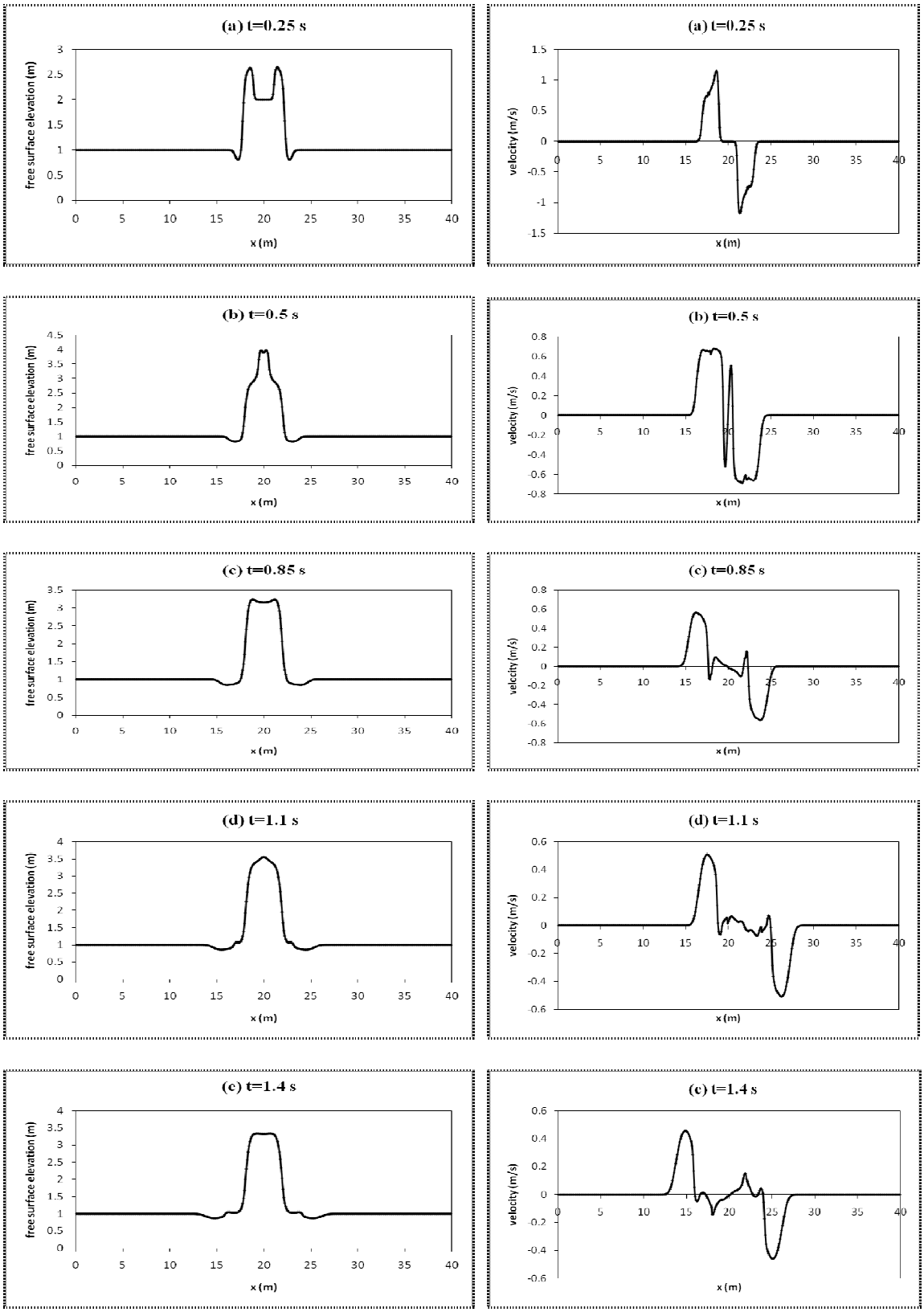


Fig. 5.13 Case 17.4. Variable density circular dam break, (ρ_{in} = 100 kg/m^3): Predicted free surface elevation and depth averaged velocity profiles at (a) t = 0.25 s, (b) t = 0.5 s, (c) t = 0.85 s, (d) t = 1.1 s and (e) t = 1.4 s

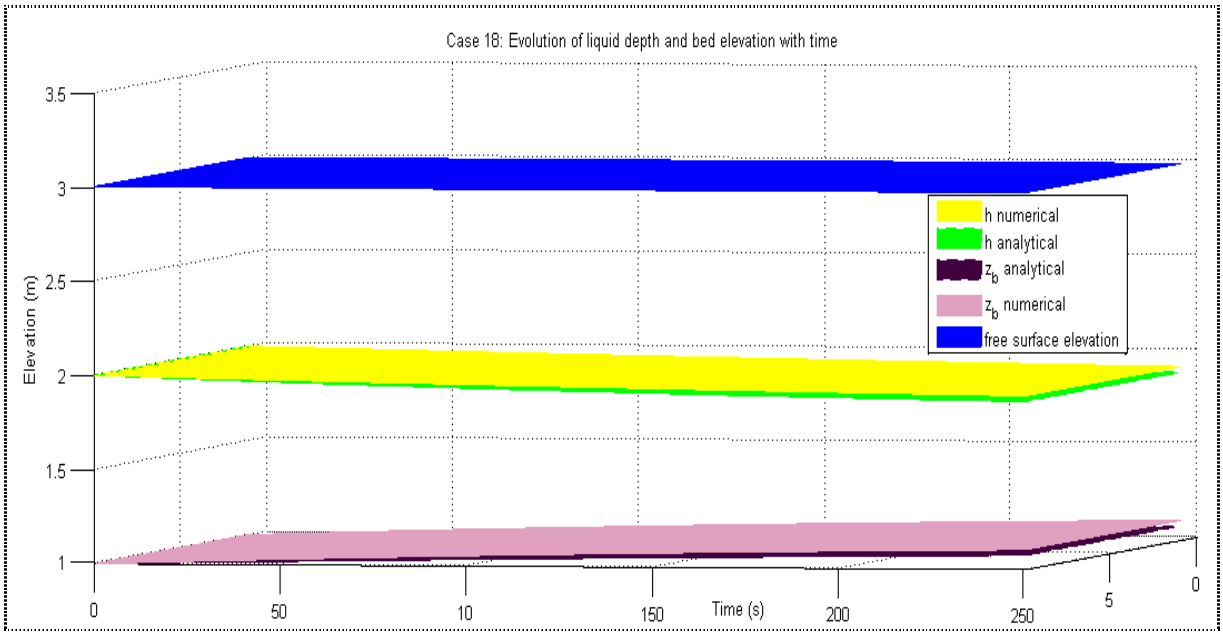


Fig. 5.14 Case 18. Deposition of dilute suspended sediment in a flat-bottomed 2-D tank with intense mixing but no net flow and no entrainment of sediment.

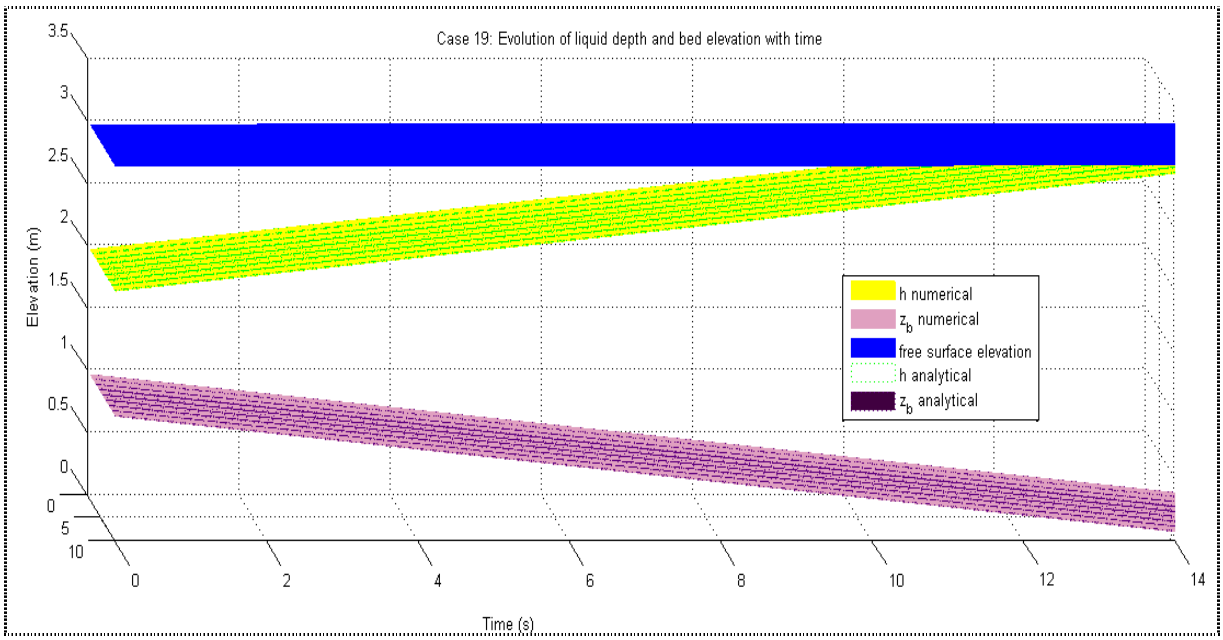


Fig. 5.15 Case 19. Entrainment of dilute suspended sediment in a flat-bottomed 2-D tank with intense mixing but no net flow and no deposition of sediment.

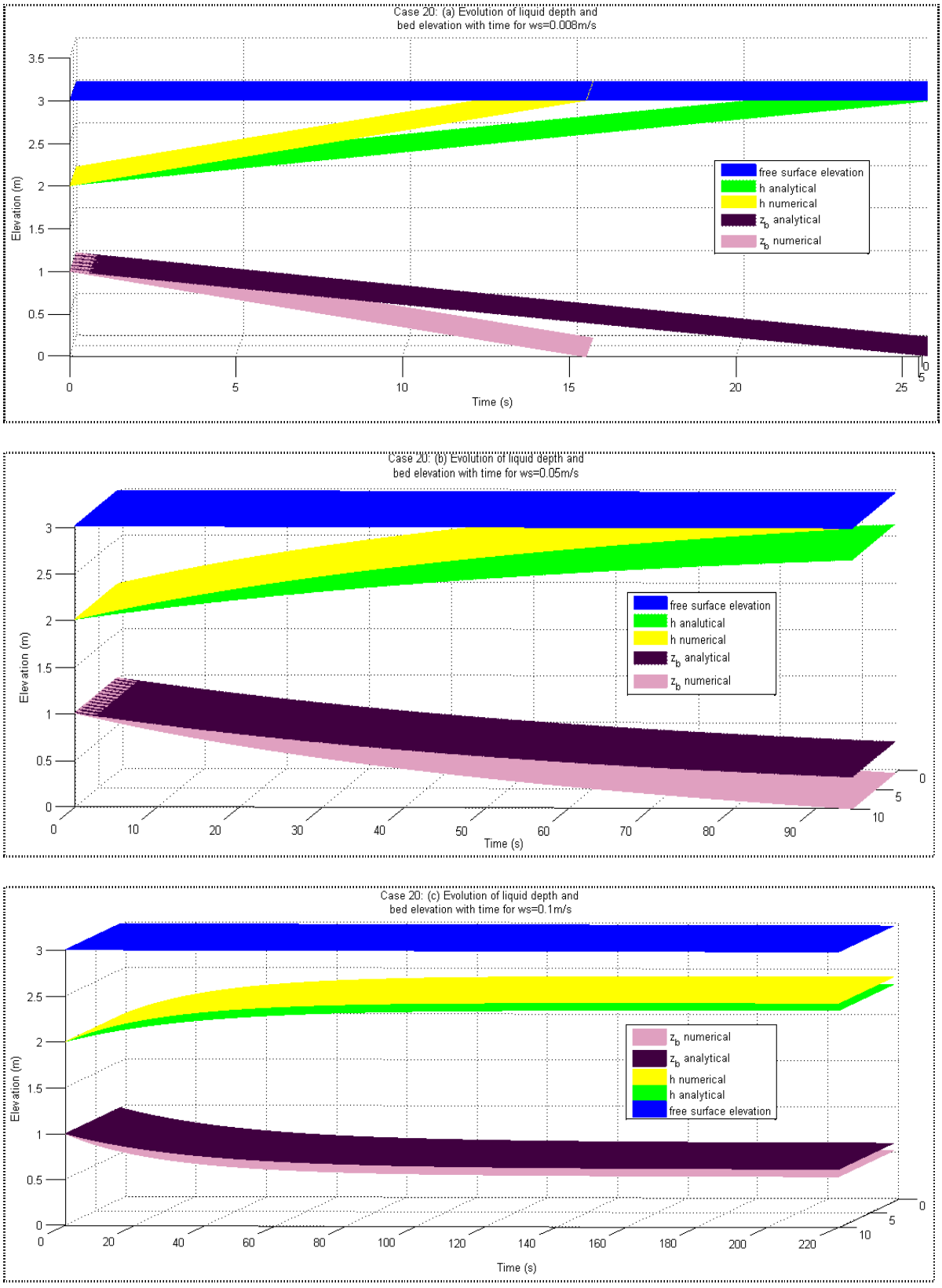
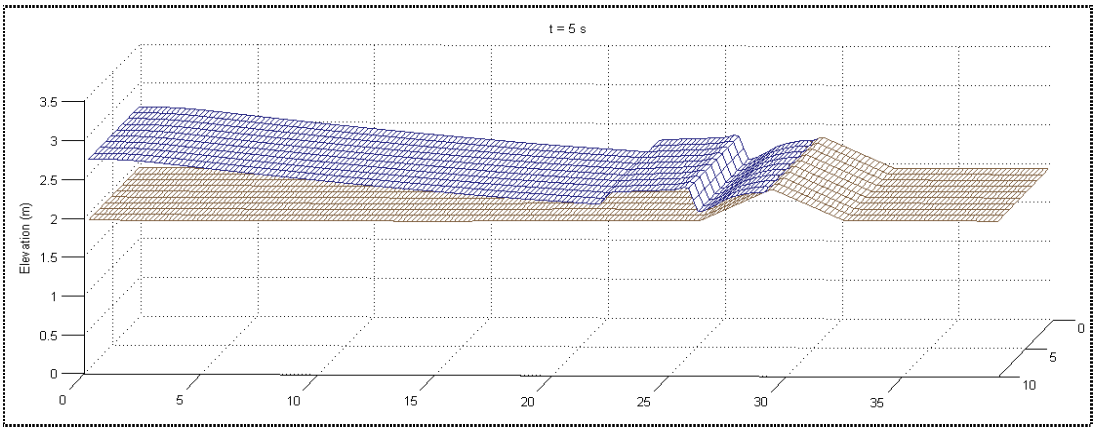
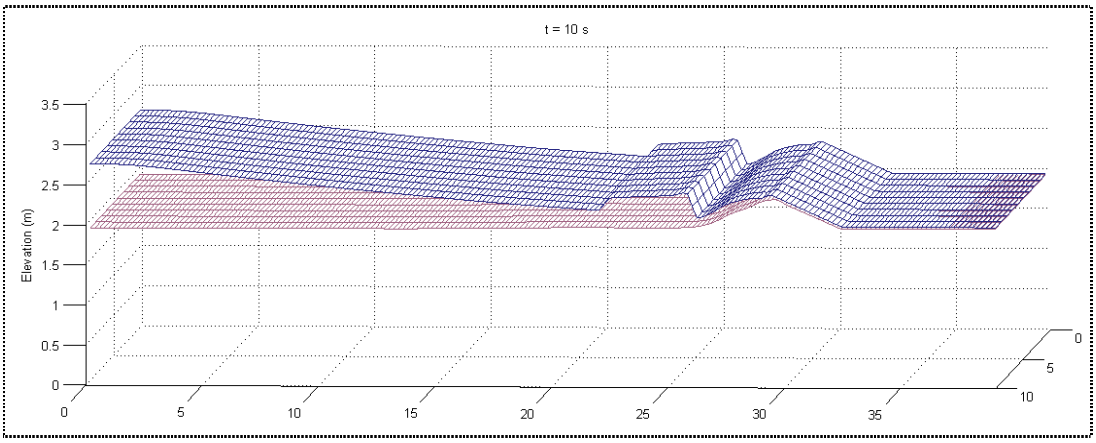
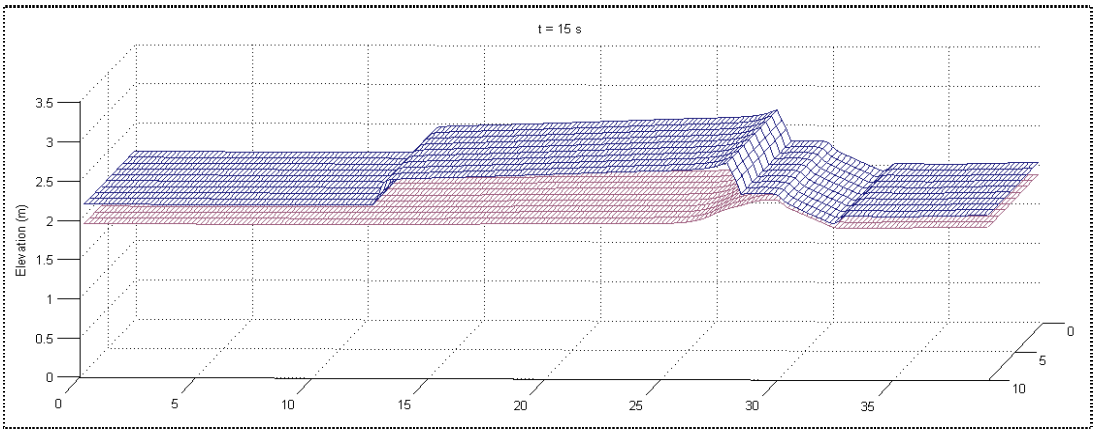
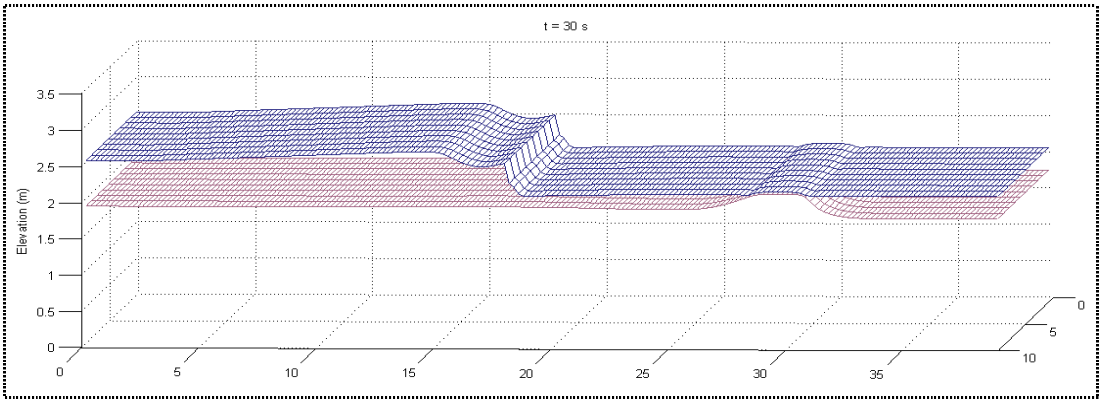


Fig. 5.16 Case 20. Simultaneous deposition and constant entrainment of dilute suspended sediment in a flat-bottomed 2-D tank with intense mixing but no net flow.


t = 5 s
Elevation (m)
3.5
3
2.5
2
1.5
1
0.5
0
0
5
10
15
20
25
30
35
0
5
10


t = 10 s
Elevation (m)
3.5
3
2.5
2
1.5
1
0.5
0
0
5
10
15
20
25
30
35
0
5
10


t = 15 s
Elevation (m)
3.5
3
2.5
2
1.5
1
0.5
0
0
5
10
15
20
25
30
35
0
5
10


t = 30 s
Elevation (m)
3.5
3
2.5
2
1.5
1
0.5
0
0
5
10
15
20
25
30
35
0
5
10

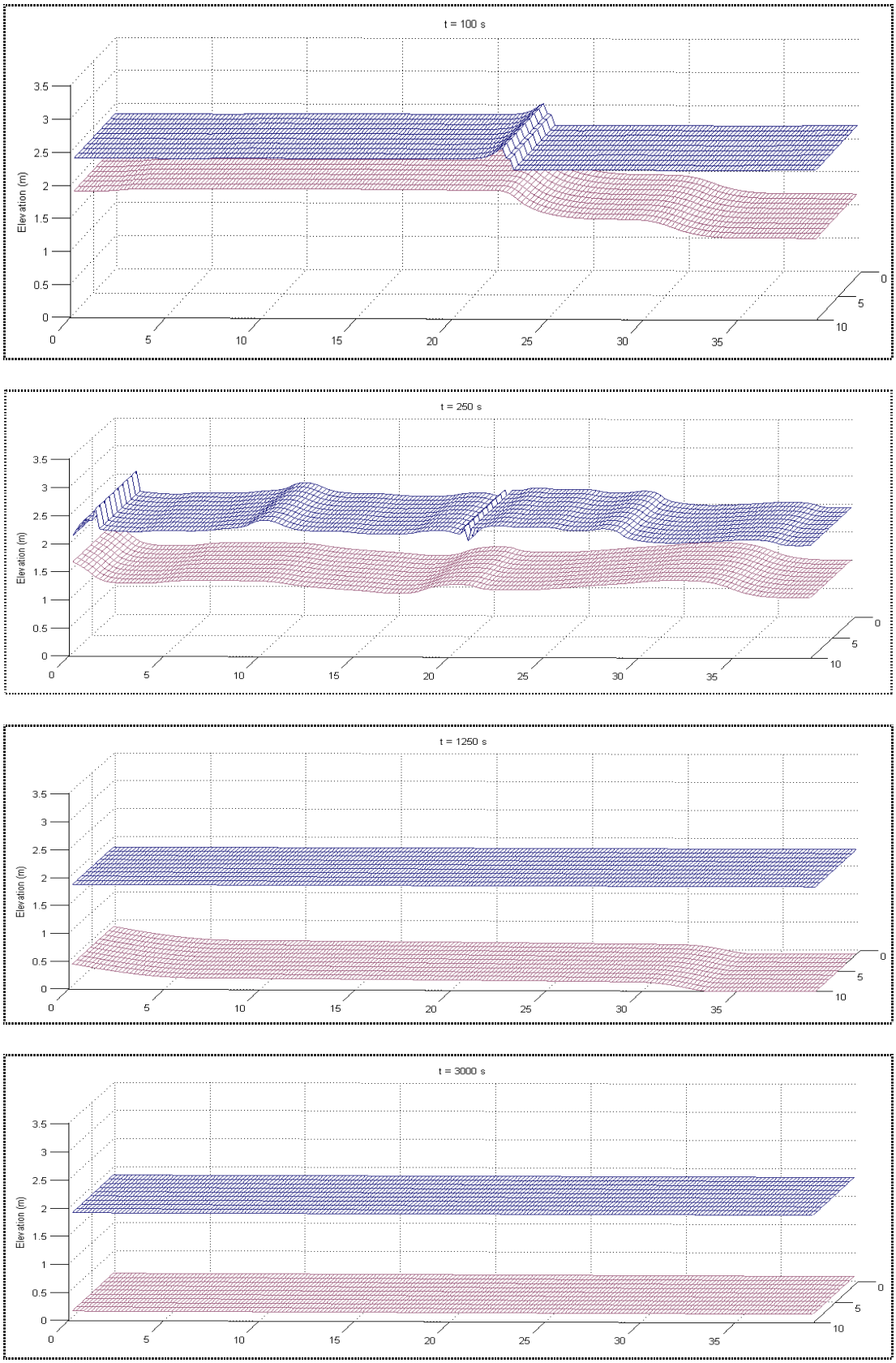
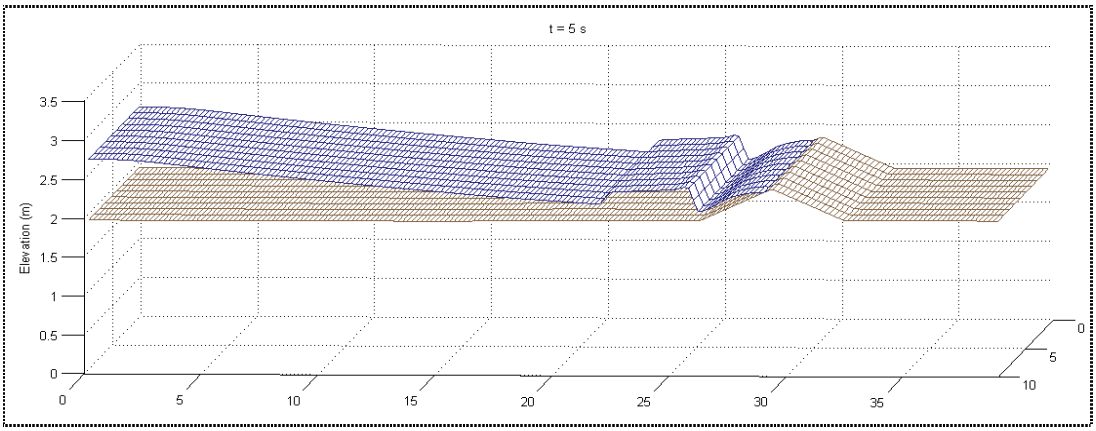
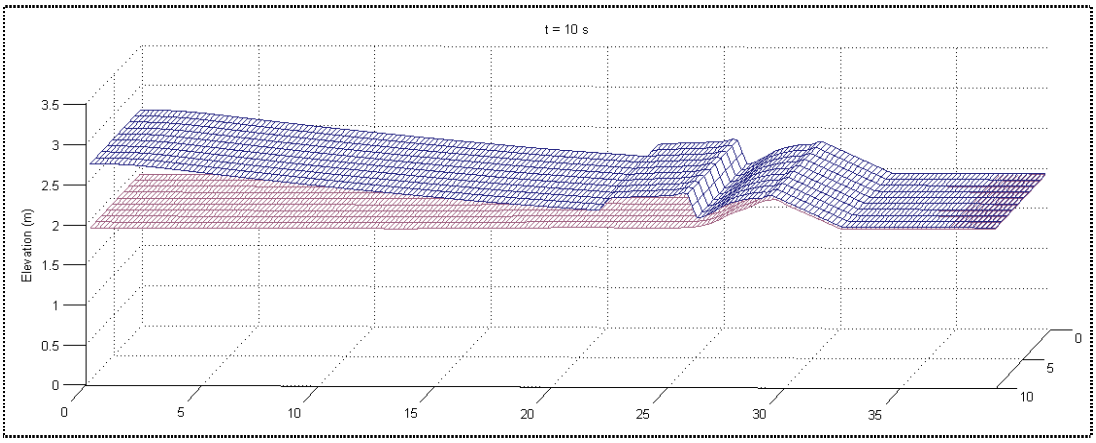
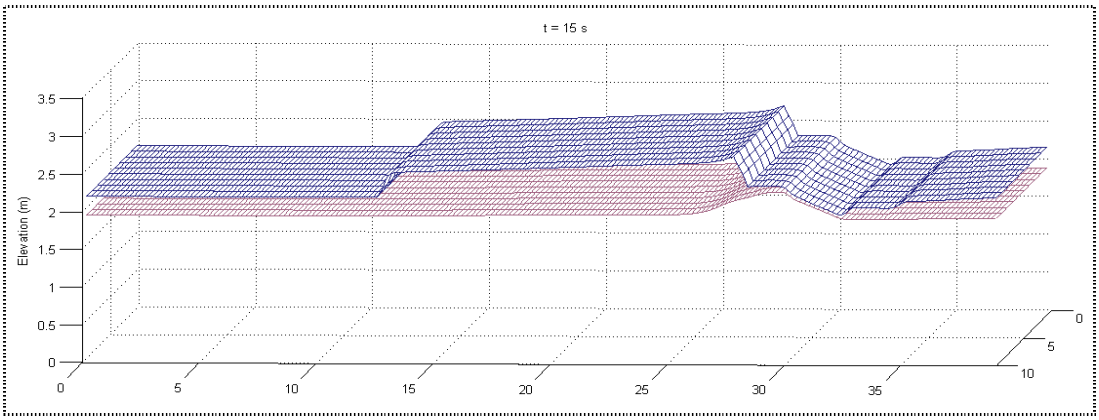
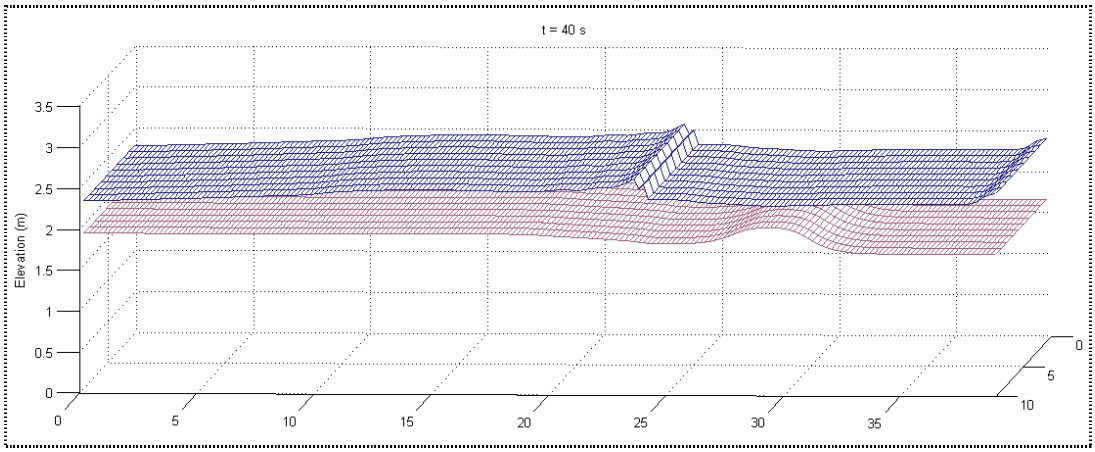


Fig. 5.17 Case 21.1. 2-D dam-break flow over a triangular obstacle with wetting and drying fronts and erodible bed - Predicted free surface and bed elevation visualisations for t = 5, 10, 15, 30, 100, 250, 1250 and 3000 s.


t = 5 s
Elevation (m)
3.5
3
2.5
2
1.5
1
0.5
0
0
5
10
15
20
25
30
35
0
5
10


t = 10 s
Elevation (m)
3.5
3
2.5
2
1.5
1
0.5
0
0
5
10
15
20
25
30
35
0
5
10


t = 15 s
Elevation (m)
3.5
3
2.5
2
1.5
1
0.5
0
0
5
10
15
20
25
30
35
0
5
10


t = 40 s
Elevation (m)
3.5
3
2.5
2
1.5
1
0.5
0
0
5
10
15
20
25
30
35
0
5
10

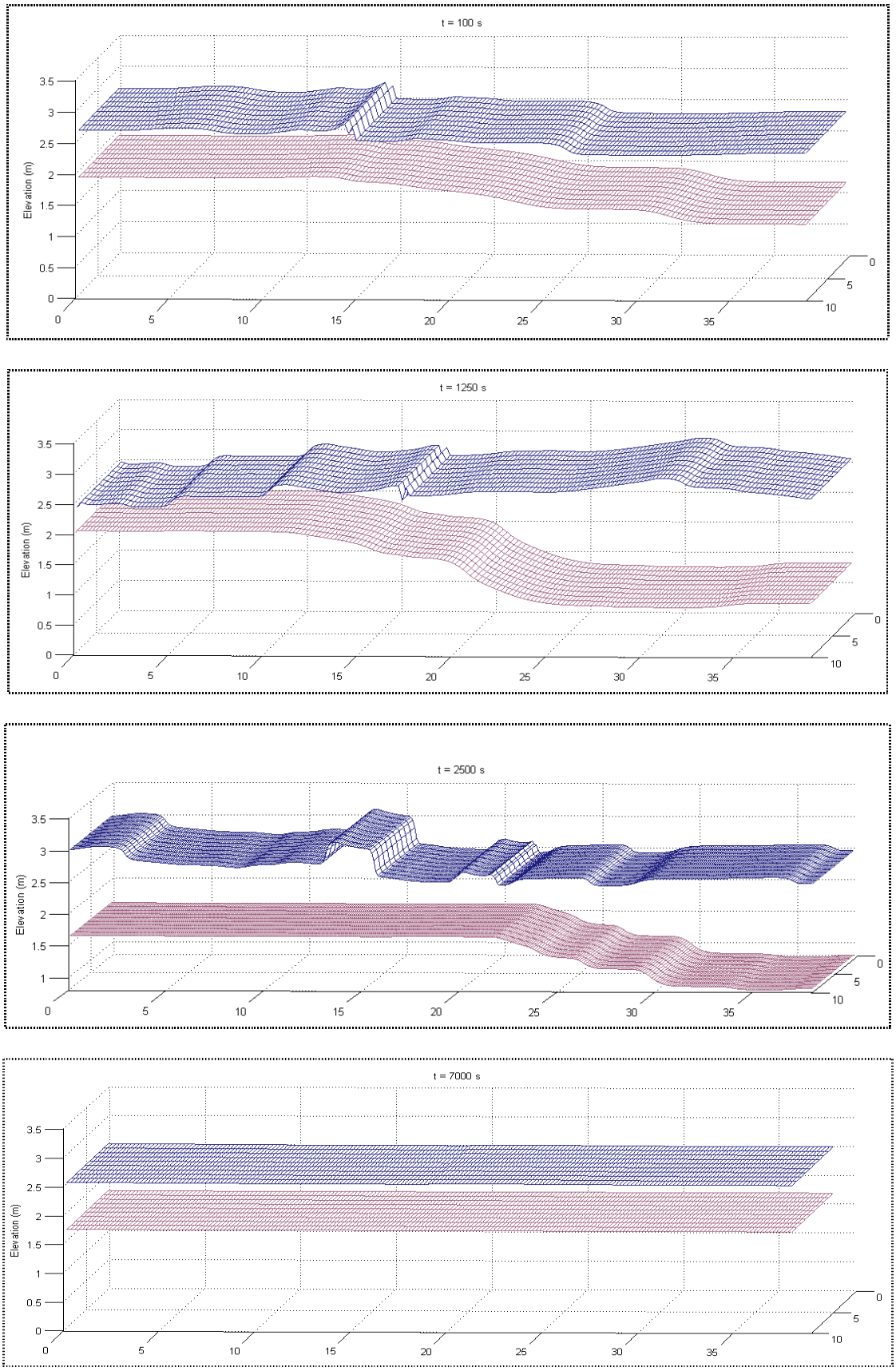
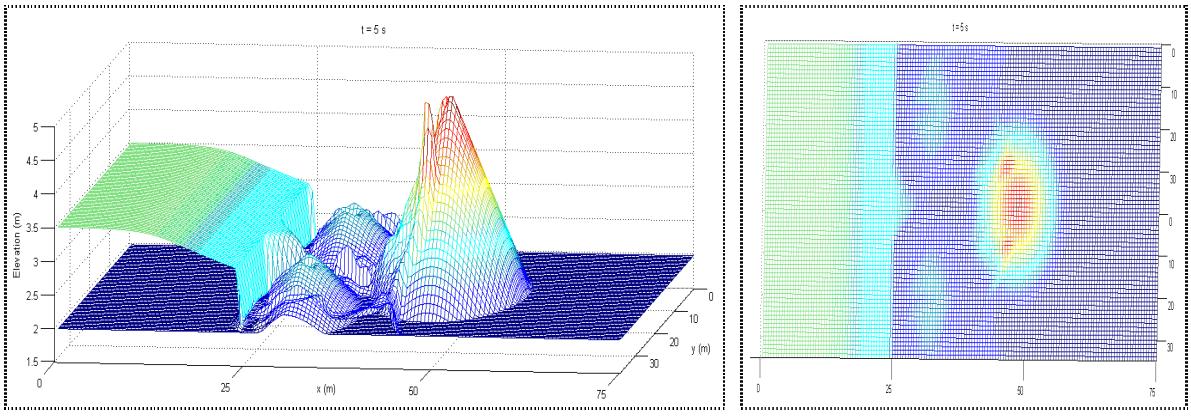
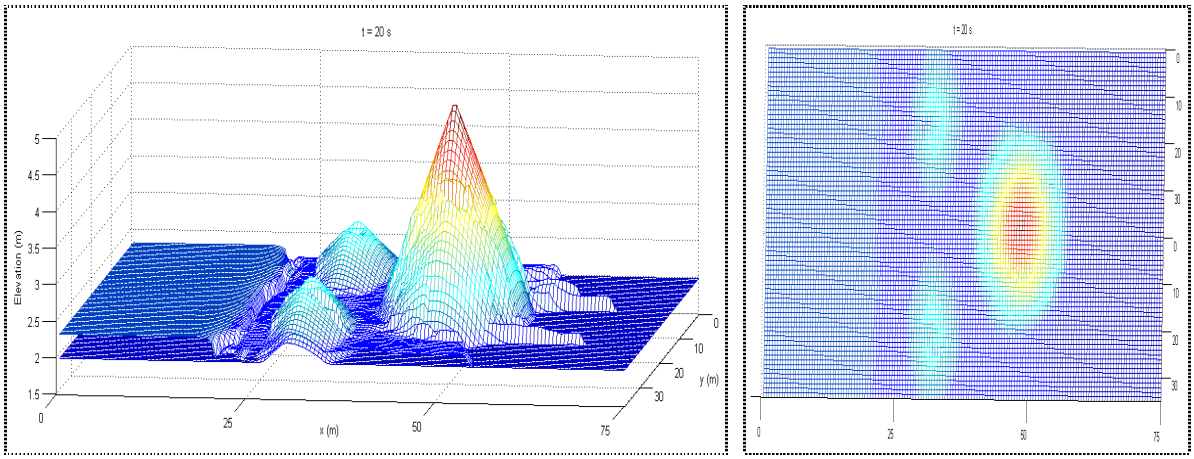


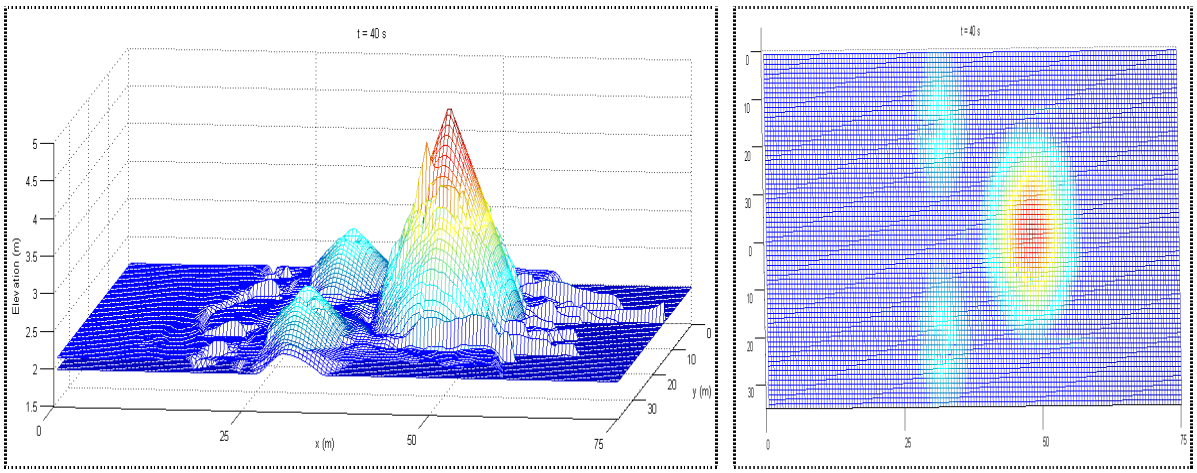
Fig. 5.18 Case 21.2. 2-D dam-break flow over a triangular obstacle with wetting and drying fronts and erodible bed (fixed boundaries) - Predicted free surface and bed elevation for t = 5, 10, 15, 40, 100, 1250, 2500 and 7000 s.


t = 5 s
Elevation (m)
x (m)
y (m)
t = 5 s

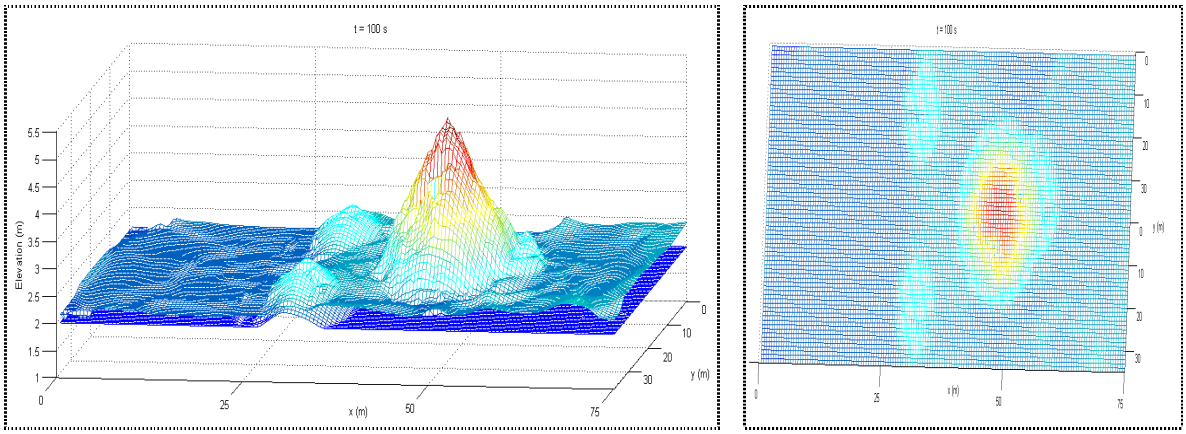
(a)


t = 20 s
Elevation (m)
x (m)
y (m)
t = 20 s

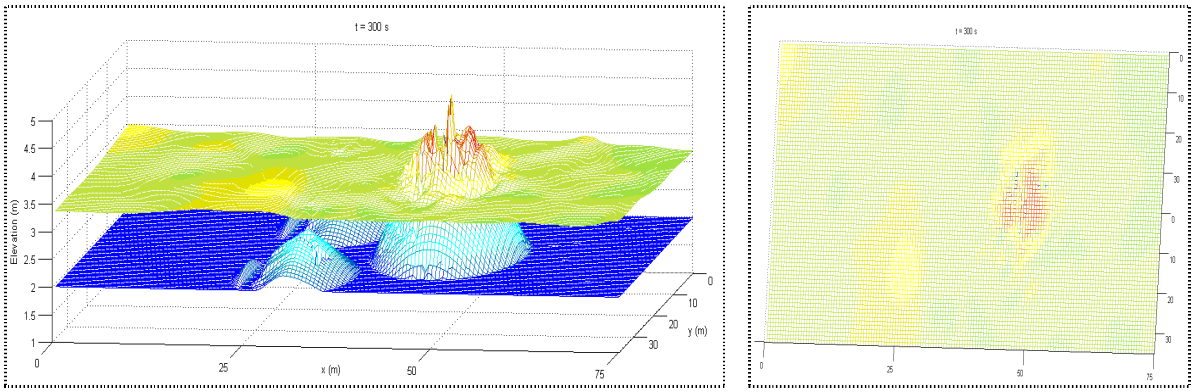
(b)


t = 40 s
Elevation (m)
x (m)
y (m)
t = 40 s

(c)



(d)



(e)

Fig. 5.19 Case 22. 2-D dam-break flow over three islands with wetting and drying and erodible bed – Free surface elevation visualisations and plan views for (a) t = 5 s, (b) t = 20 s, (c) t = 40 s, (d) t = 100 s and (e) t = 300 s.

Table 5.1			
Case 9: Variable density circular dam break – Parameter Study – Initial conditions			
Case	ρ_{in} (kg/m^3)	$(\rho h^2)_{\text{in}}$ (kg/m)	$(\rho h^2)_{\text{in}} / (\rho h^2)_{\text{out}}$
17.1	1000	4000	4
17.2	250	1000	1
17.3	200	800	0.8
17.4	100	400	0.4

Table 5.1 Case 17. Variable density circular dam break - Parameter Study – Initial conditions.

Table 5.2		
Case 17: Variable density circular dam break - Parameter Study – Equilibrium depth and radius		
Case	Equilibrium depth (m)	Equilibrium radius (m)
17.1	1	3.536
17.2	2	2.5
17.3	$\sqrt{5} \approx 2.236$	2.364
17.4	$\sqrt{10} \approx 3.162$	1.988

Table 5.2 Case 17. Variable density circular dam break - Parameter Study – Equilibrium depth and radius of the liquid circular liquid column of density ρ_{in} ..

CHAPTER 6 DEMONSTRATION CASE STUDY

6.1. Simulation of Partial Dam-Breach Flow in an Erodible Channel

This demonstration case study aims to show the ability of the numerical model to reproduce the complicated interaction between shallow flow and an erodible bed for a problem for which detailed laboratory measurements are available. The demonstration case combines most of the aspects examined throughout this research, i.e. variable density, wetting and drying, and sediment entrainment and deposition in a two-dimensional horizontal domain. The laboratory data are taken from Xia et al. (2010) who carried out experiments on a partial dam-break flow over an erodible bed in a flume in the Hydraulics Laboratory of Tsinghua University, China.

The main differences of the present numerical model compared to the one developed by Xia et al. (2010) are that it does not include the sediment transport in the form of bed load nor the process of horizontal diffusion. Nevertheless, the entrainment and the deposition of the sediment, as well as an additional equation for bed deformation are included, resulting to a successful representation of the exchange of sediment between the bed and the liquid-species mixture. On the other hand, the present numerical scheme is based on a Godunov-type finite volume HLLC approximate Riemann solver of the balanced horizontal hyperbolic variable density shallow water equations combined with MUSCL-Hancock time integration whereas Xia et al. (2010) use a finite volume method along with Roe-MUSCL scheme and solve the shallow water equations in unbalanced form.

The experiments were performed in a long channel of length 18.5 m and width 1.6 m (see Figure 6.1). The channel contained (from upstream to downstream): a thin walled dam, an

area of mobile bed composed of coal-ash, and an area with non-erodible bed. The thin-walled dam held back water of depth 0.4 m, and was situated a distance 2 m from the upstream wall of the flume. The coal-ash bed region occupies a distance of 4.5 m immediately downstream of the thin-wall. The far downstream boundary condition comprised free outflow. In the laboratory test, a 20 cm wide breach (from the crest down to the bed of the flume) was abruptly opened in the centre of the thin-walled dam at t = 0 s, which caused a shock-like bore to start travelling downstream. By t = 20 s after the partial dam break, bed elevations at certain cross sections were measured using an ultra-acoustic topographic surveying meter.

In the numerical model, the conditions for this test case are the following: g = 9.81 m/s^2; ρ_w = 1000 kg/m^3; the bed material at the mobile section of the channel is coal ash with density ρ_s = 2248 kg/m^3 and median diameter of 0.135 mm; the dry density is given as 720 kg/m^3, so the porosity of the bed was calculated as p = 0.68; the settling velocity is calculated by the formula of Soulsby (1997) as $w_s = \frac{v}{d}[(10.36^2 + 1.049(1-c)^{4.7} D_*^3)^{1/2} - 10.36]$, which takes into account the hindered settling of the sediment because of high concentration, where v is the kinematic viscosity of water taken as 1x10^{-6} m^2/s (assumed for temperature 20^{o}C as no information is given in the paper by Xia et al., 2010), d is the median diameter, c is the volumetric concentration of the sediment and D_* is the dimensionless grain size calculated as $D_* = \left[\frac{g(s-1)}{v^2}\right]^{1/3} d$, where s is the ratio of densities of grain (sediment) to water. Sediment deposition was calculated by the general formula $D = w_s c$. Entrainment was estimated by the formula of Cao et al. (2006) as

$$E = \begin{cases} \alpha(\theta - \theta_c) u h^{-1} d^{-0.2} & \text{, when } \theta \geq \theta_c \\ 0 & \text{, when } \theta < \theta_c \end{cases} \tag{6.1}$$

where h is the liquid-species mixture depth, α is an empirical dimensional coefficient (in this case, $\alpha = 1.2\text{x}10^{-6}$ $\text{m}^{1.2}$), $\theta = u_*^2/(s-1)gd$ is the Shields parameter, u_* is the friction velocity, and the threshold Shields parameter is calculated by the formula of Soulsby (1997) as $\theta_c = \frac{0.30}{1+1.2D_*} + 0.055\left[1 - \exp(-0.020D_*)\right]$.

The computational domain is also of length x_L = 18.5 m and width y_L = 1.6 m. Satisfactory grid convergence was achieved for spatial increments dx = 0.01 m and dy = 0.05 m. The time step is dt = 0.002 s. The bed shear stress is calculated with the Manning coefficient set to n = 0.015, as used by Xia et al. (2010). The dam at x = 2 m retains water with initial free surface elevation η = 0.4 m. The initial bed elevation is z_b = 0 m everywhere; the volumetric concentration and the depth averaged velocity are initially zero throughout the computational domain.

Figure 6.2 plots the post-dam-break bed elevation profiles at Cross-section 1 (situated at x = 2.5 m) and Cross-section 2 (situated at x = 3.5 m). The plots show the present results, and the experimental data and numerical model results obtained by Xia et al. (2010). For Cross-section 1 the present results are symmetrical as would be expected, given that the dam-break is symmetric with regard to the stream-wise central axis of the computational domain. The bed material and liquid conserve mass throughout the simulation. Comparison between the present numerical predictions and the experimental data shows that the numerical model overestimates the maximum erosion depth by 19.3 mm (i.e. 14% more than the experimental measurement). The simulation predicts a narrower deeper hole than that measured

experimentally. The numerical predictions of Xia et al. (2010) are closer to the experimental data, but underestimate the maximum erosion depth by 13%.

The side slopes of the scoured channel are about 1:3.75 (experimental data), and so are sufficiently steep that gravitational effects could have been important in the formation of the bed profile. The model channel has side slopes of 1:1 (approximately 45^{o} angle). This means that land slumping (not included in the present model) would have resulted in a wider channel profile, closer to the experimental results. An improvement would therefore be to include an algorithm which simulates the slumping effects that occur when the side slope exceeds the angle of repose.

For Cross-section 2, the present simulation results are again very symmetrical with respect to the central axis of the cross section. Here, the profile of the eroded bed is in satisfactory agreement with the experimental data: the numerical model underestimates the maximum erosion depth by 4.2 mm (i.e. 21% more than the experimental measurement), while the general pattern is very close to the observed one. The main difference is that the experimental bed surface line indicates the accumulation of the bed material (coal ash) at the side walls of the channel, whereas both the present model and that of Xia et al. (2010) do not predict any rise of the bed elevation above the initial zero-th line level for this cross section. This is partly because neither numerical model includes the effects of sidewall friction and boundary layers in the computations. Another reason might be that the current numerical model does not include horizontal diffusion either. Moreover, the numerical results of the present model are closer to the experimental data than the numerical predictions by Xia et al. (2010) which overestimate the maximum erosion depth by 20mm.

Figures 6.3 - 6.7 present the 3-D visualisation of the predicted free surface and the bed topography, as well as the relevant contour plots at times t = 0.5, 1, 2, 3, and 5 s. Figures 6.8 - 6.11 present the 3-D visualisation of the predicted free surface and the bed topography view at times t = 7.5, 10, 15 and 20 s.

Once the dam breach occurs at t = 0 s, a radial jet issues from the slot immediately scouring a hole in the bed. The jet is a supercritical flow, beyond which a radial bore forms downstream. By t = 0.5 s after the partial dam break (Figure 6.3), the water penetrating through the breach has begun to flood the erodible bed (coal ash) area. The evolution of both the free surface of the water-sediment mixture and the bed surface remain symmetrical in respect of the central axis of the channel. Fig 6.4 shows the free surface of the flow and the bed elevation at t = 1 s. At this time, the bore front (about 1.8 m downstream of the breach) has effectively straightened across the width of the channel. The bed has been scoured to a depth of about 0.0375 m, the trough close to 0.5 m downstream of the breach slot. Figure 6.5 depicts the situation at t = 2 s. The flow issuing from the breach has a nearly constant free surface elevation for a distance of about 2 m from the slot, while the scour hole is continuing to increase with trough depth of about 0.05 m at about 0.5 m from the slot. At a distance of almost 2 m from the slot there is a hydraulic jump to about 0.2 m depth, a free surface plateau region for almost 1 m, with the bore front having propagated to about 3.5 m from the breach. Here, the bore front is more uniform across the channel. Figure 6.6 shows the free surface and bed elevation visualisations at t = 3 s. The bore front is about 5 m from the breach slot, followed by the moving flow plateau region for about 1.5 m, the hydraulic jump, and an almost linear increase in water surface elevation from 0.14 m depth at the slot to 0.18 m depth about 3 m from the slot. There is very little evidence of transverse structure in the free surface elevation plot, whereas the scour hole is much more three-dimensional and is essentially absorbing the transverse energy content of the jet. The trough of the scour hole

remains about 0.5 m from the slot, though the hole extends about 2 m downstream from the slot, and about 1 m across the channel. Figure 6.7 shows the flow and bed patterns at t = 5 s. The scour hole has continued to extend downstream, reaching 4 m from the slot, with trough depth of about 0.08 m remaining close to the slot. The main bore front is now about 8 m downstream of the slot; the plateau has shortened to about 1 m, with the upstream jump having a smoother curved surface. The rapid breach flow seems to be forming a second wave, with a peak about 2 m from the slot, and a depression in the free surface at about 4 m from the breach. The free surface elevation above the erodible bed area has an irregular profile following the shape of the bed profile. After the liquid enters the non erodible bed the above effects occurring from the entrainment and deposition processes are fading out and while the bed profile remains intact (conserving the initial flat level), the free surface elevation appears more even with the wave induced by the dam break much smoother.

Figures 6.8 and 6.9 illustrate further evolution of the flow and bed at t = 7.5 and 10 s. The free surface elevation in the tank upstream of the breach has begun to fall to such a low level that the jet through the breach has weakened and the free surface settles progressively along the channel, downstream of the main bore and the moving hydraulic jump. Although the bore front continues to travel downstream, it is losing amplitude. The region between the bore front and hydraulic jump is also extending in length and flattening out. The trough has become fairly symmetric both along-channel and transverse to the channel. The scour hole has almost constant depth of about 0.1 m over about 4 m from the slot to the beginning of the fixed bed. By time t = 10 s (Figure 6.9), the wave caused by the partial dam break has almost reached the right hand side boundary of the computational domain.

Figures 6.10 and 6.11 show the situation at t = 15 and 20 s, after the main bore has exited the downstream open boundary. The scour hole has become deeper, with its nadir reaching

about 0.15 m deep at the interface between the fixed and erodible bed. A small step in the bed elevation is evident at the interface. By time t = 15 s (Figure 6.10), the liquid-species mixture is flowing outside of the domain from the right hand side open boundary so the overall free surface elevation is gradually decreasing. By time t = 20 s (Figure 6.11), the free surface over the erodible bed area covered by the coal ash starts settling to a new equilibrium condition while the last waves continue travelling downstream.

This case study provides a very valuable demonstration of the capability of the present numerical model to simulate unsteady shallow-water sediment motions involving mass, force, friction and stress. Despite the fact that the empirical formulas are used to estimate sediment entrainment and deposition, and that the bed load equations are not included in the model, the general picture produced by the numerical model is in reasonable agreement with the experimental data. Moreover, the model accurately conserves the mass and momentum of the liquid and sediment, and retains symmetry in the stream-wise direction. With further effort to enhance the calibration of the model to the laboratory data, and by including more physics such as slope effects, sidewall friction, horizontal diffusion, and bedload sediment transport, the model should be able to perform significantly better in future. The demonstration case indicates the potential of such models to reproduce a great variety of horizontal variable density shallow water flows encountered in environmental engineering.

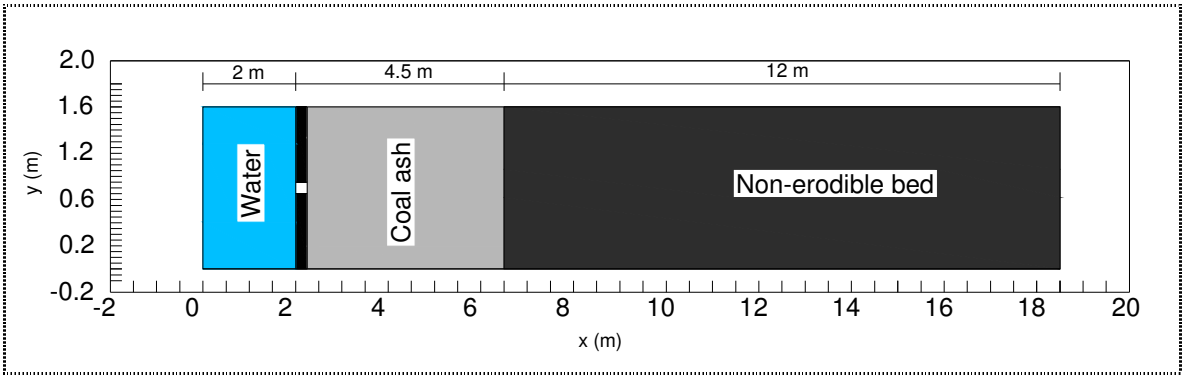


Fig. 6.1 Sketch illustrating the dam-breach flow experiment over a mobile bed as performed in Tsinghua University, China.

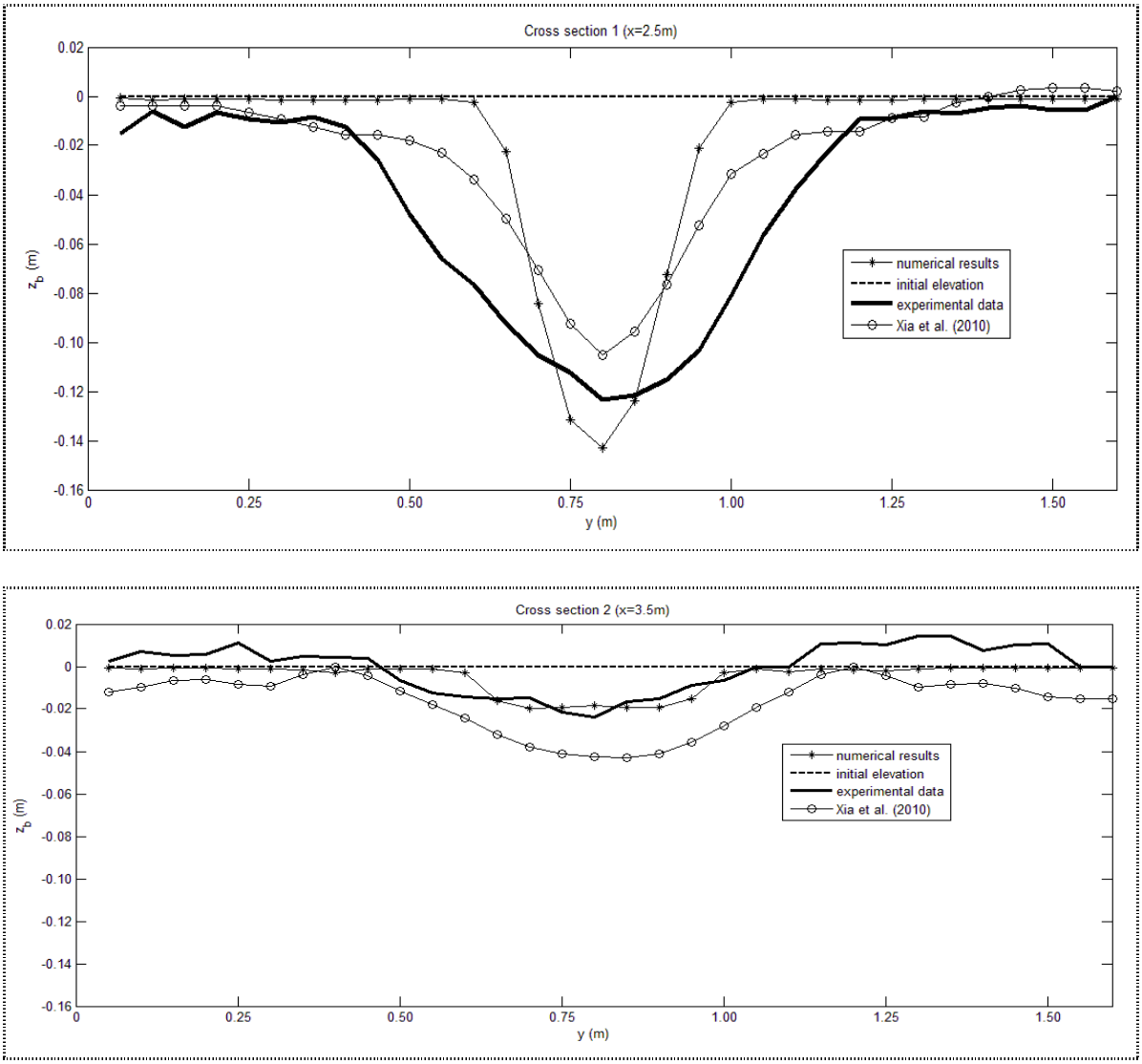


Fig. 6.2 Bed elevation at Cross-section 1 (x = 2.5 m) and Cross-section 2 (x = 3.5 m) - Comparison between present numerical model results, and the experimental data and numerical model results of Xia et al. (2010).

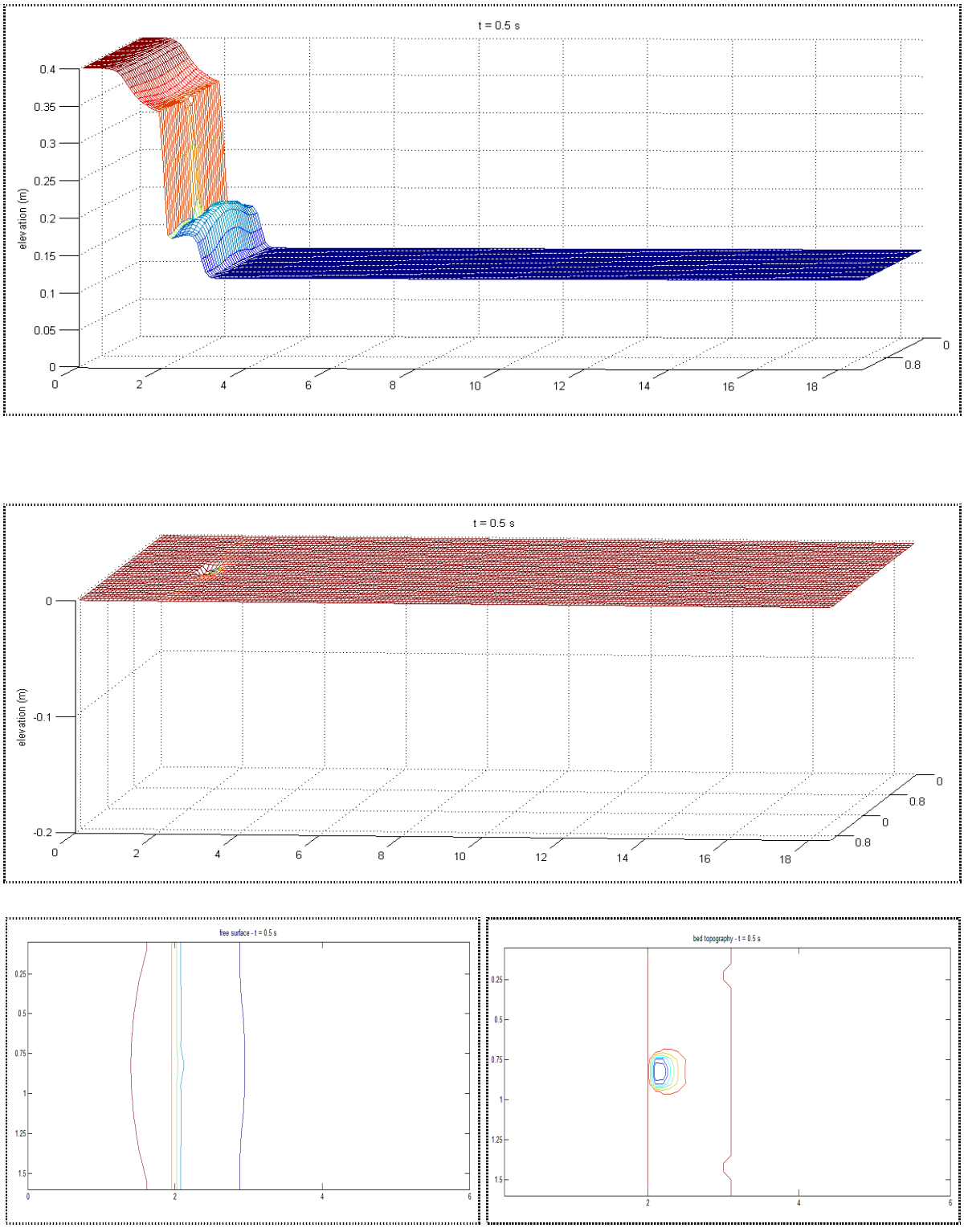


Fig. 6.3 Simulation of Partial Dam-Breach Flow in an Erodible Channel - Predicted free surface, bed elevation and relevant contour plots for $t = 0.5$ s.

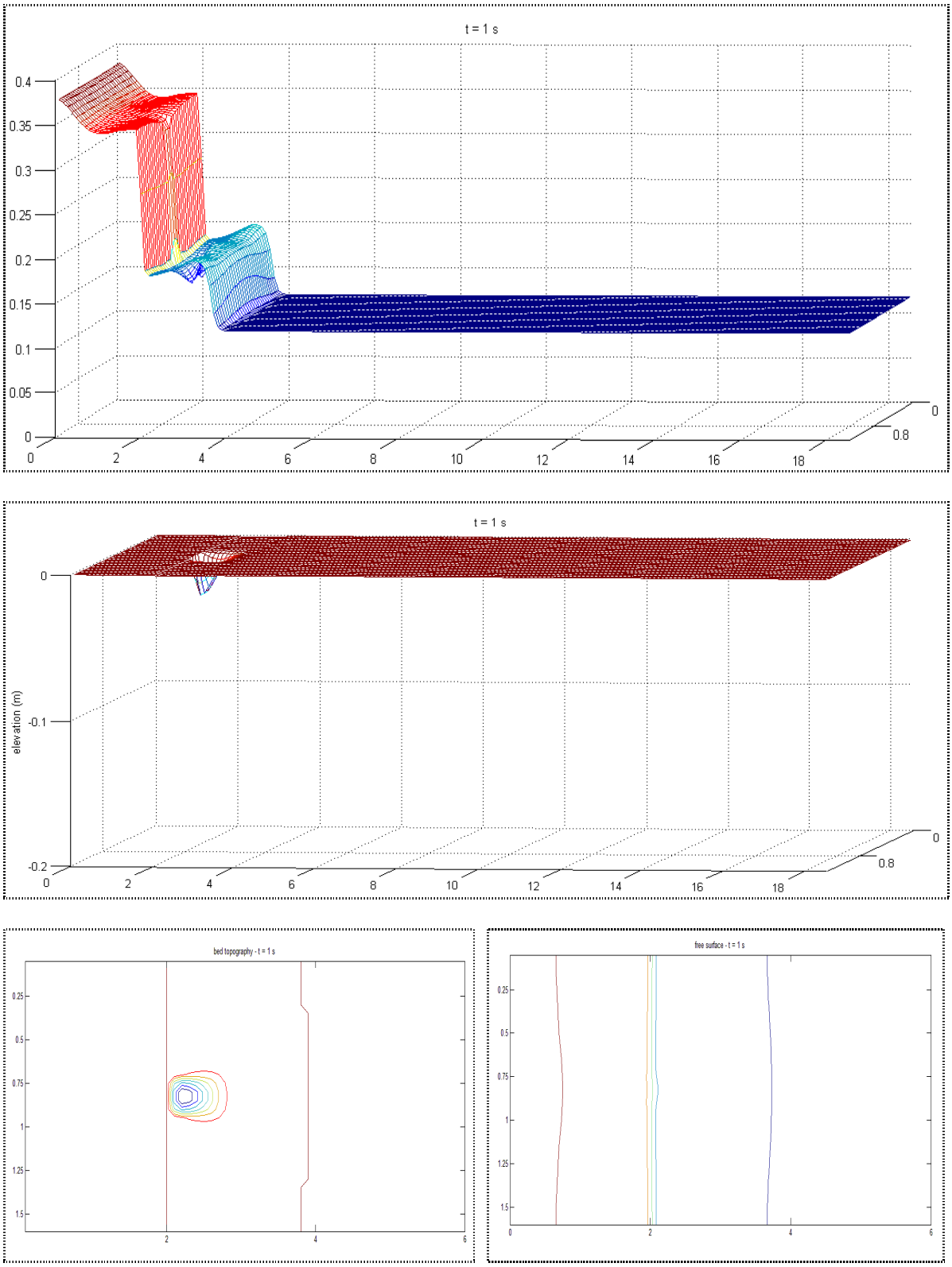


Fig. 6.4 Simulation of Partial Dam-Breach Flow in an Erodible Channel - Predicted free surface, bed elevation and relevant contour plots for t = 1 s.

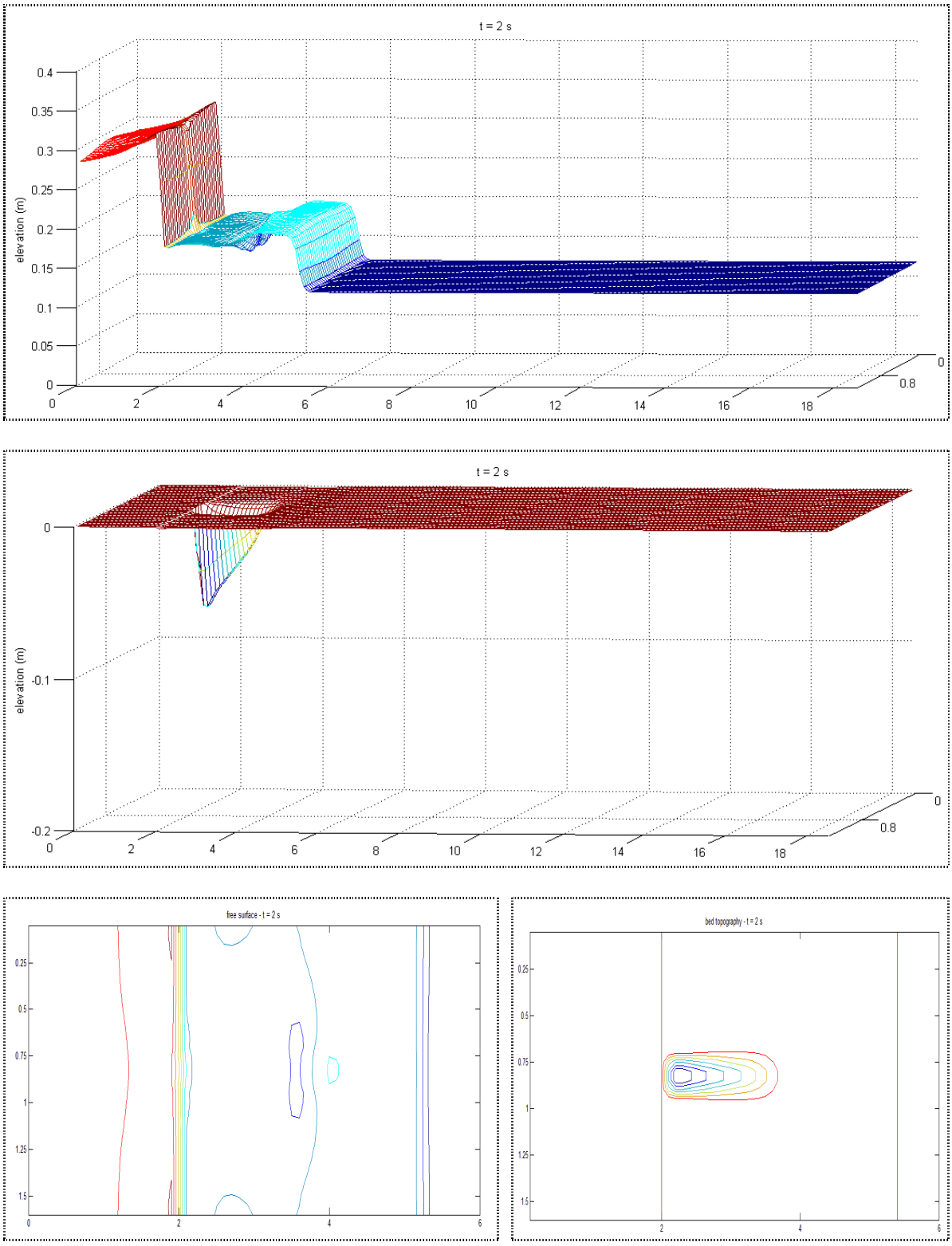


Fig. 6.5 Simulation of Partial Dam-Breach Flow in an Erodible Channel - Predicted free surface, bed elevation and relevant contour plots for $t = 2$ s.

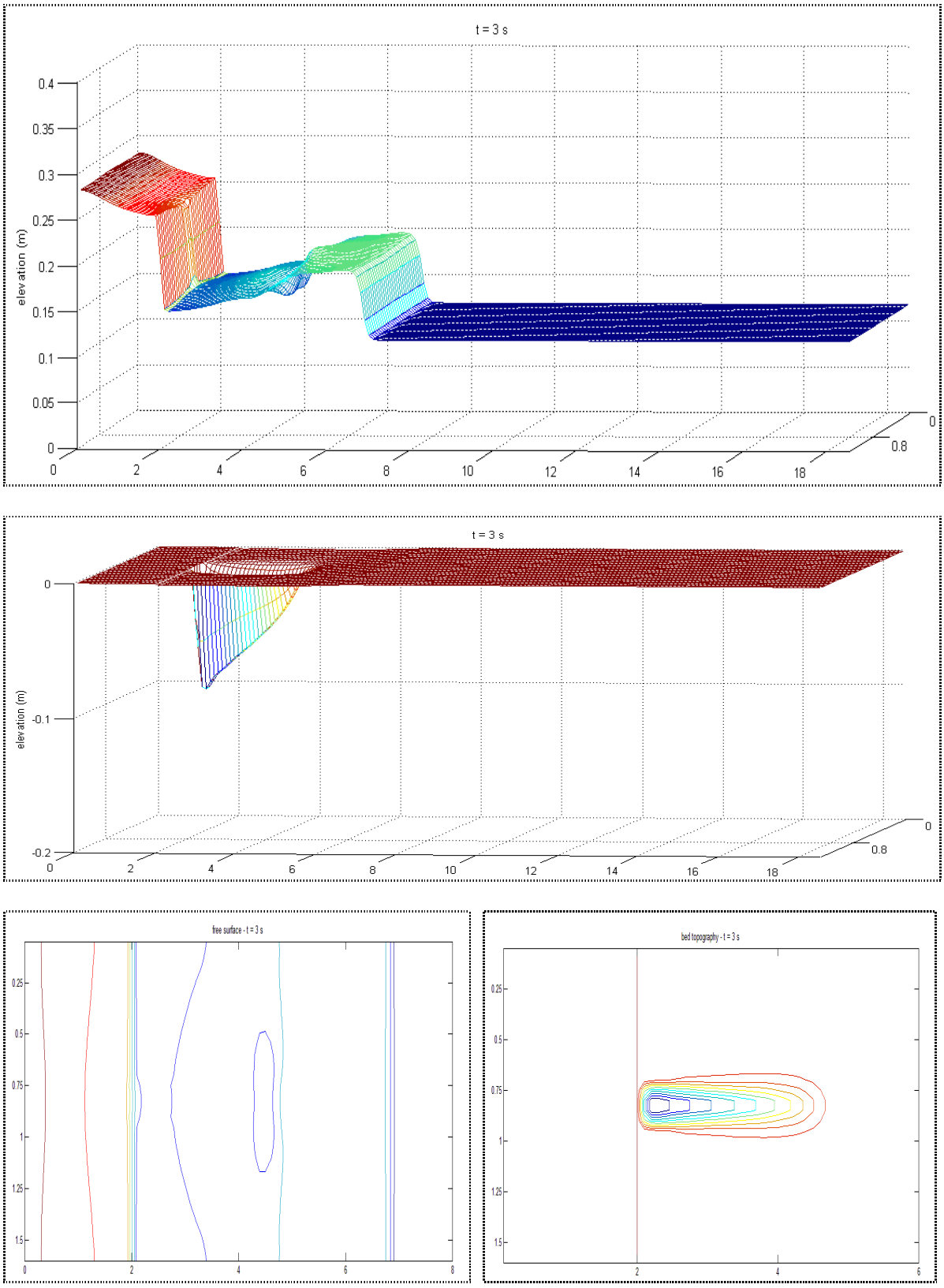


Fig. 6.6 Simulation of Partial Dam-Breach Flow in an Erodible Channel - Predicted free surface, bed elevation and relevant contour plots for t = 3 s.

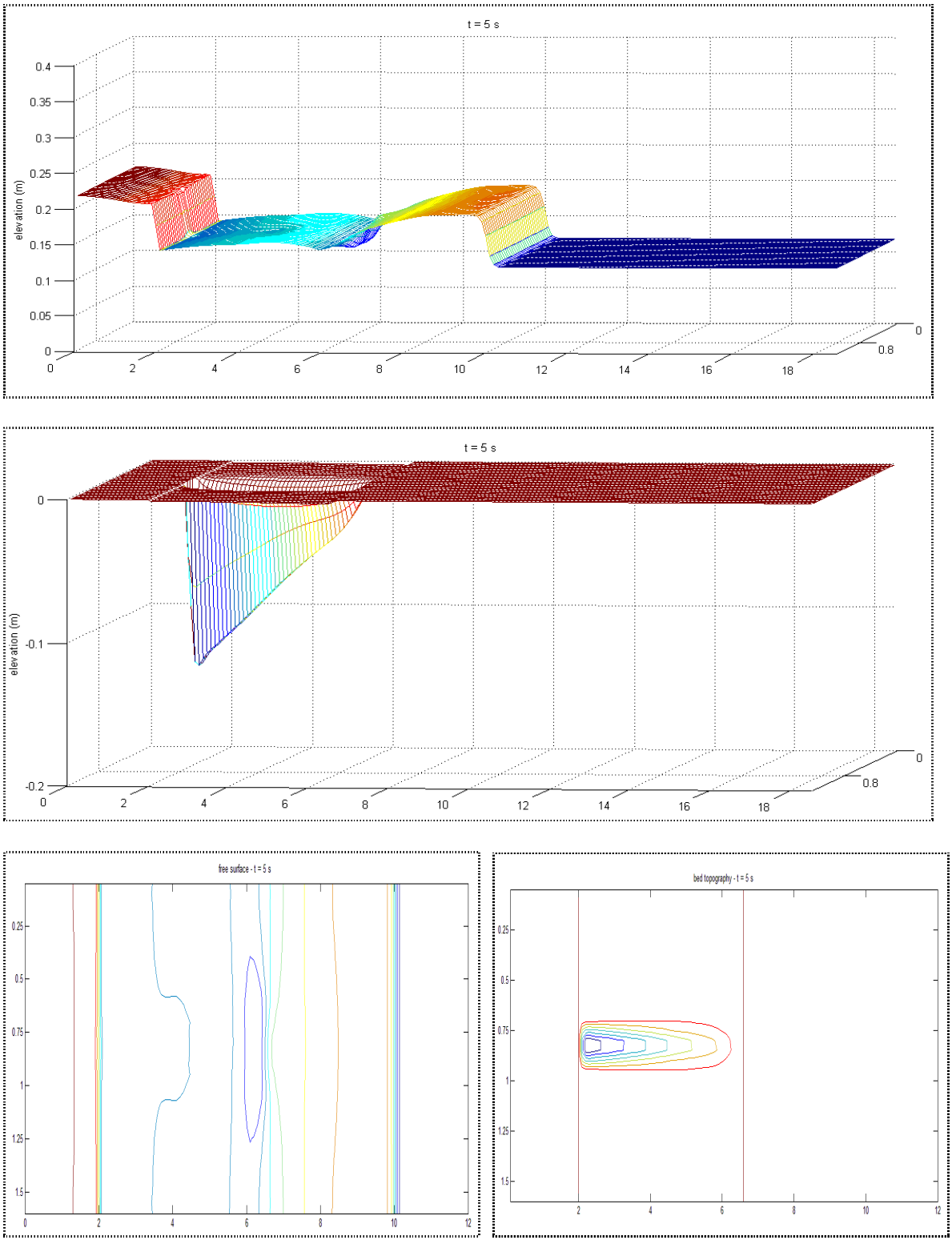


Fig. 6.7 Simulation of Partial Dam-Breach Flow in an Erodible Channel - Predicted free surface, bed elevation and relevant contour plots for $t = 5$ s.

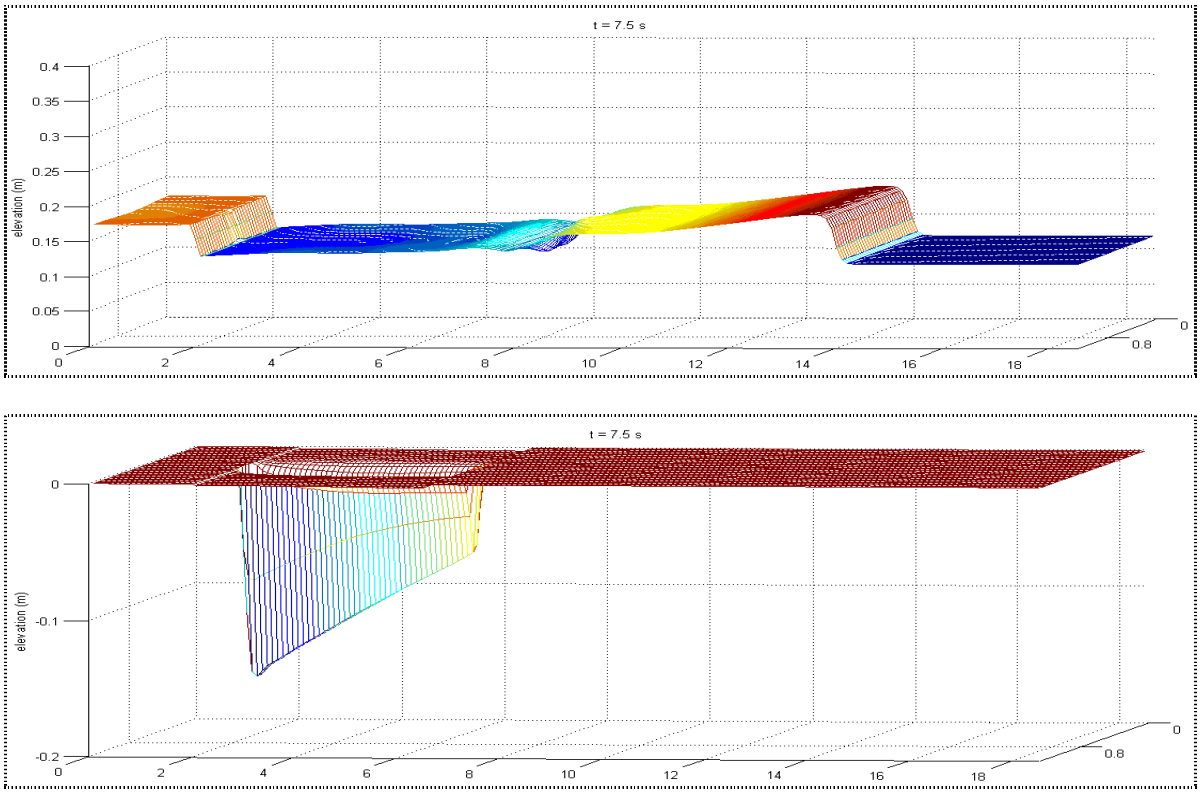


Fig. 6.8 Simulation of Partial Dam-Breach Flow in an Erodible Channel - Predicted free surface and bed elevation for t = 7.5 s.

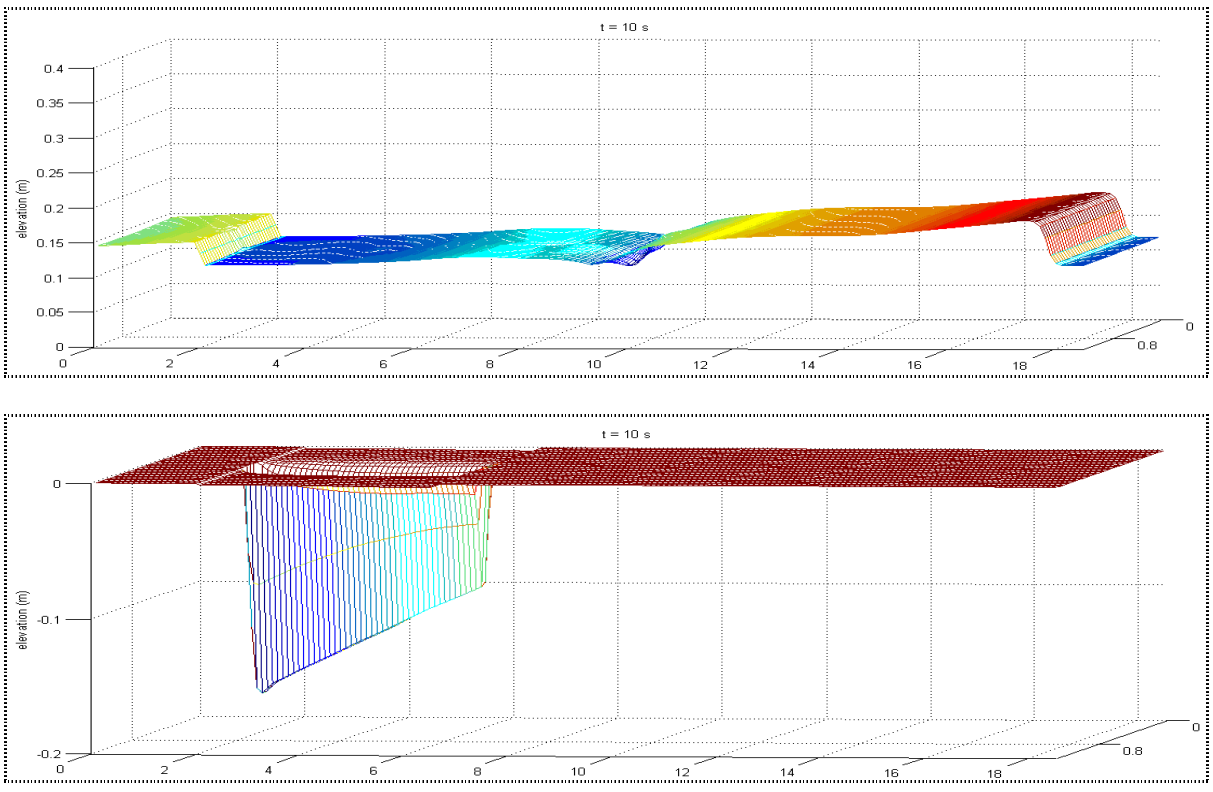


Fig. 6.9 Simulation of Partial Dam-Breach Flow in an Erodible Channel - Predicted free surface and bed elevation for t = 10 s.

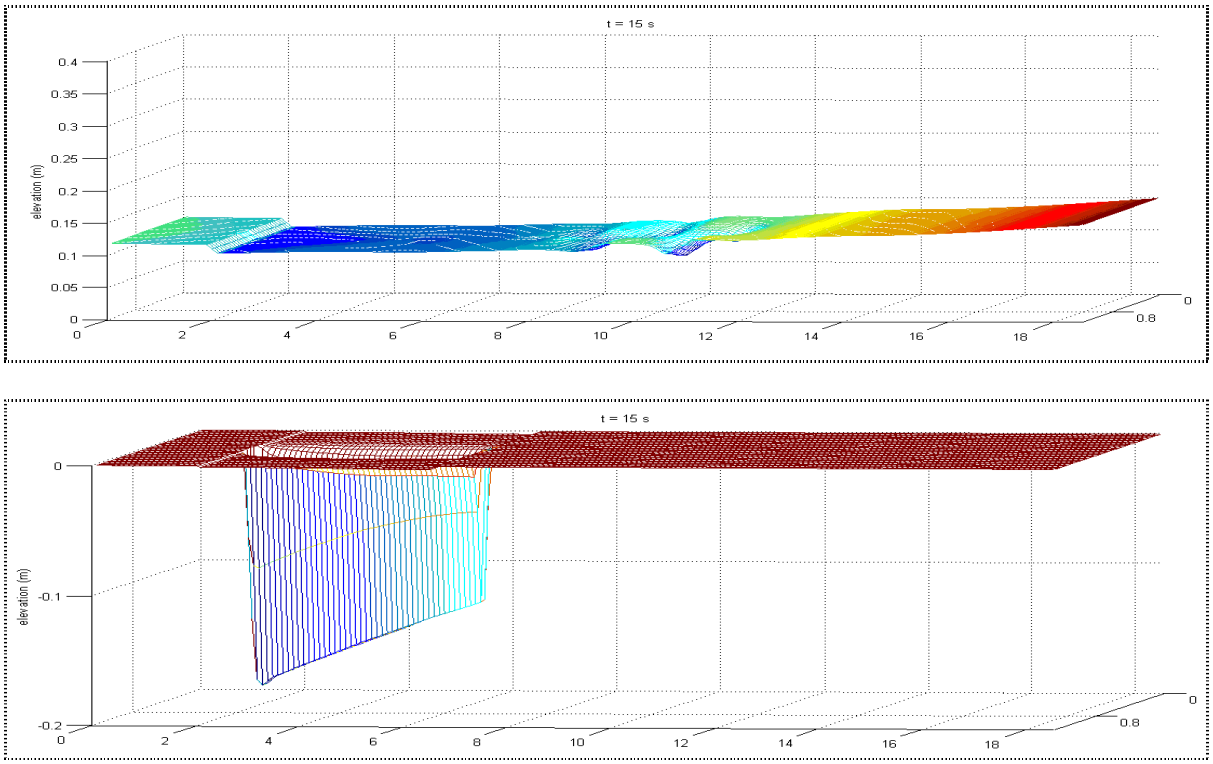


Fig. 6.10 Simulation of Partial Dam-Breach Flow in an Erodible Channel - Predicted free surface and bed elevation for t = 15 s.

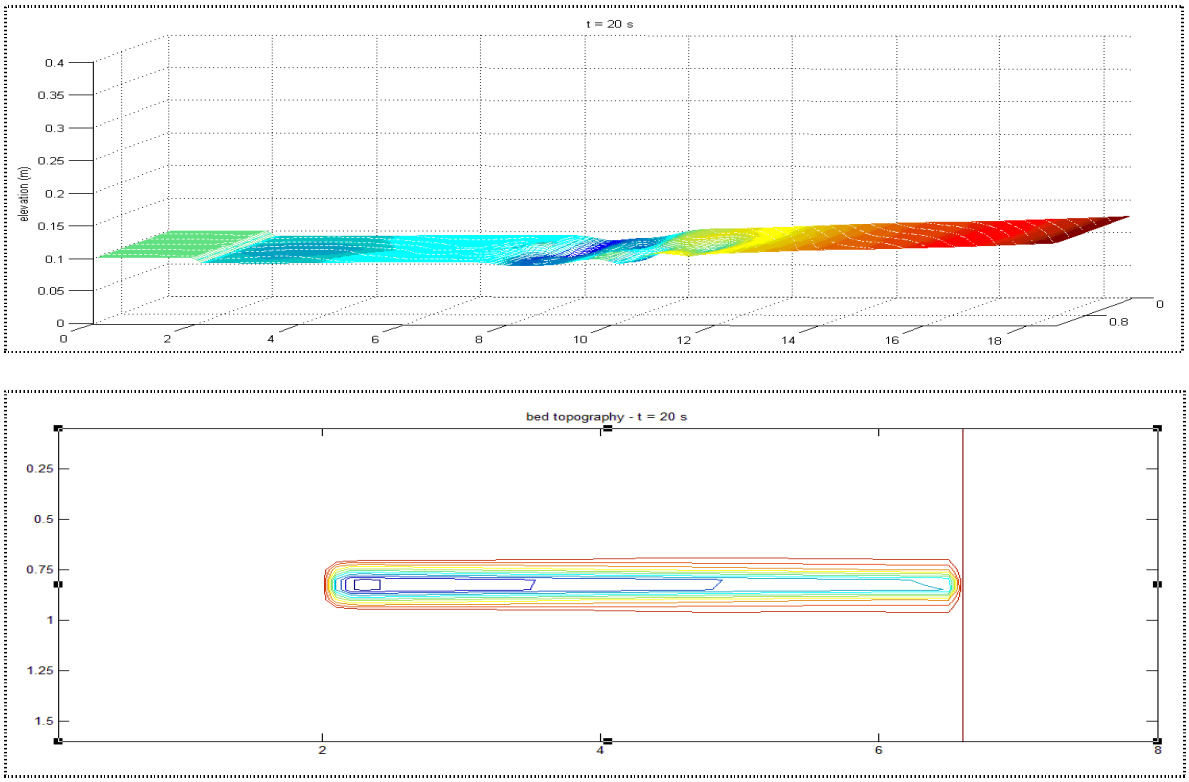


Fig. 6.11 Simulation of Partial Dam-Breach Flow in an Erodible Channel - Predicted free surface and bed elevation contour plot for t = 20 s.

CHAPTER 7 CONCLUSIONS AND RECOMMENDATIONS

7.1. Conclusions

This thesis deals with the topic of flood simulation in the context of sustainable water resources engineering. A numerical model was developed based on a Godunov-type finite volume HLLC approximate Riemann solver of the horizontal hyperbolic variable density shallow water equations combined with MUSCL-Hancock time integration and a non-linear slope limiter in order to estimate the values of fluxes across volume interfaces. The model was extended to deal with moving wet-dry fronts passing over non-uniform bed topography, and to include sediment entrainment and deposition processes. The numerical technique is based on the discrete form of the mass and momentum conservation equations. Problems of shallow flow over adverse slopes, overtopping, debris flows and bed erosion have all been modelled successfully.

Benchmark tests have been carried out in order to validate the model and the results compared to analytical solutions, experimental data, and alternative numerical results. The validation tests were chosen carefully in order to examine idealisations of realistic flood inundation cases involving locally complicated flows, such as dam-break flows over terrain with complicated topography. Convergence and stability tests were performed for each case considered. The present results indicate that the scheme works well for the range of the tests considered.

In order to model hyper-concentrated sediment laden and debris flows that characterise certain extreme flood events, the shallow water equations were modified so that they include the effect of density changes. The innovation of this work is that the new set of equations

can simulate wetting and drying processes occurring simultaneously at different elevations (such as lakes at different elevations), while representing a balanced form of the horizontal variable density shallow water equations. The model was validated against idealised problems (including still water in a domain of non-uniform bathymetry, and simple variable density tests) and then used to carry out a parameter study. Bed morphodynamics was included in the model by solving a conservation of bed mass equation in conjunction with the variable density shallow water equations. The addition of the algorithm that can encounter for the entrainment and the deposition of the sediment resulted in a robust model that can simulate a wide range of environmental flows.

The main differences/additions of the present numerical model in comparison to those developed by other researchers are the following:

- The current numerical model does not include a bed load sediment transport equation, unlike Yan (2010). Nevertheless, the model offers the option for entrainment and deposition of the sediment.

- There is no manipulation of the mixture density components (as in e.g. Cao et al., 2004, and Yan 2010). The present solver deals straightforwardly with a subset of the extended equations utilised by Cao et al. 2004. Although it incorporates less physics, the present model nevertheless gives a realistic representation of flood phenomena.

- The horizontal variable density shallow water equations are written in terms of free surface elevation as measured from a fixed horizontal datum, instead of the water depth or free surface elevation above still water level. This leads to a balance between the flux gradient and source terms in a Godunov solver, and permits application of wetting and

drying to problems involving flooding over complicated terrain (where ponds may form at different elevations). The approach has an additional advantage of preventing negative water depths occurring, causing inaccurate or even unstable results.

- A Godunov-type finite volume HLLC approximate Riemann solver of the horizontal hyperbolic variable density shallow water equations along with MUSCL-Hancock time integration has been used for first time to the author's knowledge. (It should be noted that Leighton et al. 2010 used Roe's Riemann solver in combination with Adams-Bashforth time integration to solve a depth-discharge form of the variable density shallow water equations.) The present numerical scheme is accurate, robust, and efficient, even in cases where shocks, discontinuities, or large gradients are involved.

The mathematical formulation of the model is based on the mass and the momentum conservation of the liquid-species mixture, the mass conservation of the species and the bed deformation equation. The balancing approach follows the principles outlined by Rogers et al. (2001, 2003), whereby an equilibrium solution is subtracted from the shallow water equations. This essentially means that the numerical model solves a deviatoric form of the hyperbolic governing equations. The numerical model was tested for a wide range of benchmark cases, including constant and variable density flows, wet/dry fronts, and erodible bed problems.

When applied to constant density flows, the variable density shallow flow equations effectively reduce to the constant density shallow water equations. For the constant density cases considered (e.g. dam-break, dry bed Riemann problems, damped free surface oscillations in a tank with parabolic bed, dam-break flow followed by interaction with a triangular obstacle, circular dam-break, and two-dimensional dam-break flow over three

islands), the results were in very good agreement with analytical solutions and alternative numerical data. The model results are stable and realistic for cases involving wetting and drying fronts, over simple or complicated bed topography. Finally, when required the symmetry of the results is preserved.

A parameter study was carried out for both one- and two-dimensional variable density problems following the study of Leighton (2005) and Leighton et al. (2010). The following conclusions are drawn from the one-dimensional results concerning the effect of a column of liquid of different density inserted in the middle of a liquid that otherwise has uniform density:

- The final equilibrium of the system depends on the ratio of the densities of the two liquids, provided the initial liquid depth depth is the same throughout the computational domain.

- When the density of the liquid occupying the central column is higher than the density of the liquid around it, the system's reaction after it is set free is similar to the one observed in a gravity dam break. Two bores (symmetric to the central axis of the domain) propagate outwards, followed by rarefaction waves travelling towards the opposite direction. The final equilibrium steady state leads to a wider central column with lower liquid depth than the initial column, in order to conserve mass.

- When both liquids have the same density, the system remains in equilibrium verifying that the numerical model is stable and conserves mass.

- When the density of the liquid occupying the central column is lower than the density of the liquid around it, the system's reaction is the reverse of the above. Two bores symmetric to the central axis of the domain initially propagate inwards, followed by rarefaction waves moving outwards. At the final equilibrium steady state, the central column is narrower and deeper than the initial column.

The 2-D variable density parameter study examined the effect of varying the ratio of species density to liquid density for a variable density circular dam-break driven by depth and/or density differences. The liquid depth of the central cylindrical dam was always greater than that of the surrounding liquid for all cases considered. The parameter varied was the hydrostatic pressure thrust ratio either side of the interface, i.e. $(\rho h^2)_{\text{in}} / (\rho h^2)_{\text{out}}$. The main conclusions are similar to those observed in the 1-D parameter study. When the hydrostatic pressure thrust ratio is higher than unity, the system's behaviour is close to that of the height difference (gravity) driven circular dam-break until the system settles to a new equilibrium steady state condition, when the central column has greater radius but lower liquid depth than the initial one in order for mass conservation to hold. When the hydrostatic pressure thrust ratio is equal to unity the system remains in equilibrium as expected. After several reflections of waves at the density interface and collisions between them at the centre of the cylindrical column, the system settles to a final equilibrium steady state condition where the central column has a higher liquid depth but smaller radius than the initial column.

The model was also tested for sediment entrainment and deposition processes, and the numerical predictions compared against semi-analytical solutions derived for certain erodible bed problems. When the entrainment and the deposition processes were considered separately, the numerical results were in almost perfect agreement with the analytical solutions. Nevertheless, for the combined case of simultaneous deposition and constant

entrainment of dilute suspended sediment in a flat-bottomed tank with intense mixing but no net flow different levels of agreement were obtained between the semi-analytical solutions derived and numerical results. More work is required to improve the semi-analytical model by a better choice of the species concentration equation. For the remaining cases (without semi-analytical solutions or experimental data available), the main objective was to reproduce the physical processes as realistically as possible. The final results look very reasonable even for complicated cases involving combinations of irregular topography, wetting and drying processes, and erodible bed material.

Finally, a demonstration case study was considered in order to illustrate the capability of the model to reproduce the complicated morphodynamic changes that occur to an erodible bed due to a dam-break flow in a long channel. The simulated cross-sectional bed elevation profiles (after the dam-break had passed) were in reasonable agreement with experimental measurements and alternative numerical predictions.

7.2. Recommendations

The thesis has presented a validated numerical model that can simulate a wide range of horizontal variable density shallow water environmental flows. Nevertheless, considerable future research is needed for the improvement of the model and its effectiveness when applied in real flood events.

- **Bed load sediment transport**

The momentum equation could be modified in order to include the mechanism of sediment transport in the form of bed load (Ashworth and Ferguson, 1989; Yan, 2010, Cui et al.,

2003). There are many formulas suggested in the literature (Soulsby, 1997; Einstein, 1942, Ferguson and Church, 2009; Van Rijn, 1984). Such an addition would enable the more accurate simulation of real flood events where the bed load is an important factor for the evolution of the flow (as e.g. in most of the rivers in the United Kingdom). The combination of the bed load and the entrainment and the deposition of the sediment terms in the set of equations solved would provide a complete picture of the contribution of the sediment to the flow (both fine and coarse sediment grains) and the change in bed morphodynamics, and thus enable the application of the numerical model in a wider range of debris flows.

- **Soil slumping**

Soil slump can occur where slopes have been oversteepened, vegetation is disturbed on a hillside, high velocity flows or excessive rainfall occur, causing bank erosion. Some soil slumps are large enough to cause significant changes in the flow. The movement can be relatively slow but the effect on the flow pattern can be very important for the accuracy of the simulation (Hao et al., 2011; Merritt et al., 2003). Consequently an additional equation that could accommodate such events could improve the performance of the numerical model.

- **Horizontal diffusion**

When the bed slope is very steep the mechanism of horizontal diffusion can vary the flow significantly (Stansby and Zhou, 1998; Basara and Younis, 1995; Zangl, 2002; Langhans, 2010). The addition of horizontal diffusion terms in the equations solved by the numerical model would be valuable in highly turbulent flows where the diffusion is dominating the flow pattern and the bank and/or bed erosion.

- **Lagrangian particle tracking**

A possible extension of the model would be to simulate floating particle dynamics (non-reacting and reacting particles) by using a Lagrangian particle tracking model based on the solution of the advection-diffusion equation. The underlying velocity field could be produced by the horizontal variable density shallow flow solver. This aspect of the model is of application to mixing and transport processes in environmental flows (see Liang et al. 2005, 2009). Using this method, water quality parameters, as temperature, salinity, BOD and COD, which are transported with the flow, can be traced throughout the simulation.

- **Additional validation of the numerical model**

It is suggested that the current numerical model is used for the simulation of a large scale event in order to check the accuracy and stability in lower resolution than the one validated in the thesis. A numerical model, such as the one presented, could be very useful for the prediction of the consequences that a potential flood can have to an urban or rural environment. It is recommended that the present model be extended to incorporate improved boundary fitting in order to model flows past multiple obstacles representing buildings, sinks and sources for the effects of drainage systems and underground spaces, infiltration of soil in green spaces, etc. Incorporation of the flood model within GIS software could lead to rapid, accurate simulation of the evolution of a wide range of potential flood events over complicated terrains and in urban areas. The only requirements are the digital terrain model of the area and the magnitude as well as the type of the expected event. The combined model could be useful for the development of reliable flood zonation maps, flood risk maps, and evacuation plans in case of emergency (see Pitt, 2008).

Moreover, if more laboratory or field observations are available, the results can be further compared and possibly any additional improvements towards the applicability of its features will be highlighted.

- **Smoothed particle hydrodynamics (SPH)**

A further recommendation is to couple the model presented in this thesis with smoothed particle hydrodynamics (SPH). The shallow water solver would be used to model large scale flow events, with SPH concentrating on localised features in locally important areas where fine-scale 3-D treatment is desirable (see Frank 2003, Liu et al. 2010 and Randles et al. 1996).

- **Unstructured hierarchical grid with adaptation**

The horizontal variable density shallow water model could be recoded on dynamically adaptive hierarchical (quadtree) grids that alter according to the flow geometry and internal flow features (see e.g. Borthwick et al. 2001a,b; Rogers et al. 2001, 2003; Liang et al. 2006, 2010). This should lead to a very efficient code that can deal with small and large scale features (e.g. flow around buildings in the urban environment).

- **Non-Newtonian fluids**

The present numerical model could be extended in order to simulate non-Newtonian fluid mechanics. This could be achieved by introducing a time-dependent relation between the shear stress and the shear rate of the fluid. Tensor-valued constitutive equations could be

added to the already existing ones in order to reproduce the change of the viscosity. Such a modification would enable simulation of non-Newtonian fluid flows such as sediment-laden debris flows where the fluid properties are more like those of a Bingham plastic than a Newtonian fluid.

REFERENCES

Abbott, M. B. (1979). *Computational Hydraulics*. Ashgate Publishing Co., Brookfield, Ct.

Abbott, M. B. (1992). *The theory of the hydrological model, or: the struggle for the soul of hydrology*. O'Kane JP, editor. Advances in theoretical hydrology. Elsevier; p. 237–254.

Alcrudo, F. and P. García-Navarro (1993). *A high-resolution Godunov-type scheme in finite volumes for the 2D shallow-water equations*. Int. J. Numer. Methods Fluids; **16**:489–505.

Anderson, M. G. and Bates, P. D. (2001). *Model validation: perspectives in hydrological science.* Wiley.

Armanini, A., L. Fraccarollo (1997). *Critical conditions for debris flow*. Debris Flow Hazard Mit.: Mech., Pred. and Assessment, ASCE.

Ashworth, P. J. and R. I. Ferguson (1989). *Size-selective entrainment of Bed Load in Gravel Bed Streams*. Water Resources Research; **25**(4): 627-634.

Balzano, A. (1998). *Evaluation of methods for numerical simulation of wetting and drying in shallow water flow models*. Coast. Eng.; **34**:83–107.

Basara, B. and B.A. Younis (1995). *Predictions of turbulent flows in dredged trenches*. J. Hydraul. Res.; **33**:813–824.

Bates, B. C., Z. W. Kundzewicz, S. Wu and J. P. Palutikof (2008). *Climate change and Water.* IPCC Secretariat, Geneva, 210 pp.

Bates, P. D., A. P. J. De Roo (2000). *A simple raster-based model for flood inundation simulation*. J. Hydrol.; **236**:54–77.

Bates, P. D., S. N. Lane, and R. I. Ferguson (2005). *Computational fluid dynamics: Applications in environmental hydraulics*. Wiley, Chichester, U.K.

Berz, G. (2000). *Flood disasters: lessons from the past – worries for the future.* Proceedings of the Institution of Civil Engineers, Water and Maritime Engineering, Mar.; **142**:3-8.

Beven, K. J. (2001). *Rainfall-runoff modelling—the primer*. Wiley.

Boris, J. P. and D. L. Book (1976). *Flux-Corrected Transport III. Minimal Error FCT Algorithms.* J. Comput. Phys.; **20**:397-431.

Borthwick, A. G. L. and B. Rogers (2001). *Coastal flow simulation using Roe's approximate Riemann solver.* ECCOMAS Computational Fluid Dynamics Conference 2001, Swansea, Wales, 4-7th September 2001, pp. 1-16.

Borthwick, A. G. L., S. Cruz León, and J. Józsa (2001a). *Adaptive quadtree model of shallow-flow hydrodynamics.* J. of Hydraulic Research; **39**(4):413-424.

Borthwick, A. G. L., S. Cruz León, and J. Józsa (2001b). *The shallow flow equations solved on adaptive quadtree grids*. Int. J. for Num. Methods in Fluids; **37**:691-719.

Boussinesq, J. (1877). *Essai sur la théorie des eaux courantes*. Mem. prés. div. Sav. Acad. Sci. Inst. Fr.; **23**:1–680.

Brocchini, M. and N. Dodd (2008). Nonlinear *Shallow Water Equation Modelling for Coastal Engineering.* Journal of Waterway, Port, Coastal and Ocean Engineering., Mar/Apr 2008.

Brufau, P., M. E. Vázquez-Cendon, P. García-Navarro (2002). *A numerical model for the flooding and drying of irregular domains*. International Journal for Numerical Methods in Fluids; **39**(3):247-275.

Brufau, P., P. García-Navarro, M. E. Vázquez-Cendón (2004). *Zero mass error using unsteady wetting–drying conditions in shallow flows over dry irregular topography*. Int J Numer Method Fluids; **45**:1047–82.

Brufau, P., P. Garcia-Navarro, P. Ghilardi, L. Natale and F. Savi (2000). *1D mathematical modelling of debris flow*. J. Hydraul. Res.; **38**(6):435–446.

Burger R., S. Evje, K. H. Karlsen and K. A. Lie (2000). *Numerical methods for the simulation of the settling of flocculated suspensions*. Chem. Engrg. J.; **80**:91–104.

Cao, Z., G. Pender, S. Wallis and P. Carling (2004). *Computational Dam-Break Hydraulics over Erodible Sediment Bed*. J. Hydraulic Eng., ASCE; **128**(3):306-321.

Cao, Z., G. Pender and P. Carling (2006). *Shallow water hydrodynamic models for hyperconcentrated sediment-laden floods over erodible bed*. Advances in Water Resources; **29**:546-557.

Charney, J. G., R. Fjortoft and J. von Neumann (1950). *Numerical integrations of the barotropic vorticity equation*. Tellus; **2**:237–254.

Chaudhry, M. F. (1993). *Open-channel flow*. Prentice-Hall, Englewood Cliffs, N.J.

Chen, C. L. (1988). *Generalized viscoplastic modelling of debris flow.* J. Hyd. Res., ASCE; **114**(3).

Chow, V. T., Maidment, D. R., Mays, L. W. (1988). *Applied hydrology.* Mc-Graw Hill, New York; 572 pp.

Cockburn, B. and C. W. Shu (1994). *Nonlinearly stable compact schemes for shock calculations*. SIAM J. Numer. Anal.; **31**:607–627.

Colella, P. and P. Woodward (1984). *The Piecewise parabolic Method (PPM) for Gasdynamical Simulations.* J. Comput. Phys.; **54**:174-201.

Cui, Y., G. Parker, J. Pizzuto, T. E. Lisle (2003). *Sediment pulses in mountain rivers: 2. Comparison between experiments and numerical predictions*. Water Resources, Water Resources Research; **39**(9):1240.

Cui, P., F. Q. Wei, S. M. He et al (2008). *Geo-hazards and countermeasures in 5.12 Wenchuan Earthquake Area*. Bull. Chin. Acad. Sci.; **23**(4):317–323 (in Chinese).

Cui, P., Y. Y Zhu, Y. S. Han, X. Q. Chen, J. Q. Zhuang, (2009). *The 12 May Wenchuan Earthquake-induced Landslide Lakes: Distribution and Preliminary Risk Evaluation*. Landslides; **6**:209-223.

Dean, R. and R. A. Dalrymple (1984). *Water Wave Mechanics for Engineers and Scientists*. Prentice-Hall, Englewood Cliffs, NJ, xi +353pp.

Dronkers, J. J. (1964). *Tidal Computations in Rivers and Coastal Waters.* North-Holland, New York.

Dube, S. K., P. C. Sinha and G. D. Roy (1985). *The numerical simulation of storm surges along the Bangladesh coast*. Dyn. Atmos. Oceans; **9**:121–133.

Egashira, S., K. Ashida (1987). *Sediment transport in steep slope flumes.* Proc. of Roc Japan Joint Seminar on Water Resources.

Egashira, S., K. Miyamoto, I. Takahiro (1997). *Constitutive equations of debris flows and their applicability.* Debris Flow Hazard Mit.: Mech., Pred. and Assessment, ASCE.

Einstein, H. A. (1942). *Formulas for the transportation of bed load.* Trans. Am. Soc. Civ. Eng.; **107**.

Emmett, W. W. (1970). *The hydraulics of overland flow on hillslopes.* US Geological Survey Professional Paper; **662 -A**.

Falconer, R. A. (1993). *An introduction to nearly horizontal flows*. In Coastal, Estuarial and Harbour Engineers Reference Book (Abbott, M. B. & Price, W. A., eds). E & FNSpon Ltd., London, 736 pp.

Ferguson, R. and M. Church (2009). *A critical perspective on 1D modeling of river processes: gravel load and aggradation in lower Fraser River*. Water Resources Research.

Fiedler, F. R., J. A. Ramirez (2000). *A numerical method for simulating discontinuous shallow flow over an infiltrating surface*. International Journal for Numerical Methods in Fluids; **32**:219-240.

Fraccarollo, L. (1995). *Un modello matematico bidimensionale per la mappatura del rischio da colata di detriti.* GNDCI; Linea **1**: 97-105.

Fraccarollo L, E. F. Toro (1995). *Experimental and numerical assessment of the shallow water model for two-dimension dam-break type problems*. J. Hydraul. Res.; **33**(6):843–63.

Frank J, S. Reich (2003). *Conservation properties of smoothed particle hydrodynamics applied to shallow water equations*. BIT Numerical Mathematics; **43**(1):41–55.

Garvine, R. W. (1987). *Estuary plumes and fronts in shelf waters: A layer model*. J. Phys. Oceanogr.; **17**:1877–1896.

George, D. L. (2008). *Augmented Riemann solvers for the shallow water equations over variable topography with steady states and inundation*. J. Comput. Phys.; **227:**3089-3113.

Givoli, D. (1991). *Non-reflecting boundary conditions.* J. Comput. Phys.; **94**, Issue 1, May.

Gulfnews (2010). *Floods in Pakistan worse than tsunami, Haiti*. Retrieved 2010-08-12.

Hansen, W. (1956). *Theorie und Errechnung des Wasserstandes und der Strömungen in Randmeeren nebst Anwendung*. Tellus; **8**(3):287–300.

Hao, H., C. Hartmann, J. Apichart, S. Siwaporn, S. Promsakha, G. Richard, A. Bruand and A. R. Dexter (2011). *Slumping dynamics in tilled sandy soils under natural rainfall and experimental flooding.* Soil and Tillage Research; **114**(1):9-17

Harten, A. (1983). *High Resolution Schemes for Hyperbolic Conservation Laws.* J. Comput. Phys.; **49**:357-293.

Harten, A., B. Engquist, S. Osher and S. R. Chakravarthy (1987). *Uniformly High Order Accurate Essentially Non-Oscillatory Schemes III.* J. Comput. Phys.; **71**:231-303.

Harten, A, P. D. Lax, B. van Leer (1983). *On upstream differencing and Godunov-type schemes for hyperbolic conservation-laws*. SIAM Rev.; **25**(1): 35–61.

Harten, A. and S. Osher (1987). *Uniformly high-order accurate nonoscillatory schemes*. I, SIAM J. Numer. Anal.; **24**:279–309.

Hendershott, M. C. (1981). *Long waves and ocean tides. Evolution of Physical Oceanography.* B. A. Warren and C. Wunsch, Eds., The MIT Press, 292–341.

High-level Expert Panel on Water and Disaster/UNSGAB (2009). *Water and Disaster.* URL:http://www.worldwatercouncil.org/fileadmin/wwc/Library/Publications_and_reports/Publication_Water_and_Disaster_lowres.pdf [16 February 2011].

Hines, N. (2007). *Biggest rescue effort in peacetime Britain*. URL: http://web.freepint.com/go/newsletter/64#feature [26 January 2011].

Hirano, M., T. Harada, M. E. Banihabib, K. Kawahara (1997). *Estimation of hazard area due to debris flow*. Debris Flow Hazard Mit.: Mech., Pred. and Assessment, ASCE.

Hirsch, C. (1990). *Numerical Computation of Internal and External Flows.* Computational Methods for Inviscid and Viscous Flows, Wiley; **2**.

Honda, N., S. Egashira (1997). *Prediction of debris flow characteristics in mountain torrents.* Debris Flow Hazard Mit.: Mech., Pred. and Assessment, ASCE.

Horritt, M. S., and P. D. Bates (2002). *Evaluation of 1D and 2D numerical models for predicting river flood inundation*. *J. Hydrol.*; **26**8(1–4): 87–99.

Hu, K., C. G. Mingham, D. M. Causon (2000). *Numerical simulation of wave overtopping of coastal structures using the nonlinear shallow water equations*. Journal of Coastal Engineering; **41**:433–465.

Hubbard, M. E. and P. García-Navarro (2000). *Flux difference splitting and the balancing of source terms and flux gradients*. J. Comp. Phys.; **165**(1):89–125.

Hughes, W. F. and J. A. Brighton (1999). *Schaum's Outline of Theory and Problems of Fluid Dynamics*. Third edition. New York: McGraw-Hill.

Hutter, K., B. Svendsen, and D. Rickenmann (1996). *Debris-flow modeling: A review.* Continuum Mech. Thermodyn.; **8**:1–35.

Jameson, A. and T. Baker (1983). *Solution of the Euler Equations for Complex Configurations.* AIAA Paper: 83-1929.

Jan, C. D. (1997). *A study on the numerical modelling of debris flow.* Debris Flow Hazards Mitigation: Mech., Pred. and Assessment, ASCE.

Jin, M., D. L. Fread (1997). *1D routing of mud/debris flow using NWS FLDWAV model.* Debris Flow Hazard Mit.: Mech., Pred. and Assessment, ASCE.

Kawahara, M., T. Umetsu (1986). *Finite element method for moving boundary problems in river flow*. Int J Numer Method Fluids 1986; **6**:365–86.

Laigle, D., P. Coussot (1997). *Numerical modelling of mudflows.* J. of Hyd. Eng.

Lamb, H. (1932). *Hydrodynamics*. 6th ed., Dover, New York.

Lambert, A. M. (1971). *The Making of the Dutch Landscape: An Historical Geography of the Netherlands.* Seminar Press, London.

Langhans, W. (2010). *Explicit 2nd order horizontal diffusion.* Institute for Atmospheric and Climate Science; URL: https://wiki.iac.ethz.ch/pub/Main/WolfgangLanghans/report_17.pdf [7 July 2010].

Laplace, P. S. (1775). *Recherches sur plusieur points du système du monde*. Mém. Acad. r. Sci.; **88**:75–182; **89**:177–267.

Lax, P. D. and B. Wenedroff (1960). *Systems of Conservation Laws*. Comm. Pure Appl. Math.; **13**:217–237.

Leighton, F. Z. (2005). *Numerical Modelling of Shallow Flows with Horizontal Density Variation*, Thesis (PhD), University of Oxford.

Leighton, F. Z., A. G. L. Borthwick and P. H. Taylor (2010). *1-D Numerical Modelling of Shallow Flows with Variable Horizontal Density*. International Journal for Numericak Methods in Fluids; **62**:1209–1231.

LeVeque, R. J. (1997). *Wave propagation algorithms for multi-dimensional hyperbolic systems*. J. Comput. Phys.; **131**:327-335.

Liang Q., A. G. L. Borthwick (2008). *Adaptive quadtree simulation of shallow flows with wet–dry fronts over complex topography.* Computers and Fluids, Elsevier.

Liang, Q., A. G. L. Borthwick, and P. H. Taylor (2005). *Chaotic mixing in a basin due to a sinusoidal wind field*. Int. J. for Num. Methods in Fluids; **47**:871-877.

Liang, Q., A. G. L. Borthwick, and P. H. Taylor (2006). *Wind-induced chaotic advection in shallow flow geometries. Part II: Non-circular basins*. J. of Hydraulic Research; **44**(2):180-188.

Liang, Q., P. H. Taylor, and A. G. L. Borthwick (2009). *Particle mixing and reactive front motion in chaotic but closed shallow flows*. Computers & Fluids; **38**(2):382-392.

Liggett, J. A. (1994). *Fluid Mechanics.* McGraw-Hill, New York, NY, USA.

Liu, M. B. and G. R. Liu (2010). *Smoothed Particle Hydrodynamics (SPH): an Overview and Recent Developments*. Archives of Computational Methods in Engineering; **17**:25-76.

MacCormack, R.W. (1969). *The Effect of Viscosity in Hypervelocity Impact Cratering*. AIAA Paper: 69-354.

Mason, S. J. et al. (1999). *The IRI Seasonal Climate Prediction System and the 1997/98 El Niño Event*. Bulletin of the American Meteorological Society; **80**:1853–1873.

McDowell, D. M. and B. A. O'Connor (1977). *Hydraulic Behaviour of Estuaries*. Macmillan Press, London.

McMichael, A. J., A. Haines, R. Slooff, S. Kovats (1996). *Climate Change and Human Health* (World Health Organization, Geneva, 1996).

Merritt, W.S., R. A. Letcher and A. J. Jakeman (2003). *A review of erosion and sediment transport models*. Environmental Modelling and Software; **18**:761–799.

Mingham, C. G., D. M. Causon (1998). *High-resolution finite-volume method for shallow water flows.* Journal of Hydraulic Engineering; **124**:605– 614.

Mizuyama, T., A. Yazawa (1987). *Computer simulation of debris flow depositional processes*. Proc. of the Corvallis Symp.

Néelz, S., and G. Pender (2007). *Sub-grid scale parameterisation of 2D hydrodynamic models of inundation in the urban area.* Acta Geophys. Pol.; **55(**1):65–72.

Nihoul, J. C. J. and F. C. Ronday (1975). *The influence of the ''tidal stress'' on the residual circulation*. Tellus; **27**(5):484–490.

O'Brien, J. S., P. J. Julien, W. T. Fullerton (1993). *Two-dimensional water flood and mudflow simulation.* J. of Hyd. Eng.; **119**(2).

Ogink, H. J. M. (1986). *Schatting van ruwheidslengte van zomer- bed Boven-Rijn en Waal.* (in Dutch). Rapport R2017. Water- loopkundig Laboratorium, Delft.

Osher, S. and J. A. Sethian (1988). *Fronts Propagating with Curvature De-pendent Speed Algorithms Based on Hamilton-Jacobi Formulations*. J.Computational Physics; **79**:121-49.

Pietz, D. (2002). *Engineering the State: The Huai River and Reconstruction in Nationalist China 1927–1937.* Routledge.

Pitt, M. (2008). *Learning lessons from the 2007 floods - Full Report*. URL: http://webarchive.nationalarchives.gov.uk/20100807034701/http://archive.cabinetoffice.gov.uk/pittreview/_/media/assets/www.cabinetoffice.gov.uk/flooding_review/pitt_review_full%20pdf.pdf [26 January 2011].

Platzman, G. (1972). *Two-dimensional free oscillations in natural basins*. Journal of Physical Oceanography; **2**: 117–138.

Priestnall, G., J. Jaafar, and A. Duncan (2000). *Extraction of Urban Features from LiDAR Digital Surface Models*. Computers, Environment & Urban Systems; **24**:65–78.

Randles, P.W. and L. D. Libersky (1996). Smoothed particle hydrodynamics: Some recent improvements and applications. Comput. Methods Appl. Mech. Eng.; **139**:375–408.

Remaki, M., W.G. Habashi, D. Ait-Ali-Yahia, A. Jay (2002). *A Discontinuous Galerkin method for Multiple Pure Tone Noise in Gas Turbines*. The 40th AIAA Aerospace Science Meeting and Exhibit 14–17, Reno, USA.

Rickenmann, D., T. Koch (1997). *Comparison of debris flow modelling approaches*. Debris Flow Hazards Mitigation: Mech., Pred. and Assessment, ASCE.

Ridderinkhof, H., J. T. F. Zimmermann and M. E. Philippart (1990). *Tidal exchange between the North Sea and Dutch Wadden Sea and mixing time scales of the tidal basins*. Neth. J. Sea Res., **25**:331–350.

Ritter, A. (1892). *Die Fortpflanzung der Wasserwellen*. Zeitschrift des Vereines Deutscher Ingenieure; **36**(33):947–954.

Roache, P. J. (1998). Verification *and Validation in Computational Science and Engineering*, Hermosa Publishers.

Roe, P.L. (1981). *Approximate Riemann Solvers, Parameter Vectors and Difference Schemes*. J. Comput. Phys.; **43**:357-372.

Rogers, B.D., A.G.L. Borthwick, and P.H. Taylor (2003). *Mathematical balancing of flux gradient and source terms prior to using Roe's approximate Riemann solver*. J. of Computational Physics; **192**(2):422-451.

Rogers B. D., M. Fujihara, A. G. L. Borthwick (2001). *Adaptive Q-tree Godunov-type scheme for shallow water equations*. International Journal for Numerical Methods in Fluids 2001; **35**:247–280.

de Saint-Venant, A. J. C. (1871). *Thorie du mouvement non-permanent des eaux, avec application aux crues des rivires et a l'introduction des mares dans leur lit*. C. R. Acad. Sc. Paris; **73**:147–154.

Sampson J, A. Easton, M. Singh (2005). *Moving boundary shallow water flow above parabolic bottom topography.* ANZIAM J 2006; **47**(EMAC2005):C373–87.

Schlichting, H. (1968). *Boundary Layer Theory*. McGraw-Hill, New York: 433.

Shiach J., C. Mingham, D. Ingram, and T. Bruce (2004). *The applicability of the shallow water equations for modelling violent wave overtopping.* Coastal Eng.; **51**:1–15.

Shieh, C. L., C. D. Jan, Y. F. Tsai (1996). *A numerical simulation of debris flow and its application*. Natural Hazard; **13**:39- 54.

Shokin, Y. I., L. B. Chubarov, A. G. Marchuk et al. (1989). *Numerical Experiment in the Tsunami Problem*. Novosibirsk: Nauka.

Singh, V. P. (1996). *Kinematic wave modelling in water resources: surface water hydrology*. Wiley, New York; 1399 pp.

Singh, V.P. (2001). *Kinematic wave modelling in water resources: a historical perspective*. In Hydrological Processes; **15**: 671 – 706.

Soulsby, R. L. (1997). *Dynamics of Marine Sands*. Thomas Telford Ltd, 248 pp.

Stansby, P. K. and J. G. Zhou (1998). *Shallow-water flow solver with non-hydrostatic pressure: 2D vertical plane problems*. International Journal for Numerical Methods in Fluids; **28**:541– 563.

Stelling, G. S. (1983). *On the construction of computational methods for shallow water flow problems*. Ph.D. thesis, Delft University of Technology.

Takahashi, T. (1991). *Debris Flow*. Balkema, Rotterdam.

Takahashi, T., H. Nakagawa (1994). *Flood/debris flow hydrograph due to collapse of a natural dam by overtopping*. J. of Hydroscience and Hyd. Eng.

Takahashi, T., H. Nakagawa, S. Kuang (1987). *Estimation of debris flow hydrograph on varied slope bed.* Proc. of the Corvallis Symp.

Takahashi, T., H. Tsujimoto (1985). *Delineation of the debris flow hazardous zone by a numerical simulation method.* Int. Symp. On Erosion, Debris Flow and Disast. Prevent.

Tan, W. Y. (1992). *Shallow Water Hydrodynamics: Mathematical Theory and Numerical Solution of a Two-Dimensional System of Shallow Water Equations*. Elsevier, Amsterdam.

Thomas, T. G., J. J. R. Williams (1995). *Large eddy simulation of turbulent flow in an asymmetric compound open channel*. Journal of Hydraulic Research; **33**:27–41.

Thompson, K. W. (1987). *Time dependent boundary conditions for hyperbolic systems.* J. Comput. Phys.; **68** (January).

Toro, E. F. (1999). *Riemann Solvers and Numerical Methods for Fluid Dynamics*. 2nd ed., Springer-Verlag.

Toro, E. F. (2001). *Shock-capturing methods for free-surface shallow flows*. Wiley.

Trenberth, K. E., T. J. Hoar (1996). *The 1990-1995 El Niño-Southern Oscillation Event: Longest on Record*. Geophysical Research Letters; **23**(1):57–60.

van Leer, B. (1979). *Towards the Ultimate Conservative Difference Scheme V; A Second-order Sequel to Godunov's Sequel*. J. Comput. Phys.; **32**:101-136.

van Leer, B. (1985). *On the relation between the upwind-differencing schemes of Godunov, Enguist – Osher and Roe*. SIAM Journal of Scientific and Statistical Computing; **5**:1-20.

Van Rijn, L.C. (1984). *Sediment transport, Part I: Bed load transport.* J. Hydraul. Eng., ASCE; **110**(HY1O): 1431-1456.

Van Rijn, L. C. (1993). *Principles of Sediment Transport in Rivers*, Estuaries and Coastal Seas, Aqua, Amsterdam.

Vreugdenhil, C. B. (1994). *Numerical Methods for Shallow-Water Flow*. Kluwer Academic Publishers.

White, W.R. (2001). *Water in rivers: flooding*. Water and Maritime Engineering; **148**(2):107-118.

Wind, H. G. and C. B. Vreugdenhil (1986). *Rip-current generation near structures*. J. Fluid Mech.; **171**:459–476.

Xia, J., B. Lin, R. A. Falconer and G. Wang (2010). *Modelling dam-break flows over mobile beds using a 2D coupled approach*. Advances in Water Resources.; **33**:171–183.

Yan, K. (2010). *Coastal Flood Inundation and Morphodynamic Change.* D.Phil. Thesis, University of Oxford U.K.

Younis, B. A. (1996). *Progress in turbulence modelling for open channel flows*. In: Anderson, M.G., Walling, D.E., Bates, P.D. (Eds.). Floodplain Processes, Wiley, Chichester, pp. 299–332.

Whetton, P. H., A. M. Fowler, M. R. Haylock, and A. B. Pittock (1993). *Implications of climatic change due to the enhanced greenhouse effect on floods and droughts in Australia.* Climatic Change; **25**:289–317.

Wild, M. (2010). *Looking beyond energy security to food supply*. URL: http://peakgeneration.blogspot.com/p/environmental-resource-collapse.html [26 January 2011].

Winchester, S. (1996). *The River at the Center of the World*. London: Penguin.

Zangl, G. (2002). *An improved method for computing horizontal diffusion in a sigma-coordinate model and its application to simulations over mountainous topography*. *Mon. Wea. Rev.*; **130:**1423–1432.